Controller Design and Experimental Validation for Connected Vehicle Systems subject to Digital Effects and Stochastic Packet Drops

by

Wubing Qin

A dissertation submitted in partial fulfillment
of the requirements for the degree of
Doctor of Philosophy
(Mechanical Engineering)
in the University of Michigan
2018

Doctoral Committee:

Associate Professor Gábor Orosz, Chair
Professor Jessy W. Grizzle
Associate Professor Kenn R. Oldham
Associate Professor Jeffrey T. Scruggs

Wubing Qin

wubing@umich.edu

ORCID iD: 0000-0003-2096-3405

To my parents and sister, with love and gratitude.

A C K N O W L E D G M E N T S

First of all, I would like to express my gratitude to my advisor, Prof. Gábor Orosz, who led me to the incredible world of research. Over the past few years, it is him who provided me with extensive support, recommendations and encouragement. I also would like to thank all my committee members for their insightful comments and helpful suggestions. Then I would like to thank National Science Foundation (NSF) for providing the funding support – NSF grant 1300319 – for this research. Last but not least, I would also like to thank all the members for their contributions in Connected Ground Robot Experiment (CGRE) project, including David Moiseev, Manat Singh, Billy Hass, Qianyu Liang, Kai Wu, Fangzhou Xia, Kian Khoon Amos Goh, Evan Smith, Yifei Li, Keke Lyu, Haowen Ge, Wenxuan Zhou, Liwei Wang, Yuchen Yang, Keyin Zhu, Xiangji Bu, Qinan Cao, Weilun Peng, Calvin Wang, Bingqing Zu, Zizhao Wang, Tiancheng Ge, Cong Fu, Yue Tang, Sumit Joshi, Ming-Jui Li, Qingjie Qi, Mert Selamet, Meng Qu, etc.

TABLE OF CONTENTS

Dedication . . . . . **ii**

Acknowledgments . . . . . **iii**

List of Figures . . . . . **vi**

List of Tables . . . . . **xi**

List of Appendices . . . . . **xii**

List of Abbreviations . . . . . **xiii**

Abstract . . . . . **xv**

Chapter

1 Introduction **1**

1.1 Motivation 1
1.2 Performance Requirements 3
1.3 Controller Design 5
1.4 Contributions 7
1.5 Publications 10

2 Testbed Setup and Analysis of Predecessor-follower Systems **12**

2.1 Testbed Setup 12
2.1.1 Mechanical Design and System Architecture 12
2.1.2 Control-related Software Design 16
2.2 Modeling and Analysis 18
2.3 Stability 23
2.3.1 Plant Stability 23
2.3.2 String stability 25
2.4 Summary 26

3 Experiments for Predecessor-follower Systems **27**

3.1 Two-car Predecessor-follower Systems 27
3.1.1 Experimental String Stability and Test Procedure 27
3.1.2 ACC vs. CCC 29
3.1.3 Results 31
3.2 Cascaded Predecessor-follower Systems 33

3.3 Summary . . . 39

4 Controller Design and Validation of Connected Vehicle Systems . . . 40

4.1 Modeling and Analysis . . . 40
4.2 Plant stability and head-to-tail string stability . . . 44
4.3 Experimental Validation . . . 45
4.3.1 Two-vehicle experiments . . . 45
4.3.2 Three-vehicle experiments . . . 46
4.3.3 Four-vehicle experiments . . . 49
4.3.4 Five-vehicle experiments . . . 51
4.4 Summary . . . 52

5 Stochastic Packet Drops in Predecessor-follower Systems . . . 54

5.1 Stochastic Delay Variations . . . 54
5.2 Stochastic Dynamics . . . 57
5.3 Mean and Covariance Dynamics – IID Approximation . . . 60
5.3.1 Plant Stability . . . 63
5.3.2 String Stability . . . 64
5.3.3 Stability Charts . . . 70
5.4 Real Dynamics with Stochastic Delays . . . 72
5.5 Simulations . . . 78
5.6 Summary . . . 81

6 Stochastic Packet Drops in Open Chain Systems . . . 82

6.1 Stochastic Dynamics . . . 82
6.2 Mean, Second Moment, and Covariance Dynamics . . . 87
6.3 Plant Stability and String Stability . . . 89
6.3.1 Plant Stability . . . 91
6.3.2 String Stability . . . 94
6.4 Summary . . . 101

7 Stochastic Packet Drops in Closed Ring Systems . . . 102

7.1 Dynamics . . . 102
7.2 Stability . . . 105
7.3 Comparing Open Chain and Closed Ring Results . . . 108
7.4 Summary . . . 110

8 Conclusions and Future Work . . . 112

8.1 Conclusions . . . 112
8.2 Future Work . . . 113

Appendices . . . 115

Bibliography . . . 165

LIST OF FIGURES

1.1 (a) An open chain of $(J+1)$ connected vehicles on a single lane. (b) A zoomed-in two-car predecessor-follower system where the follower only utilizes the information broadcast by its predecessor. The red dashed arrow represents V2V communication. 4
1.2 (a) Function (1.1). (b) Range policy function (1.2, 1.3). (c) Range policy function (1.2, 1.4). 5

2.1 (a) A group of robots. (b) Side view of a robot. (c) Bottom view of a robot. . . 13
2.2 Functional block diagram of a robot. 14
2.3 Human-machine interface of Android application for data transceiving and control. (a) Master view of robot chain and main control interface. (b) V2V connectivity settings. (c) Longitudinal mode settings. (d) Control interface for a single robot. (e) Individual display for control and V2X communication. . . . 16
2.4 Current tracking performance of the servo amplifier. Red solid curve and blue dashed curve represent the commanded current I_{c} and actual current I_{w} in the motor windings, respectively. 17
2.5 (a) Sampling. (b) Control with ZOH. (c) Delay variations. 20
2.6 Stability diagrams. The red curves and the enclosed shaded regions are the plant stability boundaries and plant stable domains, respectively, while the blue curves and the shaded blue regions are the string stability boundaries and string stable domains, respectively. 24

3.1 Experiment procedure. (a) Stability diagram for $\Delta t = 0.3\,[\mathrm{s}]$ and $\gamma = 0.1$ [1/s^2]. (b, c) Typical profiles in an experiment. (d) FFT results of the velocity profiles. (e) Experimental amplification ratios at different frequencies. 28
3.2 Comparison of predecessor's velocities in ACC and CCC. 30
3.3 Amplification ratios as a function of excitation frequency. The red curves are the theoretical results, while the blue and magenta error bars represent the experimental results of ACC and CCC, respectively. 32
3.4 Amplification ratio as a function of excitation frequency. 33
3.5 (a) Four string unstable vehicles follow a head vehicle. (b) Four string stable vehicles follow a head vehicle. 34
3.6 Responses to periodic excitations with four string unstable vehicles configured as shown in Figure 3.5(a). (a) $v_0^{\mathrm{amp}} = 0.25$ [m/s]. (b) $v_0^{\mathrm{amp}} = 0.375$ [m/s]. (c) $v_0^{\mathrm{amp}} = 0.5$ [m/s]. 34

3.7 Responses to aperiodic excitations with four string unstable vehicles configured as shown in Figure 3.5(a). (a) $v_0^{\text{amp}} = 0.25$ [m/s]. (b) $v_0^{\text{amp}} = 0.375$ [m/s]. (c) $v_0^{\text{amp}} = 0.5$ [m/s]. 35
3.8 Responses to excitations with four string stable vehicles configured as shown in Figure 3.5(b). (a) Periodic excitations. (b) Aperiodic excitations. 35
3.9 Vehicle configurations for different penetration rates of string stable vehicles (green) among string unstable vehicles (white). (a, b) One string stable vehicle. (c, d) Two string stable vehicles. (e, f) Three string stable vehicles. 36
3.10 Responses to periodic excitations as the penetration rate of string stable vehicle varies. 37
3.11 Amplification ratio vs. penetration rate of string stable vehicles. 38

4.1 (a) Two-vehicle configuration. (b) Stability diagram. (c) Frequency responses for points A and B marked in panel (b). (d, e) Experimental velocity profiles when vehicle 0 introduces sinusoidal velocity fluctuations at $\omega_0 = 0.15\pi$ [rad/s] in cases A and B, respectively. 45
4.2 (a) Three-vehicle configuration. (b) Stability diagram. (c) Frequency response for point C marked in panel (b). (d) Experimental velocity profiles in case C when vehicle 0 introduces sinusoidal velocity fluctuations at $\omega_0 = 0.15\pi$ [rad/s]. 47
4.3 (a) Three-vehicle configuration. (b) Stability diagram. (c) Frequency responses for points D, E and F marked in panel (b). (d, e) Experimental velocity profiles when vehicle 0 introduces sinusoidal velocity fluctuations at $\omega_0 = 0.15\pi$ [rad/s] in cases D and E, respectively. (f, g) Experimental velocity profiles for case F when vehicle 0 introduces sinusoidal velocity fluctuations at $\omega_0 = 0.15\pi$ [rad/s] and $\omega_1 = 0.95\pi$ [rad/s], respectively. 48
4.4 (a) Four-vehicle configuration. (b) Stability diagram. (c) Frequency response for point G marked in panel (b). (d) Experimental velocity profiles when vehicle 0 introduces sinusoidal velocity fluctuations at frequency $\omega_0 = 0.15\pi$ [rad/s]. 49
4.5 (a) Four-vehicle configuration. (b) Stability diagram. (c) Frequency responses for points H and I marked in panel (b). (d, e) Experimental velocity profiles when vehicle 0 introduces sinusoidal velocity fluctuations at frequency $\omega_0 = 0.15\pi$ [rad/s]. 51
4.6 (a) Four-vehicle configuration. (b) Stability diagram. (c) Frequency responses for points H and I marked in panel (b). (d, e) Experimental velocity profiles when vehicle 0 introduces sinusoidal velocity fluctuations at frequency $\omega_0 = 0.15\pi$ [rad/s]. 52
4.7 (a) Five-vehicle configuration. (b) Stability diagram. (c) Frequency responses for points J and K marked in panel (b). (d, e) Experimental velocity profiles when vehicle 0 introduces sinusoidal velocity fluctuations at frequency $\omega_0 = 0.15\pi$ [rad/s]. 53

5.1 (a) Predecessor's velocity is transmitted every Δt time, but packets may be dropped as indicated. (b) Control with ZOH based on the newest received information. (c) Follower's corresponding velocity. (d) Time delay variations in the continuous-time system (5.4, 5.5). (e) Corresponding delays in the discrete-time system (5.8). 55
5.2 (a) Plant stability diagrams in the $(K_{\mathrm{v}}, K_{\mathrm{p}})$-plane for $p = 0.8$, $\Delta t = 0.1\,[\mathrm{s}]$ and IID assumption. Red and purple curves correspond to changes in plant stability of the mean dynamics and the second moment dynamics, respectively. Red and purple shaded regions correspond to plant stable domains of the mean dynamics and second moment dynamics, respectively. (b–e) Blue stars and red crosses mark the root loci of the mean dynamics and the second moment dynamics on the z-domain, respectively, corresponding to the points A–D marked on panel (a). 65
5.3 (a) String stability diagrams in the $(K_{\mathrm{v}}, K_{\mathrm{p}})$-plane for $p = 0.8$, $\Delta t = 0.1\,[\mathrm{s}]$ and IID delay assumption. Green and blue curves correspond to changes in mean string stability and $n\sigma$ string stability, respectively. Green shaded and blue shaded regions correspond to mean string stable and 1σ string stable regions, respectively. (b–e) Blue and red curves represent the amplification ratios (5.36) and (5.60) for $n = 1$, as functions of the excitation frequency ω corresponding to the points E–H marked in panel (a). 70
5.4 Stability diagrams in the $(K_{\mathrm{v}}, K_{\mathrm{p}})$-plane for different values of packet delivery ratio p and sampling time Δt as indicated and IID delay assumption. The corresponding delay distributions (5.2) are plotted on each panel as inlets. The same notation is used in Figure 5.2(a) and Figure 5.3(a). 71
5.5 (a) Stochastic delays in the discrete-time system (5.8). (b) The relationship between counters l and k_l. (c) Number of trials $\tilde{\tau}_j$ at time instant l until a new packet is received at $k_l \Delta t$. 73
5.6 (a) Plant stability diagrams in the $(K_{\mathrm{v}}, K_{\mathrm{p}})$-plane for $p = 0.8$, $\Delta t = 0.1\,[\mathrm{s}]$ without IID delay assumption. The same color scheme is used in Figure 5.2(a). (b–e) Blue stars and red crosses mark the root loci of the mean dynamics and the covariance dynamics on the z-domain, respectively, corresponding to the points A–D in panel (a). 75
5.7 (a) String stability diagrams in the $(K_{\mathrm{v}}, K_{\mathrm{p}})$-plane for $p = 0.8$, $\Delta t = 0.1\,[\mathrm{s}]$ without IID delay assumption. The same color scheme is used in Figure 5.3(a). (b–e) Blue and red curves represent the amplification ratios (5.36) and (5.60) for $n = 1$, respectively, as functions of the excitation frequency ω corresponding to the points E–H in panel (a). 76
5.8 Stability diagrams in the $(K_{\mathrm{v}}, K_{\mathrm{p}})$-plane for different values of packet delivery ratio p and sampling time Δt as indicated and no IID delay assumption. The same notation is used as in Figure 5.4. 77

5.9 Mean and 1σ window of 1000 simulations for the linear system (5.13) and nonlinear system (5.8) subject to constant inputs $v_{j-1}(t) \equiv v_{j-1}^*$ and $\tilde{v}_{j-1}(t) \equiv 0$ with the gains corresponding to the points marked A–D in Figure 5.6(a). The initial perturbations are $\tilde{h}_j(t) = 10.2$ [m], $\tilde{v}_j(t) = 0.2$ [m/s], for $t \in [-\Delta t\,,\, 0]$. Blue curves represent the predecessor's velocity, red curves represent the follower's mean velocity, and green curves represent the follower's 1σ window. 79

5.10 Mean and 1σ window of 1000 simulations of the linear system (5.13) and the nonlinear system (5.8) subject to sinusoidal input (5.10) with $v_{j-1}^{\text{amp}} = 5$ [m/s] and the gains corresponding to the points E–H in Figure 5.7(a). Here, $\omega = 2\,[\text{rad/s}]$ for the first two rows, $\omega = 6\,[\text{rad/s}]$ for the last two rows. The initial conditions are chosen as $\tilde{h}_j(t) = 0$ m, $\tilde{v}_j(t) = 0$ [m/s], for $t \in [-\Delta t\,,\, 0]$. Blue curves represent the predecessor's velocity, red curves represent the follower's mean velocity, and green curves represent the follower's 1σ window. . 80

6.1 Plant stability simulations for an open chain of $(15 + 1)$ vehicles for different $(K_{\text{v}}, K_{\text{p}})$ gains as indicated. The blue curves represent the velocity v_0 of the head vehicle while the red, green, cyan, magenta and orange curves represent the velocities v_3, v_6, v_9, v_{12}, v_{15}, respectively. (a) Plant stable. (b) Plant unstable. 90

6.2 String stability simulations for an open chain of $(200 + 1)$ vehicles for different $(K_{\text{v}}, K_{\text{p}})$ gains as indicated. The blue curves represent the velocity v_0 of the head vehicle while the red, green, cyan, magenta and orange curves represent the velocities v_{40}, v_{80}, v_{120}, v_{160}, v_{200}, respectively. (a) String stable. (b) String unstable. (c) String unstable. 91

6.3 Plant stability diagrams for an open chain of $(J+1)$ vehicles in the $(K_{\text{v}}, K_{\text{p}})$-plane for different values of packet delivery ratio p. The corresponding delay distributions (5.2) are plotted on each panel as inlets. 93

6.4 Mean head-to-tail string stability and 1σ head-to-tail string stability diagrams for an open chain of $(J+1)$ vehicles in the $(K_{\text{v}}, K_{\text{p}})$-plane for different values of packet delivery ratio p. Each panel plots all the boundaries for mean head-to-tail string stability corresponding to $J = 3, 9, 15, 21, 27$ from light green to dark green curves, and 1σ head-to-tail string stability corresponding to $J = 3, 9, 15, 21, 27$ from light orange to dark orange curves, respectively. 97

6.5 Stability diagrams for an open chain of $(27 + 1)$ vehicles in the $(K_{\text{v}}, K_{\text{p}})$-plane for different values of packet delivery ratio p. Red, blue, green and orange curves represent boundaries for mean plant stability, second moment plant stability, mean head-to-tail string stability and 1σ head-to-tail string stability, respectively, while the light red, light blue, light green and light orange shaded regions represent the corresponding stability regions. 100

7.1 A closed ring of J connected vehicles on a single lane. Dashed red arrows indicate the information flow through wireless communication, while the solid blue arrows indicate the direction of traffic flow. 103

7.2 Simulations of a closed ring of 55 vehicles for different $(K_{\mathrm{v}},K_{\mathrm{p}})$ gains as indicated. The red, green, cyan, magenta and orange curves represent the velocities v_{11}, v_{22}, v_{33}, v_{44}, v_{55}, respectively. (a) Stable. (b) Unstable. (c) Unstable. 105
7.3 Mean stability diagrams for a closed ring of J vehicles in the $(K_{\mathrm{v}},K_{\mathrm{p}})$-plane for different values of packet delivery ratio p. The cyan curves represent stability boundaries. Each panel shows the boundaries corresponding to $J = 3, 9, 15, 21, 27$ from light cyan to dark cyan curves. 107
7.4 Second moment stability diagrams for a closed ring of J vehicles in the $(K_{\mathrm{v}},K_{\mathrm{p}})$-plane for different values of packet delivery ratio p. Each panel shows all the boundaries corresponding to $J = 3, 9, 15, 21, 27$ from light purple to dark purple curves. 108
7.5 Mean and second moment stability diagrams for a closed ring of 27 vehicles in the $(K_{\mathrm{v}},K_{\mathrm{p}})$-plane for different values of packet delivery ratio p. Cyan and purple curves represent the boundaries for mean stability and second moment stability, respectively, while the cyan and purple shaded regions represent the mean stable regions and second moment stable regions, respectively. 109
7.6 Comparison between the mean string stability of an open chain and the mean stability of a closed ring in the $(K_{\mathrm{v}},K_{\mathrm{p}})$-plane for different values of packet delivery ratio p. The solid green curves represent mean string stability boundaries for an open chain of $(3 + 1)$ vehicles, while the dashed cyan curves represent mean stability boundaries for a closed ring of infinitely many vehicles. 109
7.7 Comparison between the 1σ string stability of an open chain of (27+1) vehicles, and the second moment stability of a closed ring of 27 vehicles in the $(K_{\mathrm{v}},K_{\mathrm{p}})$-plane for different values of packet delivery ratio p. The solid orange curves and orange shaded regions correspond to the open chain, while the solid purple curves and purple shaded regions correspond to the closed ring. 110

A.1 (a) Control loop misaligned. (b) Control loop perfectly aligned. 116
A.2 (a) Histogram of communication delay. (b) Histogram of control loop alignment error. 118

LIST OF TABLES

2.1 Scaling factors from real vehicles to robots 13
2.2 Control parameters used in the experiments 14
2.3 Physical parameters of the robots 15
2.4 Summary of timing errors. 18

3.1 Control gains for different points in Figure 3.1(a). 31
3.2 The maximum critical error percentage. 33

5.1 Critical successful packet delivery ratio for different values of the sampling time. 72

6.1 Characteristics of the matrix $\bar{\bar{\mathbf{A}}}$ for $(J+1)$ connected vehicles and $N = 6$. . . 92

LIST OF APPENDICES

A Control Loop Alignment **115**

B Derivation of the Dynamic Model in Chapter 4 . . . . . **119**

C Open Chain vs. Closed Ring **122**

D Stochastic Stability **134**

E Matrix Fundamentals **136**

F Derivations of Open chain **142**

G Derivations of Closed Ring **158**

LIST OF ABBREVIATIONS

AV automated vehicle

CV connected vehicle

CAV connected automated vehicle

ACC adaptive cruise control

CACC cooperative adaptive cruise control

CCC connected cruise control

DSRC dedicated short range communication

V2V vehicle-to-vehicle

V2X vehicle-to-everything

ZOH zero-order-hold

FPGA field programmable gate array

FFT fast Fourier transform

LTI linear time invariant

ARM Advance RISC Machine

IMU inertial measurement unit

SPI serial peripheral interface

I2C inter-integrated circuit

HMI human-machine interface

MANET mobile ad-hoc network

PTP precision time protocol

SNTP simple network time protocol

PDF probability density function

SISO single-input-single-output

MIMO multiple-input-multiple-output

IID independently identically distributed

ABSTRACT

Vehicle-to-everything (V2X) communication allows vehicles to monitor the nearby traffic environment, including participants that are beyond the line of sight. Equipping conventional vehicles with V2X devices results in connected vehicles (CVs) while incorporating the information provided by V2X devices into the controllers of automated vehicles (AVs) leads to connected automated vehicles (CAVs). CAVs have great potential for improving driving comfort, reducing fuel consumption and advancing active safety for individual vehicles, as well as enhancing traffic efficiency and mobility for human-dominated traffic systems. In this dissertation, we study a class of connected cruise control (CCC) algorithms for longitudinal control of CAVs, where they respond to the motion information of one or multiple connected vehicles ahead. For validation and demonstration purposes, we utilize a scaled connected vehicle testbed consisting of a group of ground robots, which can provide us with insights about the controller design of full-size vehicles.

On the one hand, intermittencies in V2X communication combined with the digital implementation of controllers introduce information delays. To ensure the performance of individual CAVs and the overall traffic, a set of methods is proposed for design and analysis of such communication-based controllers. We validate them with the scaled testbed by conducting a series of experiments on two-car predecessor-follower systems, cascaded predecessor-follower systems, and more complex connected vehicle systems. It is demonstrated that CAVs utilizing information about multiple preceding vehicles in the CCC algorithm can improve the system performance even for low penetration levels. This can be

beneficial at the early stage of vehicle automation when human-driven vehicles still dominate the traffic system.

On the other hand, we study the delay variations caused by stochastic packet drops in V2X communication and derive the stochastic processes describing the dynamics for the predecessor-follower systems. The dynamics of the mean, second moment and covariance are utilized to obtain stability conditions. Then the results of the two-car predecessor-follower system with stochastic delay variations are extended to an open chain as well as to a closed ring of cascaded predecessor-followers where stochastic packet drops lead to heterogeneity among different V2X devices. It is shown that the proposed analytical methods allow CCC design for CAVs that can achieve stability and stochastic disturbance attenuation in the presence of stochastic packet drops in complex connected vehicle systems.

CHAPTER 1

Introduction

1.1 Motivation

The increase in the number of road vehicles over the last few decades has been causing more frequent traffic congestion [1–4], leading to increased travel time [5, 6], larger numbers of traffic accidents [7], and more wasted energy [8–10]. The large reaction time [11–14] and limited perception range of human drivers makes them unable to maintain smooth traffic flow and may lead to stop-and-go traffic jams [15, 16]. Aiming at advancing the safety of road users, during the last few decades the automotive industry has been moving toward enhanced vehicle automation. By now SAE [17] has defined six different levels of automation: level 0 - no driving automation, level 1 - driver assistance, level 2 - partial driving automation, level 3 - conditional driving automation, level 4 - high driving automation, level 5 - full driving automation. These automated vehicles (AVs) may also have a positive impact on traffic congestion once their penetration rate reaches a certain level. However, safety and congestion mitigation may require different control design, and a high penetration rate of AVs may be necessary to have a significant impact.

In the meantime, automakers and suppliers are exploring different vehicle-to-everything (V2X) communication technologies (VANET, Wi-Fi, DSRC, LTE, 5G) [18–32], in order to allow vehicles to obtain information from beyond the line of sight. The related communication technologies have been standardized by different international organizations [33–37] and in different regions, such as the US [38, 39], Europe [40–45], Japan [46–48] and China [49, 50]. These standards allow vehicles to "speak the same language". Vehicles capable of V2X communication are referred to as connected vehicles (CVs), while when V2X information is included in the motion controllers of an AV, we refer to it as a connected automated vehicle (CAV). This may result in a large variety of connectivity topologies [51] depending on how the received information is utilized. Then the key questions are whether and how such V2X information can be used to improve the performance of CAVs and the

performance of the overall traffic system.

In this dissertation we try to answer these questions (at least partially) while restricting ourselves to vehicle chains; that is, we focus on designing the longitudinal controllers for CAVs. Automating the longitudinal motion of road vehicles that follow each other in traffic, dates back to [52–62], followed by the concept of adaptive cruise control (ACC) established about two and a half decades ago [63–71]. The fundamental idea is to use range sensors (radar, lidar, camera) to measure the inter-vehicle distance and the velocity difference to the vehicle ahead, and then adjust the speed accordingly by controlling the "throttle" and the brake. If all vehicles were equipped with ACC, one might expect increased safety, fuel economy, driving comfort and traffic efficiency [72–78] due to the faster and more accurate sensing and actuation abilities. However, due to the relatively high cost of range sensors and the perception limitation by the line of sight, this technology still has a low penetration in current traffic systems.

Further improvements may be achieved by adding V2X communication to a group of ACC vehicles as cooperative control may allow vehicles to have smaller following distances yielding larger throughput. This is referred to as cooperative adaptive cruise control (CACC) [79–90], where each vehicle monitors the motion of the preceding vehicle using range sensors, as well as the motion of the group leader via V2X communication. This technology was shown to have the potential to improve traffic throughput [91–96] using simulations and experiments have been conducted in the PATH program [97–100], the SARTRE project [101, 102], and the grand cooperative driving challenges [103–108]. It is also expected to penetrate the truck industry due to its positive impact on fuel economy with reduced air drag [109–113]. However, the requirement that all vehicles must be equipped with range sensors and V2X devices hinders the deployment of such strategy, while the need for a specific connectivity structure may limit modularity of the entire transportation system.

Until the penetration rate [114–117] of CAVs reaches 100% which may take many decades, one needs to deal with human-driven vehicles, and they are expected to dominate traffic systems in the forthcoming decades. To solve this challenging problem, one may look at the design from the perspective of an individual CAV, that responds to the motion of multiple vehicles ahead without requiring all of them to be automated or being connected. While one may categorize this approach as an advanced version of CACC, we refer to it as connected cruise control (CCC) [118, 119] since it requires no cooperation. This concept can be realized for different levels of automation [17] and allow a large variety of connectivity topologies. A CCC vehicle can fully exploits the advantages of V2X communication to gather all the available information from multiple vehicles ahead (whom may be

beyond the line of sight) within the communication range [120] to achieve a more accurate perception of the surrounding traffic. Moreover, CCC is scalable for large systems and can be adopted for different penetration levels of CVs and CAVs. Finally, despite the fact that CCC is aimed primarily at benefiting individual CAVs, when designed appropriately, it can also have a positive impact on the dynamics of the vehicle chain it is embedded in.

Although CCC systems are promising in increasing safety and traffic throughput, different aspects of CCC need to be studied both theoretically and experimentally before deployments. These include delay effects, connectivity topology, nonlinearity, optimality and predictor design [121–130]. This dissertation will mainly focus on the theoretical analysis of digital effects and stochastic delay variations due to packet drops in V2X communication, and on the experimental validation of this strategy with a scaled connected vehicle testbed consisting of a group of ground robots.

1.2 Performance Requirements

In this dissertation, we focus on the performance of multi-vehicle systems on a single lane as shown in Figure 1.1(a), where the vehicles are labeled as $0\,,\,1\,,\,\ldots\,,\,J$ from the head to the tail. Figure 1.1(b) shows the simplest scenario, i.e., a *two-car predecessor-follower system* where vehicle j only responds to the motion of the preceding vehicle $j-1$. When all vehicles in the system only respond to the motion of the vehicle immediately ahead, a *cascaded predecessor-follower system* is formed. When some vehicles in the system respond to the motion of multiple vehicles ahead (that might be beyond the line of sight), a *connected vehicle system* is created. To characterize the performance of such traffic systems, plant stability [121, 131, 132], string stability [133–139], scalability [140–142] and throughput [143–145] are of the most concern. In particular, we focus on the first two aspects and provide their definitions in this section.

We say that a vehicle is *plant stable* if, assuming the vehicles ahead are traveling at a constant velocity, it can approach this velocity asymptotically. Indeed, a two-car predecessor-follower system is *plant stable* when the follower is plant stable, while a cascaded predecessor-follower system (a connected vehicle system) is *plant stable* when all the following vehicles in this system are plant stable. Plant instability leads to diverging velocity and may even result in collisions.

String stability refers to attenuation of velocity fluctuations as they propagate backward along the vehicle chain. A two-car predecessor-follower system is *string stable* if the follower attenuates the velocity perturbations of the predecessor. More careful consideration is needed when this definition is extended to multi-vehicle systems. In a cascaded

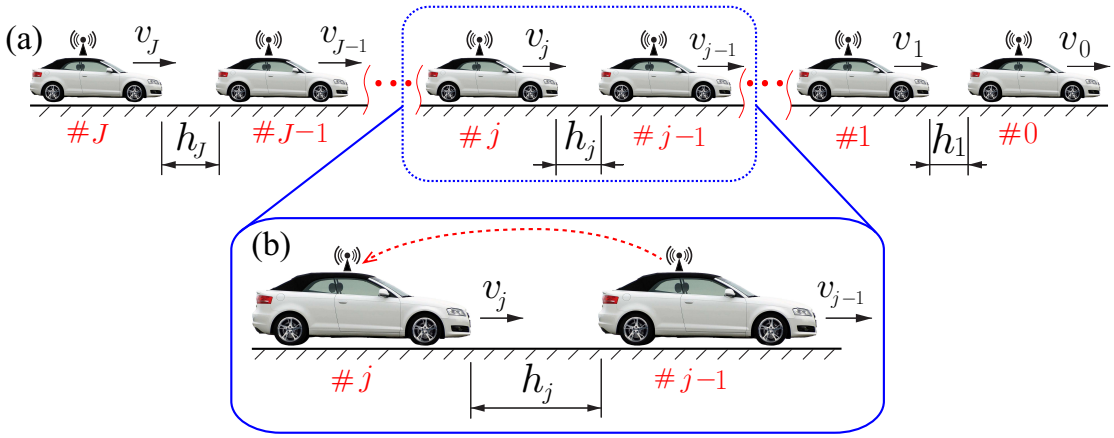

Figure 1.1: (a) An open chain of $(J+1)$ connected vehicles on a single lane. (b) A zoomed-in two-car predecessor-follower system where the follower only utilizes the information broadcast by its predecessor. The red dashed arrow represents V2V communication.

predecessor-follower system, if all vehicles are string stable, then indeed velocity perturbations decay as they propagate along the vehicle chain. Similarly, when all vehicles are string unstable, velocity perturbations keep increasing as they propagate backward along the chain. This typically results in traffic jams, as will be discussed in detail. However, when considering a mixture of vehicles, one may compare the motion of two vehicles in the system and define the system as *i-to-j string stable* ($i < j$) meaning that the velocity fluctuations of vehicle i are attenuated when arriving at vehicle j. This definition can also be extended to connected vehicle system with complex connectivity structure. Note that 0-to-J string stability (often referred to as *head-to-tail string stability* [121]) may be used to characterize the performance of the whole system. We remark that i-to-j string stability does not imply that all vehicles between i and j attenuate perturbations. This allows us to apply the definition to connected vehicle systems containing human-driven vehicles whose motion cannot be designed. As a matter of fact, humans typically amplify velocity fluctuations when responding to the motion of the preceding vehicle due to limited perception abilities and large reaction time. That is, they are $(j-1)$-to-j string unstable (often simply referred to as string unstable). Still, by equipping the j-th vehicle with connected cruise controller that utilizes motion information from multiple vehicles ahead, it may achieve i-to-j string stability when human-driven vehicles are included in between.

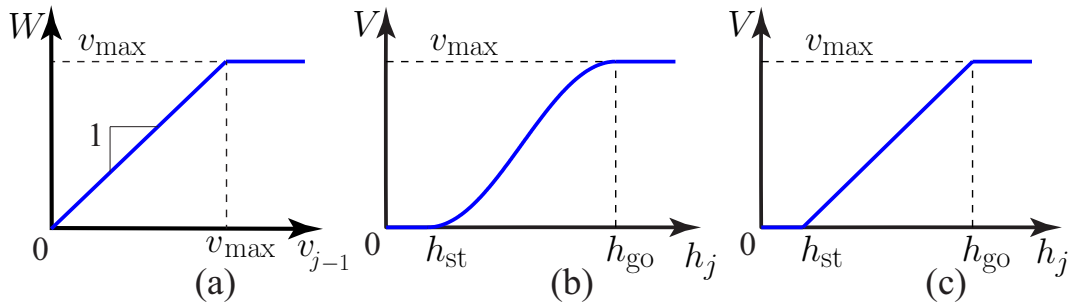

Figure 1.2: (a) Function (1.1). (b) Range policy function (1.2, 1.3). (c) Range policy function (1.2, 1.4).

1.3 Controller Design

We start the controller design considering the two-car predecessor-follower system shown in Figure 1.1(b) where v_{j-1} and v_j represent the predecessor's and the follower's velocities, respectively, while the inter-vehicle distance h_j is called *distance headway*. The controller should be able to regulate the follower's velocity v_j and the inter-vehicle distance h_j based on the predecessor's velocity v_{j-1}.

In particular, the follower shall try to match its velocity v_j to that of the predecessor v_{j-1}. However, if the predecessor's velocity exceeds the speed limit $v_{\max}$, the controller should switch from velocity matching to tracking the preset maximum velocity $v_{\max}$, which can be formulated as

$$W(v_{j-1}) = \begin{cases} v_{j-1} & \text{if} \quad v_{j-1} < v_{\max}\,, \\ v_{\max} & \text{if} \quad v_{j-1} \geq v_{\max}\,, \end{cases} \tag{1.1}$$

see Figure 1.2(a).

On the other hand, the distance regulation typically involves a *range policy* [146–148], that gives the desired velocity as a function of the distance headway h_j. While different range policies can be considered, they must satisfy the following requirements:

- continuous and monotonically increasing (the more sparse traffic is, the faster the vehicles intend to run);
- equal to zero for $h_j \leq h_{\text{st}}$ (vehicles intend to stop within a safety distance);
- equal to the speed limit for $h_j \geq h_{\text{go}}$ (vehicles intend to run with a given maximum speed in sparse traffic – often referred to as *free flow*).

This can be written as

$$V(h_j) = \begin{cases} 0 & \text{if} \quad h_j \leq h_{\text{st}}\,, \\ F(h_j) & \text{if} \quad h_{\text{st}} < h_j < h_{\text{go}}\,, \\ v_{\max} & \text{if} \quad h_j \geq h_{\text{go}}\,, \end{cases} \tag{1.2}$$

where $F(h_j)$ is strictly monotonically increasing while $F(h_{\text{st}}) = 0$ and $F(h_{\text{go}}) = v_{\max}$. Two candidates used in this thesis are shown in Figure 1.2. Figure 1.2(b) displays the sinusoidal function

$$F(h_j) = \frac{v_{\max}}{2}\Big(1 - \cos\big(\pi \frac{h_j - h_{\text{st}}}{h_{\text{go}} - h_{\text{st}}}\big)\Big)\,, \tag{1.3}$$

while Figure 1.2(c) depicts the linear function

$$F(h_j) = \frac{v_{\max}}{h_{\text{go}} - h_{\text{st}}}\big(h_j - h_{\text{st}}\big)\,. \tag{1.4}$$

The reciprocal of the slope of $F(\cdot)$, i.e.,

$$t_{\text{h}} = 1 \Big/ \frac{\mathrm{d}F}{\mathrm{d}h}\,, \tag{1.5}$$

is often referred to as *time headway*. Note that (1.3) has a varying time headway, while (1.4) uses a constant time headway.

In order to match velocity and regulate inter-vehicle distance, we propose a controller

$$\begin{aligned} a_j^{\text{com}} &= \alpha\big(V(h_j) - v_j\big) + \gamma\,\varepsilon_j + \beta\big(W(v_{j-1}) - v_j\big)\,, \\ \dot{\varepsilon}_j &= V(h_j) - v_j\,, \end{aligned} \tag{1.6}$$

to command the acceleration. Here $V(h_j) - v_j$ represents the error between the desired velocity $V(h_j)$ and the follower's velocity v_j, so the first two terms constitute a nonlinear proportional-integral controller to regulate the distance headway while the last term is proportional to the velocity matching error $W(v_{j-1}) - v_j$. Note that α and β are measured in $[1/\text{s}]$, γ is measured in $[1/\text{s}^2]$. The controller (1.6) is a generalization of the linear controller that is widely in the literature [80, 149, 150] and the range policy with (1.4) is often referred to as constant time headway policy. We also remark that in practice the controller (1.6) is digitally implemented on a micro-controller and physical limitations may result in saturation. Those effects will be studied in the following sections.

One may notice that (1.6) only relies on the motion information of the vehicle immedi-

ately ahead. In a human-dominated traffic system, CAVs may utilize position and velocity information of multiple vehicles ahead that are equipped with V2X devices, to achieve head-to-tail string stability. The controller of the CAV j can try to match its velocity v_j with the preceding vehicles' velocities v_i for $i = 0 \ldots j-1$, and also regulate the average distance headway

$$h_{j,i} = \frac{1}{j-i} \sum_{l=i+1}^{j} h_l \,, \tag{1.7}$$

between vehicle j and vehicle i. That is, the controller (1.6) on the two-car predecessor-follower system may be extended to connected cruise controller

$$\begin{aligned} a_j^{\text{com}} &= \sum_{i=0}^{j-1} \Big(\alpha_{j,i} \big(V(h_{j,i}) - v_j \big) + \beta_{j,i} \big(W(v_i) - v_j \big) \Big) + \gamma_j \, \varepsilon_j \,, \\ \dot{\varepsilon}_j &= V(h_j) - v_j \,. \end{aligned} \tag{1.8}$$

Similarly, the term $V(h_{j,i}) - v_j$ represents the error between the desired velocity $V(h_{j,i})$ and the vehicle's velocity v_j, $W(v_i) - v_j$ represents the velocity matching error, and the integrator is used to eliminate the steady-state error. Note that $\alpha_{j,i}$ and $\beta_{j,i}$ are measured in $[1/\text{s}]$, γ_j is measured in $[1/\text{s}^2]$.

1.4 Contributions

To validate the proposed controllers, we built a scaled connected vehicle testbed consisting of a group of ground robots. The robots are designed such that they would capture the longitudinal and lateral dynamics of full-size vehicles when scaled up. That is, the controller design of the robots provides us with insight about the controller design of real vehicles. The robots are also able to mimic V2X communication while exchanging information via peer-to-peer wireless communication. In Chapter 2, we provide details about the design of the robots and point out the delays in communication-based control. The low data exchanging rate, combined with onboard digital controllers, leads to digital effects [151–154] and periodically varying time delays [155–158] in the control loop. We propose a dynamic model and first study those effects theoretically on the two-car predecessor-follower system with digital control implementation [159, 160]. Plant stability and string stability are discussed in detail, and the proposed method allows us to design controllers with given stability and performance requirements.

To establish the validity of the connected vehicle testbed, in Chapter 3 we first conduct experiments on a two-car predecessor-follower system while implementing the controller

(1.6) using two robots. The performance of sensor-based control (mimicking ACC) and the V2X-based control (mimicking the simplest CCC) are compared to each other and also with the theoretical results. The design principles that allow one to ensure stability and disturbance attenuation in the presence of time delays are also laid out. Moreover, we utilize the connected vehicle testbed to evaluate the dynamics of cascaded predecessor-follower systems experimentally. It is demonstrated that when all vehicles have identical dynamics, then the string stable/unstable behavior of the two-car predecessor-follower system is inherited by cascaded systems. Thus, we show how string stability relates to traffic jam formation. Then we investigate the behaviors for different penetration rates and distributions of string stable vehicles to mimic a traffic environment where the controllers for a fraction of vehicles may be designed. In particular, we focus on how string stable CCC vehicles inserted into the flow of string unstable vehicles may be used to smooth the traffic flow.

The advantages of V2X communication is only partially exploited during the predecessor-follower experiments in Chapters 2 and 3. In order to maximize the benefits of V2X communication, in Chapter 4 we implement the CCC algorithm (1.8) on the robots using digital controllers and show that, when taking into account time delays in the corresponding model, we are able to predict string stability boundaries accurately. Using this model-based design, we construct connected vehicle systems with increasingly complex communication topologies and evaluate their performance experimentally. In particular, to mimic human-driven vehicles we incorporate string unstable vehicles that respond to the motion of the vehicle ahead by amplifying velocity perturbations. We demonstrate that when utilizing motion information obtained via V2X from multiple vehicles ahead, CCC can ensure head-to-tail string stability for the connected vehicle systems. We also show that increasing the number of V2X signals in the controller may result in further improvements and that our design remains robust against changes in the connectivity structure. Finally, we investigate the impacts of including multiple CCC vehicles in the traffic flow to demonstrate the scalability of the concept.

Up until this point, we will have only considered the scenario where no packets are dropped. However, in practice this is not really the case in V2X communication, and the delay will increase further in a random manner when packet losses occur in the communication channels [161]. Chapters 5-7 will present a comprehensive discussion on stochastic delay variations caused by stochastic packet drops. In the literature, researchers have studied the mean dynamics (the time evolution of the expected value of the state) assuming delays of equal probability [84], or continuous-time approximation with uncertainties in the delays [95]. However, the stochastic processes describing the delay variations have not yet been incorporated in the control loop, and performance of dynamic system-

s has not been characterized in the presence of stochastically varying time delays. For simplicity, these parts will only focus on predecessor-follower systems, including two-car predecessor-follower and cascaded predecessor-follower systems. In Chapter 5, we first develop a stochastic model with delay variations in the control loop in the predecessor-follower system, while still considering digital implementation, and characterize system performance in the stochastic sense.

On the one hand, evaluating the response of dynamic systems subject to stochastic delay variations depends on how convergence and stability are defined [162–166]. Preliminaries on stochastic stability are provided in Appendix D. We are particularly interested in conditions that ensure almost sure stability since it allows for the design of controllers that guarantee convergence of almost all trajectories despite having stochastic delay variations in the control loop. In Chapter 5 we consider this approach to analyze *plant stability* of the equilibrium in the stochastic sense in the two-car predecessor-follower system. On the other hand, prior to our work, no mathematical tools existed to ensure the desired frequency response under stochastic delay variations, which is needed to evaluate *string stability*. In Chapter 5 we analyze the second moment [167–170] and covariance dynamics and establish the concept of $n\sigma$ *string stability* to handle this problem. This allows us to design controllers that can ensure attenuation of perturbations despite stochastically varying time delays. We demonstrate the effectiveness of the developed mathematical techniques on the predecessor-follower system regulated by a simple controller while describing the delay variations with a Bernoulli process.

The scalability of our approach to stochastic stability and disturbance attenuation is investigated in Chapter 6. We extend the notion of $n\sigma$ *string stability* to an open chain built as a concatenation of two-car predecessor-follower pairs. To ensure scalability, a set of decomposition methods is developed to reduce the size of matrices appearing in the mean, second moment, and covariance dynamics. Moreover, the notion of $n\sigma$ *offset string stability* is proposed to characterize stability and disturbance attenuation as the number of vehicles is increased. In this way, the feasible ranges of control parameters that ensure smooth traffic flow can be characterized analytically as the number of vehicles increases.

In Chapter 7 another type of large system – a system of cascaded predecessor-followers that form a ring, is studied in detail to support the scalability arguments. Similar to the open chain system, decomposition methods are developed to make the stability analysis scalable. The stability diagrams obtained also unveil the relationship between large systems of connected vehicles of different configurations. Clearly, such comparison is not possible using numerical simulations considering the large system sizes and the requirement for enormous realizations given by the stochastically varying delays.

In Chapter 8, we conclude the results obtained in this dissertation and point out some future research directions.

1.5 Publications

One can refer to the following publications for more related work in this dissertation.

Journal Publications

[1] **W. B. Qin** and G. Orosz, "Experimental validation on connected cruise control with flexible connectivity topologies," *IEEE/ASME Transactions on Mechatronics*, under review, 2018.

[2] **W. B. Qin** and G. Orosz, "Experimental validation on connected vehicles subject to digital effects and delays," *IEEE Transactions on Control Systems Technology*, under review, 2018.

[3] J. I. Ge, S. S. Avedisov, C. R. He, **W. B. Qin**, M. Sadeghpour, and G. Orosz, "Experimental validation of connected automated vehicle design among human-driven vehicles," *Transportation Research Part C: Emerging Technologies*, vol. 91, pp. 335-352, 2018.

[4] C. R. He, **W. B. Qin**, N. Ozay, and G. Orosz, "Optimal gear shift schedule design for automated vehicles: Hybrid system based analytical approach," *IEEE Transactions on Control Systems Technology*, published online, pp. 1-13, 2017.

[5] T. G. Molnár, **W. B. Qin**, T. Insperger, and G. Orosz, "Application of predictor feedback to compensate time delays in connected cruise control," *IEEE Transactions on Intelligent Transportation Systems*, vol. 19, no. 2, pp. 545-559, 2018.

[6] G. Orosz, J. I. Ge, C. R. He, S. S. Avedisov, **W. B. Qin**, and L. Zhang, "Seeing beyond the line of sight – controlling connected automated vehicles," *ASME Mechanical Engineering Magazine*, vol. 139, no. 12, pp. S8-S12, 2017.

[7] **W. B. Qin** and G. Orosz, "Scalable stability analysis on large connected vehicle systems subject to stochastic communication delays," *Transportation Research Part C: Emerging Technologies*, vol. 83, pp. 39-60, 2017.

[8] **W. B. Qin**, M. M. Gomez, and G. Orosz, "Stability and frequency response under stochastic communication delays with applications to connected cruise control design," *IEEE Transactions on Intelligent Transportation Systems*, vol. 18, no. 2, pp. 388-403, 2017.

Conference Proceedings

[9] **W. B. Qin**, M. M. Gomez, and G. Orosz, "Moment-based plant and string stability analysis of connected cruise control with stochastic delays," in *Proceedings of American Control Conference*, pp. 2747-2752, IEEE, 2015.

[10] T. G. Molnár, **W. B. Qin**, T. Insperger, and G. Orosz, "Predictor design for connected cruise control subject to packet loss," in *Proceedings of 12th IFAC Workshop on Time Delay Systems*, pp. 428-433, IFAC, 2015.

[11] C. R. He, **W. B. Qin**, N. Ozay, and G. Orosz, "Hybrid systems based analytical approach for optimal gear shifting schedule design," in *Proceedings of the ASME Dynamic Systems and Control Conference*, DSCC2015-9943, pp. V003T41A003, ASME, 2015.

[12] **W. B. Qin**, M. M. Gomez, and G. Orosz, "Stability analysis of connected cruise control with stochastic delays," in *Proceedings of American Control Conference*, pp. 4624-4629, IEEE, 2014.

[13] M. M. Gomez, **W. B. Qin**, G. Orosz, and R. Murray, "Exact stability analysis of discrete-time linear systems with stochastic delays," in *Proceedings of American Control Conference*, pp. 5534-5539, IEEE, 2014.

[14] **W. B. Qin** and G. Orosz, "Digital effects and delays in connected vehicles: Linear stability and simulations," in *Proceedings of the ASME Dynamic Systems and Control Conference*, DSCC2013-3830, pp. V002T30A001, ASME, 2013.

CHAPTER 2

Testbed Setup and Analysis of Predecessor-follower Systems

To validate the CCC algorithms (1.6) and (1.8), we built a scaled connected vehicle testbed consisting of a group of ground robots. These robots are designed such that they would capture the longitudinal and lateral dynamics of full-size vehicles when scaled up. The controller design of the robots can provide us with insights about the controller design of real vehicles. In this chapter, we explain the details of the testbed setup and show how V2X communication introduces delays into the controller. Also, we propose a simplified physics-based vehicle model and derive the closed-loop dynamics with controller (1.6) while considering intermittent communication and digital control implementation. Moreover, plant stability and string stability are discussed, and stability diagrams are used to summarize the results. The material discussed in this section can be found in [171, 172].

2.1 Testbed Setup

The scaled connected vehicle testbed consisting of a group of ground robots is shown in Figure 2.1(a). In this section, the mechanical structure, the electronic control system and the control-related software design are explained in detail.

2.1.1 Mechanical Design and System Architecture

The mechanical components and structure of the robots are shown in Figure 2.1(b,c). The robots are rear-wheel driven (without differential) by a brushed DC motor and front-wheel steered by a servo motor via an Ackermann steering system. A pair of mini-wheels with optical encoders is pushed to the ground with the help of a suspension system that ensures the mini-wheels are always rolling on the ground.

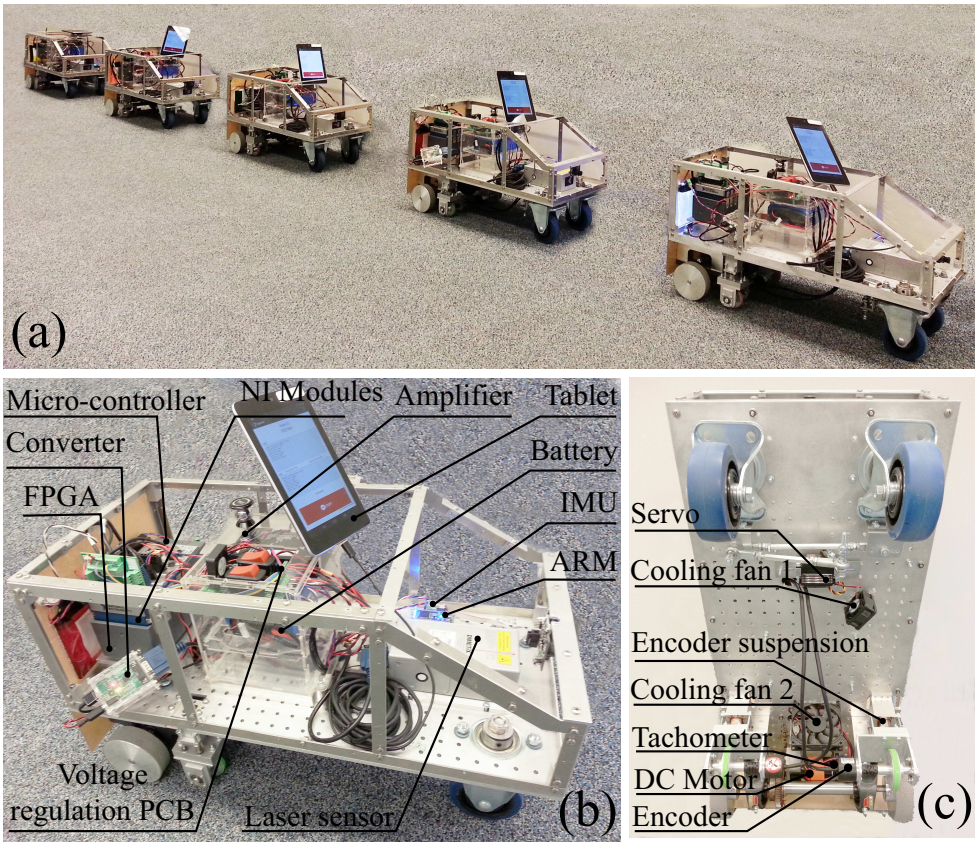

Figure 2.1: (a) A group of robots. (b) Side view of a robot. (c) Bottom view of a robot.

Table 2.1: Scaling factors from real vehicles to robots

length [m]	$1/8$
velocity [m/s]	$1/16$
time [s]	2
frequency [Hz]	$1/2$
acceleration [m/s^2]	$1/32$
control gain α [1/s]	1/2
control gain β [1/s]	1/2
control gain γ [1/s^2]	1/4

The lengths and velocities are scaled by factors of 8 and 16, respectively. This results in the scaling factors shown in Table 2.1, while Table 2.2 shows the control parameters we choose in (1.6) for real vehicles and robots based on the scaling. The remaining physical parameters of the robots are shown in Table 2.3.

Figure 2.2 shows the functional block diagram of the electronic control system, consist-

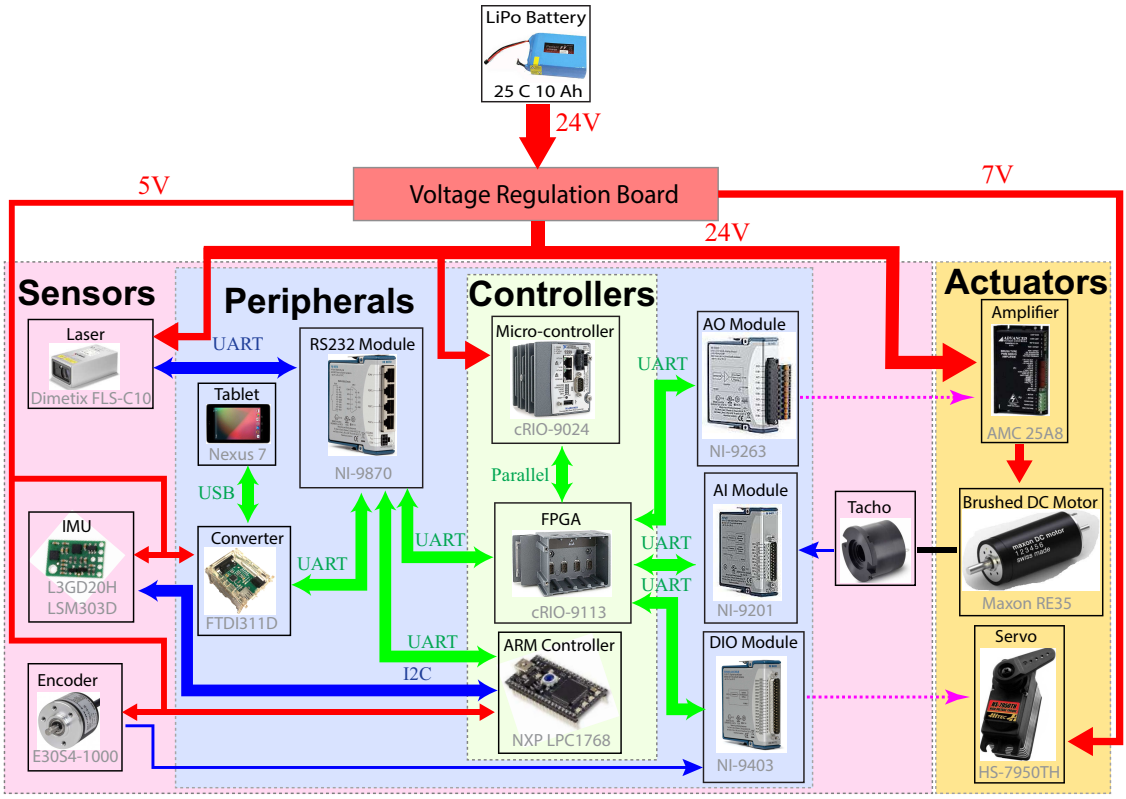

Figure 2.2: Functional block diagram of a robot.

Table 2.2: Control parameters used in the experiments

	Real Vehicles	Robots
$v_{\max}$ [m/s]	30	1.875
h_{st} [m]	5	0.625
h_{go} [m]	35	4.375
t_{h} [s]	1	2

ing of the power system, controllers, peripherals, sensors and actuators. The power system includes a 24 volts battery as the power supply and a printed circuit board regulating voltage levels for the sub-modules.

An 800 MHz micro-controller handles all the sensor data post-processing, higher-level computation, and data logging. It also communicates with a field programmable gate array (FPGA) which is connected to the peripherals through different modules and enables data encoding, decoding and processing at exact time instants. An additional Advance RISC Machine (ARM) is utilized to pre-process data and communicate with sensors via serial

Table 2.3: Physical parameters of the robots

mass of the robot m [kg]	20.2
rear wheel radius R [m]	0.045
gear ratio η	$55/18$
air drag coefficient ν [kg/m]	0 (neglected)
damping ratio b [kg/s]	0 (neglected)
rolling resistance coefficient μ	0.008

peripheral interface (SPI) and inter-integrated circuit (I2C) protocols.

Each robot is equipped with an Android tablet that enables peer-to-peer wireless communication with other robots. In particular, a mobile ad-hoc network (MANET), capable of communicating over about 100-meter range with a very low rate of packet loss, is created to mimic V2X communication. The tablet communicates with the micro-controller through a USB/UART converter, and an Android application is designed to serve as human-machine interface (HMI); see Figure 2.3.

A laser range sensor, two optical encoders and a tachometer are used to measure the inter-robot distance, the distance traveled and the angular velocity of the DC motor, respectively. Since the tachometer is attached to the motor shaft, the angular velocity is proportional to the longitudinal velocity of the robot with the assumption that the rear wheels do not slip. In addition, an inertial measurement unit (IMU) is used to measure the accelerations and angular velocities of the robot.

A servo motor steers the front wheels for lateral control, while a brushed DC motor serves as the longitudinal actuator. Since the output torque of a brushed DC motor is proportional to the current on the motor windings, a servo amplifier is set in the current mode to amplify the control signals and drive the DC motor. The current tracking performance shown in Figure 2.4 indicates that the current on the motor windings tracks the commanded current well. Thus, instead of considering the internal dynamics of the circuits, we assume that the actual current is equal to the commanded current. Therefore, the output torque T_j is equal to the commanded torque that is proportional to the commanded acceleration a_j^{com} given in (1.6). That is,

$$T_j = \frac{mR}{\eta} a_j^{\mathrm{com}}\,, \tag{2.1}$$

where the mass of the robot m, the wheel radius R, and the gear ratio η are provided in Table 2.3.

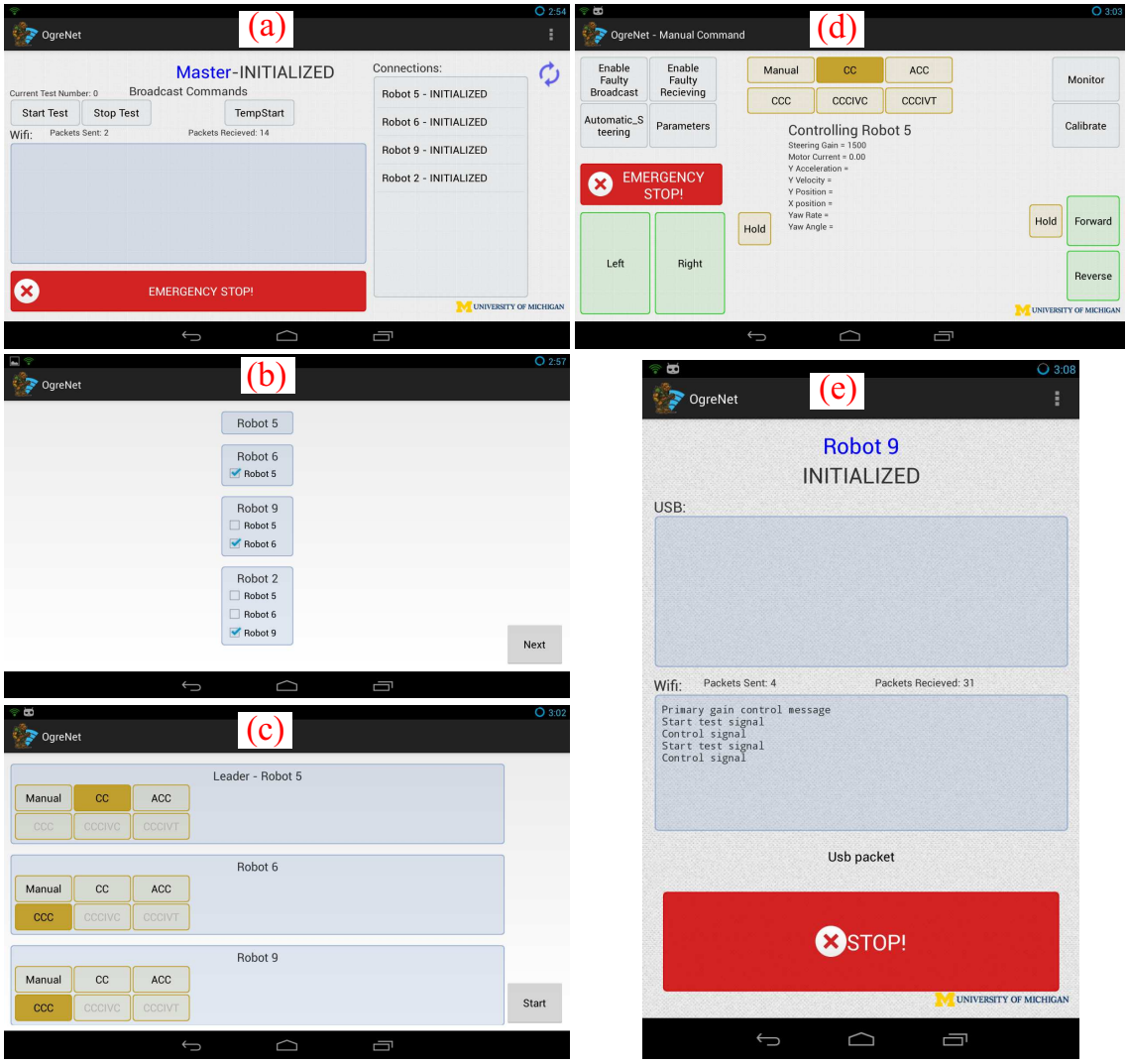

Figure 2.3: Human-machine interface of Android application for data transceiving and control. (a) Master view of robot chain and main control interface. (b) V2V connectivity settings. (c) Longitudinal mode settings. (d) Control interface for a single robot. (e) Individual display for control and V2X communication.

2.1.2 Control-related Software Design

Here we briefly discuss some control-related problems, i.e., clock synchronization, digital effects and delays, control loop alignment, and data processing.

In a multi-agent system clock synchronization plays an important role for analyzing the time-critical effects and data processing. To allow the maximum capacity in vehicle-to-vehicle (V2V) communication networks, dedicated short range communication (DSRC) devices broadcast messages in a distributed manner within each sampling period to avoid

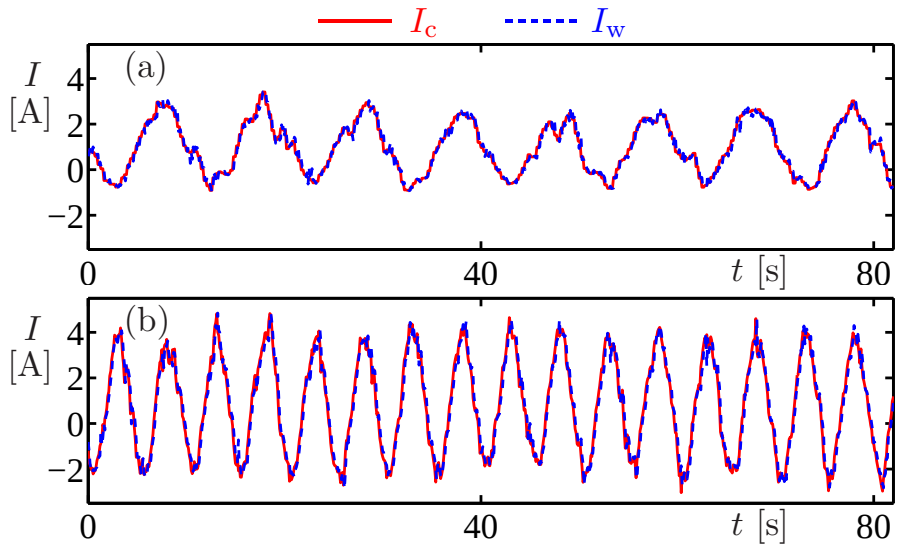

Figure 2.4: Current tracking performance of the servo amplifier. Red solid curve and blue dashed curve represent the commanded current I_c and actual current I_w in the motor windings, respectively.

channel congestion [173–175] . Precision time protocol (PTP) [176] are often used to synchronize clocks among GPS and DSRC devices with sub-microseconds accuracy. In our experiments, instead of PTP, we exploit simple network time protocol (SNTP) [177, 178] to achieve clock synchronization with milliseconds accuracy.

Since DSRC devices broadcast messages at 10 Hz [38] with milliseconds latency [179], digital effects and delays arising from intermittency and packet drops impact the performance of the controllers. As control commands are updated periodically and kept unchanged in between, infrequent data exchange increases the delay in the control system and amplifies digital effects. The following definitions are proposed to facilitate the challenges caused by delays in communication-based control.

Definition 2.1 Communication delay *is the time elapsed from the instant when the data are sampled at the transmitting vehicle to the instant when the data are available to the receiving vehicle.*

Definition 2.2 Information delay *is the time elapsed from the instant when the data are sampled at the transmitting vehicle to the instant when the data are used by the controller on the receiving vehicle.*

In general, both delays can be non-deterministic due to the stochastic nature in V2V communication. However, to ensure the repeatability of the experiments, it is desirable to

have more determinism. In Appendix A, we provide details on how we guarantee that the information delay remains constant while the communication delay varies stochastically. The key points are summarized as follows.

The communication delay is intrinsic and cannot be changed, resulting in the fact that the information about the transmitting vehicle is not immediately available to the receiving vehicle. However, from the control perspective, one cares about how much information delay has been aggregated before the controller utilizes the data. Moreover, it is shown that the range where communication delay varies is much smaller than the control period based on V2V communication. By aligning the starting time of control loops on different robots sufficiently accurately, the information about the transmitter at the current control period can be available to the receiver before the start of its next control period. Indeed, this may also be realized on real vehicles with DSRC devices. The following analysis on digital effects and delays are based on this assumption.

Last but not least, filtering also needs to be considered in the controller design. To get cleaner sensory data, filters/observers, which utilize information of previous few steps to get a better estimate of the current step, are needed. Delay appears in this process, which depends on the period of sensory data processing loop. In order to eliminate this problem, the sensory data processing loop is set to be much faster than the control loop.

The values of the timing errors in our testbed are shown in Table 2.4. Indeed, they are orders of magnitude smaller than the period in V2V communication, which typically has the order of hundreds of milliseconds. This accuracy in timing lays a solid foundation for the study of digital effects, delays and stability in the rest of the thesis.

Table 2.4: Summary of timing errors.

error source	mean value [ms]
clock synchronization error	$\leq 2 \sim 3$
control loop alignment error	≤ 1
period of sensory data processing loop	≤ 4

2.2 Modeling and Analysis

In this section, we present a model to describe the longitudinal vehicle dynamics, and derive the closed-loop dynamics when applying the controller (1.6) with the digital implementation based on the setup in Section 2.1. Subsequently, linearization and discretization are carried out for further analysis. Stability diagrams are used to summarize the results.

To model the longitudinal dynamics of vehicle j in Figure 1.1, we consider no slip condition on the wheels and neglect the flexibility of the tires and the suspension, which results in the differential equation

$$m_{\text{eff}}\,\dot{v}_j = -m\,g\sin\phi - \mu\,m\,g\cos\phi - b\,v_j - \nu\,(v_j + v_{\text{w}})^2 + \frac{\eta\,T_j}{R}\,, \tag{2.2}$$

where $m_{\text{eff}} = m + J/R^2$ is the effective mass, containing the mass of vehicle m, the moment of inertia J of the rotating elements, and the wheel radius R. Also, g is the gravitational constant, ϕ is the inclination angle, μ is the rolling resistance coefficient, b is the motor damping ratio, ν is the air drag constant, v_{w} is the velocity of the headwind, η is the gear ratio, and T_j is the actuation torque. We remark that (2.2) is a simplified model that can capture the longitudinal dynamics of real vehicles as well as the ground robots.

To simplify the analysis, the vehicles are assumed to run on a flat road with no head wind, i.e., $\phi = 0$ and $v_{\text{w}} = 0$. In addition, the moment of inertia of the rotational parts is neglected, i.e., $J \approx 0$, which implies $m_{\text{eff}} \approx m$. Also, instead of using the position, we introduce the distance headway h_j as the other state of the system, resulting in the overall dynamics

$$\begin{aligned} \dot{h}_j &= v_{j-1} - v_j\,, \\ \dot{v}_j &= -\mu\,g - \frac{b}{m}v_j - \frac{\nu}{m}v_j^2 + a_j^{\text{com}}\,, \end{aligned} \tag{2.3}$$

where (2.1) is used.

According to Section 2.1.2, the follower synchronizes its clock and aligns its control loop with the predecessor's. We assume that the kinematic information is sampled and broadcast intermittently with sampling time Δt, resulting in the time mesh $t_k = k\Delta t$, $k = 0, 1, 2, \ldots$; see Figure 2.5(a). At time instant t_k, the information available to the follower is the state of the predecessor measured at t_{k-1}. Thus, the controller on the follower outputs a control command at t_k based on the information about the predecessor at t_{k-1} and keeps it constant until the next updating instant t_{k+1}, which is known as zero-order-hold (ZOH); see Figure 2.5(b). This means that the effective delay increases from Δt to $2\,\Delta t$ during each control interval as shown in Figure 2.5(c), resulting in the average delay $1.5\,\Delta t$. Note that the physical part of the model still evolves in continuous time. Thus, the digitally

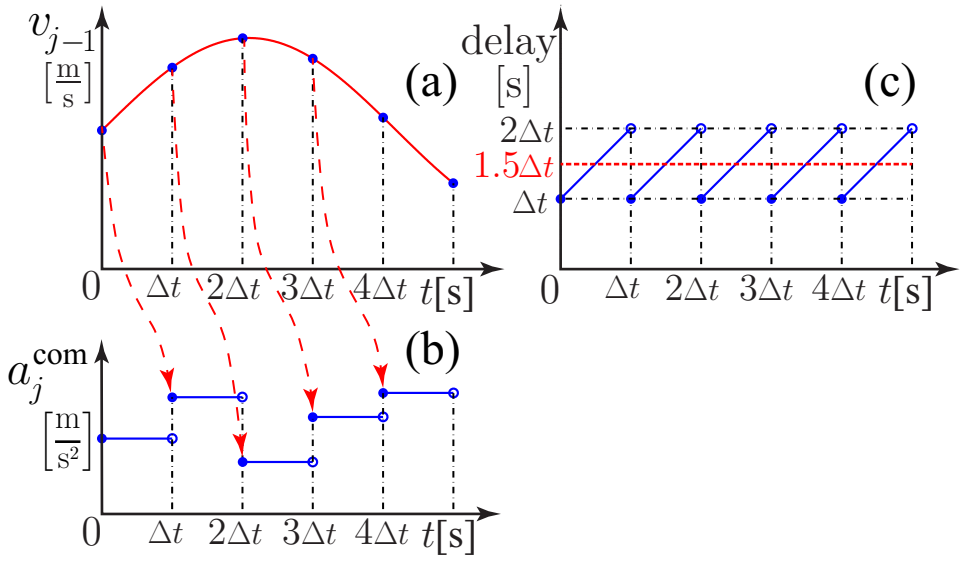

Figure 2.5: (a) Sampling. (b) Control with ZOH. (c) Delay variations.

controlled system can be written as

$$\begin{aligned}
\dot{h}_j &= v_{j-1} - v_j \,, \\
\dot{v}_j &= -\mu\, g - \frac{b}{m} v_j - \frac{\nu}{m} v_j^2 + \alpha \Big(V\big(h_j(t_{k-1})\big) - v_j(t_{k-1}) \Big) + \gamma\, \varepsilon_j(t_k) \\
&\quad + \beta \Big(W\big(v_{j-1}(t_{k-1})\big) - v_j(t_{k-1}) \Big) \,, \\
\varepsilon_j(t_k) &= \varepsilon_j(t_{k-1}) + \Big(V\big(h_j(t_{k-1})\big) - v_j(t_{k-1}) \Big)\, \Delta t \,,
\end{aligned} \tag{2.4}$$

for $t \in [t_k \,,\, t_{k+1})$. Here we use the linear range policy function (1.2, 1.4) with parameters shown in Table 2.2 for the analysis and experiments on the robots.

For $v_{j-1} \leq v_{\max}$, system (2.4) possesses the equilibrium

$$v_j^* = v_{j-1}^* = V(h_j^*) \,, \qquad \varepsilon_j^* = \frac{1}{\gamma} \big(\mu\, g + \frac{b}{m} v_j^* + \frac{\nu}{m} (v_1^*)^2 \big) \,. \tag{2.5}$$

When extended to longer vehicle chains, this is often referred to as the *uniform flow equilibrium* as vehicles travel with the same velocity while keeping the desired distance headway.

For simplicity, we linearize the system about the equilibrium (2.5) and discretize the

resulting equations. With the definition of perturbations

$$\tilde{h}_j = h_j - h_j^* \,, \qquad \tilde{v}_j = v_j - v_j^* \,, \qquad \tilde{\varepsilon}_j = \varepsilon_j - \varepsilon_j^* \,, \tag{2.6}$$

we obtain

$$\begin{aligned} \dot{\tilde{h}}_j &= \tilde{v}_{j-1} - \tilde{v}_j \,, \\ \dot{\tilde{v}}_j &= -c\,\tilde{v}_j + \frac{\alpha}{t_\mathrm{h}}\,\tilde{h}_j(k-1) + \beta\,\tilde{v}_{j-1}(k-1) - (\alpha+\beta)\,\tilde{v}_j(k-1) + \gamma\,\tilde{\varepsilon}_j(k) \\ \tilde{\varepsilon}_j(k) &= \tilde{\varepsilon}_j(k-1) + \frac{\Delta t}{t_\mathrm{h}}\,\tilde{h}_j(k-1) - \Delta t\,\tilde{v}_j(k-1) \,, \end{aligned} \tag{2.7}$$

for $t_k \leq t < t_{k+1}$, where

$$c = \frac{b + 2\,\nu\,v^*}{m} \,, \tag{2.8}$$

and the shorthand notation $\tilde{h}_j(k) = \tilde{h}_j(t_k)$, $\tilde{v}_j(k) = \tilde{v}_j(t_k)$, $\tilde{\varepsilon}_j(k) = \tilde{\varepsilon}_j(t_k)$ and $\tilde{v}_{j-1}(k) = \tilde{v}_{j-1}(t_k)$ was introduced.

Based on Fourier's theory [180], periodic signals can be represented as a countable sum of sines and cosines, which can also be extended to absolutely integrable non-periodic signals using the Fourier transform. Henceforth, assuming sinusoidal variations of the predecessor's velocity, i.e.,

$$v_{j-1}(t) = v_{j-1}^* + v_{j-1}^{\mathrm{amp}} \sin(\omega t) \implies \tilde{v}_{j-1}(t) = v_{j-1}^{\mathrm{amp}} \sin(\omega t) \,, \tag{2.9}$$

and solving (2.4) on the time interval $[t_k \,,\, t_{k+1})$, one can obtain

$$\begin{aligned} x_j(k+1) &= \boldsymbol{a}\,x_j(k) + \boldsymbol{a}_\tau\,\widehat{x}_j(k-1) + \boldsymbol{b}\,u_j(k) + \boldsymbol{b}_\tau\,u_j(k-1) \,, \\ y(k) &= \boldsymbol{c}\,x_j(k) \,, \end{aligned} \tag{2.10}$$

where the states, input and output are given by

$$x_j(k) = \begin{bmatrix} \tilde{h}_j(k) \\ \tilde{v}_j(k) \\ \tilde{\varepsilon}(k) \end{bmatrix} \,, \qquad \widehat{x}_j(k) = \begin{bmatrix} \tilde{h}_j(k) \\ \tilde{v}_j(k) \end{bmatrix} \,, \tag{2.11}$$

$$u_j(k) = \begin{bmatrix} \tilde{v}_{j-1}(k) \\ \tilde{v}_{j-1}^{\perp}(k) \end{bmatrix} \,, \qquad y(k) = \tilde{v}_j(k) \,,$$

and the matrices are

$$\boldsymbol{a} = \begin{bmatrix} 1 & -\theta_1 & -\gamma\theta_4 \\ 0 & \mathrm{e}^{-c\,\Delta\,t} & \gamma\theta_1 \\ \dfrac{\Delta\,t}{t_\mathrm{h}} & -\Delta\,t & 1 \end{bmatrix}, \qquad \boldsymbol{b} = \begin{bmatrix} \theta_2 & \theta_3 \\ 0 & 0 \\ 0 & 0 \end{bmatrix}, \qquad \boldsymbol{c} = \begin{bmatrix} 0 & 1 & 0 \end{bmatrix},$$
$$\boldsymbol{a}_\tau = \begin{bmatrix} -\dfrac{\alpha\theta_4}{t_\mathrm{h}} & (\alpha+\beta)\theta_4 \\ \dfrac{\alpha\theta_1}{t_\mathrm{h}} & -(\alpha+\beta)\theta_1 \\ 0 & 0 \end{bmatrix}, \qquad \boldsymbol{b}_\tau = \begin{bmatrix} -\beta\theta_4 & 0 \\ \beta\theta_1 & 0 \\ 0 & 0 \end{bmatrix}, \tag{2.12}$$

where

$$\theta_1 = \frac{1-\mathrm{e}^{-c\,\Delta\,t}}{c}, \quad \theta_2 = \frac{\sin(\omega\Delta\,t)}{\omega}, \quad \theta_3 = \frac{1-\cos(\omega\Delta\,t)}{\omega}, \quad \theta_4 = \frac{\Delta\,t-\theta_1}{c}, \tag{2.13}$$

and

$$\tilde{v}_{j-1}^{\perp}(t) = v_{j-1}^{\mathrm{amp}}\cos(\omega t)\,. \tag{2.14}$$

Notice that the scalar sinusoidal input (2.9) for the continuous-time system (2.4) results in the vector-valued input (2.11) for the discrete-time system (2.10) despite their independent nature. Also, notice that

$$\widehat{x}_j(k) = \widehat{\mathbf{I}}\,x_j(k)\,, \qquad\qquad u_j(k-1) = \mathbf{R}\,u_j(k)\,, \tag{2.15}$$

where

$$\widehat{\mathbf{I}} = \begin{bmatrix} 1 & 0 & 0 \\ 0 & 1 & 0 \end{bmatrix}, \qquad\qquad \mathbf{R} = \begin{bmatrix} \cos(\omega\Delta\,t) & -\sin(\omega\Delta\,t) \\ \sin(\omega\Delta\,t) & \cos(\omega\Delta\,t) \end{bmatrix}. \tag{2.16}$$

Thus, equation (2.10) can be rewritten as

$$\begin{aligned} X(k+1) &= \mathbf{A}\,X(k) + \mathbf{B}\,U(k)\,, \\ Y(k) &= \mathbf{C}\,X(k)\,, \end{aligned} \tag{2.17}$$

where

$$X(k) = \begin{bmatrix} x_j(k) \\ \widehat{x}_j(k-1) \end{bmatrix}, \qquad U(k) = u_j(k), \qquad Y(k) = y(k), \tag{2.18}$$

and

$$\mathbf{A} = \begin{bmatrix} \boldsymbol{a} & \boldsymbol{a}_\tau \\ \widehat{\mathbf{I}} & 0 \end{bmatrix}, \qquad \mathbf{B} = \begin{bmatrix} \boldsymbol{b} + \boldsymbol{b}_\tau \, \mathbf{R} \\ 0 \end{bmatrix}, \qquad \mathbf{C} = \begin{bmatrix} \boldsymbol{c} & 0' \end{bmatrix}. \tag{2.19}$$

Here, $0' = [0 \quad 0]$.

2.3 Stability

2.3.1 Plant Stability

To check plant stability, we analyze the linearized system (2.17). For plant stability of nonlinear systems, we refer the reader to [124]. Without disturbances on the predecessor's velocity, i.e., $v_{j-1}^{\text{amp}} = 0$ in (2.9, 2.14) or $u_j(k) = 0$ in (2.11), the linearized system (2.17) simplifies to a linear autonomous map. The local asymptotic stability of the uniform flow equilibrium (2.5) of system (2.4) is equivalent to the asymptotic stability of the origin of the linear autonomous map $X(k+1) = \mathbf{A}\, X(k)$. Thus, the system (2.4) is locally plant stable if all the eigenvalues of the matrix $\mathbf{A}$ in (2.17) are within the unit circle in the complex plane. These eigenvalues $z \in \mathbb{C}$ are given by the characteristic equation

$$\det\left(z\,\mathbf{I} - \mathbf{A}\right) = 0, \tag{2.20}$$

where $\mathbf{I} \in \mathbb{R}^{5\times 5}$ is the identity matrix. There are three different ways in which the system can lose stability: (i) One real eigenvalue crosses the unit circle at 1, which corresponds to non-oscillatory divergence of the solution; (ii) One real eigenvalue crosses the unit circle at -1, which corresponds to oscillatory divergence of the solutions with (the highest possible) angular frequency $\pi/\Delta t$ allowed by the discrete time steps; (iii) A pair of complex conjugate eigenvalues crosses the unit circle at $\mathrm{e}^{\pm \mathrm{j}\vartheta}$, $\vartheta \in (0, \pi)$, which corresponds to oscillatory divergence of the solutions with angular frequency $\vartheta/\Delta t \in (0, \pi/\Delta t)$. By substituting the critical eigenvalue(s) into the characteristic equation (2.20), one can obtain the stability boundaries represented in the parameter space $(\alpha, \beta, \gamma, \Delta t, t_{\mathrm{h}})$. In case (iii), one needs to separate the real and imaginary parts and equate both of them to zero to obtain the stability boundary parameterized by ϑ.

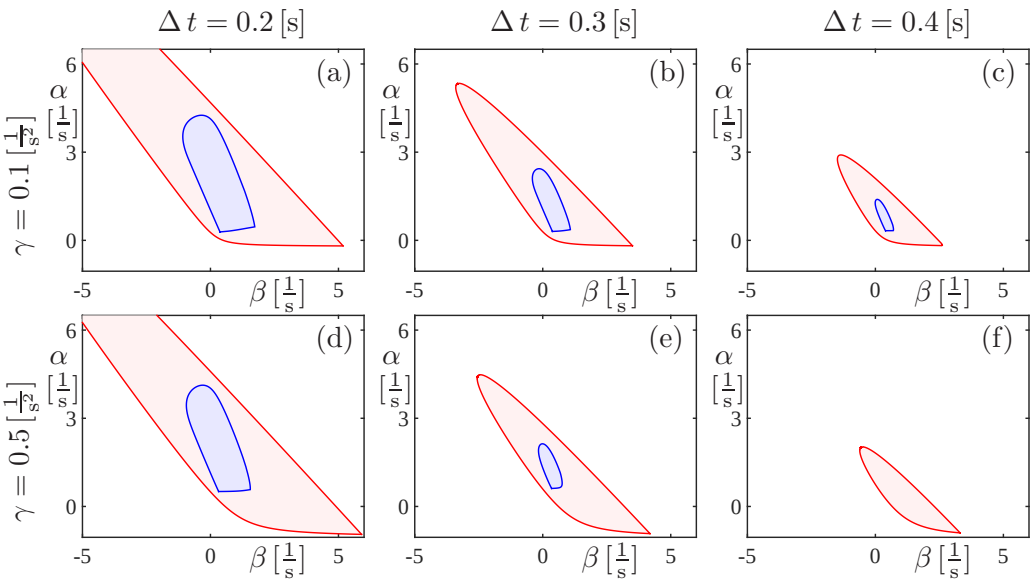

Figure 2.6: Stability diagrams. The red curves and the enclosed shaded regions are the plant stability boundaries and plant stable domains, respectively, while the blue curves and the shaded blue regions are the string stability boundaries and string stable domains, respectively.

While explicit solutions for parametric curves are difficult to obtain analytically, the boundaries can be found via a bisection method [181] combined with continuation. First, a trust region is created in the parameter space (e.g., in the $(\beta\,,\,\alpha)$-plane) and a mesh grid is generated inside it. By checking the stability criterion at each grid point, we divide the trust region into stable and unstable regions that are separated by coarse boundaries. Then, bisection is used to refine the boundaries. Finally, an interpolation-correction procedure can be applied repeatedly to smooth the stability boundaries further until the required accuracy and smoothness are achieved. The advantage of this method is that it works for a wide variety of problems, including non-smooth boundaries and non-convex stability domains.

Figure 2.6 shows the plant stability diagram in the (β, α)-plane for the robot with the parameters shown in Table 2.2 for different sampling time Δt and γ gains. The red curves correspond to plant stability boundaries while the shaded regions enclosed by them are the plant stable domains. Figure 2.6 illustrates that the plant stable domains shrink as the sampling time Δt increases, i.e., it is harder to design controllers for larger sampling time. On the other hand, changing the integral gain γ does not affect plant stability significantly except a slight shift in the stability domains.

2.3.2 String stability

To analyze string stability, we again focus on the linearized system (2.17). With the assumption that the disturbances have finite energy and are absolutely integrable, disturbance attenuation is equivalent to the attenuation of sinusoidal perturbations at all frequencies according to Fourier's theory and superposition principle of linear systems. In other words, string stability is achieved when the amplification ratio in the velocities is less than 1 for all the frequencies. From linear system theory, this amplification ratio can be obtained through transfer functions.

The contributions of the two dependent inputs $\tilde{v}_{j-1}(k)$ and $\tilde{v}^{\perp}_{j-1}(k)$ in (2.17) have to be summed up when deriving the output $\tilde{v}_j(t)$. Applying the Z transform to (2.17), we can obtain the amplification ratio and phase lag as

$$M(\omega) = \left|\Gamma(\mathrm{e}^{\mathrm{j}\,\omega\,\Delta t})\right|, \quad \psi(\omega) = \angle\,\Gamma(\mathrm{e}^{\mathrm{j}\,\omega\,\Delta t})\,, \tag{2.21}$$

where the transfer function is given by

$$\Gamma(z) = \mathbf{C}\big(z\,\mathbf{I} - \mathbf{A}\big)^{-1}\mathbf{B}\mathbf{E}\,, \tag{2.22}$$

and

$$\mathbf{E} = \begin{bmatrix} 1 & \mathrm{j} \end{bmatrix}^{\top} \tag{2.23}$$

is used to sum up the effects of two dependent inputs. Thus, the condition for string stability is given by

$$\sup_{\omega>0}\ M(\omega) < 1\,, \tag{2.24}$$

yielding the string stability boundaries

$$\begin{cases} M(\omega_{\mathrm{cr}}) = 1\,, \\ M'(\omega_{\mathrm{cr}}) = 0\,, \end{cases} \tag{2.25}$$

for critical excitation frequency $\omega_{\mathrm{cr}} > 0$, where prime denotes differentiation with respect to ω. Note that M also depends on the parameters $(\alpha, \beta, \gamma, \Delta t, t_{\mathrm{h}})$, and that $M(0) = 1, M'(0) = 0$ always hold. Therefore, string stability requires $M''(0) < 0$ and the corresponding boundary is given by

$$M''(0) = 0. \tag{2.26}$$

Similar to the plant stability boundaries, bisection method is used to trace the string stability boundaries.

In Figure 2.6, the blue curves denote the string stability boundaries, and the shaded light blue regions are string stable. We remark that there are string stable domains outside the plant stable domains which are not shown in the figure. As the sampling time Δt increases, string stable domains shrink and finally disappear, i.e., it is getting harder and finally impossible to choose gains that can ensure string stability of the system. Moreover, comparing the columns show that varying the integral gain γ may significantly influence string stability.

2.4 Summary

In this section, we studied the connected cruise controller for the predecessor-follower pair where the vehicle controls its longitudinal motion based on the information received from the predecessor via V2V communication. We investigated the system performance with the digital implementation of this controller. By examining plant stability and sting stability of the system, we showed that the arising time delays introduced by the communication and digital control impact the stability of traffic flow significantly. In particular, above a critical delay there exist no such gain combinations that can ensure string stability. While more sophisticated controllers may be designed, they will also possess similar limitations due to information delay and digital effects. In the following chapters, we will validate our results experimentally and extend the digital controller design to more advanced network structures arising in connected vehicle systems and investigate the corresponding performance of these systems.

CHAPTER 3

Experiments for Predecessor-follower Systems

To validate the theoretical analysis on digital effects and delays, we conduct experiments on predecessor-follower systems consisting of two robots in this chapter. We first start with experiments on two-car predecessor-follower systems, by using sensor-based control and V2X-based control. Then the experimental results are compared against the theoretical results obtained in Chapter 2. Finally, we conduct experiments on cascaded predecessor-follower systems to show how disturbances propagate along the vehicle chains. This will shed light on how AVs can be used to improve the traffic performance. The material discussed in this section can be found in [172].

3.1 Two-car Predecessor-follower Systems

In this part, we conduct a set of ACC and CCC experiments with two robots for the two-car predecessor-follower pairs, where the predecessor is labeled as vehicle 0, while the follower is labeled as vehicle 1. First, the experimental string stability boundaries are discussed, followed by the test procedure. Then the advantages of CCC are demonstrated experimentally.

3.1.1 Experimental String Stability and Test Procedure

To validate whether the proposed analytical method can capture the major phenomena caused by intermittency in V2V communication and digital control implementation, a set of experiments is conducted to validate the stability boundaries experimentally. For safety reasons, only string stability is tested experimentally.

Physical limitations are taken into account to avoid saturation as such nonlinearity is out of the scope of this research. First, we set the saturation limits as high as possible while still ensuring the protection of the hardware. Thus, the allowable acceleration of the robots

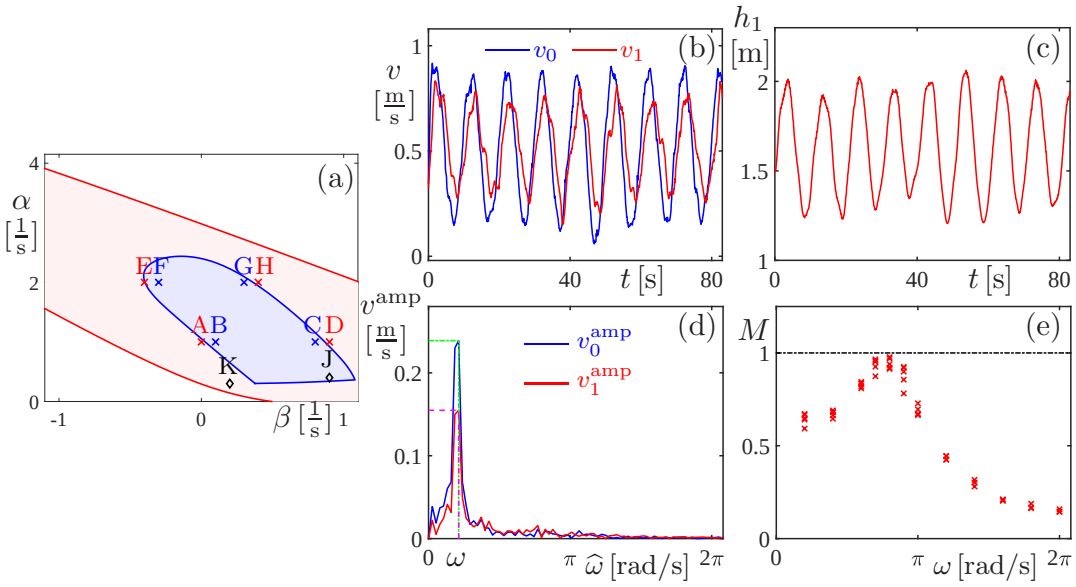

Figure 3.1: Experiment procedure. (a) Stability diagram for $\Delta t = 0.3\,[\mathrm{s}]$ and $\gamma = 0.1$ $[1/\mathrm{s}^2]$. (b, c) Typical profiles in an experiment. (d) FFT results of the velocity profiles. (e) Experimental amplification ratios at different frequencies.

is in the interval $[-a_{\max},\ a_{\max}]$ with $a_{\max} \approx 0.72$ $[\mathrm{m/s}^2]$. Then we select parameters that can prevent the robots from reaching these saturation points. In particular, the sampling interval is chosen to be $\Delta t = 0.3\,[\mathrm{s}]$, resulting in a practically feasible string stable region in the plane of given parameters; see Figure 3.1(a). Also, the amplitude of the oscillations v_0^{amp} in the predecessor's velocity is chosen to make the noise negligible while ensuring that neither the predecessor nor the follower reaches the acceleration limit $a_{\max}$. That is, according to (2.9, 2.21), we require

$$\omega\, v_0^{\mathrm{amp}} \le a_{\max}\,, \qquad\qquad \omega\, v_0^{\mathrm{amp}} M(\omega) \le a_{\max}\,. \tag{3.1}$$

To validate the theoretical string stability boundaries, we run tests corresponding to the points marked as A–H in Figure 3.1(a) (points J and K will be discussed in Section 3.2). During each test, the predecessor introduces a sinusoidal excitation signal (2.9) with frequency ω and the amplitude satisfying conditions (3.1). For case C, the time profiles of the resulting velocity and headway are shown in Figure 3.1(b, c) for frequency $\omega = 0.2\,\pi$ [rad/s] and $v^* = 0.5$ [m/s], respectively. By applying the fast Fourier transform (FFT), the velocity amplitudes can be obtained as shown in Figure 3.1(d). Then the experimental

amplification ratio is calculated as

$$M_{\text{exp}}(\omega) = \frac{v_1^{\text{amp}}(\omega)}{v_0^{\text{amp}}(\omega)}\,, \tag{3.2}$$

corresponding to a red cross in Figure 3.1(e). Through the repetition of the above process, an experimental magnitude response with mean value and error bar can be generated, and this may be repeated for different ω frequencies. In this way, the string stability boundary can be validated experimentally.

To quantify the mismatches between theoretical and experimental results, the *relative error percentage* is defined as

$$e_{\text{M}}(\omega) = \left| \frac{\bar{M}_{\text{exp}}(\omega) - M(\omega)}{M(\omega)} \right|, \tag{3.3}$$

where $\bar{M}_{\text{exp}}(\omega)$ is the mean value of all the experimental amplification ratios at the given frequency ω.

Since the frequencies with larger amplification ratios are more important when determining experimental string stability, we define the *maximum critical error percentage* as

$$\hat{e}_{\text{M}} = \max_{\omega \in \Omega} e_{\text{M}}(\omega)\,. \tag{3.4}$$

Here, Ω is a subset of the tested frequencies Ω_{test} corresponding to large enough amplification ratios, i.e.,

$$\Omega = \{\omega \in \Omega_{\text{test}} \,|\, M(\omega) > M_{\text{crit}}\}\ . \tag{3.5}$$

The error for phase lags can be defined similarly.

3.1.2 ACC vs. CCC

The control algorithm (1.6) is based on the quantities v_0, v_1 and h_1. On the one hand, they can be obtained using range sensors like radar and lidar, which is the typical way of implementing ACC in the industry. On the other hand, they can also be obtained via V2X communication which can be used to supplement sensory information. This leads to a CCC of the simplest kind. While in real vehicles sensory and communication-based information shall be fused before applying the controller, in this section we compare the pure sensor-based control (referred to as ACC) and pure connectivity-based control (referred to as CCC) with two robots to evaluate their strengths and weaknesses. In particular, we emphasize the benefits of V2X connectivity including low cost, high signal quality, and most importantly,

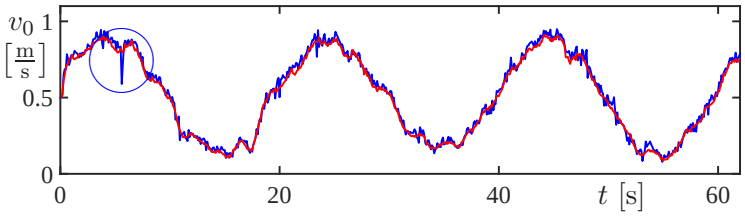

Figure 3.2: Comparison of predecessor's velocities in ACC and CCC.

being able to operate when the predecessor is beyond the line of sight.

When applying the controller (1.6), the follower needs to access its own velocity v_1, the distance headway h_1, and the predecessor's velocity v_0. In the ACC and CCC experiments, data sources are different. For ACC, we use the laser range sensor and tachometer on the following robot to measure the distance h_1 and velocity v_1, respectively. However, the predecessor's velocity v_0 is not directly accessible to the follower but can be obtained from

$$v_0 = v_1 + \dot{h}_1\,, \tag{3.6}$$

with numerical differentiation of the distance h_1. Whereas, for CCC, the predecessor broadcasts its position s_0 and velocity v_0 through V2V communication. Thus, the inter-vehicle distance is calculated as

$$h_1 = s_0 - s_1 - l, \tag{3.7}$$

where s_1 is the follower's position and l is the follower's length.

During the ACC experiments, we experienced a relatively high rate of target loss for the range sensor, that is, the predecessor went beyond the line of sight due to lateral disturbances. In real vehicles, such target loss may happen due to the limitations of onboard sensors [182] when the road is curly, or the weather conditions are not ideal, etc. In contrast, CCC does not require the predecessor to be within the line of sight.

Utilizing V2V communication also increases the quality of feedback signals used in the controller. Figure 3.2 shows a comparison of the predecessor's velocity, where the blue curve is the filtered signals of (3.6) in ACC while the red curve is obtained through V2V communication in CCC. Notice that the follower experiences high-frequency noise in the former but not in the latter case. Also, jitters may occur due to numerical differentiation when, due to uneven road surface, the distance measured by the range sensor jumps as highlighted by the blue circle in Figure 3.2. On the other hand, numerical differentiation is not needed when predecessor measures its states with onboard sensors and broadcasts

these via V2V communication. Both high-frequency noise and jitter degrade the driving comfort. Indeed, one can spend efforts designing better filters/observers to improve the signal quality. However, this introduces larger phase lags between real states and estimated states, potentially leading to unstable behaviors.

Besides the advantages mentioned here, challenges exist in order to make CCC practically feasible. As discussed in Section 2.1.2, intermittent communication amplifies digital effects in the system. Also, packet drops in V2X communication increases the information delay that will be discussed further in later chapters. Thus, CCC design requires the preservation of string stability in the presence of increased information delay.

3.1.3 Results

In order to validate the experimental string stability boundaries, here we present the results of ACC and CCC experiments for the gain combinations marked as A–H in Figure 3.1(a); see Table 3.1 for the corresponding numerical values. We remark that in ACC the feedback information is intentionally held for one period to achieve the same timing as in CCC; see the discussion in Section 2.1.2.

Table 3.1: Control gains for different points in Figure 3.1(a).

point	β [1/s]	α [1/s]	γ [1/s^2]
A	0	1	0.1
B	0.1	1	0.1
C	0.8	1	0.1
D	0.9	1	0.1
E	-0.3	2	0.1
F	-0.4	2	0.1
G	0.3	2	0.1
H	0.4	2	0.1
J	0.9	0.4	0.1
K	0.2	0.3	0.1

Figure 3.3 shows the resulting amplification ratios for different cases. The red solid curves represent the theoretical results, while the blue and magenta symbols with error bars denote the results of ACC and CCC experiments, respectively. As illustrated, the experimental amplification ratios match very well with the theoretical ones. We remark that similar matching can be observed for phase lags but are not shown here to avoid repetition. In other words, the theoretical analysis shown in Section 2 is able to capture the behavior,

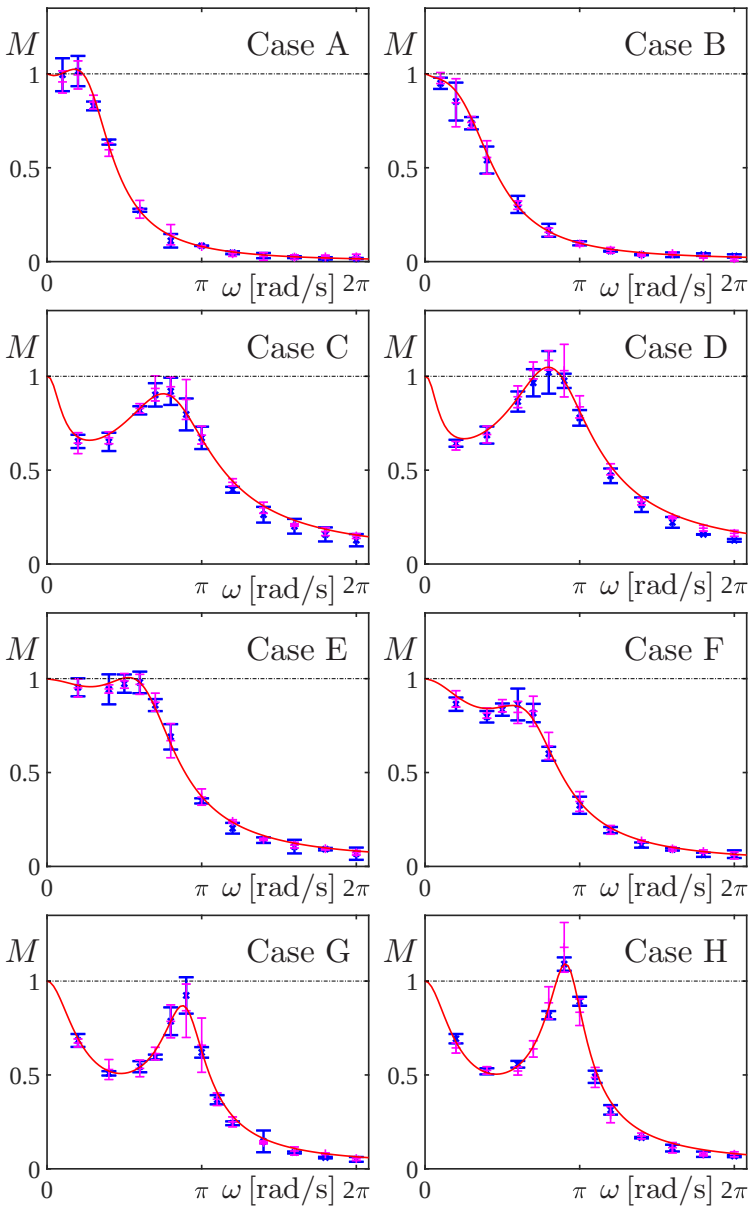

Figure 3.3: Amplification ratios as a function of excitation frequency. The red curves are the theoretical results, while the blue and magenta error bars represent the experimental results of ACC and CCC, respectively.

and the results indicate that string stability can be achieved experimentally in the presence of relatively large information delay. Finally, we remark that CCC achieves the same level of performance as ACC: the maximum critical error percentages for all the experiments are listed in Table 3.2 when $M_{\text{crit}} = 0.5$; cf. (3.3, 3.4, 3.5).

Table 3.2: The maximum critical error percentage.

	ACC		CCC	
	amplification ratio	phase lag	amplification ratio	phase lag
case A	6.2%	12.6%	4.6%	14.0%
case B	6.1%	16.5%	6.7%	17.7%
case C	6.0%	4.4%	9.0%	6.4%
case D	10.1%	3.7%	6.8%	7.1%
case E	5.7%	3.2%	3.6%	4.5%
case F	5.2%	4.5%	5.6%	3.3%
case G	7.7%	4.3%	4.9%	7.5%
case H	8.1%	5.6%	8.7%	3.3%

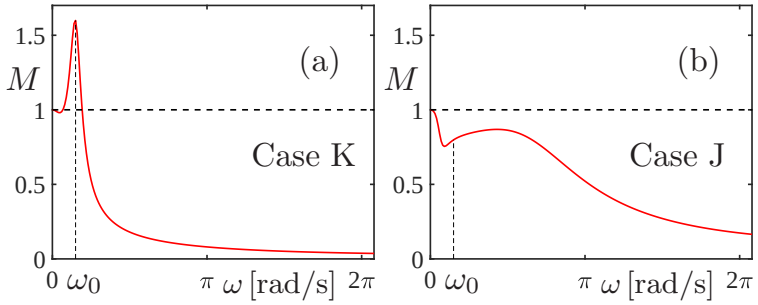

Figure 3.4: Amplification ratio as a function of excitation frequency.

3.2 Cascaded Predecessor-follower Systems

In this section, to demonstrate the importance of string stability in traffic flow, experiments are conducted using five robots that constitute a cascaded predecessor-follower system. First, we show the overall performance of a chain of string unstable vehicles and a chain of string stable vehicles, respectively. Then mixed chains of string stable and string unstable vehicles are studied to evaluate the impact of different penetration rates on traffic dynamics.

In Section 3.1.3, experiments showed a satisfactory correspondence with the theoretical results. Here, two sets of gains corresponding to points K and J are chosen on the stability diagram in Figure 3.1(a), so that the difference in amplification can be easily captured without running the FFT as fluctuations propagate along the chain. The theoretical amplification ratios are shown in Figure 3.4. Vehicles using gains corresponding to case K are referred to as string unstable while those gains corresponding to case J are referred to as string stable from now on. They are depicted as white and green vehicles, respectively while the head vehicle, that introduces the velocity fluctuations, is distinguished as black;

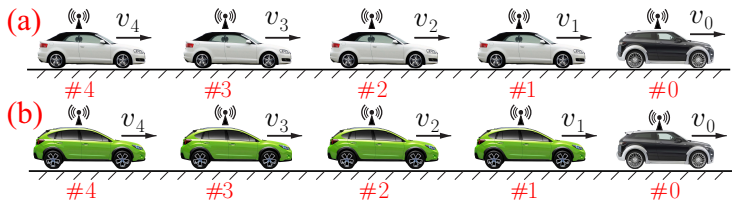

Figure 3.5: (a) Four string unstable vehicles follow a head vehicle. (b) Four string stable vehicles follow a head vehicle.

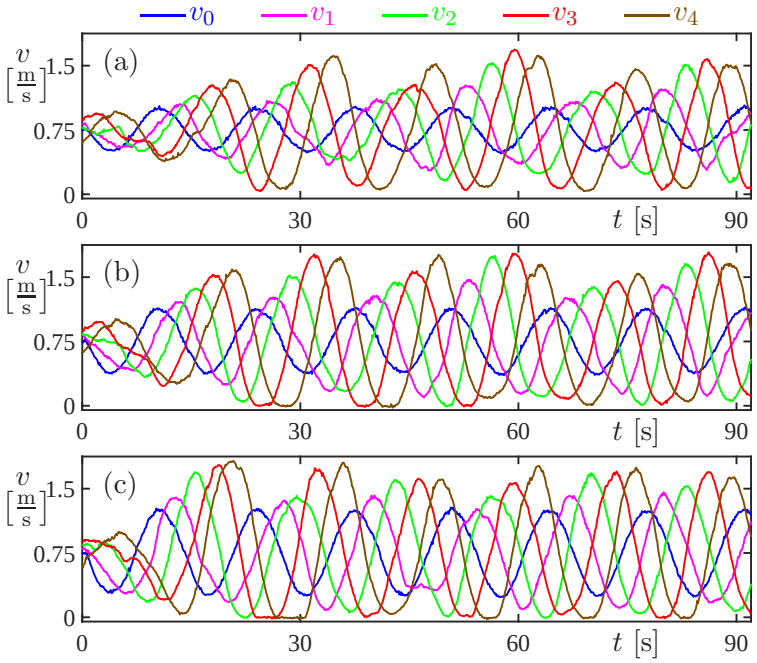

Figure 3.6: Responses to periodic excitations with four string unstable vehicles configured as shown in Figure 3.5(a). (a) $v_0^{\text{amp}} = 0.25$ [m/s]. (b) $v_0^{\text{amp}} = 0.375$ [m/s]. (c) $v_0^{\text{amp}} = 0.5$ [m/s].

see Figure 3.5. The frequency $\omega_0 = 0.15\,\pi$ [rad/s] highlighted in Figure 3.4 is used as the excitation frequency for periodic fluctuations in the rest of this chapter. Also, we set $v_0^* = 0.75$ [m/s].

First, we demonstrate how string unstable vehicles amplify fluctuations in traffic flow using the configuration in Figure 3.5(a) where the following four vehicles are all string stable. Figure 3.6 shows the velocity profiles for periodic excitations of different sizes. One can see that the fluctuations are gradually amplified along the chain in all cases, and a full stop may be reached when the amplified fluctuations are large enough.

In practice, excitations are typically not periodic but contain signals of different fre-

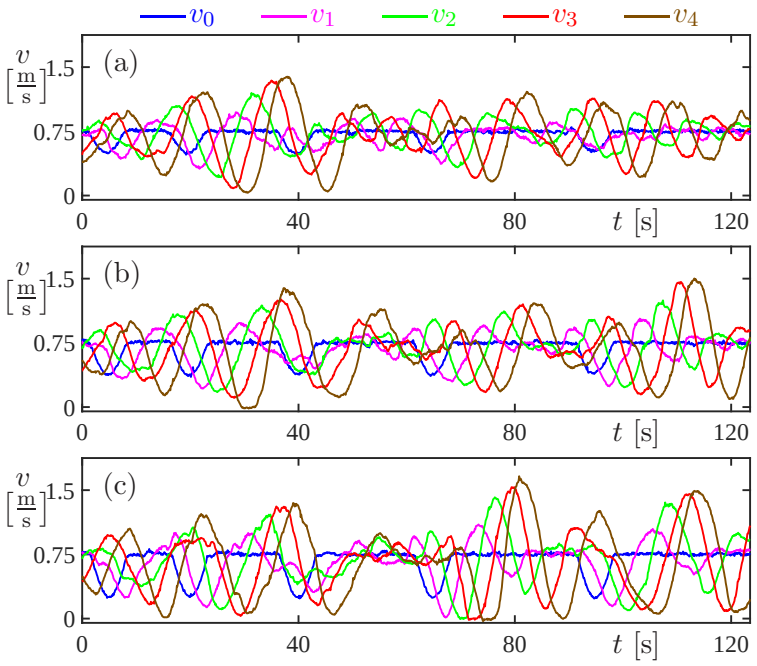

Figure 3.7: Responses to aperiodic excitations with four string unstable vehicles configured as shown in Figure 3.5(a). (a) $v_0^{\text{amp}} = 0.25$ [m/s]. (b) $v_0^{\text{amp}} = 0.375$ [m/s]. (c) $v_0^{\text{amp}} = 0.5$ [m/s].

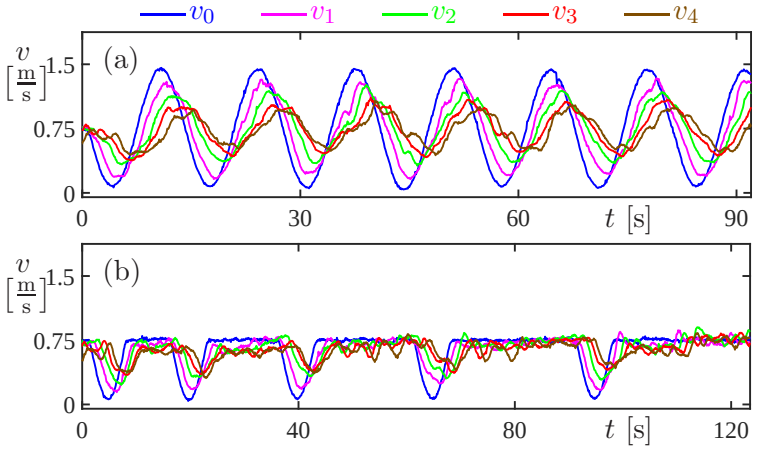

Figure 3.8: Responses to excitations with four string stable vehicles configured as shown in Figure 3.5(b). (a) Periodic excitations. (b) Aperiodic excitations.

quencies. Thus, fluctuations at string unstable frequencies are amplified while those at string stable frequencies are attenuated. To demonstrate this phenomenon, another set of experiments is conducted where the head vehicle generates aperiodic velocity excitations and the results are shown in Figure 3.7 for different sizes of perturbations. It can be seen

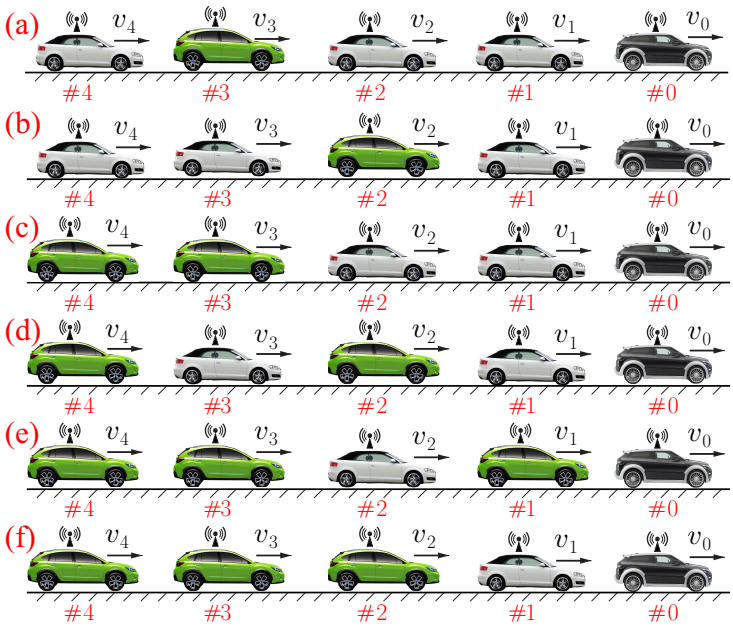

Figure 3.9: Vehicle configurations for different penetration rates of string stable vehicles (green) among string unstable vehicles (white). (a, b) One string stable vehicle. (c, d) Two string stable vehicles. (e, f) Three string stable vehicles.

that perturbations are amplified as propagating along the vehicle chain, and full stops are also reached for large enough perturbations. Figs. 3.6 and 3.7 show that the amplification phenomena are similar regardless of the sizes of perturbations. Thus, in the following experiments, we choose a particular excitation size such that the amplification effects are distinguishable from other disturbances.

In order to show how string stable vehicles attenuate fluctuations in traffic flow, we use the configuration in Figure 3.5(b) where the following four vehicles are all string stable. The corresponding velocity profiles for periodic and aperiodic excitations are shown in Figure 3.8(a) and (b), respectively. They indicate that a chain of string stable vehicles are able to attenuate oscillations introduced by the head vehicle. In Figure 3.8(b), tiny velocity fluctuations are still observable in the following vehicles when the velocity of the head vehicle is almost constant. This is caused by the disturbances in the road grade variations, steering efforts, measurement noise, etc.

Comparing the results between Figure 3.6 and Figure 3.8(a), or those between Figure 3.7 and Figure 3.8(b), one can see the differences are significant depending on whether the vehicles in the chain are string stable or not. In the following part, we study the behaviors for mixed chains of string stable and string unstable vehicles. String unstable vehicles are used to mimic the behaviors of human drivers, while string stable vehicles represent

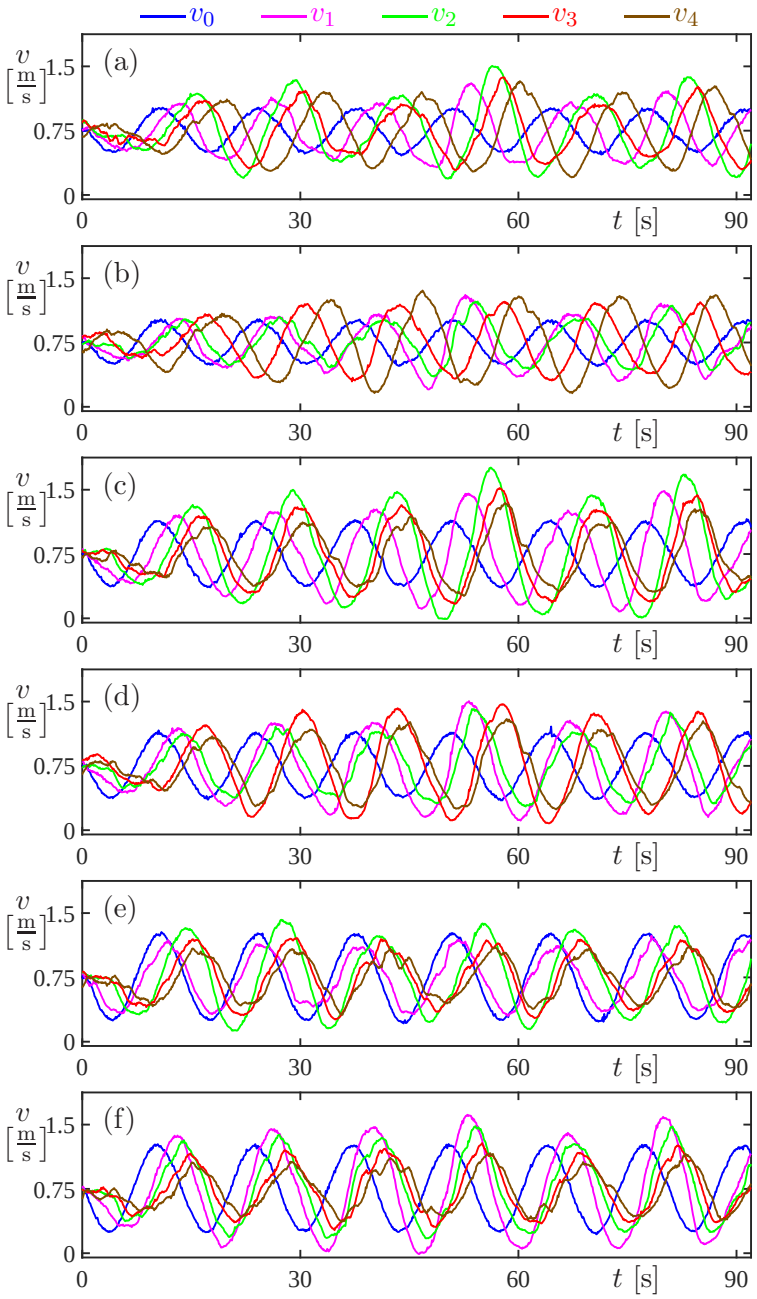

Figure 3.10: Responses to periodic excitations as the penetration rate of string stable vehicle varies.

automated vehicles. Figure 3.9 depicts different configurations where out of the following four vehicles, one, two and three of them are set to be string stable to represent 25%, 50% and 75% penetration rates, respectively. Indeed, there are $2^4 = 16$ different configurations, but only two of them will be demonstrated for each penetration rate when there exists multiple.

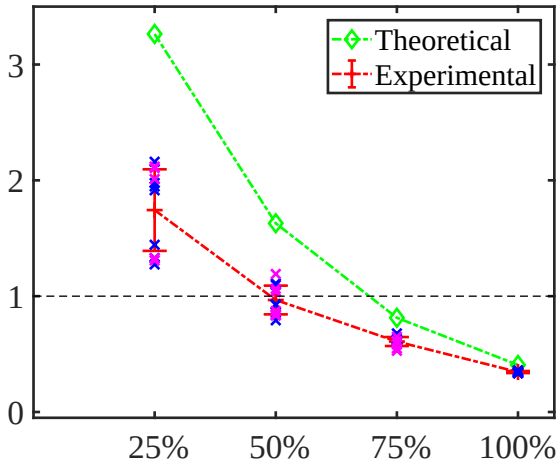

Figure 3.11: Amplification ratio vs. penetration rate of string stable vehicles.

Figure 3.10 shows the velocity profiles for the configurations depicted in Figure 3.9. In Figure 3.10(a) and (b), with only one string stable vehicle in the chain, the oscillation amplitude of v_4 is much larger than that of v_0. However, as the number of string stable vehicles increases, the amplification of fluctuations becomes less pronounced as illustrated in panels (c) and (d) where two string stable vehicles are included. Panels (e) and (f) indicate that the fluctuations can be attenuated when the number of string stable vehicles is increased to three. Note that the difference in the amplification ratio for the same penetration rate is negligible when comparing the results between panels (a) and (b), between panels (c) and (d), or between panels (e) and (f).

To quantify the phenomena above, each test is repeated multiple times for all the configurations shown in Figure 3.9. After each test, the FFT is used to obtain the amplification ratio at a given frequency as discussed in Section 3.1.1. The results are summarized in Figure 3.11. The blue and magenta crosses represent the results of two different configurations. One can see for the same penetration rate the experimental distributions are similar regardless of the difference in configurations. Thus, they are treated equally when calculating the mean value and standard deviation of the experimental amplification ratios, which are represented by the dashed red curve with error bars. The dashed green curve with diamond markers represents the theoretical amplification ratio at the same frequency. The mismatches between the experimental and theoretical results at low penetration rates are mainly caused by the actuator limitations and nonlinear effects in the presence of large oscillations. The results indicate that when the penetration rate of string stable vehicles exceeds 50%, fluctuations can be attenuated in our experiments.

3.3 Summary

In this chapter we experimentally investigated the two-car predecessor-follower system with controller (1.6) using sensor-based control (ACC) as well as V2X-based connected cruise control. The model-based design in Chapter 2 is demonstrated to be valid while incorporating time delays in deriving the plant stability and string stability conditions for the closed-loop system. We also showed that the V2X-based control can achieve the same level of performance as sensor-based control without having the line-of-sight limitation.

In order to investigate the scalability of CCC to larger traffic systems, we conducted a set of experiments on cascaded predecessor-follower systems with five robots. We demonstrated that when all the vehicles are string unstable, fluctuations keep increasing as they propagate backwards along the chain of vehicles and may even lead to full stops. On the contrary, when all the vehicles are string stable, the fluctuations decay leading to smooth traffic flow. In mixed traffic scenarios containing both string stable and string unstable vehicles, our experiments showed that a high enough penetration of the former type may allow one to attenuate the fluctuations and smooth out the ripples in traffic. In practice, since AVs (or CAVs) can be designed to maintain string stability while human drivers can rarely achieve that, having a high penetration rate of AVs (or CAVs) is expected to impact traffic positively.

CHAPTER 4

Controller Design and Validation of Connected Vehicle Systems

We have theoretically and experimentally designed a connected cruise controller for the simplest connectivity structure in the previous chapters, where the follower only utilized the information broadcast by the direct predecessor via V2X communication. However, the greatest advantage of V2X-based control is the ability to respond to the motion of multiple preceding vehicles even to those that are beyond the line of sight. Thus, in order to maximize the benefits of V2X communication in improving the dynamic behaviors of individual CAVs as well as overall traffic performance, we study the CCC controller (1.8) that incorporates the information of multiple vehicles ahead. We investigate increasingly complex connectivity topologies and conduct experiment by utilizing the scaled connected vehicle testbed. The material discussed in this section can be found in [183].

4.1 Modeling and Analysis

In this section, we use the same model as in Chapter 2.2 to describe the vehicle dynamics, and then derive the closed-loop dynamics by incorporating the extended connected cruise controller (1.8) with digital implementation. After linearization and discretization, stability conditions are derived theoretically in order to guide the experiments for connected vehicle systems.

Let us consider a chain of connected vehicles as shown in Figure 1.1 and assume that all the vehicles have identical dynamics given by (2.3), i.e.,

$$\begin{aligned} \dot{h}_j &= v_{j-1} - v_j \,, \\ \dot{v}_j &= -\mu\, g - \frac{b}{m} v_j - \frac{\nu}{m} v_j^2 + a_j^{\rm com} \,. \end{aligned} \tag{4.1}$$

Concerning digital implementation, we made the same assumptions about clock synchronization, data sampling, and control mechanism as those in Chapter 2. Thus, with connected cruise controller (1.8), the digitally controlled system becomes

$$\begin{aligned}
\dot{h}_j &= v_{j-1} - v_j \,, \\
\dot{v}_j &= -\mu\, g - \frac{b}{m} v_j - \frac{\nu}{m} v_j^2 + \sum_{i=0}^{j-1} \Big(\alpha_{j,\,i} \Big(V\big(h_{j,\,i}(t_{k-1})\big) - v_j(t_{k-1}) \Big) \\
&\qquad + \beta_{j,\,i} \Big(W\big(v_i(t_{k-1})\big) - v_j(t_{k-1}) \Big) \Big) + \gamma_j\, \varepsilon_j(t_k) \,, \\
\varepsilon_j(t_k) &= \varepsilon_j(t_{k-1}) + \Big(V\big(h_j(t_{k-1})\big) - v_j(t_{k-1}) \Big)\, \Delta t \,,
\end{aligned} \tag{4.2}$$

for $j = 1\,,\,\ldots\,,\,J$ when $t \in [t_k,\, t_{k+1})$. Here we use the linear range policy function (1.2, 1.4) with parameters shown in Table 2.2 for the analysis and experiments on the robots. When the velocities do not exceed the speed limit, system (4.2) possesses the equilibrium

$$v_j^* = V(h_j^*) = v_0 \,, \qquad\qquad \varepsilon_j^* = \frac{1}{\gamma_j} \big(\mu\, g + \frac{b}{m} v_j^* + \frac{\nu}{m} (v_j^*)^2 \big) \,, \tag{4.3}$$

for $j = 1\,,\,\ldots\,,\,J$, where vehicles travel with the same velocity as the head vehicle while keeping the desired inter-vehicle distance. This is called the *uniform flow equilibrium*.

We linearize the system about the equilibrium (4.3) and discretize the obtained linear equations. Using the perturbations defined in (2.6), one may obtain

$$\dot{\tilde{h}}_j = \tilde{v}_{j-1} - \tilde{v}_j \,, \tag{4.4}$$

$$\begin{aligned}
\dot{\tilde{v}}_j &= -c\, \tilde{v}_j + \sum_{i=0}^{j-1} \Big(\frac{\alpha_{j,\,i}}{t_{\rm h}} \cdot \frac{1}{j-i} \sum_{l=i+1}^{j} \tilde{h}_l(k-1) \\
&\qquad + \beta_{j,\,i} \tilde{v}_i(k-1) - (\alpha_{j,\,i} + \beta_{j,\,i})\, \tilde{v}_j(k-1) \Big) + \gamma_j\, \tilde{\varepsilon}_j(k) \,,
\end{aligned} \tag{4.5}$$

$$\tilde{\varepsilon}_j(k) = \tilde{\varepsilon}_j(k-1) + \frac{\Delta t}{t_{\rm h}}\, \tilde{h}_j(k-1) - \Delta t\, \tilde{v}_j(k-1) \,, \tag{4.6}$$

for $j = 1\,,\,\ldots\,,\,J$ when $t \in [t_k,\, t_{k+1})$, where $t_{\rm h}$ is defined in (1.5), and c is defined in (2.8).

Again we assume sinusoidal variations in the head vehicle's velocity, i.e.,

$$v_0(t) = v_0^* + v_0^{\rm amp} \sin(\omega\, t) \implies \tilde{v}_0(t) = v_0^{\rm amp} \sin(\omega\, t) \,, \tag{4.7}$$

and solving the system (4.4, 4.5, 4.6) from t_k to t_{k+1}, one can obtain

$$
\begin{aligned}
x_1(k+1) &= \boldsymbol{a}_{1,1}\, x_1(k) + \boldsymbol{a}_{1,1}^{\tau}\, \widehat{x}_1(k-1) + \boldsymbol{b}_0\, u(k) + \boldsymbol{b}_1^{\tau} u(k-1)\,, \\
x_j(k+1) &= \boldsymbol{a}_{j,\,j}\, x_j(k) + \boldsymbol{a}_{j,\,j-1}\, x_{j-1}(k) + \sum_{l=1}^{j} \boldsymbol{a}_{j,\,l}^{\tau}\, \widehat{x}_l(k-1) + \boldsymbol{b}_j^{\tau} u(k-1)\,,
\end{aligned}
\tag{4.8}
$$

for $j = 2\,, \ldots\,,\, J$, where the states and input are given by

$$
x_j(k) = \begin{bmatrix} \tilde{h}_j(k) \\ \tilde{v}_j(k) \\ \tilde{\varepsilon}(k) \end{bmatrix}\,, \qquad \widehat{x}_j(k) = \begin{bmatrix} \tilde{h}_j(k) \\ \tilde{v}_j(k) \end{bmatrix}\,, \qquad u(k) = \begin{bmatrix} \tilde{v}_0(k) \\ \tilde{v}_0^{\perp}(k) \end{bmatrix}\,, \tag{4.9}
$$

with

$$
\tilde{v}_0^{\perp}(t) = v_0^{\mathrm{amp}} \cos(\omega\, t)\,, \tag{4.10}
$$

The derivations and matrices $\boldsymbol{a}_{j,\,j}$, $\boldsymbol{a}_{j,\,j-1}$, $\boldsymbol{a}_{j,\,l}^{\tau}$, $\boldsymbol{b}_0$ and $\boldsymbol{b}_j^{\tau}$ are provided in Appendix B.

Similar to the predecessor-follower system, the scalar sinusoidal input (4.7) for the continuous-time system (4.2) results in the vector-valued input (4.9) for the discrete-time system (4.8), and

$$
\widehat{x}_j(k) = \widehat{\mathbf{I}}\, x_j(k)\,, \qquad\qquad u(k-1) = \mathbf{R}\, u(k)\,, \tag{4.11}
$$

where $\widehat{\mathbf{I}}$ and $\mathbf{R}$ are the same as those given in (2.16). Thus, equation (4.8) can be rewritten as

$$
X_j(k+1) = \sum_{l=1}^{j} \mathbf{A}_{j,\,l}\, X_l(k) + \mathbf{B}_j\, u(k)\,, \tag{4.12}
$$

for $j = 1,\, \ldots\,,\, J$, where

$$
X_j(k) = \begin{bmatrix} x_j(k) \\ \widehat{x}_j(k-1) \end{bmatrix}\,. \tag{4.13}
$$

The matrices in (4.12) are

$$
\mathbf{A}_{j,\,j} = \begin{bmatrix} \boldsymbol{a}_{j,\,j} & \boldsymbol{a}_{j,\,j}^{\tau} \\ \widehat{\mathbf{I}} & 0 \end{bmatrix}\,, \tag{4.14}
$$

for $j = 1\,,\,\ldots\,,\,J$,

$$\mathbf{A}_{j,\,j-1} = \begin{bmatrix} \boldsymbol{a}_{j,\,j-1} & \boldsymbol{a}_{j,\,j-1}^{\tau} \\ 0 & 0 \end{bmatrix}\,, \qquad\qquad \mathbf{B}_j = \begin{bmatrix} \boldsymbol{b}_j^{\tau}\,\mathbf{R} \\ 0 \end{bmatrix}\,, \tag{4.15}$$

for $j = 2\,,\,\ldots\,,\,J$,

$$\mathbf{A}_{j,\,l} = \begin{bmatrix} 0 & \boldsymbol{a}_{j,\,l}^{\tau} \\ 0 & 0 \end{bmatrix}\,, \tag{4.16}$$

for $j = 3\,,\,\ldots\,,\,J\,,\;l = 1\,,\,\ldots\,,\,j-2$, and

$$\mathbf{B}_1 = \begin{bmatrix} \boldsymbol{b}_0 + \boldsymbol{b}_1^{\tau}\,\mathbf{R} \\ 0 \end{bmatrix}\,. \tag{4.17}$$

Thus, the overall system becomes

$$\begin{aligned} X(k+1) &= \mathbf{A}X(k) + \mathbf{B}\,U(k)\,, \\ Y(k) &= \mathbf{C}X(k)\,, \end{aligned} \tag{4.18}$$

where the state, the input and the output are given by

$$X(k) = \begin{bmatrix} X_1(k) \\ X_2(k) \\ \vdots \\ X_J(k) \end{bmatrix}\,, \qquad U(k) = u(k)\,, \qquad Y(k) = \tilde{v}_J(k)\,, \tag{4.19}$$

and the matrices are

$$\begin{aligned} \mathbf{A} &= \begin{bmatrix} \mathbf{A}_{1,1} & & & \\ \mathbf{A}_{2,1} & \mathbf{A}_{2,2} & & \\ \vdots & \ddots & \ddots & \\ \mathbf{A}_{J,1} & \cdots & \mathbf{A}_{J,\,J-1} & \mathbf{A}_{J,\,J} \end{bmatrix}\,, \qquad \mathbf{B} = \begin{bmatrix} \mathbf{B}_1 \\ \mathbf{B}_2 \\ \vdots \\ \mathbf{B}_J \end{bmatrix}\,, \\ \mathbf{C} &= \begin{bmatrix} o & \ldots & o & C \end{bmatrix}\,. \end{aligned} \tag{4.20}$$

Here, $o \in \mathbb{R}^{1\times 5}$ is the zero vector and $C = \begin{bmatrix} 0 & 1 & 0 & 0 & 0 \end{bmatrix}$.

4.2 Plant stability and head-to-tail string stability

To investigate plant stability, we analyze the linearized system (4.18). Without velocity disturbances on the head vehicle, i.e., $v_0^{\text{amp}} = 0$ in (4.7, 4.10) or $u(k) = 0$ in (4.9), we obtain a linear autonomous map. The local asymptotic stability of the uniform flow equilibrium (4.3) of the system (4.2) is equivalent to the asymptotic stability of the trivial solution of the map $X(k+1) = \mathbf{A}X(k)$, which is ensured when all the eigenvalues of the matrix $\mathbf{A}$ in (4.18) are within the unit circle in the complex plane. The eigenvalues $z \in \mathbb{C}$ are given by the characteristic equation

$$\det\big(z\,\mathbf{I} - \mathbf{A}\big) = 0\,, \tag{4.21}$$

where $\mathbf{I} \in \mathbb{R}^{5J\times 5J}$ is the identity matrix. The bisection method explained in Chapter 2.3.1 will be used later to trace the boundaries in the parameter space.

To evaluate head-to-tail string stability, we again use the linearized system (4.18) and make the same assumption about the disturbances in the head vehicle's velocity as in Chapter 2. We use transfer functions to derive the amplification ratio from $\tilde{v}_0$ to $\tilde{v}_J$ and sum up the contributions of two dependent components in the input (4.9). Applying the Z transform to (4.18), we can derive the amplification ratio and phase lag as

$$M(\omega) = \big|\Gamma(\mathrm{e}^{\mathrm{j}\,\omega\,\Delta t})\big|\,, \qquad\qquad \psi(\omega) = \angle\,\Gamma(\mathrm{e}^{\mathrm{j}\,\omega\,\Delta t}), \tag{4.22}$$

where the transfer function is

$$\Gamma(z) = \mathbf{C}\big(z\,\mathbf{I} - \mathbf{A}\big)^{-1}\mathbf{B}\mathbf{E}\,, \tag{4.23}$$

and

$$\mathbf{E} = \begin{bmatrix} 1 & \mathrm{j} \end{bmatrix}^{\top} \tag{4.24}$$

is used to sum up the effects of two dependent components. Thus, the condition for head-to-tail string stability becomes

$$\sup_{\omega>0}\; M(\omega) < 1\,, \tag{4.25}$$

where M also depends on the system parameters. Similar to the plant stability boundaries, bisection method will be used to trace the string stability boundaries in the parameter space.

Indeed, if the longitudinal controller can be designed for every vehicle, string stability can be achieved. However, in order to mimic scenarios when CCC vehicles are inserted to a chain of human-driven vehicles we will deliberately set some robots to be string unstable (while responding to the motion of the vehicle immediately ahead).

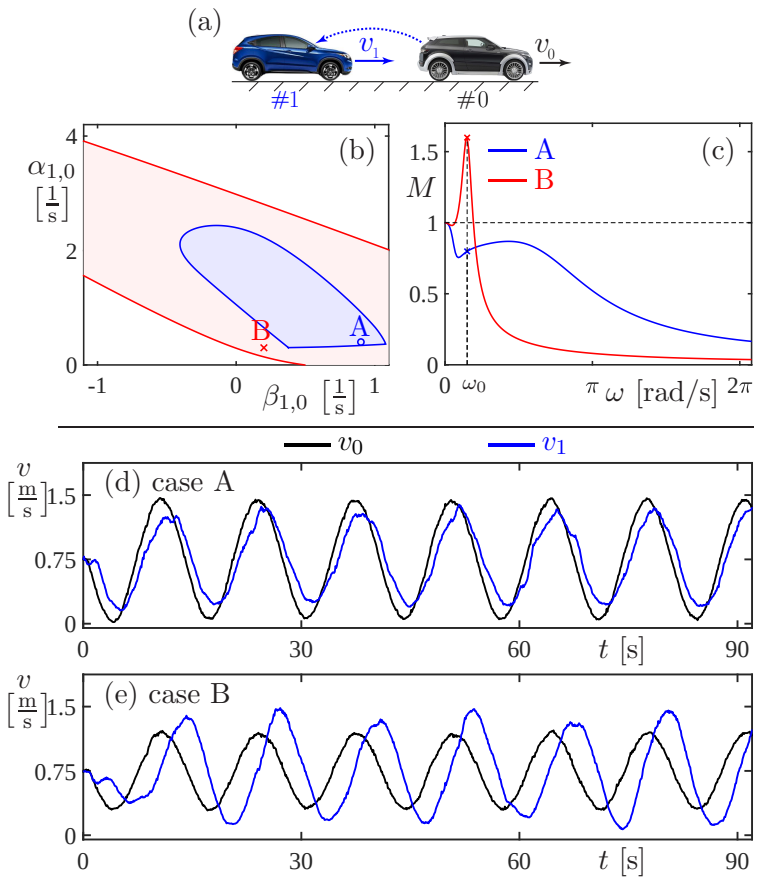

Figure 4.1: (a) Two-vehicle configuration. (b) Stability diagram. (c) Frequency responses for points A and B marked in panel (b). (d, e) Experimental velocity profiles when vehicle 0 introduces sinusoidal velocity fluctuations at $\omega_0 = 0.15\pi$ [rad/s] in cases A and B, respectively.

4.3 Experimental Validation

In this section, we present the experimental results with different connectivity topologies to demonstrate the effectiveness and flexibility of the controller (1.8) when the CCC vehicle is operating among string unstable vehicles. The design rules for connected vehicle systems are gradually built up via experiments of increasing complexity. The sampling time Δt is set to 0.3 [s] to get implementable gains, the integral gains γ_j-s are set to 0.1 [1/s^2], and we use $v_0^* = 0.75$ [m/s]. The other parameters are shown in Table 2.2.

4.3.1 Two-vehicle experiments

To demonstrate that string stability is achievable when the longitudinal controller can be designed for every vehicle, we first study a predecessor-follower system consisting of two

vehicles. Apart from experimentally validating the string stable gain combinations, we also conduct experiments to illustrate string unstable behavior when mimicking the driving behaviors of humans.

Figure 4.1(a) depicts the two-car system where the follower controls its motion based on the data of its predecessor, while Figure 4.1(b) shows the corresponding stability diagram generated based on the conditions in Section 4.2. The red curves and blue curves represent the plant stability and string stability boundaries, respectively. The union of red and blue regions indicates the plant stable domain, while the blue shaded region is the string stable domain. The coloring scheme for stability diagrams is kept the same throughout this chapter.

Experiments are conducted on the robots with two sets of gains, that is, $(\alpha_{1,0}\,,\,\beta_{1,0}) = (0.4,\,0.9)$ and $(0.3,\,0.2)$, marked as points A and B in Figure 4.1(b). The corresponding frequency response curves (4.22) are plotted in Figure 4.1(c). Case A is string stable for all frequencies, while case B is string unstable with the maximum around $\omega_0 = 0.15\pi$ [rad/s]. Figure 4.1(d, e) show the corresponding experimental velocity profiles when vehicle 0 introduces sinusoidal velocity fluctuations with frequency ω_0. Notice that the follower attenuates the fluctuations in case A, but amplified in case B. Similar results can be obtained experimentally for other frequencies, but we choose the frequency ω_0 to emphasize the differences between string stable and string unstable scenarios.

For consistency, we use the following color coding for vehicles in different configurations in the rest of this chapter. Black indicates the head vehicle introducing velocity fluctuations, red vehicles represent string unstable vehicles configured the same way as case B in Figure 4.1 and blue represents CCC vehicles with gain parameters to be designed.

4.3.2 Three-vehicle experiments

Here we use three vehicles to demonstrate that in the presence of string unstable vehicles, it may not be possible to ensure head-to-tail string stability when the CCC vehicle only utilizes motion information from its immediate predecessor. However, this goal can be achieved when CCC vehicle utilizes information from two vehicles ahead (the second one is beyond the line of sight).

Figure 4.2(a) shows a chain of three vehicles where the following vehicles only rely on their direct predecessor for longitudinal control. Vehicle 1 is a string unstable vehicle with gains used for case B in Figure 4.1. The stability diagram in Figure 4.2(b) indicates that the system cannot achieve head-to-tail string stability whatever gains are selected for vehicle 3 with controller (1.8). To demonstrate this behavior we marked point C at

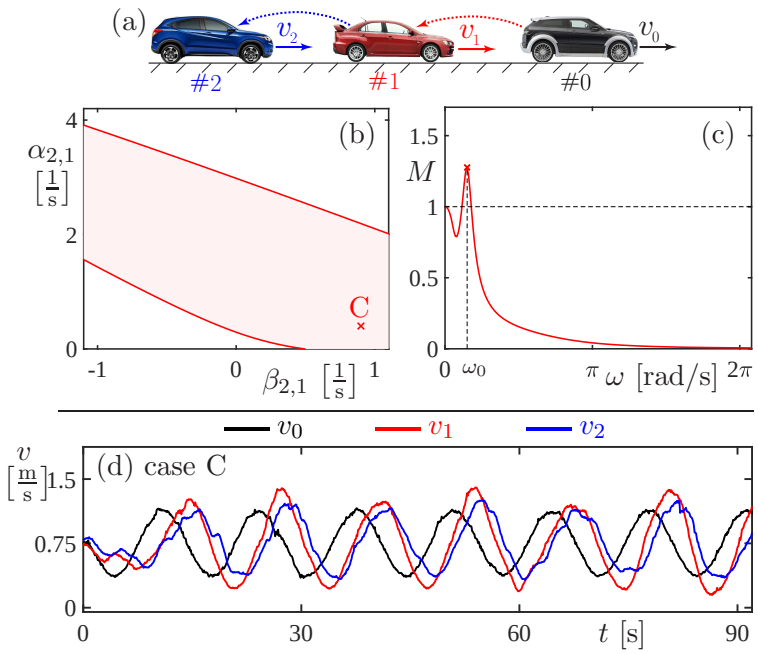

Figure 4.2: (a) Three-vehicle configuration. (b) Stability diagram. (c) Frequency response for point C marked in panel (b). (d) Experimental velocity profiles in case C when vehicle 0 introduces sinusoidal velocity fluctuations at $\omega_0 = 0.15\pi$ [rad/s].

$(\alpha_{2,1}\,,\,\beta_{2,1}) = (0.4,\,0.9)$ in Figure 4.2(b), that is, vehicle 2 is configured the same way as case A in Figure 4.1, i.e., it is 1-to-2 string stable. However, as shown by the (head-to-tail) frequency response in Figure 4.2(c), the overall system is head-to-tail string unstable. The experimental velocity profiles are shown in Figure 4.2(d) at frequency ω_0. Observe that the velocity fluctuations of vehicle 1 are attenuated slightly by vehicle 2. However, the amplitude of vehicle 2 is still greater than that of vehicle 0.

To improve the performance, the CCC vehicle can take advantage of V2X communication and utilize the information from both predecessors; see Figure 4.3(a). For the rest communication links, the control gains are kept the same as case C in Figure 4.2. The stability diagram in Figure 4.3(b) is plotted in the plane of the control gains between vehicles 0 and 2. It can be seen that with appropriately chosen parameters for this extra link the overall system can achieve head-to-tail string stability. In Figure 4.3(b), the points D, E, and F mark the gain combinations $(\alpha_{2,0}\,,\,\beta_{2,0}) = (0.1,\,0.3)$, $(0,\,0.1)$, and $(0,\,1)$. The corresponding (head-to-tail) frequency responses shown in Figure 4.3(c) indicate that case D is head-to-tail string stable, while case E and case F are head-to-tail string unstable with critical frequencies around $\omega_0 = 0.15\pi$ [rad/s] and $\omega_1 = 0.95\pi$ [rad/s], respectively.

Experiments are conducted for cases D and E using sinusoidal velocity fluctuations for vehicle 0 at frequency ω_0. The resulting velocity profiles shown in Figure 4.3(d, e)

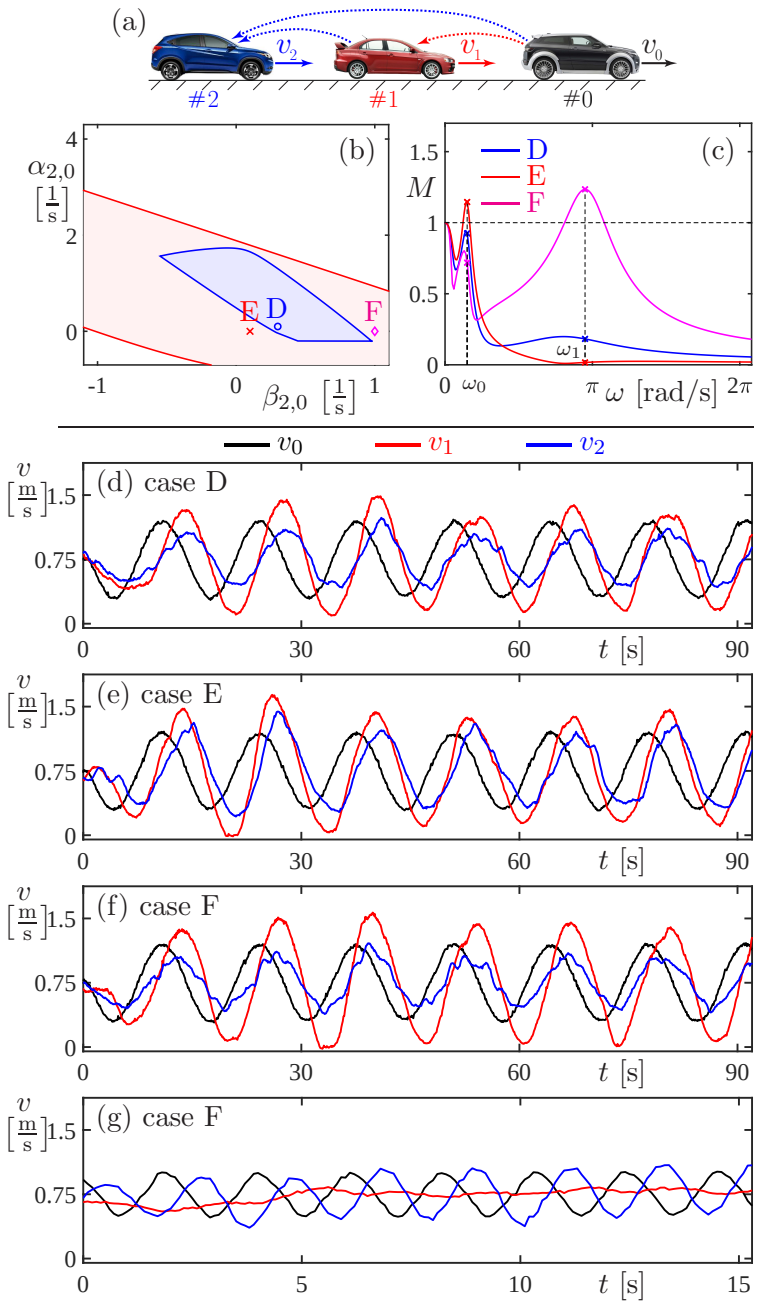

Figure 4.3: (a) Three-vehicle configuration. (b) Stability diagram. (c) Frequency responses for points D, E and F marked in panel (b). (d, e) Experimental velocity profiles when vehicle 0 introduces sinusoidal velocity fluctuations at $\omega_0 = 0.15\pi$ [rad/s] in cases D and E, respectively. (f, g) Experimental velocity profiles for case F when vehicle 0 introduces sinusoidal velocity fluctuations at $\omega_0 = 0.15\pi$ [rad/s] and $\omega_1 = 0.95\pi$ [rad/s], respectively.

indicate that vehicle 2 can make the fluctuations smaller than those of vehicle 0 in case D, but cannot achieve such disturbance attenuation in case E. Experiments for case F show

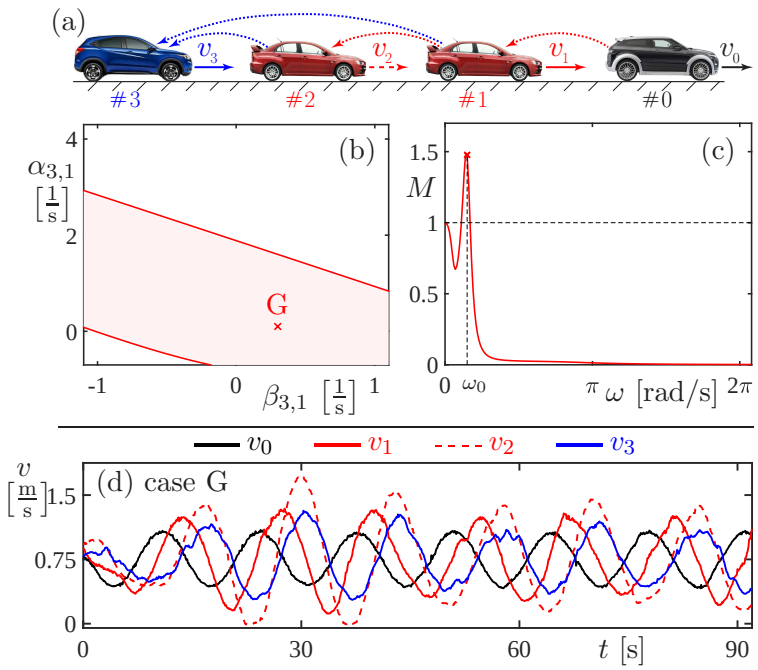

Figure 4.4: (a) Four-vehicle configuration. (b) Stability diagram. (c) Frequency response for point G marked in panel (b). (d) Experimental velocity profiles when vehicle 0 introduces sinusoidal velocity fluctuations at frequency $\omega_0 = 0.15\pi$ [rad/s].

a scenario where vehicle 2 attenuates the fluctuations of vehicle 0 at ω_0 but amplifies the fluctuations at ω_1 even though vehicle 1 attenuate those, as shown in Figure 4.3(f, g). Case F is head-to-tail string unstable due to amplifying high-frequency signals. This emphasizes that CCC must be appropriately designed; otherwise, unexpected oscillations may impair the system performance.

4.3.3 Four-vehicle experiments

In this section, we incorporate more string unstable vehicles into the system and show that it is beneficial to utilize more beyond-line-of-sight information in CCC design. We also demonstrate that the resulting connectivity topology has some flexibility to tolerate the absence of certain communication links.

Figure 4.4(a) delineates a scenario that includes two string unstable vehicles with gains corresponding to case B in Figure 4.1, while the CCC vehicle at the tail relies on the motion of its two immediate predecessors while using the same gains as that in Figure 4.3(a), i.e., $(\alpha_{3,2}\,,\,\beta_{3,2}) = (0.4,\,0.9)$. The stability diagram in Figure 4.4(b), plotted in the plane of the control gains between vehicles 1 and 3, shows that head-to-tail string stability is not achievable. We choose the set of gains $(\alpha_{3,1}\,,\,\beta_{3,1}) = (0.1,\,0.3)$, corresponding to point G

in Figure 4.4(b), so that the subsystem consisting vehicles 1, 2 and 3 is equivalent to the system for case D in Figure 4.3. The corresponding (head-to-tail) frequency response in Figure 4.4(c) indicates head-to-tail string instability with the maximum around $\omega_0 = 0.15\pi$ [rad/s], and the experimental velocity profiles at this frequency are shown in Figure 4.4(d). It can be observed that the fluctuations of vehicle 0 are amplified by vehicles 1 and 2, but then attenuated by vehicle 3. However, the amplitude of fluctuations for vehicle 3 is between the amplitudes for vehicles 0 and 1. This means that the subsystem consisting of vehicles 1, 2 and 3 is 1-to-3 string stable, whereas the overall system is head-to-tail string unstable.

To improve the performance, we consider a scenario where information from all three predecessors is utilized by the CCC vehicle 3, as shown in Figure 4.5(a). The control gains are kept the same for all the communication links that exist in case G in Figure 4.4. Figure 4.5(b) shows the stability diagram in the plane of control gains between vehicles 0 and 3, indicating that the overall system can achieve head-to-tail string stability with appropriate gains for the additional link. The points H and I are marked in Figure 4.5(b) at $(\alpha_{3,0}\,,\, \beta_{3,0}) = (0.5,\, 0.4)$ and $(0,\, 0.1)$ and the (head-to-tail) frequency response curves in Figure 4.5(c) show that in case H one can achieve head-to-tail string stability, but this is not true in case I. The experimental velocity profiles for case H are shown in Figure 4.5(d), indicating that the amplitude of the fluctuations of vehicle 3 is less than that of vehicle 0, and noticeable fluctuations around π [rad/s] also arise in vehicle 3 in correspondence with the extra peak in Figure 4.5(c). On the other hand, the experimental result shown in Figure 4.5(e) for case I reveals vehicle 3 still amplifies the velocity fluctuations of vehicle 0 if the gains are not chosen appropriately.

Finally, we test a scenario where the motion information from some vehicles are not available (which is the case when having human-driven vehicles that are not equipped with V2X devices). Figure 4.6(a) shows a scenario similar to the one in Figure 4.5(a) except the lack of communication link between vehicles 1 and 3, while all the control gains are kept unchanged. The stability diagram in Figure 4.6(b) is plotted in the plane of control gains for the link between vehicles 0 and 3, indicating that head-to-tail string stability is still achievable without this link. The (head-to-tail) frequency response curves corresponding to the points marked H and I are shown in Figure 4.6(b). Observe that, despite the missing link, in case H head-to-tail string stability is still maintained apart from a slight increase in the amplification ratio around ω_0, while case I is indeed still head-to-tail string unstable. The experimental velocity profiles in Figure 4.6(d, e) are consistent with the theoretical results.

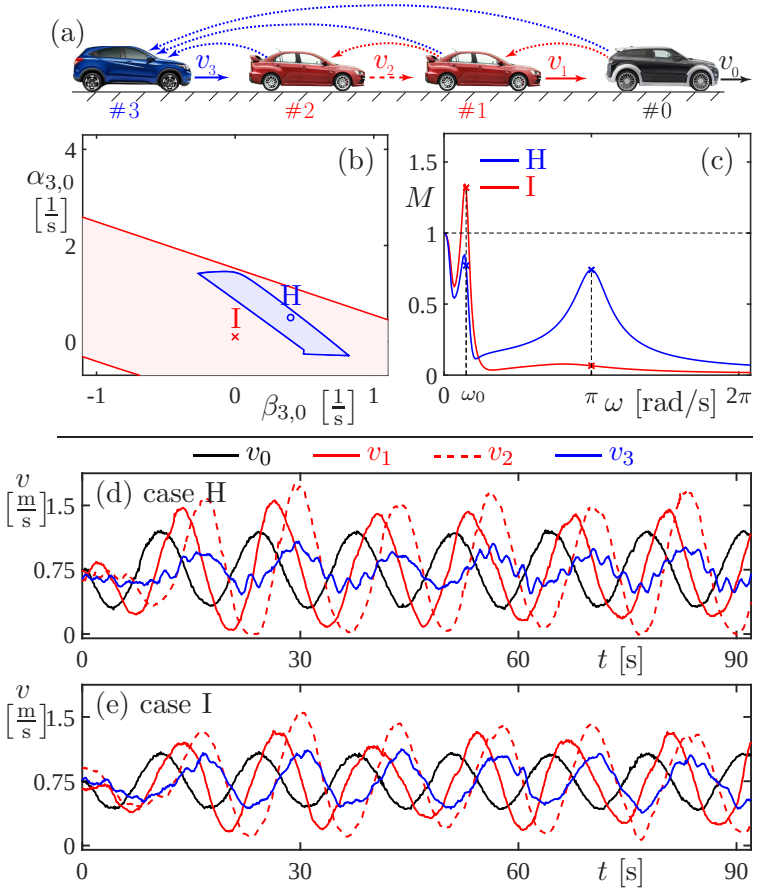

Figure 4.5: (a) Four-vehicle configuration. (b) Stability diagram. (c) Frequency responses for points H and I marked in panel (b). (d, e) Experimental velocity profiles when vehicle 0 introduces sinusoidal velocity fluctuations at frequency $\omega_0 = 0.15\pi$ [rad/s].

4.3.4 Five-vehicle experiments

Here we study whether the performance can be further improved by including multiple CCC vehicles. Figure 4.7(a) shows a cascaded configuration of two identical systems used in Figure 4.3, except the addition of an extra communication link between vehicles 0 and 4. The red vehicles still represent string unstable vehicles as discussed in Section 4.3.1, while the blue and green vehicles use the control scheme on their two direct predecessors according to case D in Figure 4.3. The stability diagram in Figure 4.7(b) is plotted in the plane of the control gains of the longest link, and the points marked J and K correspond to $(\alpha_{4,0}\,,\,\beta_{4,0}) = (0,\,0)$ and $(0.1,\,0.3)$. The corresponding (head-to-tail) frequency response curves shown in Figure 4.7(c) indicate that both cases are head-to-tail string stable but the amplification ratio at frequency ω_0 is smaller in case K.

The experimental velocity profiles are shown in Figure 4.7(d, e). In case J where the

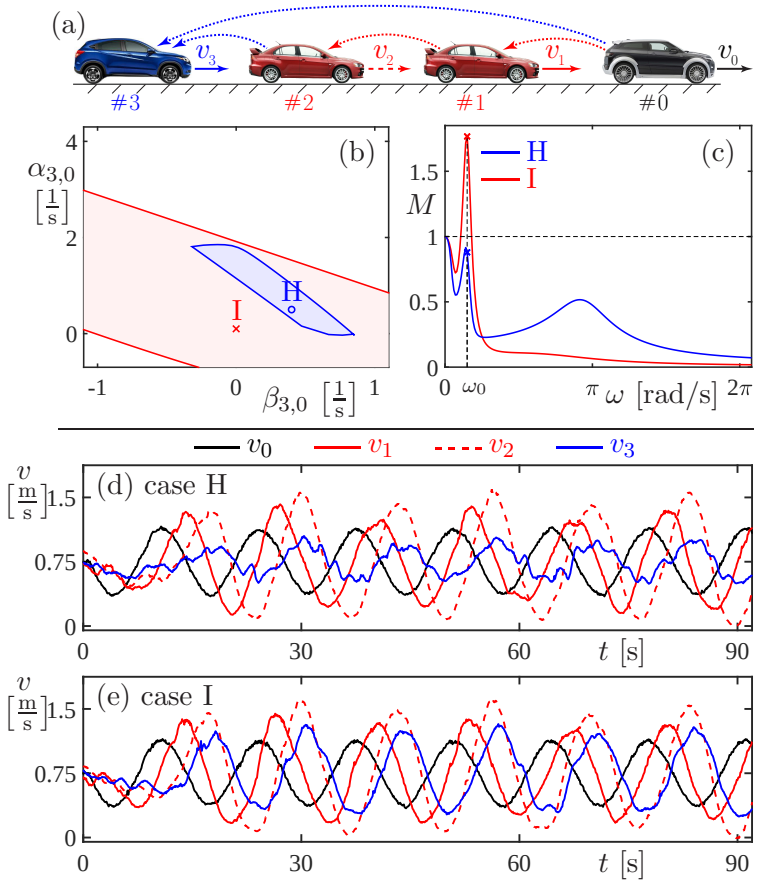

Figure 4.6: (a) Four-vehicle configuration. (b) Stability diagram. (c) Frequency responses for points H and I marked in panel (b). (d, e) Experimental velocity profiles when vehicle 0 introduces sinusoidal velocity fluctuations at frequency $\omega_0 = 0.15\pi$ [rad/s].

extra long link is not utilized, the amplified fluctuations in vehicle 1 are first attenuated by vehicle 2, then amplified by vehicle 3, and finally attenuated again when reaching vehicle 4. Similar behaviors can be observed from Figure 4.7(e) for the experiment in case K except that vehicle 4 has smaller fluctuations than that in Figure 4.7(d) for case J.

4.4 Summary

In this chapter, we investigated a class of connected cruise controllers (1.8) for connected automated vehicles that allowed us to exploit information from multiple connected vehicles ahead using V2X communication. The control algorithms were designed by using mathematical models representing the continuous-time vehicle dynamics subject to digital control. The theoretical results about plant stability and string stability were summarized

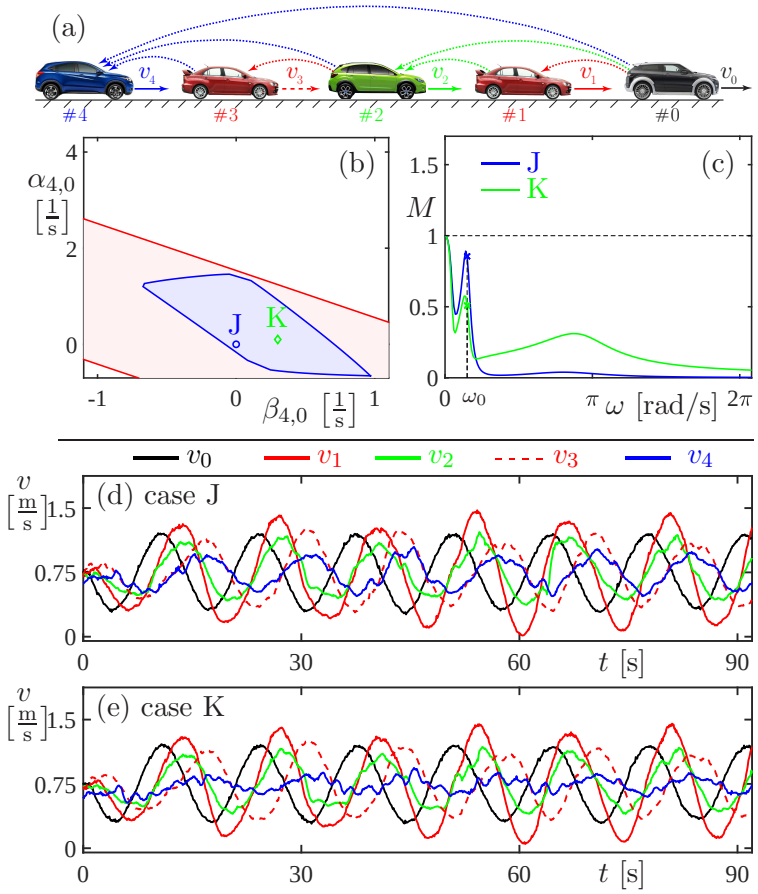

Figure 4.7: (a) Five-vehicle configuration. (b) Stability diagram. (c) Frequency responses for points J and K marked in panel (b). (d, e) Experimental velocity profiles when vehicle 0 introduces sinusoidal velocity fluctuations at frequency $\omega_0 = 0.15\pi$ [rad/s].

using stability diagrams.

Through a sequence of experiments on the scaled connected vehicle testbed, we demonstrated that CAV may significantly benefit the smoothness of human-dominated traffic by attenuating velocity perturbations that are typically amplified by human drivers. We found that, while limited improvements can be achieved by AVs (without connectivity), utilizing beyond-line-of-sight information provided by V2X connectivity significantly enhances the impact of automation. By utilizing our model-based design, adding more connectivity can lead to more benefits regarding mitigating velocity fluctuations while remaining robust against the loss of certain communication links. Finally, the proposed design remains scalable as penetration of CAVs increases, making real-world deployment feasible.

CHAPTER 5

Stochastic Packet Drops in Predecessor-follower Systems

In Chapters 2-4, we have designed and studied connected cruise controllers with the assumption that every packet is delivered successfully. From this chapter on, stochastic packet losses in V2X communication will be incorporated. In this chapter, we first develop a model with stochastic delay variations in the two-car predecessor-follower system while still considering the digital implementation of the controller. One can resort to the definitions of stochastic convergence and stochastic stability in Appendix D. We aim at almost sure stability since it guarantees convergence of almost all trajectories despite having stochastic delay variations. In particular, we derive a discrete-time linear system with stochastic delays and analyze the mean, the second moment and the covariance dynamics to guarantee plant stability and to characterize disturbance attenuation. For the latter case we introduce the concept of $n\sigma$ string stability. The material discussed in this section can be found in [184–187].

5.1 Stochastic Delay Variations

In this section, we present the stochastic model of the two-car predecessor-follower shown in Figure 1.1(b) with the controller (1.6) that includes stochastic delay variations in the communication links. Same assumptions are made on the clock synchronization and control loop alignment as those in Chapter 2, except that packets may not be delivered during the V2X communication process.

We still assume that vehicles broadcast their kinematic information intermittently with the sampling time Δt, which results in the time mesh $t_k = k\Delta t$ for $k = 0, 1, 2, \ldots$; see Figure 5.1(a). According to V2X communication protocol, the transmitter is unaware whether a packet has been successfully delivered and no packets are resent. We assume that at time

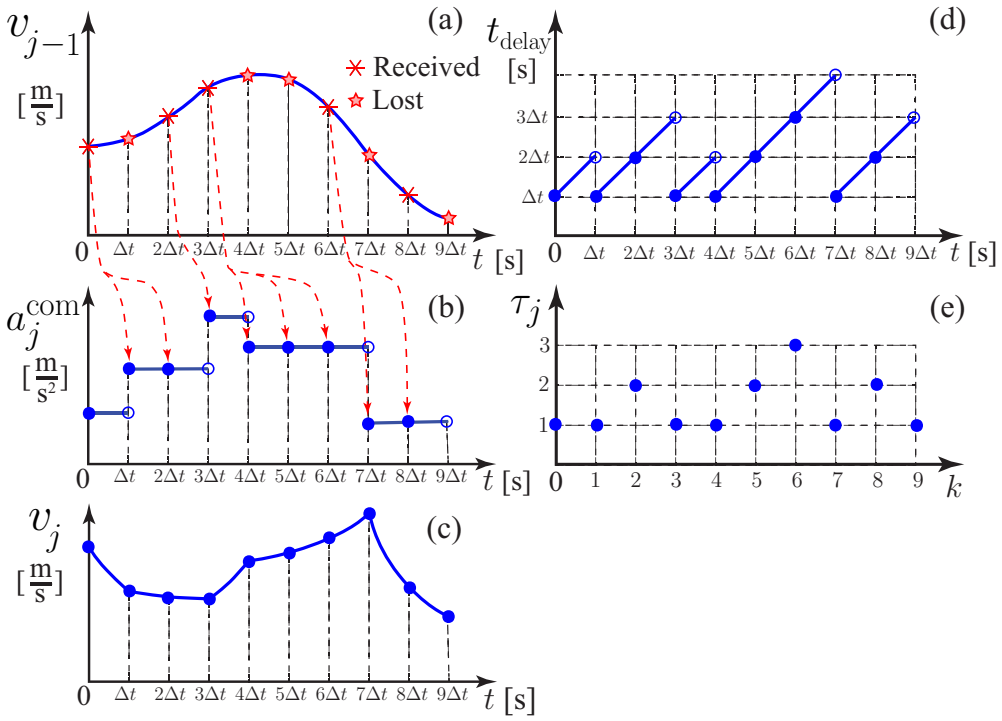

Figure 5.1: (a) Predecessor's velocity is transmitted every Δt time, but packets may be dropped as indicated. (b) Control with ZOH based on the newest received information. (c) Follower's corresponding velocity. (d) Time delay variations in the continuous-time system (5.4, 5.5). (e) Corresponding delays in the discrete-time system (5.8).

instant t_k, the previous $\tau_j(k) - 1$ packets have been dropped consecutively. Thus, the last packet successfully received was at time instant $t_{k-\tau_j(k)}$. The controller outputs a command based on this information at $t_{k-\tau_j(k)+1}$ that is kept constant until t_{k+1} using a ZOH, as no new packet is delivered successfully until t_k; see Figure 5.1(b). We assume that the packet drop dynamics are governed by a stochastic process, that is, the digitally controlled system is forced by piecewise constant inputs of stochastically varying length.

The methods developed below can be applied to other vehicle models subject to digital control under any (stationary) stochastic process describing the packet drop dynamics. However, in order to make the problem tractable, we assume that the parameters of the stochastic process (e.g., packet delivery ratio) are constant (or vary much slower than the vehicle dynamics). In reality, the state of vehicles (speed and distance) as well as the environment (geography, buildings, weather) may influence the packet drop dynamics. Studying such effects is left for future research.

To further simplify the matter, we model the packet drop dynamics using Bernoulli

trials [188]. That is, the time evolution of $\tau_j(k)$ can be formulated as

$$\tau_j(k+1) = \begin{cases} 1, & \text{if a packet is received during } [t_k,\, t_{k+1}), \\ \tau_j(k)+1, & \text{otherwise.} \end{cases} \tag{5.1}$$

According to the Bernoulli process, we assume that the successful delivery of a packet is independent of the delivery status of other packets, and we denote the packet delivery ratio by p. To avoid infinitely long delays, we also assume that the maximum of $\tau_j(k)$ is N, i.e., $\tau_j(k+1) = 1$ if $\tau_j(k) = N$. This yields the probability density function (PDF)

$$f_{\tau_j(k)}(\xi) = \sum_{r=1}^{\infty} w_r \delta(\xi - r), \tag{5.2}$$

where $\delta(*)$ denotes the Dirac delta function and

$$w_r = \begin{cases} p(1-p)^{r-1} & \text{if} \quad r = 1\,,\, \ldots\,,\, N-1\,, \\ 1 - \sum_{i=1}^{N-1} w_i = (1-p)^{N-1} & \text{if} \quad r = N\,, \\ 0 & \text{if} \quad r > N\,. \end{cases} \tag{5.3}$$

We remark that N is chosen such that $\sum_{r=1}^{N-1} w_r \geq p_{\text{cr}}$ holds where p_{cr} is the critical cumulative delivery ratio. For example, considering $p = 0.6$ and setting $p_{\text{cr}} = 0.99$, the maximum value is $N = 6$. These assumptions are supported by the experimental results in [189].

Notice that even though the probability distribution of $\tau_j(k+1)$ is not independent of $\tau_j(k)$, i.e., (5.1) describes a non-Markovian stochastic process, the probability distributions are still identically geometrically distributed for each discrete time k. In Section 5.3, we will simplify the analysis by using the distribution (5.2, 5.3) while substituting the non-Markovian stochastic process (5.1) with a Markovian one. In Section 5.4, we will return to the original problem and demonstrate that the mathematical tools developed can be extended to a general stationary stochastic process. Finally, we emphasize that while the packet drop dynamics are described in discrete time due to the intermittent communication, the dynamics of the vehicles still evolve in continuous time; see Figure 5.1(c). The corresponding effective delay increases from $\tau_j(k)\Delta t$ to $\big(\tau_j(k)+1\big)\Delta t$ linearly during each sampling interval, as shown in Figure 5.1(d).

5.2 Stochastic Dynamics

As mentioned in Section 5.1, vehicle models of different levels of fidelity and controllers of different levels of complexity may be considered. We refer back to the vehicle model (2.2) presented in Chapter 2 and controller (1.6) presented in Chapter 1. Notice that the integral controller was used to eliminate the steady-state error caused by rolling resistance, air drag and damping effects. Here we make further simplifications to the model, omitting the rolling resistance and air drag effects in the physics-based model (2.3), which leads to the simplified dynamics

$$\begin{aligned} \dot{h}_j(t) &= v_{j-1}(t) - v_j(t)\,, \\ \dot{v}_j(t) &= a_j^{\mathrm{com}}(t_{k-\tau_j(k)})\,, \end{aligned} \tag{5.4}$$

for $t \in [t_k,\, t_{k+1})$. Meanwhile, we leave out the integral controller in (1.6), which results in the controller

$$a_j^{\mathrm{com}}(t) = K_{\mathrm{p}}\Big(V\big(h_j(t)\big) - v_j(t)\Big) + K_{\mathrm{v}}\Big(W\big(v_{j-1}(t)\big) - v_j(t)\Big)\,. \tag{5.5}$$

Note that we change the notation from α and β to K_{p} and K_{v}, respectively. Also, from this chapter on, we use the sinusoidal range policy function (1.2, 1.3) instead of the linear one used in the previous chapters. For $v_{j-1} \leq v_{\max}$, system (5.4, 5.5) still possesses the uniform flow equilibrium

$$v_{j-1}^* = v_j^* = V(h_j^*)\,. \tag{5.6}$$

Our goal is to design the control gains K_{p}, K_{v} to ensure that the system can reach this equilibrium (i.e., plant stability is satisfied) and also attenuate perturbations introduced by the predecessor (i.e., string stability holds) in the presence of stochastic communication delays.

By noticing that in the time interval $t \in [t_k,\, t_{k+1})$, $a_j^{\mathrm{com}}(t_{k-\tau_j(k)})$ is a constant, one can solve the differential equation (5.4) directly with initial values $h_j(t_k), v_j(t_k)$ and input $v_{j-1}(t)$ given at time instant t_k, which results in

$$\begin{aligned} h_j(t) &= h_j(t_k) + \int_{t_k}^{t_{k+1}} v_{j-1}(t)\,\mathrm{d}t - v_j(t_k)(t-t_k) - \frac{1}{2}a_j^{\mathrm{com}}(t_{k-\tau_j(k)})(t-t_k)^2\,, \\ v_j(t) &= v_j(t_k) + a_j^{\mathrm{com}}(t_{k-\tau_j(k)})(t-t_k)\,. \end{aligned} \tag{5.7}$$

Then by calculating the values at time instant $t = t_{k+1}$ and substituting $a_j^{\mathrm{com}}(t_{k-\tau_j(k)})$ using

(5.5), one may derive the discrete-time nonlinear map

$$\begin{aligned}\begin{bmatrix} h_j(t_{k+1}) \\ v_j(t_{k+1}) \end{bmatrix} &= \begin{bmatrix} 1 & -\Delta t \\ 0 & 1 \end{bmatrix} \begin{bmatrix} h_j(t_k) \\ v_j(t_k) \end{bmatrix} + \begin{bmatrix} \int_{t_k}^{t_{k+1}} v_{j-1}(t)\mathrm{d}t \\ 0 \end{bmatrix} \\ &+ \begin{bmatrix} 0 & \frac{1}{2}\Delta t^2(K_\mathrm{p}+K_\mathrm{v}) \\ 0 & -\Delta t(K_\mathrm{p}+K_\mathrm{v}) \end{bmatrix} \begin{bmatrix} h_j\big(t_{k-\tau_j(k)}\big) \\ v_j\big(t_{k-\tau_j(k)}\big) \end{bmatrix} \\ &+ \begin{bmatrix} -\frac{1}{2}\Delta t^2 K_\mathrm{p} \\ \Delta t K_\mathrm{p} \end{bmatrix} V\Big(h_j\big(t_{k-\tau_j(k)}\big)\Big) + \begin{bmatrix} -\frac{1}{2}\Delta t^2 K_\mathrm{v} \\ \Delta t K_\mathrm{v} \end{bmatrix} W\Big(v_{j-1}\big(t_{k-\tau_j(k)}\big)\Big), \end{aligned} \tag{5.8}$$

where $\tau_j(k)$ plays the role of a discrete stochastic delay; see Figure 5.1(e). Note that (5.8) is a nonlinear stochastic difference equation since the stochasticity in $\tau_j(k)$ leads to the stochasticity in $h_j(k)$ and $v_j(k)$. Indeed, one may try to derive the probability distribution of the states given the probability distribution of the time delay. Since this may not be done in closed form, we approach the problem by focusing on the moment dynamics.

Regarding plant stability of the stochastic system, Lyapunov stability theorems are often used to obtain stability conditions for continuous and discrete time systems [190–193], but they typically lead to very conservative stability conditions. One may also derive deterministic equations that describe the time evolution of the moments. For a nonlinear system the time evolution of the lower moments are influenced by the higher moments and "moment closure" may not be achievable in general [194]. If we linearize the system, the results on plant stability can be obtained locally. Moreover, Theorem D.1 in Appendix D states that there is a correspondence between the second moment stability and almost sure stability for discrete-time linear stochastic systems under certain conditions.

Concerning string stability, we notice the following relationships for the deterministic systems as shown in Appendix C. There is a correspondence between head-to-tail string stability of an open chain of cascaded predecessor-follower pairs, and the stability of the cascaded closed ring system. We conjecture such correspondence would also hold for stochastic systems. Below we show that such correspondence can be proven to exist for the mean dynamics. However, for the second moment dynamics, we do not have the definition of string stability at hand to characterize disturbance attenuation. Thus, we propose the definition of $n\sigma$ string stability and establish the correspondence through stability diagrams.

To characterize the stochastic dynamics, we first linearize the stochastic system (5.8) about the equilibrium (5.6) and then derive the equations describing the time evolution of the first and second moments. In this case, the dynamics of the first moment is self-contained while the dynamics of the second moment is driven by that of the first moment.

We define the perturbations

$$\tilde{h}_j(t) = h_j(t) - h_j^* \,, \qquad\qquad \tilde{v}_j(t) = v_j(t) - v_j^* \,, \tag{5.9}$$

and again assume sinusoidal variations of the predecessor's velocity, i.e.,

$$v_{j-1}(t) = v_{j-1}^* + v_{j-1}^{\text{amp}} \sin(\omega\, t) \Longrightarrow \tilde{v}_{j-1}(t) = v_{j-1}^{\text{amp}} \sin(\omega\, t), \tag{5.10}$$

and $v_{j-1}(t) < v_{\max}$.

By defining the state, the input and the output as

$$x_j(k) = \begin{bmatrix} \tilde{h}_j(t_k) \\ \tilde{v}_j(t_k) \end{bmatrix} , \qquad u_j(k) = \begin{bmatrix} \tilde{v}_{j-1}(t_k) \\ \tilde{v}_{j-1}^{\perp}(t_k) \end{bmatrix} , \qquad y(k) = \tilde{v}_j(t_k) \,, \tag{5.11}$$

where

$$\tilde{v}_{j-1}^{\perp}(t) = v_{j-1}^{\text{amp}} \cos(\omega t), \tag{5.12}$$

the linearization of (5.8) becomes

$$\begin{aligned} x_j(k+1) &= \boldsymbol{a}\, x_j(k) + \boldsymbol{a}_\tau\, x_j\big(k - \tau_j(k)\big) + \boldsymbol{b}\, u_j(k) + \boldsymbol{b}_\tau\, u_j\big(k - \tau_j(k)\big), \\ y(k) &= \mathbf{c}\, x_j(k) \,, \end{aligned} \tag{5.13}$$

with matrices

$$\begin{aligned} \boldsymbol{a} &= \begin{bmatrix} 1 & -\Delta t \\ 0 & 1 \end{bmatrix} , & \boldsymbol{b} &= \begin{bmatrix} \theta_2 & \theta_3 \\ 0 & 0 \end{bmatrix} , \\ \boldsymbol{a}_\tau &= \begin{bmatrix} -\frac{1}{2}\Delta t^2 K_{\text{p}} N_* & \frac{1}{2}\Delta t^2 (K_{\text{p}} + K_{\text{v}}) \\ \Delta t K_{\text{p}} N_* & -\Delta t (K_{\text{p}} + K_{\text{v}}) \end{bmatrix} , & \boldsymbol{b}_\tau &= \begin{bmatrix} -\frac{1}{2}\Delta t^2 K_{\text{v}} & 0 \\ \Delta t K_{\text{v}} & 0 \end{bmatrix} , \\ \mathbf{c} &= \begin{bmatrix} 0 & 1 \end{bmatrix} , \end{aligned} \tag{5.14}$$

where θ_2 and θ_3 are the same as those defined in (2.13), and

$$N_* = V'(h_j^*) = V'\big(V^{-1}(v_j^*)\big) = \begin{cases} \dfrac{\pi \sqrt{v_j^*(v_{\max} - v_j^*)}}{h_{\text{go}} - h_{\text{st}}} & \text{if} \quad h_{\text{st}} < h < h_{\text{go}} \,, \\ 0 & \text{elsewhere} \,, \end{cases} \tag{5.15}$$

cf. (1.2, 1.3). We remark again that the scalar sinusoidal input (5.10) for the continuous-time system (5.4) results in the vector-valued input (5.11) for the discrete-time system (5.13) that satisfies (2.15).

Defining the augmented state, the input and the output as

$$X(k) = \begin{bmatrix} x_j(k) \\ x_j(k-1) \\ \vdots \\ x_j(k-N) \end{bmatrix} \in \mathbb{R}^{2(N+1)}, \quad U(k) = u_j(k) \in \mathbb{R}^2, \quad Y(k) = y(k) \in \mathbb{R}, \quad (5.16)$$

respectively, (5.13) can be written as

$$\begin{aligned} X(k+1) &= \mathbf{A}_{\tau_j(k)}\, X(k) + \mathbf{B}_{\tau_j(k)}\, U(k), \\ Y(k) &= \mathbf{C}\, X(k)\,, \end{aligned} \quad (5.17)$$

where $\mathbf{A}_{\tau_j(k)} \in \mathbb{R}^{2(N+1)\times 2(N+1)}$ and $\mathbf{B}_{\tau_j(k)} \in \mathbb{R}^{2(N+1)\times 2}$ can take the values

$$\boldsymbol{A}_r = \begin{bmatrix} \boldsymbol{a} & \delta_{1r}\,\boldsymbol{a}_\tau & \delta_{2r}\,\boldsymbol{a}_\tau & \cdots & \delta_{Nr}\,\boldsymbol{a}_\tau \\ \mathbf{I} & \mathbf{0} & \mathbf{0} & \cdots & \mathbf{0} \\ \mathbf{0} & \mathbf{I} & \mathbf{0} & \cdots & \mathbf{0} \\ \vdots & & \ddots & \ddots & \vdots \\ \mathbf{0} & \cdots & \mathbf{0} & \mathbf{I} & \mathbf{0} \end{bmatrix}, \qquad \mathbf{B}_r = \begin{bmatrix} \boldsymbol{b} + \boldsymbol{b}_\tau\, \mathbf{R}^r \\ \mathbf{0} \\ \vdots \\ \mathbf{0} \end{bmatrix}, \quad (5.18)$$

for $r = 1, \ldots, N$; cf. (5.14). Here, δ_{sr} denotes the Kronecker delta, while $\mathbf{I} \in \mathbb{R}^{2\times 2}$ and $\mathbf{0} \in \mathbb{R}^{2\times 2}$ denote the identity and zero matrices, respectively. Also, we have

$$\mathbf{C} = \begin{bmatrix} \boldsymbol{c} & 0 & \cdots & 0 \end{bmatrix} \in \mathbb{R}^{1\times 2(N+1)}\,. \quad (5.19)$$

5.3 Mean and Covariance Dynamics – IID Approximation

In order to find the stability condition, the mean, the second moment, and the covariance dynamics shall be derived. In (5.17), $\mathbf{A}_{\tau_j(k)}$ depends on $\mathbf{A}_{\tau_j(k-1)}$ according to (5.1), which is also the case for $\mathbf{B}_{\tau_j(k)}$ and $\mathbf{B}_{\tau_j(k-1)}$, implying that (5.17) describes a non-Markovian stochastic process. In order to simplify the analysis, instead of using (5.1) we assume that $\tau_j(k)$-s are independently identically distributed (IID) while still keeping the probability density function (5.2, 5.3), which results in Markovian dynamics. In Section 5.4, we will demonstrate that this gives a good approximation of the true stability.

With the IID assumption of $\tau_j(k)$, one can obtain the joint PDF of $\mathbf{A}_{\tau_j(k)}$ and $\mathbf{B}_{\tau_j(k)}$

from (5.2) as

$$f_{\mathbf{A}_{\tau_j(k)},\mathbf{B}_{\tau_j(k)}}(\mathbf{A},\mathbf{B}) = \sum_{r=1}^{\infty}\sum_{s=1}^{\infty} w_r\delta_{rs}\,\delta(\mathbf{A}-\mathbf{A}_r)\delta(\mathbf{B}-\mathbf{B}_s)\,. \tag{5.20}$$

From this, the marginal PDF-s of $\mathbf{A}_{\tau_j(k)}$ and $\mathbf{B}_{\tau_j(k)}$ can be obtained as

$$f_{\mathbf{A}_{\tau_j(k)}}(\mathbf{A}) = \sum_{r=1}^{\infty} w_r\delta(\mathbf{A}-\mathbf{A}_r)\,, \qquad f_{\mathbf{B}_{\tau_j(k)}}(\mathbf{B}) = \sum_{r=1}^{\infty} w_r\delta(\mathbf{B}-\mathbf{B}_r)\,, \tag{5.21}$$

respectively. Notice that $\mathbf{A}_{\tau_j(k)}$ and $X(k)$ are mutually independent, which is also the case for $\mathbf{B}_{\tau_j(k)}$ and $X(k)$.

Let us define the deterministic variables

$$\bar{X}(k) = \mathbb{E}[X(k)] \in \mathbb{R}^{2(N+1)}\,, \;\; \bar{Y}(k) = \mathbb{E}[Y(k)] \in \mathbb{R}\,, \tag{5.22}$$

where $\mathbb{E}[\cdot]$ denotes the expected value. By taking expectations of both sides in (5.17) and using independence between state variables and the PDF-s (5.21), one can derive the mean dynamics

$$\begin{aligned} \bar{X}(k+1) &= \bar{\mathbf{A}}\,\bar{X}(k) + \bar{\mathbf{B}}\,U(k)\,,\\ \bar{Y}(k) &= \bar{\mathbf{C}}\,\bar{X}(k)\,, \end{aligned} \tag{5.23}$$

where the matrices are

$$\bar{\mathbf{A}} = \sum_{r=1}^{N} w_r\mathbf{A}_r\,, \qquad \bar{\mathbf{B}} = \sum_{r=1}^{N} w_r\mathbf{B}_r\,, \qquad \bar{\mathbf{C}} = \mathbf{C}\,. \tag{5.24}$$

Notice that the mean dynamics (5.22, 5.23, 5.24) can be rewritten for the mean of the variables used in (5.11, 5.13) as a deterministic distributed delay difference equation with delay distribution (5.2), i.e.,

$$\begin{aligned} \bar{x}_j(k+1) &= \boldsymbol{a}\,\bar{x}_j(k) + \sum_{r=1}^{N} w_r\boldsymbol{a}_r\,\bar{x}_j(k-r) + \boldsymbol{b}\,u_j(k) + \sum_{r=1}^{N} w_r\boldsymbol{b}_r\,u_j(k-r),\\ \bar{y}(k) &= \mathbf{c}\,\bar{x}_j(k)\,, \end{aligned} \tag{5.25}$$

where

$$\bar{x}_j(k) = \mathbb{E}[x_j(k)] \in \mathbb{R}^2\,, \;\; \bar{y}(k) = \mathbb{E}[y(k)] \in \mathbb{R}\,. \tag{5.26}$$

Let us define the second moments

$$\hat{\bar{X}}(k) = \mathbb{E}[X(k) \otimes X(k)] \in \mathbb{R}^{4(N+1)^2}, \qquad \hat{\bar{Y}}(k) = \mathbb{E}[Y(k) \otimes Y(k)] \in \mathbb{R}. \tag{5.27}$$

By taking expectations and using independence between variables and the PDF-s (5.20, 5.21), one can obtain the second moment dynamics

$$\begin{aligned}
\hat{\bar{X}}(k+1) &= \big(\sum_{r=1}^{N} w_r \mathbf{A}_r \otimes \mathbf{A}_r\big)\hat{\bar{X}}(k) + \big(\sum_{r=1}^{N} w_r \mathbf{A}_r \otimes \mathbf{B}_r\big)\big(\bar{X}(k) \otimes U(k)\big) \\
&\quad + \big(\sum_{r=1}^{N} w_r \mathbf{B}_r \otimes \mathbf{A}_r\big)\big(U(k) \otimes \bar{X}(k)\big) + \big(\sum_{r=1}^{N} w_r \mathbf{B}_r \otimes \mathbf{B}_r\big)\big(U(k) \otimes U(k)\big), \\
\hat{\bar{Y}}(k) &= \big(\mathbf{C} \otimes \mathbf{C}\big)\hat{\bar{X}}(k).
\end{aligned} \tag{5.28}$$

Moreover, the covariance can be defined as

$$\begin{aligned}
\bar{\bar{X}}(k) &= \mathbb{E}\big[\big(X(k) - \bar{X}(k)\big) \otimes \big(X(k) - \bar{X}(k)\big)\big] \in \mathbb{R}^{4(N+1)^2}, \\
\bar{\bar{Y}}(k) &= \mathbb{E}\big[\big(Y(k) - \bar{Y}(k)\big) \otimes \big(Y(k) - \bar{Y}(k)\big)\big] \in \mathbb{R},
\end{aligned} \tag{5.29}$$

and it can be shown that

$$\begin{aligned}
\bar{\bar{X}}(k) &= \mathbb{E}[X(k) \otimes X(k)] - \bar{X}(k) \otimes \bar{X}(k), \\
\bar{\bar{Y}}(k) &= \mathbb{E}[Y(k) \otimes Y(k)] - \bar{Y}(k) \otimes \bar{Y}(k).
\end{aligned} \tag{5.30}$$

Thus, using (5.23) and (5.28), one can obtain the covariance dynamics

$$\begin{aligned}
\bar{\bar{X}}(k+1) &= \bar{\bar{\mathbf{A}}}\bar{\bar{X}}(k) + \bar{\bar{\mathbf{H}}}_1\big(\bar{X}(k) \otimes U(k)\big) + \bar{\bar{\mathbf{H}}}_2\big(U(k) \otimes \bar{X}(k)\big) \\
&\quad + \bar{\bar{\mathbf{H}}}_3\big(U(k) \otimes U(k)\big) + \bar{\bar{\mathbf{H}}}_4\big(\bar{X}(k) \otimes \bar{X}(k)\big), \\
\bar{\bar{Y}}(k) &= \bar{\bar{\mathbf{C}}}\bar{\bar{X}}(k),
\end{aligned} \tag{5.31}$$

where

$$\begin{aligned}
&\bar{\bar{\mathbf{A}}} = \textstyle\sum_{r=1}^{N} w_r \mathbf{A}_r \otimes \mathbf{A}_r, && \bar{\bar{\mathbf{H}}}_1 = \sum_{r=1}^{N} w_r \mathbf{A}_r \otimes \mathbf{B}_r - \bar{\mathbf{A}} \otimes \bar{\mathbf{B}}, \\
&\bar{\bar{\mathbf{H}}}_2 = \sum_{r=1}^{N} w_r \mathbf{B}_r \otimes \mathbf{A}_r - \bar{\mathbf{B}} \otimes \bar{\mathbf{A}}, && \bar{\bar{\mathbf{H}}}_3 = \sum_{r=1}^{N} w_r \mathbf{B}_r \otimes \mathbf{B}_r - \bar{\mathbf{B}} \otimes \bar{\mathbf{B}}, \\
&\bar{\bar{\mathbf{H}}}_4 = \sum_{r=1}^{N} w_r \mathbf{A}_r \otimes \mathbf{A}_r - \bar{\mathbf{A}} \otimes \bar{\mathbf{A}}, && \bar{\bar{\mathbf{C}}} = \mathbf{C} \otimes \mathbf{C},
\end{aligned} \tag{5.32}$$

cf. (5.23, 5.24). The time evolution of the mean and the covariance is described by the system (5.23, 5.31) such that (5.31) is driven by (5.23).

5.3.1 Plant Stability

Here we evaluate plant stability for both the mean and second moment dynamics. On the one hand, plant stability for the mean dynamics requires that the mean of the follower's velocity approaches the predecessor's velocity. This is a necessary condition for the plant stability of the stochastic system (5.17). On the other hand, the plant stability for the second moment dynamics (5.28) (or the covariance dynamics (5.31)) requires that the variance of the follower's velocity converges to zero. This provides a sufficient condition for (almost sure) plant stability of the stochastic system (5.31) according to Theorem D.3 in Appendix D.

For plant stability of the mean dynamics $\bar{X}(k+1) = \bar{\mathbf{A}}\,\bar{X}(k)$ (cf. (5.23) with $U(k) = 0$), all eigenvalues $z \in \mathbb{C}$ of the matrix $\bar{\mathbf{A}}$ must lie within the unit circle in the complex plane. These eigenvalues are given by the characteristic equation

$$\det\left(z\,\bar{\mathbf{I}} - \bar{\mathbf{A}}\right) = 0\,, \tag{5.33}$$

where $\bar{\mathbf{I}} \in \mathbb{R}^{2(N+1)\times 2(N+1)}$ is the identity matrix. There are three different ways in which the system can lose stability as explained in Chapter 2.3.1, and again we use the bisection method to trace the boundaries in the parameter space.

Theorem D.2 in Appendix D implies that stability of the second moment dynamics and the stability of the covariance dynamics are equivalent when the mean dynamics are stable. Consequently, only the plant stability for the second moment dynamics is discussed here. Similar to the mean dynamics, to ensure plant stability of the second moment dynamics $\hat{\bar{X}}(k+1) = \bar{\bar{\mathbf{A}}}\hat{\bar{X}}(k)$ (cf. (5.28) with $U(k) = 0$ and $\bar{\bar{\mathbf{A}}}$ as defined in (5.32)), all eigenvalues $z \in \mathbb{C}$ of the matrix $\bar{\bar{\mathbf{A}}}$ must lie within the unit circle in the complex plane. These eigenvalues are given by the characteristic equation

$$\det\left(z\,\bar{\bar{\mathbf{I}}} - \bar{\bar{\mathbf{A}}}\right) = 0\,, \tag{5.34}$$

where $\bar{\bar{\mathbf{I}}} \in \mathbb{R}^{4(N+1)^2\times 4(N+1)^2}$ is the identity matrix. The corresponding stability boundaries can also be obtained by the bisection method as explained in Chapter 2.3.1.

Figure 5.2(a) shows the plant stability diagram in the $(K_\mathrm{v}, K_\mathrm{p})$-plane for the parameters $v_\mathrm{max} = 30\,[\mathrm{m/s}]$, $h_\mathrm{st} = 5\,[\mathrm{m}]$, $h_\mathrm{go} = 35\,[\mathrm{m}]$, $v_j^* = 15\,[\mathrm{m/s}]$ (cf. (1.2, 1.3, 5.6)), which will be kept the same throughout the whole chapter. Here, we also consider the packet delivery

ratio $p = 0.8$ and the sampling time $\Delta t = 0.1\,[\mathrm{s}]$. For the mean dynamics (5.23), the horizontal red line and the red curve correspond to the critical cases (i) and (iii) explained in Chapter 2.3.1, respectively. The oscillation frequency is zero along the horizontal red line while the frequency $\vartheta/\Delta t$ increases monotonically along the red curve, that is, the further we are from the origin (along the curve), the higher the frequency of the arising oscillations is. The region enclosed by these curves, i.e., the union of the red and purple shaded regions, is the mean plant stable region. For the second moment dynamics (5.28), the purple horizontal line and purple curve both correspond to the critical case (i). That is, the oscillation frequency is zero along the horizontal purple line as well as along the purple curve, implying that the covariance can only lose plant stability via non-oscillatory divergence. The purple shaded region enclosed by these two curves is the second moment plant stable region.

The root loci for the points A–D marked in Figure 5.2(a) are plotted in Figure 5.2(b–e). Blue stars indicate the roots of (5.33) for the mean while red crosses indicate the roots of (5.34) for the second moment. In case A, there are two eigenvalues located outside the unit circle for the mean dynamics and four for the second moment dynamics. As K_p decreases, the eigenvalues of the mean dynamics move inside the unit circle while there is still one eigenvalue outside the unit circle for the second moment dynamics, as shown in case B. Decreasing K_p further, the eigenvalues of the second moment dynamics also move inside the unit circle as shown in case C and the system becomes stable. Decreasing K_p even further, a pair of complex conjugate eigenvalues "meet" at the real axis for the mean dynamics, and then they split into two real eigenvalues. One of them crosses the unit circle at 1 and moves outside as shown in case D. Meanwhile, an eigenvalue for the second moment dynamics also moves outside the unit circle at 1.

5.3.2 String Stability

For deterministic linear systems string stability is equivalent to the attenuation of sinusoidal signals at all frequencies which can be evaluated using transfer functions [84, 121] as discussed in the previous chapters. However, an equivalent notion of string stability does not exist for stochastic systems. One may use the mean dynamics (5.23) to characterize string stability as this provides a necessary condition for the string stability of the stochastic system (5.17). However, this may still allow a large fraction of trajectories to be string unstable. To resolve this issues we use the covariance dynamics (5.31) to establish the concept of $n\sigma$ string stability. This guarantees that all trajectories within the mean's neighborhood of radius n times the standard deviation are string stable (i.e., the amplifica-

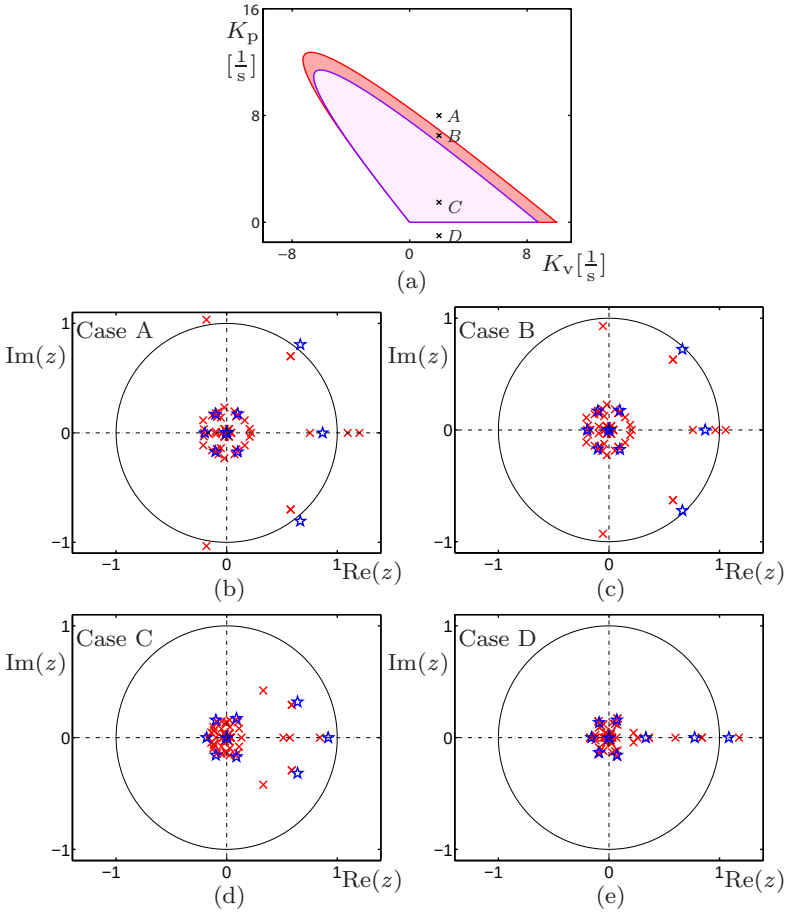

Figure 5.2: (a) Plant stability diagrams in the $(K_\mathrm{v}, K_\mathrm{p})$-plane for $p = 0.8$, $\Delta t = 0.1\,[\mathrm{s}]$ and IID assumption. Red and purple curves correspond to changes in plant stability of the mean dynamics and the second moment dynamics, respectively. Red and purple shaded regions correspond to plant stable domains of the mean dynamics and second moment dynamics, respectively. (b–e) Blue stars and red crosses mark the root loci of the mean dynamics and the second moment dynamics on the z-domain, respectively, corresponding to the points A–D marked on panel (a).

tion ratio is less than 1 for trajectories within this set). This characterization allows us to design controllers that are robust against stochastic delay variations to a given degree.

To evaluate string stability of the mean dynamics (5.23), we make the same assumption about the disturbances in the predecessor's velocity $\tilde{v}_{j-1}(t)$ as that in Chapter 2, and apply the Z transform to (5.23) to derive the steady-state output as

$$\bar{Y}_\mathrm{ss}(k) = \bar{M}(\omega)\, \tilde{v}_{j-1}^\mathrm{amp}\, \sin\big(k\omega\Delta t + \bar{\psi}(\omega)\big), \tag{5.35}$$

where the amplification ratio and phase lag are

$$\bar{M}(\omega) = \left|\bar{\Gamma}(\mathrm{e}^{\mathrm{j}\,\omega\,\Delta t})\right|, \qquad \bar{\psi}(\omega) = \angle\bar{\Gamma}(\mathrm{e}^{\mathrm{j}\,\omega\,\Delta t})\,. \tag{5.36}$$

Here, the transfer function is

$$\bar{\Gamma}(z) = \bar{\mathbf{C}}\big(z\,\bar{\mathbf{I}} - \bar{\mathbf{A}}\big)^{-1}\bar{\mathbf{B}}\bar{\mathbf{E}}, \tag{5.37}$$

and

$$\bar{\mathbf{E}} = \begin{bmatrix} 1 & \mathrm{j} \end{bmatrix}^{\mathrm{T}}, \tag{5.38}$$

is used to sum up the effects of two dependent components.

The condition for mean string stability is given by

$$\sup_{\omega>0}\ \bar{M}(\omega) < 1\,, \tag{5.39}$$

yielding the string stability boundaries

$$\begin{cases} \bar{M}(\bar{\omega}_{\mathrm{cr}}) = 1\,, \\ \bar{M}'(\bar{\omega}_{\mathrm{cr}}) = 0\,, \end{cases} \tag{5.40}$$

for critical excitation frequency $\bar{\omega}_{\mathrm{cr}} > 0$, where prime denotes differentiation with respect to ω. Note that $\bar{M}$ also depends on the parameters $(K_{\mathrm{p}}, K_{\mathrm{v}}, w, v^*, \Delta t)$. Similar to the plant stability boundaries, the parametric string stability boundary (5.40) cannot be obtained analytically but can be found using the bisection method. Finally, one may show that $\bar{M}(0) = 1, \bar{M}'(0) = 0$ always hold. Therefore, string stability requires $\bar{M}''(0) < 0$ and the corresponding boundary is given by

$$\bar{M}''(0) = 0. \tag{5.41}$$

Equation (5.31) describing covariance dynamics is nonlinear and also contains terms driven by the mean dynamics (5.23). To determine $n\sigma$ string stability only the steady-state dynamics of the mean and the covariance are needed, but the covariance dynamics (5.31) do not provide a direct input-output relationship like the mean dynamics (5.23) do. To simplify the analysis, we assume that the mean dynamics are plant stable and already at steady state. In this case, the steady-state response shares the same form with the input,

i.e., it is a sinusoidal signal. Thus, at steady state, one can assume

$$\bar{X}(k) = \mathbf{Q}\, U(k)\,. \tag{5.42}$$

Substituting this into the mean dynamics (5.23) and using the property (2.15), one can get

$$\mathbf{Q} - \bar{\mathbf{A}}\mathbf{Q}\mathbf{R} = \bar{\mathbf{B}}\mathbf{R}\,, \tag{5.43}$$

which can be rewritten into the form

$$(\mathbf{I} \otimes \bar{\mathbf{I}} - \mathbf{R}^{\mathrm{T}} \otimes \bar{\mathbf{A}})\overline{\mathrm{vec}}(\mathbf{Q}) = \overline{\mathrm{vec}}(\bar{\mathbf{B}}\mathbf{R})\,, \tag{5.44}$$

with the help of property (E.2) in Appendix E.1. We remark that $\mathbf{Q}$ can also be obtained by using transfer functions; cf. (5.35). Substituting (5.42) into (5.31) yields the simplified covariance dynamics

$$\begin{aligned} \bar{\bar{X}}(k+1) &= \bar{\bar{\mathbf{A}}}\bar{\bar{X}}(k) + \bar{\bar{\mathbf{B}}}\bar{\bar{U}}(k)\,, \\ \bar{\bar{Y}}(k) &= \bar{\bar{\mathbf{C}}}\bar{\bar{X}}(k)\,, \end{aligned} \tag{5.45}$$

where

$$\bar{\bar{U}}(k) = U(k) \otimes U(k)\,, \tag{5.46}$$

and $\bar{\bar{\mathbf{A}}}$ and $\bar{\bar{\mathbf{C}}}$ are given by (5.32), while

$$\begin{aligned} \bar{\bar{\mathbf{B}}} &= \bar{\bar{\mathbf{H}}}_1(\mathbf{Q} \otimes \mathbf{I}) + \bar{\bar{\mathbf{H}}}_2(\mathbf{I} \otimes \mathbf{Q}) + \bar{\bar{\mathbf{H}}}_3(\mathbf{I} \otimes \mathbf{I}) + \bar{\bar{\mathbf{H}}}_4(\mathbf{Q} \otimes \mathbf{Q}) \\ &= \sum_{r=1}^{N} w_r \big(\mathbf{A}_r\mathbf{Q} + \mathbf{B}_r\big) \otimes \big(\mathbf{A}_r\mathbf{Q} + \mathbf{B}_r\big) - \big(\bar{\mathbf{A}}\mathbf{Q} + \bar{\mathbf{B}}\big) \otimes \big(\bar{\mathbf{A}}\mathbf{Q} + \bar{\mathbf{B}}\big)\,. \end{aligned} \tag{5.47}$$

By substituting the input (5.11) into (5.46), one may notice that the input $\bar{\bar{U}}(k)$ can be separated into a constant part and a harmonic excitation part, i.e.,

$$\bar{\bar{U}}(k) = \bar{\bar{U}}_0 + \bar{\bar{U}}_1(k)\,, \tag{5.48}$$

where

$$\bar{\bar{U}}_0 = \frac{1}{2}\big(v_{j-1}^{\mathrm{amp}}\big)^2 \bar{\bar{u}}_0\,, \quad \bar{\bar{U}}_1(k) = \frac{1}{2}\big(v_{j-1}^{\mathrm{amp}}\big)^2 \bar{\bar{u}}_1(k)\,, \tag{5.49}$$

and

$$\bar{\bar{u}}_0 = \begin{bmatrix} 1 \\ 0 \\ 0 \\ 1 \end{bmatrix}, \quad \bar{\bar{u}}_1(k) = \begin{bmatrix} -\cos(2k\omega\Delta t) \\ \sin(2k\omega\Delta t) \\ \sin(2k\omega\Delta t) \\ \cos(2k\omega\Delta t) \end{bmatrix}. \tag{5.50}$$

According to the superposition principle, the particular solution of the linear system (5.45) is the sum of particular solution $\bar{\bar{Y}}_0$ to $\bar{\bar{U}}_0$ and particular solution $\bar{\bar{Y}}_1(k)$ to $\bar{\bar{U}}_1(k)$. For input $\bar{\bar{U}}_0$, the response of the system (5.45) is given by

$$\bar{\bar{Y}}_0 = \left(v_{j-1}^{\text{amp}}\right)^2 \bar{\bar{M}}_0(\omega)\,, \tag{5.51}$$

with

$$\bar{\bar{M}}_0(\omega) = \frac{1}{2}\bar{\bar{\mathbf{C}}}\left(\bar{\bar{\mathbf{I}}} - \bar{\bar{\mathbf{A}}}\right)^{-1}\bar{\bar{\mathbf{B}}}\bar{\bar{u}}_0\,. \tag{5.52}$$

For $\bar{\bar{U}}_1(k)$, similar to the mean dynamics, taking the Z-transform of (5.45) and summing the contributions of each individual inputs of $\bar{\bar{u}}_1(k)$ in (5.50), we obtain the corresponding steady-state output

$$\bar{\bar{Y}}_{1,\text{ss}}(k) = \left(v_{j-1}^{\text{amp}}\right)^2 \bar{\bar{M}}_1(\omega)\sin\left(2k\omega\Delta t + \bar{\bar{\psi}}(\omega)\right). \tag{5.53}$$

with

$$\bar{\bar{M}}_1(\omega) = \left|\bar{\bar{\Gamma}}(\mathrm{e}^{\mathrm{j}\omega\Delta t})\right|, \qquad \bar{\bar{\psi}}(\omega) = \angle\bar{\bar{\Gamma}}(\mathrm{e}^{\mathrm{j}\omega\Delta t}), \tag{5.54}$$

where

$$\bar{\bar{\Gamma}}(z) = \frac{1}{2}\bar{\bar{\mathbf{C}}}\left(z\,\bar{\bar{\mathbf{I}}} - \bar{\bar{\mathbf{A}}}\right)^{-1}\bar{\bar{\mathbf{B}}}\bar{\bar{\mathbf{E}}}, \tag{5.55}$$

and

$$\bar{\bar{\mathbf{E}}} = \begin{bmatrix} -\mathrm{j} & 1 & 1 & \mathrm{j} \end{bmatrix}^{\mathrm{T}}. \tag{5.56}$$

Therefore, the superposition principle yields that the steady-state response to (5.48) is

$$\bar{\bar{Y}}_{\text{ss}}(k) = \bar{\bar{Y}}_0 + \bar{\bar{Y}}_{1,\text{ss}}(k) = \left(v_{j-1}^{\text{amp}}\right)^2\left(\bar{\bar{M}}_0(\omega) + \bar{\bar{M}}_1(\omega)\sin\left(2k\omega\Delta t + \bar{\bar{\psi}}(\omega)\right)\right). \tag{5.57}$$

Recall that $\bar{Y}(k) = \mathbb{E}[\tilde{v}_j(k)] \in \mathbb{R}$ and $\bar{\bar{Y}}(k) = \mathbb{E}[\tilde{v}_j^2(k)] - \mathbb{E}[\tilde{v}_j(k)]^2 \in \mathbb{R}$ and define

$$\mu = \bar{Y}_{\text{ss}}(k)\,, \qquad \sigma^2 = \bar{\bar{Y}}_{\text{ss}}(k)\,, \tag{5.58}$$

respectively, as the mean and variance of $\tilde{v}_j(k)$ at steady state. Note that the variance $\bar{\bar{Y}}(k)$

is non-negative, and thus, (5.57) implies $\bar{\bar{M}}_0(\omega) \geq \bar{\bar{M}}_1(\omega)$. Motivated by Chebyshev's inequality [195], we know that the probability of $\tilde{v}_j(k)$ being outside the window $[\mu - n\sigma, \mu + n\sigma]$, $n \in \mathbb{R}^+$ is rather small when $n \geq 1$. Therefore, using (5.35, 5.57), we calculate

$$\begin{aligned} \mu \pm n\sigma = v_{j-1}^{\mathrm{amp}} \Big[& \bar{M}(\omega) \sin\left(k\omega\Delta t + \bar{\psi}(\omega)\right) \\ & \pm n\sqrt{\bar{\bar{M}}_0(\omega) + \bar{\bar{M}}_1(\omega) \sin\left(2k\omega\Delta t + \bar{\bar{\psi}}(\omega)\right)} \Big] , \end{aligned} \tag{5.59}$$

which is a periodic function with period $T = \frac{2\pi}{\omega\Delta t}$. Thus, the total amplification ratio becomes

$$\begin{aligned} \bar{\bar{M}}(\omega) = \max_{0 \leq k \leq T} \Big\{ \Big| & \bar{M}(\omega) \sin\left(k\omega\Delta t + \bar{\psi}(\omega)\right) \\ & \pm n\sqrt{\bar{\bar{M}}_0(\omega) + \bar{\bar{M}}_1(\omega) \sin\left(2k\omega\Delta t + \bar{\bar{\psi}}(\omega)\right)} \Big| \Big\} . \end{aligned} \tag{5.60}$$

Definition 5.1 *The system is said to be $n\sigma$ string stable if the amplitude v_{j-1}^{amp} of the input $\tilde{v}_{j-1}(k)$ is attenuated such that $|\mu \pm n\sigma| < v_{j-1}^{\mathrm{amp}}$.*

Henceforth, the condition for $n\sigma$ string stability is given by

$$\sup_{\omega > 0} \ \bar{\bar{M}}(\omega) < 1 , \tag{5.61}$$

and the corresponding boundaries can be found by the bisection method. Note that when $n = 0$, the $n\sigma$ string stability gives the mean string stability.

Figure 5.3(a) shows the $n\sigma$ string stability diagram in the $(K_{\mathrm{v}}, K_{\mathrm{p}})$-plane for packet delivery ratio $p = 0.8$ and sampling time $\Delta t = 0.1[\mathrm{s}]$ for different values of n. The green curve and the green straight lines correspond to the mean string stability boundaries (5.40) and (5.41), respectively. The union of the green and blue shaded regions enclosed by these curves is the mean string stable region. The blue curves correspond to the $n\sigma$ string stability boundaries for $n = 1,\ 2,\ 3$, respectively. The blue shaded region corresponds to the 1σ string stable region. For the mean dynamics, the critical frequency $\bar{\omega}_{\mathrm{cr}}$ is zero along the straight lines but positive along the curve, and similar behavior occurs for the covariance dynamics.

The amplification ratios for the mean and covariance dynamics are plotted in Figure 5.3(b–e) for $n = 1$ corresponding to the points E–H marked in Figure 5.3(a). In case E, the system is mean string unstable for $0 < \omega < \bar{\omega}$ and 1σ string unstable for $0 < \omega < \bar{\bar{\omega}}$, but string stable in both sense for larger frequencies. As K_{v} is increased, the amplification

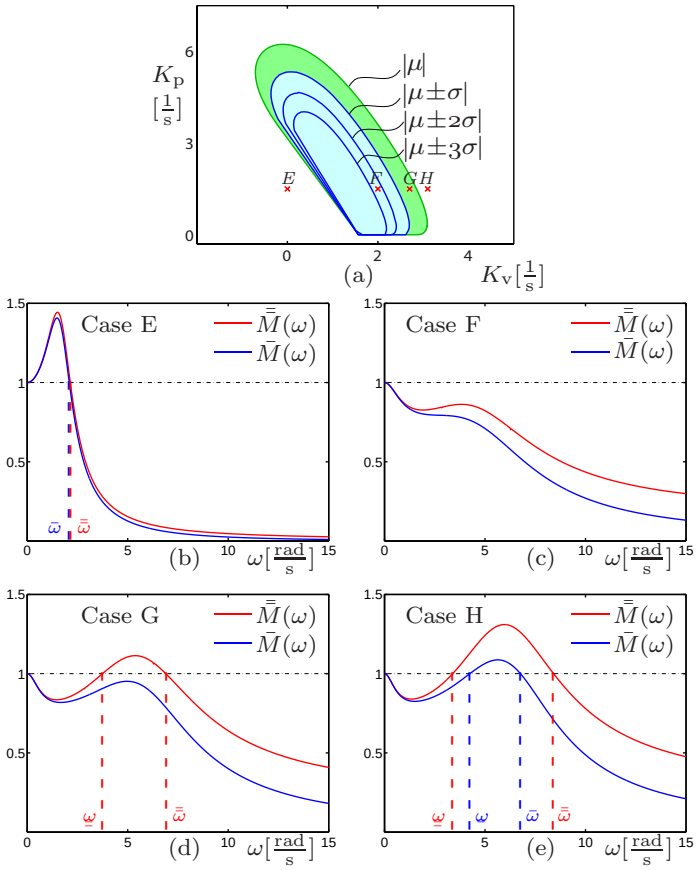

Figure 5.3: (a) String stability diagrams in the $(K_\mathrm{v}, K_\mathrm{p})$-plane for $p = 0.8$, $\Delta t = 0.1$ [s] and IID delay assumption. Green and blue curves correspond to changes in mean string stability and $n\sigma$ string stability, respectively. Green shaded and blue shaded regions correspond to mean string stable and 1σ string stable regions, respectively. (b–e) Blue and red curves represent the amplification ratios (5.36) and (5.60) for $n = 1$, as functions of the excitation frequency ω corresponding to the points E–H marked in panel (a).

ratios (5.36, 5.60) go below 1 for all frequencies, leading to mean string stability and $n\sigma$ string stability as shown in case F. However, as K_v is increased further, another peak of the amplification ratio (5.60) arises, resulting in the system being 1σ string unstable in the frequency domain $\underline{\bar{\omega}} < \omega < \bar{\bar{\omega}}$ as shown in case G. As K_v is increased even further, a similar peak of the mean amplification ratio (5.36) appears, and the system becomes mean string unstable for $\underline{\omega} < \omega < \bar{\omega}$.

5.3.3 Stability Charts

Figure 5.4 shows the stability diagrams in the $(K_\mathrm{v}, K_\mathrm{p})$-plane for different values of the packet delivery ratio p and sampling time Δt. The inlets show the probability distribution

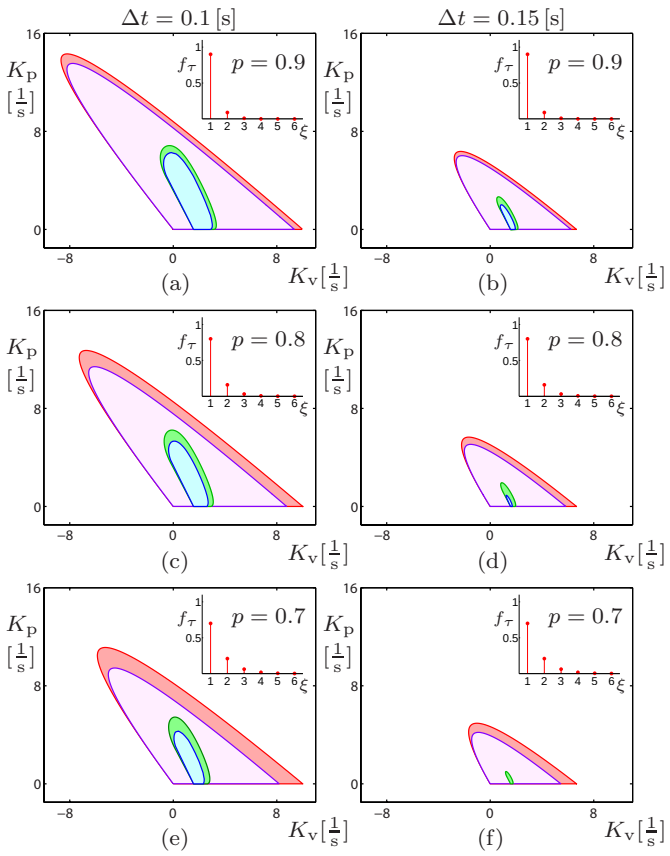

Figure 5.4: Stability diagrams in the $(K_\mathrm{v}, K_\mathrm{p})$-plane for different values of packet delivery ratio p and sampling time Δt as indicated and IID delay assumption. The corresponding delay distributions (5.2) are plotted on each panel as inlets. The same notation is used in Figure 5.2(a) and Figure 5.3(a).

of the discrete stochastic delay given by (5.2). The same color scheme is used as that in Figure 5.2(a) and Figure 5.3(a). The mean string stable domains and the 1σ string stable domains are embedded in the corresponding plant stable regions. We remark that there are string stable domains outside the plant stable domain which are not shown here. For plant stability, both the mean and covariance plant stable domains shrink as the packet delivery ratio p decreases and as sampling time Δt increases. Similar behavior can be observed for the mean string stable and 1σ string stable domains. When exceeding critical values, the string stable domains disappear, in which case there exist no gain combinations that can maintain string stability. Table 5.1 shows the approximate critical packet delivery ratio p_cr for different sampling time Δt.

Table 5.1: Critical successful packet delivery ratio for different values of the sampling time.

$\Delta t\ [s]$	0.1	0.15	0.2
p_{cr}	0.35	0.62	0.92

5.4 Real Dynamics with Stochastic Delays

So far the stability condition for the stochastic system (5.17) have been derived while having the simplifying assumption of IID delay variations. However, as mentioned above, considering the stochastic delay dynamics (5.1), the system (5.17) describes a non-Markovian stochastic process, since $\mathbf{A}_{\tau_j(k)}$ and $\mathbf{B}_{\tau_j(k)}$ depends on $\mathbf{A}_{\tau_j(k-1)}$ and $\mathbf{B}_{\tau_j(k-1)}$. To handle this problem, here we select a subsequence from the dynamics (5.17) such that the new stochastic variable is IID and the resulting dynamics are described by a Markovian stochastic process. Then we apply the tools developed in Section 5.3 to analyze the dynamics.

Let us consider the subsequence of states $X(k_l)$, inputs $U(k_l)$ and outputs $Y(k_l)$ at time instants k_l where $\tau_j(k_l) = 1$; cf. Figure 5.5(a), that is, where new packets are delivered successfully, and denote them

$$\tilde{X}(l) = X(k_l), \quad \tilde{U}(l) = U(k_l), \quad \tilde{Y}(l) = Y(k_l). \tag{5.62}$$

Also, define $\tilde{\tau}_j(l) = \tau_j(k_l - 1)$; cf. Figure 5.5(c), which is the maximum delay in the time interval $[k_{l-1}\Delta t,\ k_l\Delta t]$. This construction implies that $\tilde{\tau}_j(l)$-s are independently, identically distributed with the probability distribution function

$$f_{\tilde{\tau}_j(l)}(\xi) = \sum_{r=1}^{\infty} w_r \delta(\xi - r)\,, \tag{5.63}$$

where w_r is given by (5.3). The counter k_l and the delay $\tilde{\tau}_j(l)$ are shown in Figure 5.5(b) and (c), respectively.

Using system dynamics (5.17) recursively between k_l and k_{l+1} and exploiting the input property (2.15), we can obtain

$$\begin{aligned} \tilde{X}(l+1) &= \tilde{\mathbf{A}}_{\tilde{\tau}_j(l)}\, \tilde{X}(l) + \tilde{\mathbf{B}}_{\tilde{\tau}_j(l)}\, \tilde{U}(l), \\ \tilde{Y}(l) \quad &= \mathbf{C}\, \tilde{X}(l)\,, \end{aligned} \tag{5.64}$$

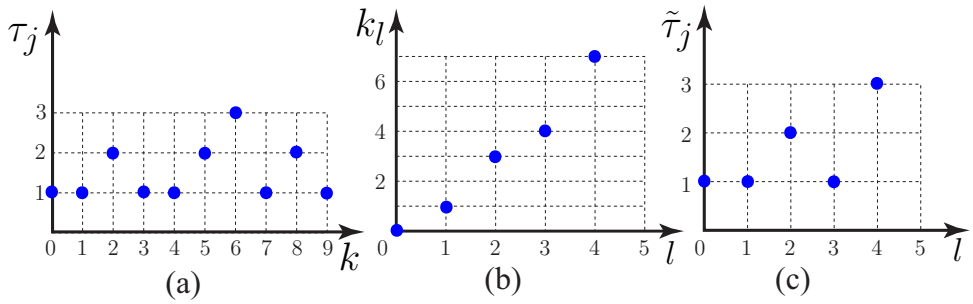

Figure 5.5: (a) Stochastic delays in the discrete-time system (5.8). (b) The relationship between counters l and k_l. (c) Number of trials $\tilde{\tau}_j$ at time instant l until a new packet is received at $k_l \Delta t$.

where $\tilde{\mathbf{A}}_{\tilde{\tau}_j(l)} \in \mathbb{R}^{2(N+1)\times 2(N+1)}$ and $\tilde{\mathbf{B}}_{\tilde{\tau}_j(l)} \in \mathbb{R}^{2(N+1)\times 2}$ can take values

$$\tilde{\mathbf{A}}_r = \prod_{i=1}^{r} \mathbf{A}_i \,, \qquad r = 1, \ldots, N \,, \tag{5.65}$$

$$\tilde{\mathbf{B}}_r = \begin{cases} \mathbf{B}_1, & r = 1, \\ \mathbf{A}_r \tilde{\mathbf{B}}_{r-1} + \mathbf{B}_r \big(\mathbf{R}^{-1}\big)^{r-1}, & r = 2, \ldots, N. \end{cases}$$

Here, $\tilde{\mathbf{A}}_{\tilde{\tau}_j(l)}$ are independently, identically distributed, which is also the case for $\tilde{\mathbf{B}}_{\tilde{\tau}_j(l)}$, meaning that system (5.64) describes a discrete-time Markov process and stability in the second moment implies almost sure stability; cf. Theorem D.3 in Appendix D. Also, for $\tilde{\mathbf{A}}_{\tilde{\tau}_j(l)}$ and $\tilde{\mathbf{B}}_{\tilde{\tau}_j(l)}$, the joint PDF and the marginal PDF-s have the same form as (5.20) and (5.21), respectively. Finally, notice that $\tilde{\mathbf{A}}_{\tilde{\tau}_j(l)}$ and $\tilde{X}(l)$ are mutually independent, which is also the case for $\tilde{\mathbf{B}}_{\tilde{\tau}_j(l)}$ and $\tilde{X}(l)$. Now we can state that the stochastic system (5.17) subject to stochastic delays described by (5.1) is stable if and only if system (5.64) subject to (5.63) is stable in the same sense. This is because there are finitely many jumps between time instants l and $(l+1)$, since $(k_{l+1} - k_l) \leq N$ and because during each jump, the matrix $\mathbf{A}_r$ has a finite norm for any $r \in \{1, 2, \ldots, N\}$. Thus, the stability of the subsequence (at time instants k_l) ensures the stability of the whole sequence (at time instants k). Henceforth, the stability of the system (5.64) gives us the same stability as the original system.

Following the same method as in Section 5.3, one can obtain the mean dynamics

$$\begin{aligned} \bar{X}(l+1) &= \bar{\mathbf{A}}\, \bar{X}(l) + \bar{\mathbf{B}}\, \tilde{U}(l) \,, \\ \bar{Y}(l) &= \bar{\mathbf{C}}\, \bar{X}(l) \,, \end{aligned} \tag{5.66}$$

by redefining the state and output as

$$\bar{X}(l) = \mathbb{E}[\tilde{X}(l)]\,, \quad \bar{Y}(l) = \mathbb{E}[\tilde{Y}(l)]\,, \tag{5.67}$$

and the matrices as

$$\bar{\mathbf{A}} = \sum_{r=1}^{N} w_r \tilde{\mathbf{A}}_r\,, \quad \bar{\mathbf{B}} = \sum_{r=1}^{N} w_r \tilde{\mathbf{B}}_r\,, \quad \bar{\mathbf{C}} = \mathbf{C}, \tag{5.68}$$

cf. (5.22, 5.23, 5.24). Also, the covariance dynamics under the assumption that the mean is at steady state is given by

$$\begin{aligned} \bar{\bar{X}}(l+1) &= \bar{\bar{\mathbf{A}}}\bar{\bar{X}}(l) + \bar{\bar{\mathbf{B}}}\bar{\bar{U}}(l)\,, \\ \bar{\bar{Y}}(l) &= \bar{\bar{\mathbf{C}}}\bar{\bar{X}}(l)\,, \end{aligned} \tag{5.69}$$

where the state, the input and the output are defined as

$$\begin{aligned} \bar{\bar{X}}(l) &= \mathbb{E}[\tilde{X}(l) \otimes \tilde{X}(l)] - \bar{X}(l) \otimes \bar{X}(l)\,, \\ \bar{\bar{U}}(l) &= \tilde{U}(l) \otimes \tilde{U}(l)\,, \\ \bar{\bar{Y}}(l) &= \mathbb{E}[\tilde{Y}(l) \otimes \tilde{Y}(l)] - \bar{Y}(l) \otimes \bar{Y}(l)\,, \end{aligned} \tag{5.70}$$

the matrices are given by

$$\begin{aligned} &\bar{\bar{\mathbf{A}}} = \textstyle\sum_{r=1}^{N} w_r \tilde{\mathbf{A}}_r \otimes \tilde{\mathbf{A}}_r\,, \\ &\bar{\bar{\mathbf{B}}} = \textstyle\sum_{r=1}^{N} w_r \big(\tilde{\mathbf{A}}_r\tilde{\mathbf{Q}} + \tilde{\mathbf{B}}_r\big) \otimes \big(\tilde{\mathbf{A}}_r\tilde{\mathbf{Q}} + \tilde{\mathbf{B}}_r\big) - \big(\bar{\mathbf{A}}\tilde{\mathbf{Q}} + \bar{\mathbf{B}}\big) \otimes \big(\bar{\mathbf{A}}\tilde{\mathbf{Q}} + \bar{\mathbf{B}}\big)\,, \\ &\bar{\bar{\mathbf{C}}} = \mathbf{C} \otimes \mathbf{C}\,, \end{aligned} \tag{5.71}$$

and $\tilde{\mathbf{Q}}$ is the solution of

$$\tilde{\mathbf{Q}} - \bar{\mathbf{A}}\tilde{\mathbf{Q}}\mathbf{R} = \bar{\mathbf{B}}\mathbf{R}\,, \tag{5.72}$$

cf. (5.30, 5.32, 5.43, 5.45, 5.46, 5.47).

Following the same method as in Section 5.3.1, one can obtain the mean and covariance plant stability boundaries based on the characteristic equations (5.33) and (5.34), where $\bar{\mathbf{A}}$ and $\bar{\bar{\mathbf{A}}}$ are given by (5.68) and (5.71), respectively. Figure 5.6(a) shows the plant stability diagram in the $(K_\mathrm{v}, K_\mathrm{p})$-plane for the mean and covariance dynamics. The same color scheme is used as that in Figure 5.2(a). The stability domains in Figure 5.6(a) are similar to those in Figure 5.2(a) except that the size difference between the mean and covariance plant stable domains is larger. The root loci for points marked A–D in Figure 5.6(a) are

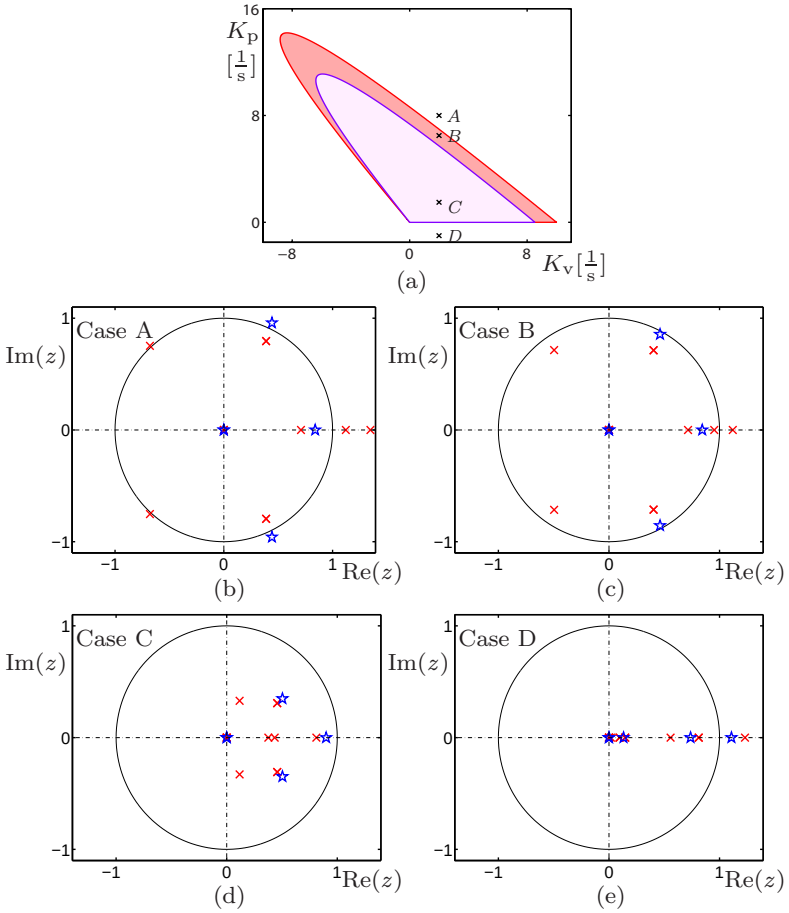

Figure 5.6: (a) Plant stability diagrams in the $(K_\mathrm{v}, K_\mathrm{p})$-plane for $p = 0.8$, $\Delta t = 0.1\,[\mathrm{s}]$ without IID delay assumption. The same color scheme is used in Figure 5.2(a). (b–e) Blue stars and red crosses mark the root loci of the mean dynamics and the covariance dynamics on the z-domain, respectively, corresponding to the points A–D in panel (a).

plotted in Figure 5.6(b–e). Note that the locations of these points are the same as in Figure 5.2(a). Comparing the corresponding panels in Figure 5.2 and Figure 5.6, one may notice that there are more zero eigenvalues in the second case, which is caused by the singularities in $\bar{\mathbf{A}}$ and $\bar{\bar{\mathbf{A}}}$ given in (5.68) and (5.71) coming from the singularity of $\tilde{\mathbf{A}}_r$-s in (5.65).

Similarly, following the same method as in Section 5.3.2, the mean and covariance string stability boundaries can be obtained based on the amplification ratios (5.36, 5.60), where ($\bar{\mathbf{A}}$, $\bar{\mathbf{B}}$, $\bar{\mathbf{C}}$) and ($\bar{\bar{\mathbf{A}}}$, $\bar{\bar{\mathbf{B}}}$, $\bar{\bar{\mathbf{C}}}$) are given in (5.68) and (5.71). Figure 5.7(a) shows the $n\sigma$ string stability diagram in the $(K_\mathrm{v}, K_\mathrm{p})$-plane, using the same color scheme as in Figure 5.3(a). One may notice that the mean string stable domain is larger in Figure 5.7(a), but the domain shrinks much faster as the value of n increases. In particular, the $n\sigma$ string stable domain disappears for $n = 3$ whereas it is still present in Figure 5.3(a). This justifies that

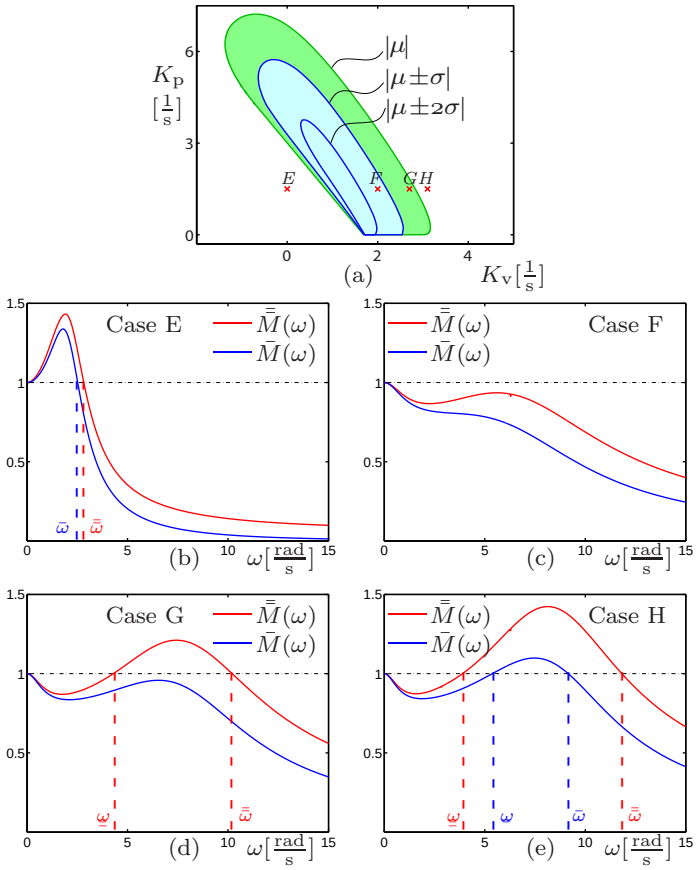

Figure 5.7: (a) String stability diagrams in the $(K_{\mathrm{v}}, K_{\mathrm{p}})$-plane for $p = 0.8$, $\Delta t = 0.1\,[\mathrm{s}]$ without IID delay assumption. The same color scheme is used in Figure 5.3(a). (b–e) Blue and red curves represent the amplification ratios (5.36) and (5.60) for $n = 1$, respectively, as functions of the excitation frequency ω corresponding to the points E–H in panel (a).

considering the correct stochastic delay dynamics is important. The amplification ratios for the mean and covariance dynamics are plotted in Figure 5.7(b–e) corresponding to the points E–H marked in Figure 5.7(a) that are at the same locations as those in Figure 5.3(a). The curves look qualitatively similar to those in Figure 5.3, except the height difference between the mean and the second moment amplification ratio curves.

Figure 5.8 shows the stability diagrams in the $(K_{\mathrm{v}}, K_{\mathrm{p}})$-plane for different values of the packet delivery ratio p and sampling time Δt. The same notations is used as those in Figure 5.4. The mean string stable domains and the 1σ string stable domain are embedded in the corresponding plant stable regions. In general, they look similar to those in Figure 5.4, but one may also notice some differences. On the one hand, the differences between mean plant stable domains and the covariance plant stable domains become larger compared to Figure 5.4, and this also holds for the differences between the mean string stable domains and 1σ

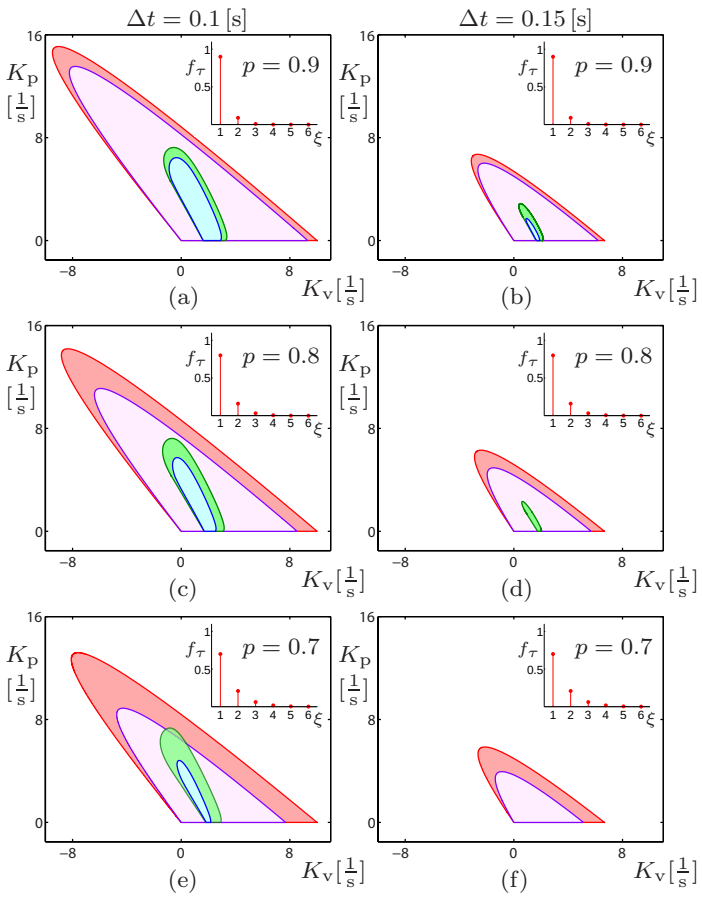

Figure 5.8: Stability diagrams in the $(K_\mathrm{v}, K_\mathrm{p})$-plane for different values of packet delivery ratio p and sampling time Δt as indicated and no IID delay assumption. The same notation is used as in Figure 5.4.

string stable domains. Moreover, the covariance stability domains shrink faster in Figure 5.8 than in Figure 5.4. Finally, there is an intersection between covariance plant stable domain and mean string stable domain in panel (e). These again justify that considering the correct stochastic delay dynamics is important.

In Section 5.1, the geometric distribution was truncated with the maximum delay N based on a critical cumulative packet delivery ratio. To validate this truncation, stability diagrams for different N-s in the same parameter space can be compared to check whether the results converge to a certain limit as N increases. Our results show that for realistic values of the packet delivery ratio, the stability domains converge so fast that there is almost no difference between plant stability boundaries for $N = 3$ and $N \geq 4$, and between string stability boundaries for $N = 6$ and $N \geq 7$. This justifies our truncation method and validates our stability analysis for large N.

5.5 Simulations

In this section, we use numerical simulations to demonstrate the stability results generated above for the real stochastic delay dynamics discussed in Section 5.4. We show that the conditions of linear plant and string stability obtained above can give a guidance when selecting control gains to achieve desired behavior.

Figure 5.9 shows the mean and 1σ window of 1000 numerical simulations for the linear stochastic system (5.13) on the left and for the nonlinear stochastic system (5.8) on the right, subject to the inputs $v_{j-1}(t) \equiv v_{j-1}^*$ and $\tilde{v}_{j-1}(t) \equiv 0$; cf. (5.10). Cases A–D correspond to the cases in Figure 5.6. In case A, there are eigenvalues located outside the unit circle for the mean and covariance dynamics, and simulation results show that both the mean and variance of the velocity diverge in an oscillatory way. As K_{p} decreases, the mean dynamics become stable while the variance still diverges as shown in case B. This implies the necessity of analyzing the covariance dynamics together with the mean dynamics. Decreasing K_{p} more, the covariance dynamics are also stabilized as shown in case C, and both the mean and the variance converge to the equilibrium. Decreasing K_{p} even further, both the mean and the variance lose stability in a non-oscillatory way corresponding to the positive real roots outside the unit circle.

The linear system and nonlinear system show similar behaviors concerning plant stability, implying that the linear system can predict the stability of the nonlinear system in the neighborhood of the equilibrium. However, the linear system diverges faster than the nonlinear system, since the nonlinear system has some saturation that prevents the system from diverging to infinity. Most importantly, in case C, one can observe that the mean of the follower's velocity converges to the predecessor's velocity while the 1σ window converges to the mean, yielding that the variance converges to zero. Thus, the system in case C is almost surely stable even though it is subject to stochastic delay variations, which is our ultimate goal when designing a controller for a stochastic system.

Figure 5.10 shows the mean and 1σ window of 1000 numerical simulations for the linear stochastic system (5.13) on the left and for the nonlinear stochastic system (5.8) on the right, subject to sinusoidal input (5.10) with $v_{j-1}^{\mathrm{amp}} = 5$ [m/s]. Cases E–H correspond to the cases in Figure 5.7. In case E, the system is mean string unstable and 1σ string unstable for lower frequencies. The corresponding simulations show that amplification indeed happens for excitation frequency $\omega = 2$ [rad/s]. As K_{v} is increased, the system becomes both mean string stable and 1σ string stable as shown in case F, and the amplitude of the sinusoidal input is attenuated for the mean as well as for the 1σ window. However, as K_{v} is increased further, the system becomes 1σ string unstable for higher frequencies as

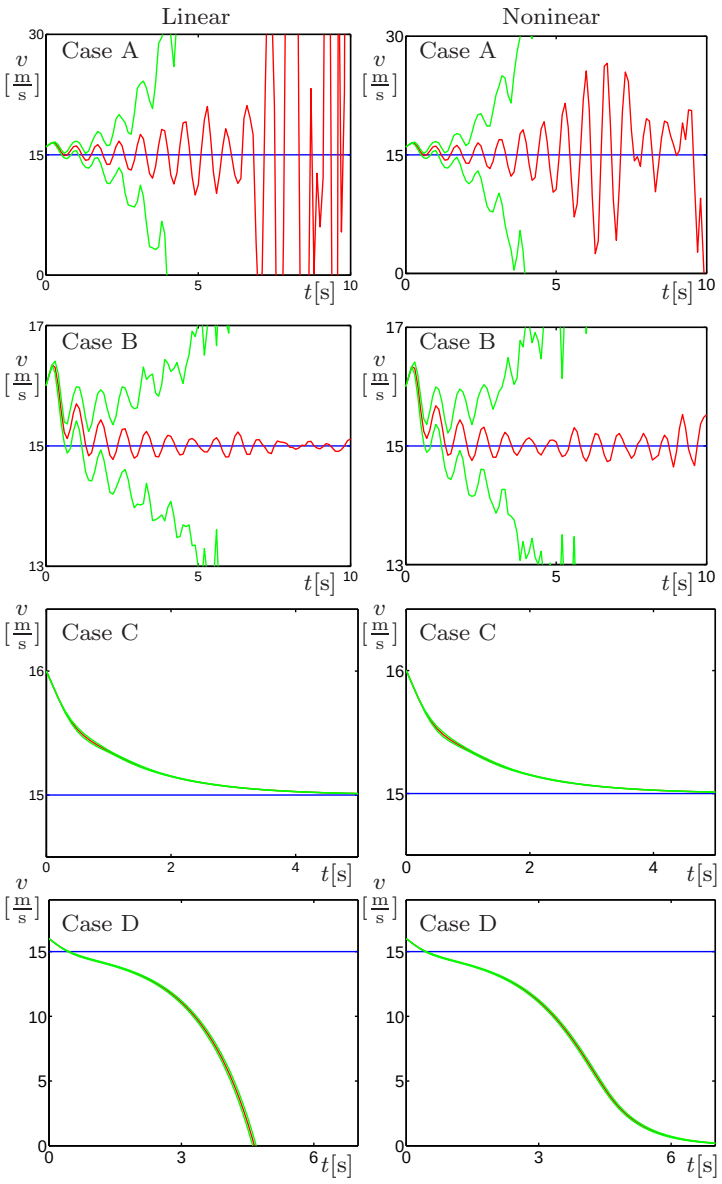

Figure 5.9: Mean and 1σ window of 1000 simulations for the linear system (5.13) and nonlinear system (5.8) subject to constant inputs $v_{j-1}(t) \equiv v^*_{j-1}$ and $\tilde{v}_{j-1}(t) \equiv 0$ with the gains corresponding to the points marked A–D in Figure 5.6(a). The initial perturbations are $\tilde{h}_j(t) = 10.2$ [m], $\tilde{v}_j(t) = 0.2$ [m/s], for $t \in [-\Delta t\,,\, 0]$. Blue curves represent the predecessor's velocity, red curves represent the follower's mean velocity, and green curves represent the follower's 1σ window.

shown in case G. The corresponding simulations show amplification in the 1σ window but attenuation in the mean for the sinusoidal input with excitation frequency $\omega = 6$ [rad/s]. As K_{v} is increased even further, the system becomes string unstable both in terms of mean and covariance dynamics at higher frequencies and the corresponding simulations show

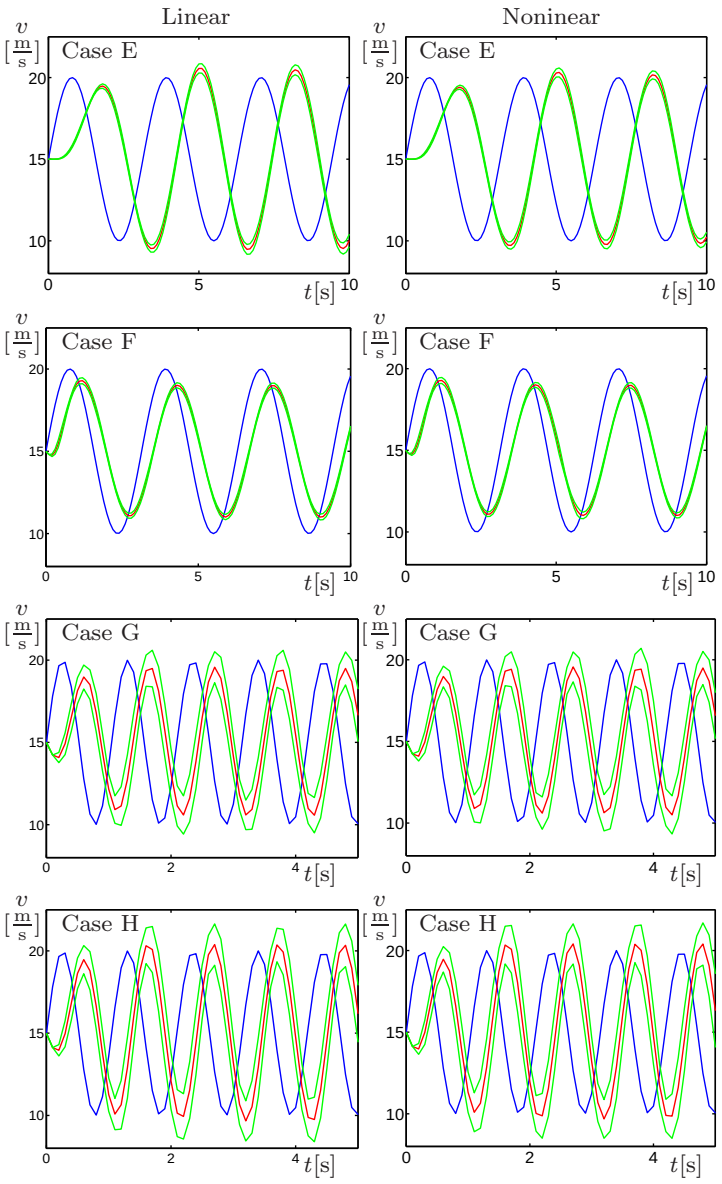

Figure 5.10: Mean and 1σ window of 1000 simulations of the linear system (5.13) and the nonlinear system (5.8) subject to sinusoidal input (5.10) with $v_{j-1}^{\mathrm{amp}} = 5$ [m/s] and the gains corresponding to the points E–H in Figure 5.7(a). Here, $\omega = 2\,[\mathrm{rad/s}]$ for the first two rows, $\omega = 6\,[\mathrm{rad/s}]$ for the last two rows. The initial conditions are chosen as $\tilde{h}_j(t) = 0$ m, $\tilde{v}_j(t) = 0$ [m/s], for $t \in [-\Delta t\,,\, 0]$. Blue curves represent the predecessor's velocity, red curves represent the follower's mean velocity, and green curves represent the follower's 1σ window.

amplification both in the mean and in the 1σ window as depicted in case H.

One may notice that there is not too much difference between the simulations of linear stochastic systems and nonlinear stochastic systems, which again validates the use of the

linearized system to test string stability. For larger variations, some discrepancies appear between them due to the saturation in the nonlinear stochastic system. Furthermore, corresponding to the stochastic nature of packet drops, simulations show amplitude variations which are "not uniformly" string unstable. We emphasize that in case F we achieve our design goal since we achieve string stability for a system subject to stochastic delay variations. Finally, we remark that in some cases simulations show string stable behavior where analytical results predict high-frequency ($\omega \geq 6$ [rad/s]) string instability. This is because high-frequency signals are filtered by the low sampling rates ($\Delta t \geq 0.1$ [s]). Investigating such effects is left for future research.

5.6 Summary

In this chapter, the effects of stochastic delays on the dynamics of connected vehicles were studied by analyzing both the mean and covariance dynamics. Plant stability and $n\sigma$ string stability conditions were derived, and it was shown that almost sure plant stability and $n\sigma$ string stability could be achieved in the presence of stochastic delay variations. We also demonstrated that the stability domains shrink when the packet drop ratio or the sampling time increases and above a critical limit string stability cannot be achieved by any gain combinations. This gives requirements for the sampling frequency and reliability of V2X devices.

CHAPTER 6

Stochastic Packet Drops in Open Chain Systems

To ensure the scalability of the proposed method in Chapter 5, we extend the two-car predecessor-follower system to an open chain system of $(J+1)$ cascaded predecessor-follower pairs as shown in Figure 1.1(a). Due to the asynchronously changing delays caused by stochastic packet drops, the analysis of the open chain subject to stochastic communication delays cannot be simplified to the analysis of a single predecessor-follower, but requires one to analyze the dynamics of the large stochastic connected vehicle system. In this chapter, a stochastic model is built for the open chain system, and a set of decomposition methods is developed to significantly reduce the size of matrices appearing in the mean, second moment, and covariance dynamics. The notion of $n\sigma$ string stability is extended to $n\sigma$ *head-to-tail string stability*, and the notion of $n\sigma$ *offset head-to-tail string stability* is proposed to characterize stability and disturbance attenuation. In this way, the feasible ranges of control parameters that ensure smooth traffic flow can be characterized analytically as the number of vehicles is increased. The material discussed in this section can be found in [196].

6.1 Stochastic Dynamics

The setup used in this chapter also allows vehicle models and controllers of different levels of complexity. For simplicity, we consider that all vehicles have identical dynamics given by (5.4). That is,

$$\begin{aligned} \dot{h}_j(t) &= v_{j-1}(t) - v_j(t)\,, \\ \dot{v}_j(t) &= a_j^{\mathrm{com}}(t_{k-\tau_j(k)})\,, \quad j = 1\,,\, 2\,,\, \ldots\,,\, J\,, \end{aligned} \tag{6.1}$$

for $t_k \leq t < t_{k+1}$, where $a_j^{\mathrm{com}}(t)$ is the controller and the delay $\tau_j(k)$ is a stochastic variable due to stochastic packet drops, satisfying (5.2, 5.3). Moreover, all vehicles use the same

controller (5.5), i.e.,

$$a_j^{\rm com}(t) = K_{\rm p}\Big(V\big(h_j(t)\big) - v_j(t)\Big) + K_{\rm v}\Big(W\big(v_{j-1}(t)\big) - v_j(t)\Big)\,, \tag{6.2}$$

to form an open chain of cascaded predecessor-follower systems. It is also assumed that the control gains are the same for all the vehicles, which allows us to summarize the stability results in low dimensional parameter space. The methods presented below are applicable to connected vehicle system of complex topology and non-identical vehicles, and it is expected that such heterogeneity can improve string stability. Finally, we assume that clock synchronization, data sampling and control mechanism are the same as those in the previous chapters, and the stochastic delay $\tau_j(k)$-s are IID with the distribution (5.2, 5.3).

The overall dynamics of the open chain system of $(J+1)$ vehicles are given by (6.1, 6.2) for $j = 1,\ \ldots,\ J$. For simplicity of notation, the argument k of the delay $\tau_j(k)$ is not spelled out in the rest of this chapter. Notice that in the time interval $t \in [t_k,\, t_{k+1})$, the control signal $a_j^{\rm com}(t_{k-\tau_j})$ is a constant. Thus, one can solve the differential equation (6.1) using the input $v_0(t)$ and initial values $h_j(t_k), v_j(t_k)$, which results in the discrete-time nonlinear map

$$\begin{aligned}
h_1(t_{k+1}) &= h_1(t_k) - v_1(t_k)\Delta t - \frac{1}{2}a_1^{\rm com}(t_{k-\tau_1})\Delta t^2 + \textstyle\int_{t_k}^{t_{k+1}} v_0(t)\,{\rm d}t\,,\\
v_1(t_{k+1}) &= v_1(t_k) + a_1^{\rm com}(t_{k-\tau_1})\Delta t\,,\\
h_j(t_{k+1}) &= h_j(t_k) + \big(v_{j-1}(t_k) - v_j(t_k)\big)\Delta t + \frac{1}{2}\big(u_{j-1}(t_{k-\tau_{j-1}}) - a_j^{\rm com}(t_{k-\tau_j})\big)\Delta t^2\,,\\
v_j(t_{k+1}) &= v_j(t_k) + a_j^{\rm com}(t_{k-\tau_j})\Delta t\,,
\end{aligned} \tag{6.3}$$

for $j = 2\,,\ \ldots\ ,\ J$. When the velocities do not exceed the speed limit $v_{\max}$, the system (6.3) possesses the uniform flow equilibrium

$$v_j^* = V(h_j^*) = v_0\,, \tag{6.4}$$

for $j = 1\,,\ \ldots\ ,\ J$. In order to analyze the stability of the stochastic system (6.3), we define small variations about the equilibrium (6.4), i.e.,

$$\tilde{h}_j(t) = h_j(t) - h_j^*\,, \qquad\qquad \tilde{v}_j(t) = v_j(t) - v_j^*\,, \tag{6.5}$$

for $j = 1\,,\ \ldots\ ,\ J$, and again assume sinusoidal velocity variations for the head vehicle, i.e.,

$$v_0(t) = v_0^* + v_0^{\rm amp}\sin(\omega t) \implies \tilde{v}_0(t) = v_0^{\rm amp}\sin(\omega\, t)\,, \tag{6.6}$$

and $v_0(t) < v_{\max}$.

Let us define the state, the output and the input as

$$x_j(k) = \begin{bmatrix} \tilde{h}_j(t_k) \\ \tilde{v}_j(t_k) \end{bmatrix}, \qquad y(k) = \tilde{v}_J(t_k)\,, \qquad u(k) = \begin{bmatrix} \tilde{v}_0(t_k) \\ \tilde{v}_0^{\perp}(t_k) \end{bmatrix}, \tag{6.7}$$

where

$$\tilde{v}_0^{\perp}(t) = v_0^{\text{amp}} \cos(\omega t)\,. \tag{6.8}$$

Using the controller (6.2) in (6.3), after linearization we obtain

$$\begin{aligned}
x_1(k+1) &= \boldsymbol{a}_1\, x_1(k) + \boldsymbol{a}_3\, x_1\big(k-\tau_1\big) + \boldsymbol{b}_1\, u(k) + \boldsymbol{b}_2\, u(k-\tau_1)\,, \\
x_2(k+1) &= \boldsymbol{a}_2\, x_1(k) + \boldsymbol{a}_1\, x_2(k) + \boldsymbol{a}_5\, x_1\big(k-\tau_1\big) + \boldsymbol{a}_4\, x_1\big(k-\tau_2\big) \\
&\quad + \boldsymbol{a}_3\, x_2\big(k-\tau_2\big) + \boldsymbol{b}_3\, u(k-\tau_1)\,, \\
x_j(k+1) &= \boldsymbol{a}_2\, x_{j-1}(k) + \boldsymbol{a}_1\, x_j(k) + \boldsymbol{a}_6\, x_{j-2}\big(k-\tau_{j-1}\big) + \boldsymbol{a}_5\, x_{j-1}\big(k-\tau_{j-1}\big) \\
&\quad + \boldsymbol{a}_4\, x_{j-1}\big(k-\tau_j\big) + \boldsymbol{a}_3\, x_j(k-\tau_j)\,, \qquad\qquad j = 3\,,\,\ldots\,,\,J\,, \\
y(k) &= c_1\, x_J(k)\,,
\end{aligned} \tag{6.9}$$

with the matrices

$$\begin{aligned}
\boldsymbol{a}_1 &= \begin{bmatrix} 1 & -\Delta t \\ 0 & 1 \end{bmatrix}, & \boldsymbol{a}_2 &= \begin{bmatrix} 0 & \Delta t \\ 0 & 0 \end{bmatrix}, \\
\boldsymbol{a}_3 &= \begin{bmatrix} -\frac{1}{2}\Delta t^2 K_{\text{p}} N_* & \frac{1}{2}\Delta t^2 (K_{\text{p}} + K_{\text{v}}) \\ \Delta t K_{\text{p}} N_* & -\Delta t (K_{\text{p}} + K_{\text{v}}) \end{bmatrix}, & \boldsymbol{a}_4 &= \begin{bmatrix} 0 & -\frac{1}{2}\Delta t^2 K_{\text{v}} \\ 0 & \Delta t K_{\text{v}} \end{bmatrix}, \\
\boldsymbol{a}_5 &= \begin{bmatrix} \frac{1}{2}\Delta t^2 K_{\text{p}} N_* & -\frac{1}{2}\Delta t^2 (K_{\text{p}} + K_{\text{v}}) \\ 0 & 0 \end{bmatrix}, & \boldsymbol{a}_6 &= \begin{bmatrix} 0 & \frac{1}{2}\Delta t^2 K_{\text{v}} \\ 0 & 0 \end{bmatrix}, \\
\boldsymbol{b}_1 &= \begin{bmatrix} \theta_2 & \theta_3 \\ 0 & 0 \end{bmatrix}, & \boldsymbol{b}_2 &= \begin{bmatrix} -\frac{1}{2}\Delta t^2 K_{\text{v}} & 0 \\ \Delta t K_{\text{v}} & 0 \end{bmatrix}, \\
\boldsymbol{b}_3 &= \begin{bmatrix} \frac{1}{2}\Delta t^2 K_{\text{v}} & 0 \\ 0 & 0 \end{bmatrix}, & c_1 &= \begin{bmatrix} 0 & 1 \end{bmatrix},
\end{aligned} \tag{6.10}$$

where θ_2 and θ_3 are given in (2.13) and N_* is given in (5.15).

Again the scalar sinusoidal input (6.6) that drives the continuous-time system (6.1) results in the vector-valued input (6.7) for the discrete-time system (6.9) that satisfies (2.15).

By augmenting j-th vehicle's state with the delayed values as

$$X_j(k) = \begin{bmatrix} x_j(k) \\ x_j(k-1) \\ \vdots \\ x_j(k-N) \end{bmatrix} \in \mathbb{R}^{2(N+1)}\,, \tag{6.11}$$

(6.9) can be rewritten as

$$\begin{aligned} X_1(k+1) &= \boldsymbol{\alpha}_{1,\tau_1} X_1(k) + \boldsymbol{\beta}_{1,\tau_1} u(k)\,, \\ X_2(k+1) &= (\boldsymbol{\alpha}_{3,\tau_1} + \boldsymbol{\alpha}_{2,\tau_2}) X_1(k) + \boldsymbol{\alpha}_{1,\tau_2} X_2(k) + \boldsymbol{\beta}_{2,\tau_1} u(k)\,, \\ X_j(k+1) &= \boldsymbol{\alpha}_{4,\tau_{j-1}} X_{j-2}(k) + (\boldsymbol{\alpha}_{3,\tau_{j-1}} + \boldsymbol{\alpha}_{2,\tau_j}) X_{j-1}(k) + \boldsymbol{\alpha}_{1,\tau_j} X_j(k)\,, \\ & \qquad\qquad j = 3\,,\,\ldots\,,\,J\,, \\ y(k) &= \boldsymbol{c}\, X_j(k)\,, \end{aligned} \tag{6.12}$$

where

$$\boldsymbol{c} = \begin{bmatrix} c_1 & 0' & \ldots & 0' \end{bmatrix}\,, \tag{6.13}$$

is the output matrix with

$$0' = \begin{bmatrix} 0 & 0 \end{bmatrix}\,. \tag{6.14}$$

In this case, $\boldsymbol{\alpha}_{1,\tau_j}$, $\boldsymbol{\alpha}_{2,\tau_j}$, $\boldsymbol{\alpha}_{3,\tau_j}$, $\boldsymbol{\alpha}_{4,\tau_j} \in \mathbb{R}^{2(N+1)\times 2(N+1)}$ and $\boldsymbol{\beta}_{1,\tau_1}$, $\boldsymbol{\beta}_{2,\tau_1} \in \mathbb{R}^{2(N+1)\times 2}$ are random matrices that may take values

$$\begin{aligned} \boldsymbol{\alpha}_{1,r_j} &= \begin{bmatrix} \boldsymbol{a}_1 & \delta_{1r_j}\boldsymbol{a}_3 & \ldots & \delta_{Nr_j}\boldsymbol{a}_3 \\ \mathbf{I} & & & \\ & \ddots & & \\ & & \mathbf{I} & \end{bmatrix}\,, \quad \boldsymbol{\alpha}_{2,r_j} = \begin{bmatrix} \boldsymbol{a}_2 & \delta_{1r_j}\boldsymbol{a}_4 & \ldots & \delta_{Nr_j}\boldsymbol{a}_4 \\ \mathbf{0} & \mathbf{0} & \ldots & \mathbf{0} \end{bmatrix}\,, \\ \boldsymbol{\alpha}_{3,r_j} &= \begin{bmatrix} \mathbf{0} & \delta_{1r_j}\boldsymbol{a}_5 & \ldots & \delta_{Nr_j}\boldsymbol{a}_5 \\ \mathbf{0} & \mathbf{0} & \ldots & \mathbf{0} \end{bmatrix}\,, \quad \boldsymbol{\alpha}_{4,r_j} = \begin{bmatrix} \mathbf{0} & \delta_{1r_j}\boldsymbol{a}_6 & \ldots & \delta_{Nr_j}\boldsymbol{a}_6 \\ \mathbf{0} & \mathbf{0} & \ldots & \mathbf{0} \end{bmatrix}\,, \\ \boldsymbol{\beta}_{1,r_1} &= \begin{bmatrix} \boldsymbol{b}_1 + \sum_{n=1}^{N} \delta_{nr_1}\boldsymbol{b}_2\mathbf{R}^n \\ \mathbf{0} \\ \vdots \\ \mathbf{0} \end{bmatrix}\,, \qquad \boldsymbol{\beta}_{2,r_1} = \begin{bmatrix} \sum_{n=1}^{N} \delta_{nr_1}\boldsymbol{b}_3\mathbf{R}^n \\ \mathbf{0} \\ \vdots \\ \mathbf{0} \end{bmatrix}\,, \end{aligned} \tag{6.15}$$

for r_j =1, 2, $\cdots$, N, where δ_{ir_j} denotes the Kronecker delta, and j =1, 2, ..., J.

By defining the overall state, the input and the output

$$X(k) = \begin{bmatrix} X_1(k) \\ X_2(k) \\ \vdots \\ X_J(k) \end{bmatrix} \in \mathbb{R}^{2J(N+1)}\,, \quad U(k) = u(k) \in \mathbb{R}^2\,, \quad Y(k) = \tilde{v}_j(k) \in \mathbb{R}\,, \tag{6.16}$$

(6.12) can be rewritten as

$$\begin{aligned} X(k+1) &= \mathbf{A}_{\boldsymbol{\tau}}\, X(k) + \mathbf{B}_{\tau_1}\, U(k)\,, \\ Y(k) &= \mathbf{C}\, X(k)\,, \end{aligned} \tag{6.17}$$

where the output matrix is

$$\mathbf{C} = \begin{bmatrix} \mathbf{0} & \dots & \mathbf{0} & \boldsymbol{c} \end{bmatrix}\,, \tag{6.18}$$

and $\mathbf{0} \in \mathbb{R}^{\mathbf{2(N+1)\times 1}}$ is a row vector with zeros. Here $\boldsymbol{\tau}$ collects the random variables $\tau_1\tau_2\cdots\tau_J$, i.e., $\mathbf{A}_{\boldsymbol{\tau}}$ denotes $\mathbf{A}_{\tau_1\tau_2\cdots\tau_J}$. The possible values for $\mathbf{A}_{\boldsymbol{\tau}}$ and $\mathbf{B}_{\tau_1}$ are

$$\begin{aligned} \mathbf{A}_{\boldsymbol{r}} &= \begin{bmatrix} \boldsymbol{\alpha}_{1,r_1} & & & & & \\ \boldsymbol{\alpha}_{3,r_1} + \boldsymbol{\alpha}_{2,r_2} & \boldsymbol{\alpha}_{1,r_2} & & & & \\ \boldsymbol{\alpha}_{4,r_2} & \boldsymbol{\alpha}_{3,r_2} + \boldsymbol{\alpha}_{2,r_3} & \boldsymbol{\alpha}_{1,r_3} & & & \\ & \ddots & \ddots & \ddots & & \\ & & \boldsymbol{\alpha}_{4,r_{j-1}} & \boldsymbol{\alpha}_{3,r_{J-1}} + \boldsymbol{\alpha}_{2,r_J} & \boldsymbol{\alpha}_{1,r_J} \end{bmatrix}\,, \\ \mathbf{B}_{r_1} &= \begin{bmatrix} \boldsymbol{\beta}_{1,r_1} \\ \boldsymbol{\beta}_{2,r_1} \\ \mathbf{0} \\ \vdots \\ \mathbf{0} \end{bmatrix}\,, \end{aligned} \tag{6.19}$$

for $r_j = 1\,,\, 2,\, \cdots\,,\, N$ and $j = 1\,,\, 2\,,\, \dots\,,\, J$; cf. (6.15).

We remark that there is another way to rewrite (6.9) into state space form by inserting different vehicles' states into a vector first, and then augmenting the resulting states over time. However, the way presented above better supports physical intuition and make the forthcoming calculations technically less challenging.

6.2 Mean, Second Moment, and Covariance Dynamics

In order to find stability conditions, the mean, the second moment, and the covariance dynamics need to be derived in the same way as in Chapter 5. With the IID assumption of $\boldsymbol{\tau}(k)$ explained in Section 5.3, one can obtain the PDF-s of $\mathbf{A}_{\boldsymbol{\tau}}$ and $\mathbf{B}_{\tau_1}$ as

$$f_{\mathbf{A}_{\boldsymbol{\tau}}}(\mathbf{A}) = \sum_{\boldsymbol{r}=1}^{\infty} w_{\boldsymbol{r}} \delta(\mathbf{A} - \mathbf{A}_{\boldsymbol{r}}) \,, \qquad f_{\mathbf{B}_{\tau_1}}(\mathbf{B}) = \sum_{r_1=1}^{\infty} w_{r_1} \delta(\mathbf{B} - \mathbf{B}_{r_1}) \,, \tag{6.20}$$

respectively, where $\boldsymbol{r}$ is the set of realization for $\boldsymbol{\tau}$, i.e., $\mathbf{A}_{\boldsymbol{r}}$ denotes $\mathbf{A}_{r_1 r_2 \cdots r_J}$ and $\sum_{\boldsymbol{r}=1}^{N} w_{\boldsymbol{r}}$ denotes $\sum_{r_1=1}^{N} \sum_{r_2=1}^{N} \cdots \sum_{r_J=1}^{N} w_{r_1} w_{r_2} \cdots w_{r_J}$. Notice that $\mathbf{A}_{\boldsymbol{\tau}}$ and $X(k)$ are mutually independent, which is also the case for $\mathbf{B}_{\tau_1}$ and $X(k)$.

The mean values of state variables can be defined as

$$\bar{X}(k) = \mathbb{E}[X(k)] \in \mathbb{R}^{2J(N+1)} \,, \qquad \bar{Y}(k) = \mathbb{E}[Y(k)] \in \mathbb{R} \,. \tag{6.21}$$

By taking expected value of both sides in (6.17) with the PDF-s (6.20) and using independence of variables, one can derive the mean dynamics

$$\begin{aligned} \bar{X}(k+1) &= \bar{\mathbf{A}}\, \bar{X}(k) + \bar{\mathbf{B}}\, U(k) \,, \\ \bar{Y}(k) &= \bar{\mathbf{C}}\, \bar{X}(k) \,. \end{aligned} \tag{6.22}$$

Here the state matrix, the input matrix and the output matrix are the expected values of corresponding matrices given in (6.19), i.e.,

$$\begin{aligned} \bar{\mathbf{A}} &= \sum_{\boldsymbol{r}=1}^{N} w_{\boldsymbol{r}} \mathbf{A}_{\boldsymbol{r}} = \begin{bmatrix} \bar{\boldsymbol{\alpha}}_1 & & & & \\ \bar{\boldsymbol{\alpha}}_3 + \bar{\boldsymbol{\alpha}}_2 & \bar{\boldsymbol{\alpha}}_1 & & & \\ \bar{\boldsymbol{\alpha}}_4 & \bar{\boldsymbol{\alpha}}_3 + \bar{\boldsymbol{\alpha}}_2 & \bar{\boldsymbol{\alpha}}_1 & & \\ & \ddots & \ddots & \ddots & \\ & & \bar{\boldsymbol{\alpha}}_4 & \bar{\boldsymbol{\alpha}}_3 + \bar{\boldsymbol{\alpha}}_2 & \bar{\boldsymbol{\alpha}}_1 \end{bmatrix} \\ \bar{\mathbf{B}} &= \sum_{r_1=1}^{N} w_{r_1} \mathbf{B}_{r_1} = \begin{bmatrix} \bar{\boldsymbol{\beta}}_1 \\ \bar{\boldsymbol{\beta}}_2 \\ \mathbf{0} \\ \vdots \\ \mathbf{0} \end{bmatrix} \,, \qquad \bar{\mathbf{C}} = \mathbf{C} \,, \end{aligned} \tag{6.23}$$

with

$$\bar{\boldsymbol{\alpha}}_1 = \sum_{r_j=1}^{N} w_{r_j} \boldsymbol{\alpha}_{1,r_j} = \begin{bmatrix} \boldsymbol{a}_1 & w_1 \boldsymbol{a}_3 & \dots & w_N \boldsymbol{a}_3 \\ \mathbf{I} & & & \\ & \ddots & & \\ & & \mathbf{I} & \end{bmatrix},$$

$$\bar{\boldsymbol{\alpha}}_2 = \sum_{r_j=1}^{N} w_{r_j} \boldsymbol{\alpha}_{2,r_j} = \begin{bmatrix} \boldsymbol{a}_2 & w_1 \boldsymbol{a}_4 & \dots & w_N \boldsymbol{a}_4 \\ \mathbf{0} & \mathbf{0} & \dots & \mathbf{0} \end{bmatrix},$$

$$\bar{\boldsymbol{\alpha}}_3 = \sum_{r_j=1}^{N} w_{r_j} \boldsymbol{\alpha}_{3,r_j} = \begin{bmatrix} \mathbf{0} & w_1 \boldsymbol{a}_5 & \dots & w_N \boldsymbol{a}_5 \\ \mathbf{0} & \mathbf{0} & \dots & \mathbf{0} \end{bmatrix}, \tag{6.24}$$

$$\bar{\boldsymbol{\alpha}}_4 = \sum_{r_j=1}^{N} w_{r_j} \boldsymbol{\alpha}_{4,r_j} = \begin{bmatrix} \mathbf{0} & w_1 \boldsymbol{a}_6 & \dots & w_N \boldsymbol{a}_6 \\ \mathbf{0} & \mathbf{0} & \dots & \mathbf{0} \end{bmatrix},$$

$$\bar{\boldsymbol{\beta}}_1 = \sum_{r_j=1}^{N} w_{r_j} \boldsymbol{\beta}_{1,r_j} = \begin{bmatrix} \boldsymbol{b}_1 + \boldsymbol{b}_2 \bar{\mathbf{R}} \\ \mathbf{0} \\ \vdots \\ \mathbf{0} \end{bmatrix}, \qquad \bar{\boldsymbol{\beta}}_2 = \sum_{r_j=1}^{N} w_{r_j} \boldsymbol{\beta}_{2,r_j} = \begin{bmatrix} \boldsymbol{b}_3 \bar{\mathbf{R}} \\ \mathbf{0} \\ \vdots \\ \mathbf{0} \end{bmatrix},$$

where

$$\bar{\mathbf{R}} = \sum_{n=1}^{N} w_n \, \mathbf{R}^n \,. \tag{6.25}$$

Similarly, the second moments of variables can be defined as

$$\hat{\bar{X}}(k) = \mathbb{E}[X(k) \otimes X(k)] \in \mathbb{R}^{2^2 J^2 (N+1)^2}, \qquad \hat{\bar{Y}}(k) = \mathbb{E}[Y(k) \otimes Y(k)] \in \mathbb{R} \,. \tag{6.26}$$

By taking expected value with the PDF-s (6.20) and using independence of variables, one can obtain the second moment dynamics

$$\begin{aligned} \hat{\bar{X}}(k+1) = {} & \big(\sum_{\boldsymbol{r}=1}^{N} w_{\boldsymbol{r}} \mathbf{A}_{\boldsymbol{r}} \otimes \mathbf{A}_{\boldsymbol{r}}\big) \hat{\bar{X}}(k) + \big(\sum_{\boldsymbol{r}=1}^{N} w_{\boldsymbol{r}} \mathbf{A}_{\boldsymbol{r}} \otimes \mathbf{B}_{\boldsymbol{r}}\big) \big(\bar{X}(k) \otimes U(k)\big) \\ & + \big(\sum_{\boldsymbol{r}=1}^{N} w_{\boldsymbol{r}} \mathbf{B}_{\boldsymbol{r}} \otimes \mathbf{A}_{\boldsymbol{r}}\big) \big(U(k) \otimes \bar{X}(k)\big) + \big(\sum_{\boldsymbol{r}=1}^{N} w_{\boldsymbol{r}} \mathbf{B}_{\boldsymbol{r}} \otimes \mathbf{B}_{\boldsymbol{r}}\big) \big(U(k) \otimes U(k)\big) \,, \\ \hat{\bar{Y}}(k) = {} & \big(\mathbf{C} \otimes \mathbf{C}\big) \hat{\bar{X}}(k) \,. \end{aligned} \tag{6.27}$$

Finally, the covariance can be defined as

$$\begin{aligned}\bar{\bar{X}}(k) &= \mathbb{E}\big[\big(X(k)-\bar{X}(k)\big)\otimes\big(X(k)-\bar{X}(k)\big)\big] \in \mathbb{R}^{2^2J^2(N+1)^2}\,,\\ \bar{\bar{Y}}(k) &= \mathbb{E}\big[\big(Y(k)-\bar{Y}(k)\big)\otimes\big(Y(k)-\bar{Y}(k)\big)\big] \in \mathbb{R}\,,\end{aligned} \tag{6.28}$$

and it can be shown that

$$\begin{aligned}\bar{\bar{X}}(k) &= \mathbb{E}[X(k)\otimes X(k)] - \bar{X}(k)\otimes\bar{X}(k)\,,\\ \bar{\bar{Y}}(k) &= \mathbb{E}[Y(k)\otimes Y(k)] - \bar{Y}(k)\otimes\bar{Y}(k)\,.\end{aligned} \tag{6.29}$$

Thus, using (6.22) and (6.27), one can obtain the covariance dynamics

$$\begin{aligned}\bar{\bar{X}}(k+1) &= \bar{\bar{\mathbf{A}}}\bar{\bar{X}}(k) + \bar{\bar{\mathbf{K}}}_1\big(\bar{X}(k)\otimes\bar{X}(k)\big) + \bar{\bar{\mathbf{K}}}_2\big(\bar{X}(k)\otimes U(k)\big)\\ &\quad + \bar{\bar{\mathbf{K}}}_3\big(U(k)\otimes\bar{X}(k)\big) + \bar{\bar{\mathbf{K}}}_4\big(U(k)\otimes U(k)\big)\,,\\ \bar{\bar{Y}}(k) &= \bar{\bar{\mathbf{C}}}\bar{\bar{X}}(k)\,,\end{aligned} \tag{6.30}$$

where

$$\begin{aligned}\bar{\bar{\mathbf{A}}} &= \sum_{\boldsymbol{r}=1}^{N} w_{\boldsymbol{r}}\mathbf{A}_{\boldsymbol{r}}\otimes\mathbf{A}_{\boldsymbol{r}}\,, & \bar{\bar{\mathbf{C}}} &= \mathbf{C}\otimes\mathbf{C}\,,\\ \bar{\bar{\mathbf{K}}}_1 &= \sum_{\boldsymbol{r}=1}^{N} w_{\boldsymbol{r}}\mathbf{A}_{\boldsymbol{r}}\otimes\mathbf{A}_{\boldsymbol{r}} - \bar{\mathbf{A}}\otimes\bar{\mathbf{A}}\,, & \bar{\bar{\mathbf{K}}}_2 &= \sum_{\boldsymbol{r}=1}^{N} w_{\boldsymbol{r}}\mathbf{A}_{\boldsymbol{r}}\otimes\mathbf{B}_{\boldsymbol{r}} - \bar{\mathbf{A}}\otimes\bar{\mathbf{B}}\,,\\ \bar{\bar{\mathbf{K}}}_3 &= \textstyle\sum_{\boldsymbol{r}=1}^{N} w_{\boldsymbol{r}}\mathbf{B}_{\boldsymbol{r}}\otimes\mathbf{A}_{\boldsymbol{r}} - \bar{\mathbf{B}}\otimes\bar{\mathbf{A}}\,, & \bar{\bar{\mathbf{K}}}_4 &= \sum_{\boldsymbol{r}=1}^{N} w_{\boldsymbol{r}}\mathbf{B}_{\boldsymbol{r}}\otimes\mathbf{B}_{\boldsymbol{r}} - \bar{\mathbf{B}}\otimes\bar{\mathbf{B}}\,,\end{aligned} \tag{6.31}$$

cf. (6.22, 6.23). The time evolution of the mean and the covariance is described by the nonlinear system (6.22, 6.30) such that (6.30) is driven by (6.22).

6.3 Plant Stability and String Stability

As explained in Chapter 1, in an open chain system, plant stability indicates whether all following vehicles are able to approach the constant desired velocity dictated by the head vehicle. The importance of plant stability lies in the fact that plant unstable traffic systems can lead to collisions. Figure 6.1 shows two simulation results of an open chain of $(15+1)$ connected vehicles for different $(K_{\mathrm{v}}, K_{\mathrm{p}})$ gains for the parameters $v_{\max} = 30\,[\mathrm{m/s}]$, $h_{\mathrm{st}} = 5\,[\mathrm{m}]$, $h_{\mathrm{go}} = 35\,[\mathrm{m}]$, $v_0^* = 15\,[\mathrm{m/s}]$, $\Delta t = 0.1\,[\mathrm{s}]$ (cf. (1.2, 1.3, 6.4)), which will be kept the same throughout the whole chapter. Here, the packet delivery ratio is $p = 0.6$, and

only the velocities of every third vehicle are shown. Figure 6.1(a) shows the time profiles for a simulation demonstrating plant stability as all velocities approach the head vehicle's velocity despite the initial perturbations and stochastic packet drops. Thus, one can say that this realization is plant stable. However, to check whether this pair of $(K_{\mathrm{v}}, K_{\mathrm{p}})$ gains is plant stable in the stochastic sense, one has to investigate all possible realizations (that is clearly not feasible via simulations). Figure 6.1(b) shows the time profiles for one plant unstable simulation, where the vehicles are unable to maintain the same constant velocity prescribed by the head vehicle.

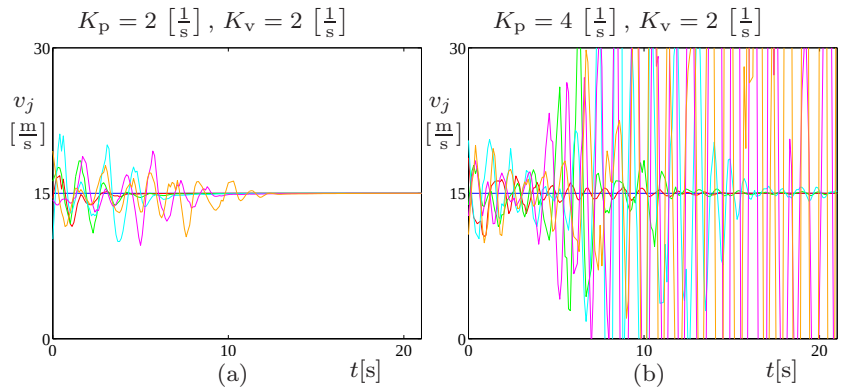

Figure 6.1: Plant stability simulations for an open chain of $(15 + 1)$ vehicles for different $(K_{\mathrm{v}}, K_{\mathrm{p}})$ gains as indicated. The blue curves represent the velocity v_0 of the head vehicle while the red, green, cyan, magenta and orange curves represent the velocities v_3, v_6, v_9, v_{12}, v_{15}, respectively. (a) Plant stable. (b) Plant unstable.

For an open chain system of cascaded predecessor-followers, head-to-tail string stability requires attenuation of fluctuations between the head vehicle and the tail vehicle. String unstable traffic systems may exhibit stop-and-go motion, sometimes referred to as phantom traffic jams. Figure 6.2 shows three simulation results for an open chain of $(200 + 1)$ vehicles when the head vehicle is introducing a sinusoidal fluctuation into the system, and the packet delivery ratio is $p = 0.4$. Here, only the velocities of every 40-th vehicle are shown, and the other parameters remain the same as those for Figure 6.1. It can be seen from Figure 6.2(a) that the fluctuation introduced by the head vehicle is attenuated by all vehicles shown in the figure, including the tail vehicle.

However, similar to the argument for plant stability, to check whether this pair of $(K_{\mathrm{v}}, K_{\mathrm{p}})$ gains is head-to-tail string stable in the stochastic sense, one has to investigate all the possible realizations for all the possible excitation frequencies. Figure 6.2(b, c) show the time profiles for two string unstable scenarios, where the tail vehicle is unable to attenuate the fluctuation introduced by the head vehicle. In Figure 6.2(b), the fluctuations

introduced by the head vehicle are amplified as they propagate upstream. Such fluctuations deteriorate driving comfort and fuel economy. Because of the stochasticity in packet drops, one may notice that the fluctuations are not perfectly sinusoidal. Whereas, in Figure 6.2(c), the single-frequency oscillation introduced by the head vehicle triggers oscillations with different frequencies in the following vehicles due to the stochastic nature in the packet delivery, which gives rise to stop-and-go waves traveling upstream. In the controller design, we need to assure string stability in order to prevent such phenomena.

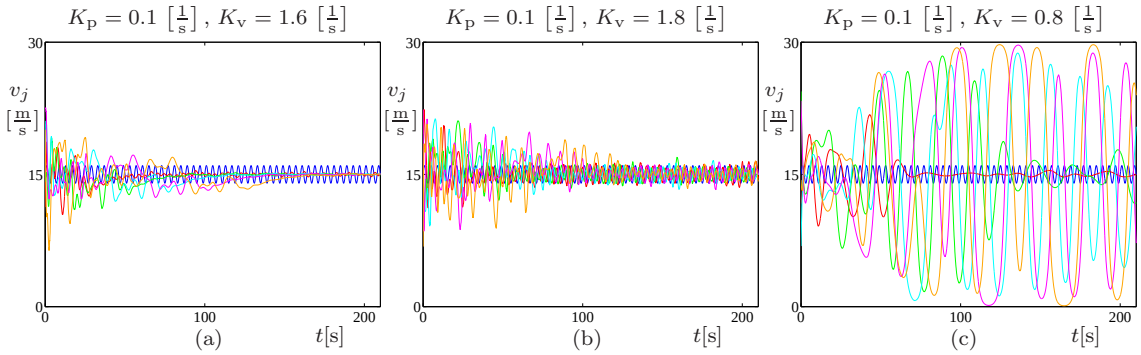

Figure 6.2: String stability simulations for an open chain of $(200 + 1)$ vehicles for different $(K_\mathrm{v}, K_\mathrm{p})$ gains as indicated. The blue curves represent the velocity v_0 of the head vehicle while the red, green, cyan, magenta and orange curves represent the velocities v_{40}, v_{80}, v_{120}, v_{160}, v_{200}, respectively. (a) String stable. (b) String unstable. (c) String unstable.

In this section, we derive and simplify conditions on both plant stability and head-to-tail string stability for the dynamics of the mean (6.22) and the covariance (6.30) for open chain systems subject to stochastic packet drops.

6.3.1 Plant Stability

Similar to Chapter 5, we will evaluate plant stability for both the mean and second moment dynamics. To test plant stability, we set the head vehicle's velocity to be a constant, i.e., $v_0^{\mathrm{amp}} = 0$ in (6.6, 6.8) or $u(k) \equiv 0$ in (6.7). For plant stability of the mean dynamics $\bar{X}(k+1) = \bar{\mathbf{A}}\,\bar{X}(k)$ (cf. (6.22) with $U(k) \equiv 0$), all the eigenvalues of the matrix $\bar{\mathbf{A}}$ must lie within the unit circle in the complex plane. By observing (6.23), one may notice that the eigenvalues of $\bar{\mathbf{A}}$ consist of all the eigenvalues of $\bar{\boldsymbol{\alpha}}_1$, each with multiplicity J; cf. (6.24). In order to assure that the mean dynamics are plant stable, all eigenvalues of matrix $\bar{\boldsymbol{\alpha}}_1$ must lie within the unit circle in the complex plane. Again we use the bisection method to trace the stability boundaries in the $(K_\mathrm{v}, K_\mathrm{p})$-plane. We remark that the plant stability

boundaries depend on the parameters $(K_{\mathrm{p}}, K_{\mathrm{v}}, p, v_0^*, \Delta t)$, but independent of the number of cars J.

In Appendix D, it was shown that stability of the second moment dynamics and the stability of the covariance dynamics are equivalent when the mean dynamics are stable. Consequently, only the plant stability for the second moment dynamics is discussed here. Similar to the mean dynamics, to ensure plant stability of the second moment dynamics $\hat{\bar{X}}(k+1) = \bar{\bar{\mathbf{A}}}\hat{\bar{X}}(k)$ (cf. (6.27) with $U(k) \equiv 0$ and $\bar{\bar{\mathbf{A}}}$ defined in (6.31)), all eigenvalues of the matrix $\bar{\bar{\mathbf{A}}}$ must lie within the unit circle in the complex plane.

While solving this problem, we are faced with three issues. The first one lies in the construction of the possible values for the Kronecker product $\mathbf{A}_{\boldsymbol{r}} \otimes \mathbf{A}_{\boldsymbol{r}}$ due to its huge size. Matrix $\mathbf{A}_{\boldsymbol{r}} \otimes \mathbf{A}_{\boldsymbol{r}}$ is of the dimension $2^2J^2(N+1)^2$, where J is the number of vehicles and N is the maximum delay. Table 6.1 shows how this dimension changes while varying numbers of cars J when the maximum delay is $N = 6$. It also shows how much RAM space is needed to store one matrix, given that each entry takes 8-byte storage space. The second issue is the difficulty in enumerating all the N^J possible values of $\mathbf{A}_{\boldsymbol{r}} \otimes \mathbf{A}_{\boldsymbol{r}}$, when calculating the weighted sum in (6.31). As J increases, N^J increases dramatically; cf. Table 6.1. The third and the most critical issue is to determine plant stability changes while varying parameters, that is, frequent eigenvalue calculations on huge matrices with a high multiplicity of eigenvalues. (The appearance of the high multiplicity of eigenvalues will be shown later.) In this case accuracy of eigenvalues degrades significantly as the size of the matrix and the eigenvalue multiplicity increase; see [197]. Henceforth, decomposition must be done to assure scalability of plant stability computations.

Table 6.1: Characteristics of the matrix $\bar{\bar{\mathbf{A}}}$ for $(J+1)$ connected vehicles and $N = 6$.

	J	3	9	15	21	27
Before	$2^2J^2(N+1)^2$	1764	15876	44100	86436	142884
Decom-	storage (GB)	0.023	1.878	14.490	55.665	152.110
position	N^J	216	1.1×10^7	4.7×10^{11}	2.2×10^{16}	1.0×10^{21}
After	$2^2(N+1)^2$	196	196	196	196	196
Decom-	storage (GB)	< 0.001	< 0.001	< 0.001	< 0.001	< 0.001
position	N	6	6	6	6	6

The decomposition procedure outlined in Appendix F.1 relies on applying properties of the Kronecker product [198–200] and using perfect shuffle [200, 201], which are provided in Appendix E.1. This allows us to transform matrix $\bar{\bar{\mathbf{A}}}$ to a block diagonal matrix $\tilde{\bar{\mathbf{A}}}$, that can be constructed using a weighted sum of N Kronecker products (rather than N^J). Also, instead of enumerating $\mathbf{A}_{\boldsymbol{r}} \otimes \mathbf{A}_{\boldsymbol{r}}$, we enumerate $\boldsymbol{\alpha}_{i_1,\tau_{j_1}} \otimes \boldsymbol{\alpha}_{i_2,\tau_{j_2}}$; cf. (6.15, 6.19), that is,

the matrix dimension decreases from $2^2J^2(N+1)^2$ to $2^2(N+1)^2$. Table 6.1 also shows the characteristics for $\tilde{\bar{\mathbf{A}}}$. Due to the fact that the eigenvalues of similar matrices are the same, the eigenvalues of matrix $\bar{\bar{\mathbf{A}}}$ are the same as the eigenvalues of matrix $\tilde{\bar{\mathbf{A}}}$. In particular, they are given by the eigenvalues of

$$\bar{\bar{\boldsymbol{\alpha}}}_{11} = \bar{\boldsymbol{\alpha}}_1 \otimes \bar{\boldsymbol{\alpha}}_1 \,, \tag{6.32}$$

each with multiplicity $J(J-1)$, and the eigenvalues of

$$\bar{\bar{\boldsymbol{\alpha}}}_{11} = \sum_{l=1}^{N} w_l \, \boldsymbol{\alpha}_{1,l} \otimes \boldsymbol{\alpha}_{1,l} \,, \tag{6.33}$$

each with multiplicity J; cf. (6.15).

Moreover, when plant stability of the second moment is concerned, plant stability of the mean dynamics must be guaranteed first. That is, all eigenvalues of matrix $\bar{\boldsymbol{\alpha}}_1$ lie inside the unit circle in the complex plane, which yields that the eigenvalues of matrix $\bar{\bar{\boldsymbol{\alpha}}}_{11}$ also lie inside the unit circle according to the properties of Kronecker product [198]. Thus, the plant stability condition of the second moment is simplified to assure that the eigenvalues of $\bar{\bar{\boldsymbol{\alpha}}}_{11}$ lie inside the unit circle. Notice that $\bar{\bar{\boldsymbol{\alpha}}}_{11}$ is the weighted sum of N Kronecker products of matrices with dimension $2^2(N+1)^2$ and that $\bar{\bar{\boldsymbol{\alpha}}}_{11}$ is independent of J, that is, the plant stability condition does not depend on the number of cars. Similar to the argument for mean dynamics, the plant stability boundaries of the second moment dynamics still depend on the parameters $(K_\mathrm{p}, K_\mathrm{v}, p, v_0^*, \Delta t)$.

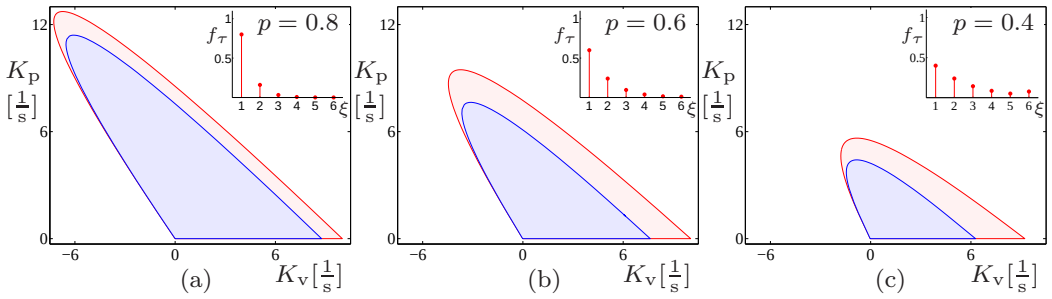

Figure 6.3: Plant stability diagrams for an open chain of $(J+1)$ vehicles in the $(K_\mathrm{v}, K_\mathrm{p})$-plane for different values of packet delivery ratio p. The corresponding delay distributions (5.2) are plotted on each panel as inlets.

Figure 6.3 shows the plant stability diagrams in the $(K_\mathrm{v}, K_\mathrm{p})$-plane for different packet delivery ratios. The inlets are the probability distributions of stochastic delay given by (5.2). The red curves correspond to plant stability boundaries for the mean dynamics. The regions enclosed by these curves, i.e., the union of the light red and light blue shaded regions, are

the mean plant stable regions. The blue curves correspond to plant stability boundaries for the second moment dynamics. The light blue shaded regions enclosed by them are the second moment plant stable regions. It can be seen that the difference between plant stability boundaries for the mean dynamics and second moment dynamics is increasing while the successful packet delivery ratio p decreases, i.e., the second moment dynamics play an important role when packet drops happen frequently in the V2V communication.

6.3.2 String Stability

In this part, we extend the notion presented in Chapter 5 to determine head-to-tail string stability for the mean and covariance dynamics of the open chain system using transfer functions. This allows us to evaluate disturbance attenuation along the open chain under stochastic delay variations. To test head-to-tail string stability, we use the periodic disturbances (6.6) for the head vehicle's velocity. Moreover, we use the Z transform of (6.22) to derive the amplification ratio and phase lag

$$\bar{M}(\omega) = \left|\bar{\Gamma}(\mathrm{e}^{\mathrm{j}\omega\Delta t})\right|, \quad \bar{\psi}(\omega) = \angle\bar{\Gamma}(\mathrm{e}^{\mathrm{j}\omega\Delta t}), \tag{6.34}$$

for the mean, where the transfer function is given by

$$\bar{\Gamma}(z) = \bar{\mathbf{C}}\big(z\,\bar{\mathbf{I}} - \bar{\mathbf{A}}\big)^{-1}\bar{\mathbf{B}}\bar{\mathbf{E}}, \tag{6.35}$$

and

$$\bar{\mathbf{E}} = \begin{bmatrix} 1 & \mathrm{j} \end{bmatrix}^{\mathrm{T}} \tag{6.36}$$

is used to sum up the effects of the two inputs. From (6.23), one may notice that $\bar{\mathbf{A}}$ is a block lower triangular matrix and $\bar{\mathbf{B}}$ has many zero elements. Thus, the calculation of transfer function of mean dynamics can be further simplified to the calculation of matrices with much lower dimensions using block matrix inverse [202]; see Appendix E.2. Such simplification is explained in detail in Appendix F.3.

The head-to-tail string stability condition for mean dynamics is given by

$$\sup_{\omega>0} \bar{M}(\omega) < 1\,. \tag{6.37}$$

We remark that $\bar{M}(\omega)$ also depends on the parameters $(K_{\mathrm{p}}, K_{\mathrm{v}}, p, v_0^*, \Delta t, J)$. Again we trace the stability boundaries using bisection method.

Figure 6.4 shows head-to-tail string stability diagrams for the mean dynamics in the $(K_{\mathrm{v}}, K_{\mathrm{p}})$-plane for different values of packet delivery ratio p and numbers of cars J. The

green curves correspond to the mean head-to-tail string stability boundaries, while the green shaded regions enclosed by them are the mean head-to-tail string stable regions. (The orange curves, and the orange shaded regions will be explained later.) Note that the mean head-to-tail string stable regions must be embedded in the corresponding mean plant stable regions because plant stability is the prerequisite for head-to-tail string stability. In each panel, the boundaries corresponding to $J = 3, 9, 15, 21, 27$, are plotted together such that the larger J is, the darker the green boundary is. However, the differences between different J-s are tiny and possibly caused by numerical errors. In other words, the mean head-to-tail string stability boundaries seem to be independent of the number of cars. Thus, the mean head-to-tail string stability condition for open chain systems with few number of cars gives a good estimate of that for the case with large number of cars.

To elaborate more on this, we use $\bar{M}(\omega;\, J)$ to spell out its dependence on the number of cars J. Suppose the amplification ratio of the mean dynamics from the head vehicle to the first vehicle is $\bar{M}(\omega;\, 1)$ where $\omega > 0$, then it can be used to approximate the amplification ratio from the j-th vehicle to the $(j+1)$-th vehicle if we neglect the difference between the perfect sinusoidal fluctuations in the head vehicle and triggered fluctuations in the j-th vehicle. This implies that

$$\bar{M}(\omega;\, J) \approx \bar{M}(\omega;\, 1)^J\,, \quad \omega > 0\,, \tag{6.38}$$

and the approximation of (6.37) becomes

$$\sup_{\omega>0}\ \bar{M}(\omega;\, 1)^J < 1 \quad \Longrightarrow \quad \sup_{\omega>0}\ \bar{M}(\omega;\, 1) < 1\,, \tag{6.39}$$

since the amplification ratio is positive. That is, the mean head-to-tail string stability is independent of the number of cars J.

In order to derive head-to-tail string stability conditions for the covariance dynamics (6.30), only the steady-state response to the sinusoidal input (6.5) is needed. However, the covariance dynamics (6.30) do not provide a direct input-output relationship as the mean dynamics (6.22) do, because the covariance dynamics (6.30) are nonlinear and also contain terms driven by the mean dynamics (6.22). To simplify the analysis, we assume that the mean dynamics are plant stable and already at steady state, that is,

$$\bar{X}(k) = \mathbf{Q}U(k)\,, \tag{6.40}$$

where $\mathbf{Q}$ satisfies

$$\mathbf{Q} - \bar{\mathbf{A}}\mathbf{Q}\mathbf{R} = \bar{\mathbf{B}}\mathbf{R}\,, \tag{6.41}$$

which can be obtained by substituting equation (6.40) into mean dynamics (6.22) and using the property (2.15).

Substituting (6.40) into (6.30) yields the simplified covariance dynamics

$$\begin{aligned} \bar{\bar{X}}(k+1) &= \bar{\bar{\mathbf{A}}}\bar{\bar{X}}(k) + \bar{\bar{\mathbf{B}}}\bar{\bar{U}}(k)\,, \\ \bar{\bar{Y}}(k) &= \bar{\bar{\mathbf{C}}}\bar{\bar{X}}(k)\,, \end{aligned} \tag{6.42}$$

where

$$\bar{\bar{U}}(k) = U(k) \otimes U(k)\,, \tag{6.43}$$

and $\bar{\bar{\mathbf{A}}}$ and $\bar{\bar{\mathbf{C}}}$ are given in (6.31), while

$$\bar{\bar{\mathbf{B}}} = \bar{\bar{\mathbf{K}}}_1(\mathbf{Q} \otimes \mathbf{Q}) + \bar{\bar{\mathbf{K}}}_2(\mathbf{Q} \otimes \mathbf{I}) + \bar{\bar{\mathbf{K}}}_3(\mathbf{I} \otimes \mathbf{Q}) + \bar{\bar{\mathbf{K}}}_4\,. \tag{6.44}$$

Similar to $\bar{\bar{\mathbf{A}}}$, the matrices $\bar{\bar{\mathbf{K}}}_1$, $\bar{\bar{\mathbf{K}}}_2$, $\bar{\bar{\mathbf{K}}}_3$ and $\bar{\bar{\mathbf{K}}}_4$ are difficult to construct due to enormous enumeration of possibilities and huge sizes. Therefore, decomposition based on block matrix calculation of Kronecker product and perfect shuffle are used to simplify the calculations; see Appendix F.2 for more details.

Recall that $\bar{Y}(k) = \mathbb{E}[\tilde{v}_J(k)] \in \mathbb{R}$ and $\bar{\bar{Y}}(k) = \mathbb{E}[\tilde{v}_J^2(k)] - \mathbb{E}[\tilde{v}_J(k)]^2 \in \mathbb{R}$ are the mean and variance of the velocity $\tilde{v}_J(k)$ of the tail vehicle. If we define

$$\mu = \bar{Y}_{\mathrm{ss}}(k)\,, \qquad\qquad \sigma^2 = \bar{\bar{Y}}_{\mathrm{ss}}(k)\,, \tag{6.45}$$

as the mean and variance of $\tilde{v}_J(k)$ at steady state, respectively, then the following definition can be proposed to extend the notion of $n\sigma$ string stability in Chapter 5.

Definition 6.1 *The system is $n\sigma$ head-to-tail string stable if the amplitude v_0^{amp} of the input is attenuated such that $|\mu \pm n\sigma| < v_0^{\mathrm{amp}}$.*

Note that when $n = 0$, the $n\sigma$ head-to-tail string stability condition gives the mean head-to-tail string stability condition. As n is increased, $n\sigma$ head-to-tail string stability condition gets stronger since fewer trajectories are allowed to be outside the interval $[\mu - n\sigma, \mu + n\sigma]$. Thus, the $n\sigma$ head-to-tail string stability with $n \geq 1$ implies that the mean head-to-tail string stability is satisfied. Also, we remark that the natural choice of n is $n = 1$. In Section 7.3 we will use stability diagrams to demonstrate that 1σ head-to-tail string stability of the open chain system is analogous to the second moment stability of the closed ring system.

From linear system theory, the steady state of the mean value is

$$\mu = v_0^{\mathrm{amp}} \bar{M}(\omega) \sin\left(k\omega\Delta t + \bar{\psi}(\omega)\right), \tag{6.46}$$

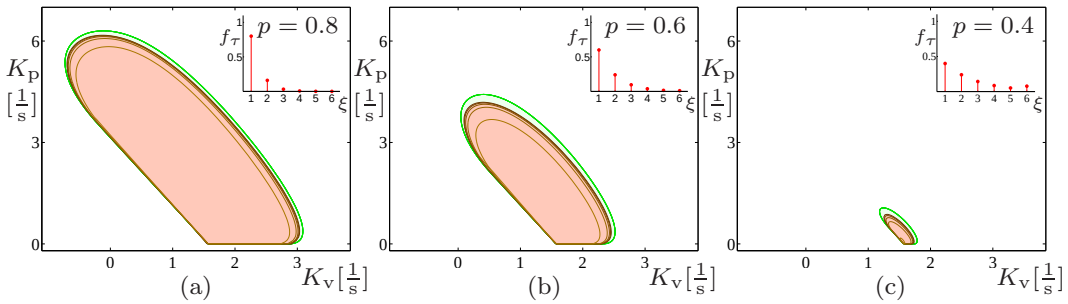

Figure 6.4: Mean head-to-tail string stability and 1σ head-to-tail string stability diagrams for an open chain of $(J+1)$ vehicles in the $(K_\mathrm{v}, K_\mathrm{p})$-plane for different values of packet delivery ratio p. Each panel plots all the boundaries for mean head-to-tail string stability corresponding to $J = 3, 9, 15, 21, 27$ from light green to dark green curves, and 1σ head-to-tail string stability corresponding to $J = 3, 9, 15, 21, 27$ from light orange to dark orange curves, respectively.

cf. (6.34). The steady state of the variance can be obtained similarly as that in Chapter 5. By substituting the input (6.7) into (6.43), one may notice that the input $\bar{\bar{U}}(k)$ can be separated into a constant part and a harmonic excitation part, i.e.,

$$\bar{\bar{U}}(k) = \bar{\bar{U}}_0 + \bar{\bar{U}}_1(k)\,, \tag{6.47}$$

where

$$\bar{\bar{U}}_0 = \frac{1}{2}\big(v_0^{\mathrm{amp}}\big)^2 \bar{\bar{u}}_0\,, \quad \bar{\bar{U}}_1(k) = \frac{1}{2}\big(v_0^{\mathrm{amp}}\big)^2 \bar{\bar{u}}_1(k)\,, \tag{6.48}$$

and

$$\bar{\bar{u}}_0 = \begin{bmatrix} 1 \\ 0 \\ 0 \\ 1 \end{bmatrix}\,, \quad \bar{\bar{u}}_1(k) = \begin{bmatrix} -\cos(2k\omega\Delta t) \\ \sin(2k\omega\Delta t) \\ \sin(2k\omega\Delta t) \\ \cos(2k\omega\Delta t) \end{bmatrix}\,. \tag{6.49}$$

According to the superposition principle, the particular solution of the linear system (6.42) is the sum of particular solution $\bar{\bar{Y}}_0$ to $\bar{\bar{U}}_0$ and particular solution $\bar{\bar{Y}}_1(k)$ to $\bar{\bar{U}}_1(k)$. For input $\bar{\bar{U}}_0$, the response of the system (6.42) is given by

$$\bar{\bar{Y}}_0 = \big(v_0^{\mathrm{amp}}\big)^2 \bar{\bar{M}}_0(\omega)\,, \tag{6.50}$$

with

$$\bar{\bar{M}}_0(\omega) = \frac{1}{2}\bar{\bar{\mathbf{C}}}\big(\bar{\bar{\mathbf{I}}} - \bar{\bar{\mathbf{A}}}\big)^{-1}\bar{\bar{\mathbf{B}}}\bar{\bar{u}}_0\,. \tag{6.51}$$

We remark that $\bar{\bar{M}}_0(\omega)$ depends on ω because matrix $\bar{\bar{\mathbf{B}}}$ depends on ω; cf. (6.10, 6.24, 6.23,

6.31, 6.44). For $\bar{\bar{U}}_1(k)$, similar to the mean dynamics, taking the Z transform of (6.42) and summing the contributions of each individual inputs of $\bar{\bar{u}}_1(k)$ in (6.49), we obtain the corresponding steady-state output

$$\bar{\bar{Y}}_{1,\mathrm{ss}}(k) = \left(v_0^{\mathrm{amp}}\right)^2 \bar{\bar{M}}_1(\omega) \sin\left(2k\omega\Delta t + \bar{\bar{\psi}}(\omega)\right). \tag{6.52}$$

Here, the amplification ratio and phase lag are

$$\bar{\bar{M}}_1(\omega) = \left|\bar{\bar{\Gamma}}(\mathrm{e}^{\mathrm{j}\omega\Delta t})\right|, \qquad \bar{\bar{\psi}}(\omega) = \angle\bar{\bar{\Gamma}}(\mathrm{e}^{\mathrm{j}\omega\Delta t}), \tag{6.53}$$

where

$$\bar{\bar{\Gamma}}(z) = \frac{1}{2}\bar{\bar{\mathbf{C}}}\left(z\,\bar{\bar{\mathbf{I}}} - \bar{\bar{\mathbf{A}}}\right)^{-1}\bar{\bar{\mathbf{B}}}\bar{\bar{\mathbf{E}}}, \tag{6.54}$$

and

$$\bar{\bar{\mathbf{E}}} = \begin{bmatrix} -\mathrm{j} & 1 & 1 & \mathrm{j} \end{bmatrix}^{\mathrm{T}}. \tag{6.55}$$

Therefore, the superposition principle yields that the steady-state response to (6.47) is

$$\sigma^2 = \bar{\bar{Y}}_0 + \bar{\bar{Y}}_{1,\mathrm{ss}}(k) = \left(v_0^{\mathrm{amp}}\right)^2 \left(\bar{\bar{M}}_0(\omega) + \bar{\bar{M}}_1(\omega) \sin\left(2k\omega\Delta t + \bar{\bar{\psi}}(\omega)\right)\right). \tag{6.56}$$

The non-negativity of the variance yields that $\bar{\bar{M}}_0(\omega) \geq \bar{\bar{M}}_1(\omega)$. Hitherto we can calculate

$$\begin{aligned} \mu \pm n\sigma = v_0^{\mathrm{amp}} \Big[& \bar{M}(\omega) \sin\left(k\omega\Delta t + \bar{\psi}(\omega)\right) \\ & \pm n\sqrt{\bar{\bar{M}}_0(\omega) + \bar{\bar{M}}_1(\omega) \sin\left(2k\omega\Delta t + \bar{\bar{\psi}}(\omega)\right)} \Big], \end{aligned} \tag{6.57}$$

which is a periodic function with period $T = 2\pi/(\omega\Delta t)$. Thus, the total amplification ratio becomes

$$\begin{aligned} \bar{\bar{M}}(\omega) = \max_{0\leq k\leq T} \Big\{ \Big| & \bar{M}(\omega) \sin\left(k\omega\Delta t + \bar{\psi}(\omega)\right) \\ & \pm n\sqrt{\bar{\bar{M}}_0(\omega) + \bar{\bar{M}}_1(\omega) \sin\left(2k\omega\Delta t + \bar{\bar{\psi}}(\omega)\right)} \Big| \Big\}, \end{aligned} \tag{6.58}$$

and the condition for $n\sigma$ head-to-tail string stability is given by

$$\sup_{\omega>0} \bar{\bar{M}}(\omega) < 1. \tag{6.59}$$

Again we remark that $\bar{\bar{M}}_0(\omega)$, $\bar{\bar{M}}_1(\omega)$ and $\bar{\bar{M}}(\omega)$ depend on the parameters (K_{p}, K_{v}, p, v_0^*, Δt, J). The corresponding boundaries can be found numerically by the bisection method.

Figure 6.4 also shows the 1σ head-to-tail string stability diagrams in the $(K_{\rm v}, K_{\rm p})$-plane for different values of packet delivery ratio p and number of cars J. The orange curves correspond to the 1σ head-to-tail string stability boundaries for an open chain of different number of cars such that the larger J is, the darker the orange boundary is. The light orange shaded regions are the 1σ head-to-tail string stable regions for an open chain of $J = 27$ cars. Indeed, the 1σ head-to-tail string stable regions are embedded in the corresponding covariance plant stable regions. Figure 6.4 illustrates that the 1σ head-to-tail string stable regions expand as the number of vehicles J increases. Also, the 1σ head-to-tail string stable region converges to a limit as the number of vehicles J goes to infinity. Since this limit cannot be obtained explicitly, we use $J = 27$ which is the largest number of vehicles that we can compute the 1σ head-to-tail string stable domains. We remark that similar results can be obtained for $n\sigma$ head-to-tail string stability when $n \neq 1$.

To better understand the above phenomena, we investigate the dependence of $\bar{\bar{M}}_0(\omega;\, J)$, $\bar{\bar{M}}_1(\omega;\, J)$ and $\bar{\bar{M}}(\omega;\, J)$ on the number of cars J. Similar to the argument made for the amplification ratio $\bar{M}(\omega;\, J)$ of the mean dynamics (cf. (6.38)), $\bar{\bar{M}}_1(\omega;\, J)$ can also be approximated by

$$\bar{\bar{M}}_1(\omega;\, J) \approx \bar{\bar{M}}_1(\omega;\, 1)^J\,, \quad \omega > 0\,, \tag{6.60}$$

where $\bar{\bar{M}}_1(\omega;\, 1)^J$ is the amplification ratio of the harmonic fluctuation in the covariance dynamics from the head vehicle to the first vehicle. When $n\sigma$ head-to-tail string stability with $n \geq 1$ is considered, mean head-to-tail string stability condition (6.37) is the minimum requirement. One can check numerically that

$$\bar{\bar{M}}_1(\omega;\, J) < 1\,, \quad \omega > 0, \tag{6.61}$$

is always satisfied when mean head-to-tail string stability condition holds. Thus, as the number of cars J increases, $\bar{M}(\omega;\, J)$ and $\bar{\bar{M}}_1(\omega;\, J)$ decrease exponentially when mean head-to-tail string stability condition (6.37) holds; cf. (6.38, 6.60). In other words, the $n\sigma$ head-to-tail string stable condition (6.59) gets weaker as J increases, resulting in the expansion of $n\sigma$ head-to-tail string stable regions.

However, $\bar{\bar{M}}_0(\omega;\, J)$ cannot be approximated in the similar way as (6.38, 6.60). Indeed, this constant excitation "propagates along the chain" and becomes the leading part of (6.58) when (6.37) is satisfied and J is sufficiently large. Therefore, we have the following weaker conditions for 1σ head-to-tail string stability.

Definition 6.2 *The system is $n\sigma$ offset head-to-tail string stable if the amplitude $v_0^{\rm amp}$ of*

the input is attenuated such that

$$\sup_{\omega>0} \bar{M}(\omega) < 1, \quad \sup_{\omega>0} \bar{\bar{M}}_0(\omega) < \frac{1}{n^2}. \tag{6.62}$$

Note that the condition above provides an easier way to check head-to-tail string stability. According to the exponential decaying property in $\bar{M}(\omega;\, J)$ and $\bar{\bar{M}}_1(\omega;\, J)$, we have the following proposition.

Proposition 6.1 *As the number of cars J in the open chain increases, $n\sigma$ head-to-tail string stability and $n\sigma$ offset head-to-tail string stability approximate each other. Moreover, they converge to the same limit as J goes to infinity.*

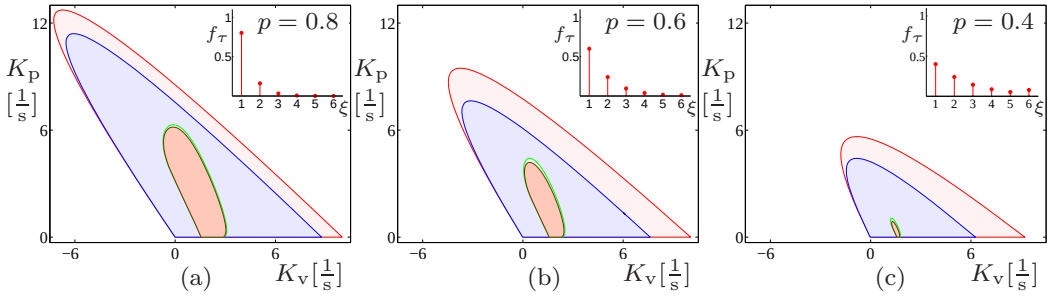

Figure 6.5: Stability diagrams for an open chain of $(27+1)$ vehicles in the $(K_{\mathrm{v}}, K_{\mathrm{p}})$-plane for different values of packet delivery ratio p. Red, blue, green and orange curves represent boundaries for mean plant stability, second moment plant stability, mean head-to-tail string stability and 1σ head-to-tail string stability, respectively, while the light red, light blue, light green and light orange shaded regions represent the corresponding stability regions.

Figure 6.5 summarizes the stability diagrams in the $(K_{\mathrm{v}}, K_{\mathrm{p}})$-plane for different values of packet delivery ratio p when $J = 27$. The same color scheme is used as those in Figures 6.3 and 6.4. The mean head-to-tail string stable regions and the 1σ head-to-tail string stable regions are embedded in the corresponding plant stable regions as discussed above. For plant stability, as the packet delivery ratio p decreases, both the mean and covariance plant stable regions shrink, and the differences between them increase. Similar behavior can be observed for the mean head-to-tail string stable and 1σ head-to-tail string stable regions. Figure 6.5 also demonstrates that the mean head-to-tail string stability can be used as a reasonable estimate for the 1σ head-to-tail string stability when the open chain is sufficiently long.

6.4 Summary

In this chapter, we analyzed the dynamics of an open chain of connected vehicles. We showed that packet drops lead to stochastic delay variations, and we derived the mean, second moment, and covariance dynamics to characterize the dynamics in the vicinity of the uniform flow equilibrium. We established novel decomposition techniques that allowed us to significantly simplify the eigenvalue problems when analyzing stability.

Plant stability and $n\sigma$ head-to-tail string stability results were illustrated using stability diagrams on the plane of gain parameters while varying the packet delivery ratio and the number of vehicles. It was found that both the mean and the second moment plant stability are independent of the number of vehicles in the system. The mean head-to-tail string stability has a very weak dependence on the number of vehicles while the 1σ head-to-tail string stable region expands as the number of vehicles increases. Our results demonstrated that for large numbers of vehicles and sufficiently large packet delivery ratio the mean head-to-tail string stability can be used as a reasonable estimate for the 1σ head-to-tail string stability.

Our results illustrate the feasibility of using connected vehicles to change the large-scale dynamics of transportation systems in the presence of packet drops and provide the necessary mathematical tools to design connectivity-based controllers that can ensure smooth traffic flow.

CHAPTER 7

Stochastic Packet Drops in Closed Ring Systems

In some cases, it may be difficult to use a large open chain system to replicate some traffic phenomena which only appear occasionally. For example, the phantom stop-and-go traffic jams only happen for a string unstable open chain system of large scale when the head vehicle introduces some perturbations. However, this traffic jam will propagate upstream and finally "disappear". Therefore, researchers [123, 128] resort to closed ring vehicle systems as shown in Figure 7.1 that allows to observe such phenomena as sustained oscillations. However, this has only been achieved for deterministic systems in continuous-time domain. In this chapter, we consider a closed ring system of predecessor-followers with stochastic delays and derive the evolution for the mean and second moment dynamics to evaluate the stability properties. The material discussed in this section can be found in [196].

7.1 Dynamics

Assuming that all vehicles on the closed ring in Figure 7.1 are described by the equations (5.4, 5.5), we can obtain the dynamics for the overall system

$$\begin{aligned} \dot{h}_1(t) &= v_J(t) - v_1(t)\,, \\ \dot{v}_1(t) &= u_1(t_{k-\tau_1(k)})\,, \\ \dot{h}_j(t) &= v_{j-1}(t) - v_j(t)\,, \\ \dot{v}_j(t) &= u_j(t_{k-\tau_j(k)})\,, \qquad\qquad j = 2\,,\,\ldots\,,\,J\,, \end{aligned} \tag{7.1}$$

for $t_k \leq t < t_{k+1}$. Using the fact that $u_j(t_{k-\tau_j})$ is a constant in the time interval $t \in [t_k,\, t_{k+1})$, one can solve the differential equation (7.1) directly with initial values $h_j(t_k)$,

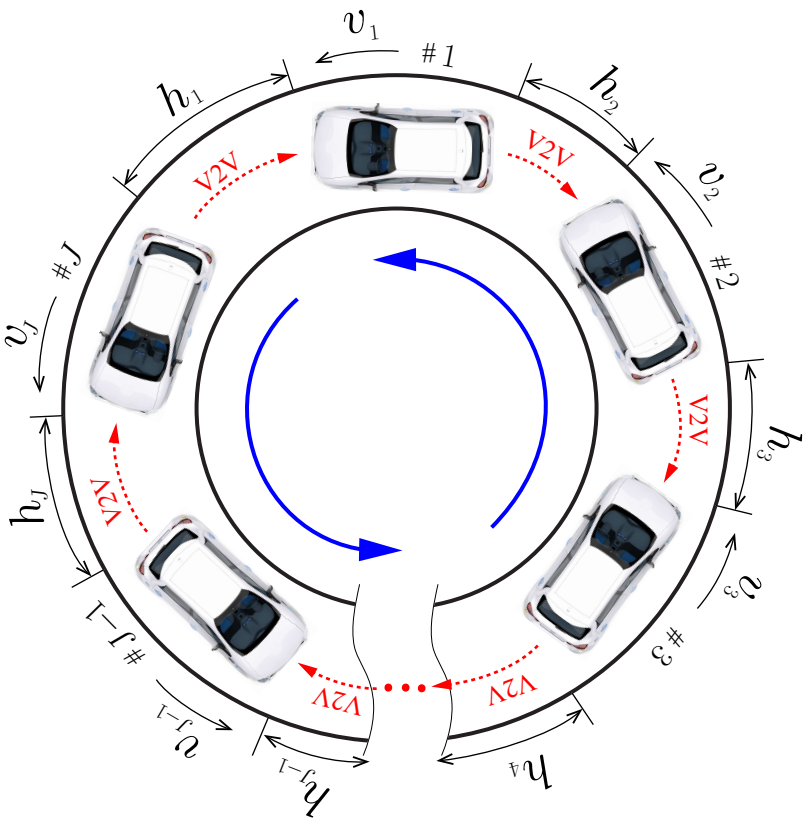

Figure 7.1: A closed ring of J connected vehicles on a single lane. Dashed red arrows indicate the information flow through wireless communication, while the solid blue arrows indicate the direction of traffic flow.

$v_j(t_k)$, yielding the discrete-time nonlinear map

$$\begin{aligned}
h_1(t_{k+1}) &= h_1(t_k) + \big(v_J(t_k) - v_1(t_k)\big)\Delta t + \frac{1}{2}\big(u_J(t_{k-\tau_J}) - u_1(t_{k-\tau_1})\big)\Delta t^2\,,\\
v_1(t_{k+1}) &= v_1(t_k) + u_1(t_{k-\tau_1})\Delta t\,,\\
h_j(t_{k+1}) &= h_j(t_k) + \big(v_{j-1}(t_k) - v_j(t_k)\big)\Delta t + \frac{1}{2}\big(u_{j-1}(t_{k-\tau_{j-1}}) - u_j(t_{k-\tau_j})\big)\Delta t^2\,,\\
v_j(t_{k+1}) &= v_j(t_k) + u_j(t_{k-\tau_j})\Delta t\,, \qquad\qquad j = 2\,,\,\ldots\,,\,J\,.
\end{aligned} \tag{7.2}$$

The uniform flow equilibrium is achieved when all the vehicles reach the same velocity and distance headway given in (6.4). Recall that for the open chain, the head vehicle determines the equilibrium velocity and (6.4) is used to devise the equilibrium distance headway; while for the closed ring, the length of the road and the number of cars determine the equilibrium distance headway and (6.4) is used to obtain the equilibrium velocity.

Following the same process as we discussed in Chapter 6 for open chain systems, we

can define perturbations, states and augmented states as (6.5, 6.7, 6.11, 6.16), and obtain the stochastic dynamics

$$X(k+1) = \mathbf{A}^{\mathrm{R}}_{\boldsymbol{\tau}} X(k)\,, \tag{7.3}$$

where the possible values for $\mathbf{A}^{\mathrm{R}}_{\boldsymbol{\tau}}$ are

$$\mathbf{A}^{\mathrm{R}}_{\boldsymbol{r}} = \begin{bmatrix} \boldsymbol{\alpha}_{1,r_1} & & & & \boldsymbol{\alpha}_{4,r_J} & \boldsymbol{\alpha}_{3,r_J} + \boldsymbol{\alpha}_{2,r_1} \\ \boldsymbol{\alpha}_{3,r_1} + \boldsymbol{\alpha}_{2,r_2} & \boldsymbol{\alpha}_{1,r_2} & & & & \boldsymbol{\alpha}_{4,r_1} \\ \boldsymbol{\alpha}_{4,r_2} & \boldsymbol{\alpha}_{3,r_2} + \boldsymbol{\alpha}_{2,r_3} & \boldsymbol{\alpha}_{1,r_3} & & & \\ & \ddots & \ddots & \ddots & & \\ & & \boldsymbol{\alpha}_{4,r_{j-1}} & \boldsymbol{\alpha}_{3,r_{J-1}} + \boldsymbol{\alpha}_{2,r_J} & & \boldsymbol{\alpha}_{1,r_J} \end{bmatrix}, \tag{7.4}$$

for $r_j = 1\,,\, 2\,,\, \cdots\,,\, N$, and $j = 1\,,\, 2\,,\, \ldots\,,\, J$. The matrices $\boldsymbol{\alpha}_{1,r_1}\,,\ \boldsymbol{\alpha}_{2,r_1}\,,\ \boldsymbol{\alpha}_{3,r_1}\,,\ \boldsymbol{\alpha}_{4,r_1}$ are given in (6.15).

With the IID assumption for the delays and the definition of the deterministic variable $\bar{X}(k)$ in (6.21), one can derive the equation for the mean dynamics

$$\bar{X}(k+1) = \bar{\mathbf{A}}^{\mathrm{R}}\, \bar{X}(k)\,, \tag{7.5}$$

by taking expectations of both sides in (7.3), where

$$\bar{\mathbf{A}}^{\mathrm{R}} = \sum_{\boldsymbol{r}=1}^{N} w_{\boldsymbol{r}} \mathbf{A}^{\mathrm{R}}_{\boldsymbol{r}} = \begin{bmatrix} \bar{\boldsymbol{\alpha}}_1 & & & \bar{\boldsymbol{\alpha}}_4 & \bar{\boldsymbol{\alpha}}_3 + \bar{\boldsymbol{\alpha}}_2 \\ \bar{\boldsymbol{\alpha}}_3 + \bar{\boldsymbol{\alpha}}_2 & \bar{\boldsymbol{\alpha}}_1 & & & \bar{\boldsymbol{\alpha}}_4 \\ \bar{\boldsymbol{\alpha}}_4 & \bar{\boldsymbol{\alpha}}_3 + \bar{\boldsymbol{\alpha}}_2 & \bar{\boldsymbol{\alpha}}_1 & & \\ & \ddots & \ddots & \ddots & \\ & & \bar{\boldsymbol{\alpha}}_4 & \bar{\boldsymbol{\alpha}}_3 + \bar{\boldsymbol{\alpha}}_2 & \bar{\boldsymbol{\alpha}}_1 \end{bmatrix}, \tag{7.6}$$

cf. (6.24).

Similarly, using the definition of the variable $\hat{\bar{X}}(k)$ in (6.26), one can obtain the second moment dynamics

$$\hat{\bar{X}}(k+1) = \bar{\bar{\mathbf{A}}}^{\mathrm{R}} \hat{\bar{X}}(k)\,, \tag{7.7}$$

where

$$\bar{\bar{\mathbf{A}}}^{\mathrm{R}} = \sum_{\boldsymbol{r}=1}^{N} w_{\boldsymbol{r}} \mathbf{A}_{\boldsymbol{r}}^{\mathrm{R}} \otimes \mathbf{A}_{\boldsymbol{r}}^{\mathrm{R}} \,. \tag{7.8}$$

We remark that the covariance dynamics can also be obtained for the closed ring system. However, it is not needed for stability analysis.

7.2 Stability

In this section, we investigate the stability of the mean dynamics (7.5) and the second moment dynamics (7.7) of the closed ring system shown in Figure 7.1, following the method discussed in the case of open chain systems, in order to find the relationship between two different systems in the stochastic sense in discrete-time domain. We also provide a detailed explanation on this relationship for deterministic systems in Appendix C; see also [128].

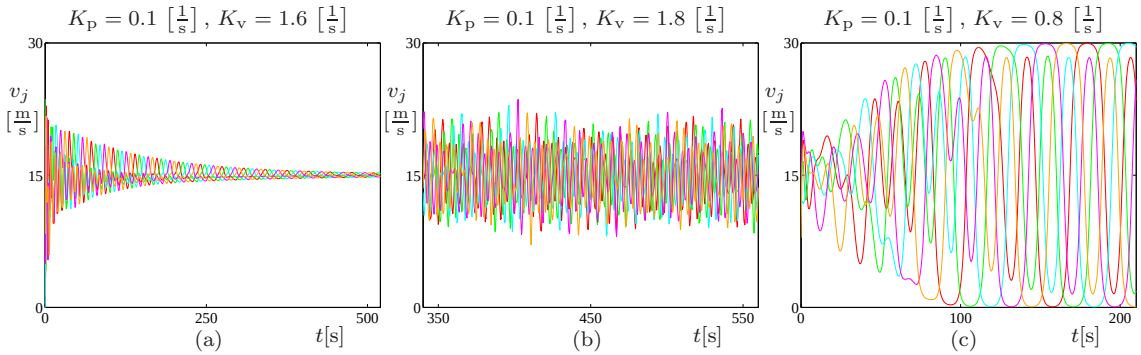

Figure 7.2: Simulations of a closed ring of 55 vehicles for different $(K_{\mathrm{v}},K_{\mathrm{p}})$ gains as indicated. The red, green, cyan, magenta and orange curves represent the velocities v_{11}, v_{22}, v_{33}, v_{44}, v_{55}, respectively. (a) Stable. (b) Unstable. (c) Unstable.

To demonstrate stability, Figure 7.2 shows three simulation results for a closed ring of 55 vehicles for different $(K_{\mathrm{v}},K_{\mathrm{p}})$ gains when the packet delivery ratio $p = 0.4$. The other parameters are the same as in Figure 6.1. Again only the velocities of every 11-th vehicle are plotted. Figure 7.2(a) shows a case when the equilibrium is stable. It can be seen that the velocities approach the desired equilibrium velocity despite the initial perturbations and stochastic packet drops. In this sense, this realization for the stochastic closed ring system is stable. However, similar to the argument for the open chain system, to check whether this pair of $(K_{\mathrm{v}},K_{\mathrm{p}})$ gains is stable in the stochastic sense, one has to investigate all possible realizations. Figure 7.2(b, c) show two different scenarios when the equilibrium

is unstable. In Figure 7.2(b), the vehicles are unable to settle down to the desired velocity and keep oscillating around it due to the stochastic packet drops. Such oscillations could deteriorate fuel economy and driving comfort. However, more severe oscillations occur in Figure 7.2(c), where the stop-and-go traffic jams develop. The goal of the controller design is to eliminate such behaviors by ensuring stability of the uniform flow equilibrium.

For stability of the mean dynamics (7.5), all eigenvalues of matrix $\bar{\mathbf{A}}^{\mathrm{R}}$ must lie within the unit circle in the complex plane. Notice that $\bar{\mathbf{A}}^{\mathrm{R}}$ (cf. (7.6)) is a banded block circulant matrix [199,203], so it is unitarily similar to a block diagonal complex matrix with diagonal blocks

$$\bar{\mathbf{\Lambda}}_i = \bar{\boldsymbol{\alpha}}_1 + \bar{\boldsymbol{\alpha}}_4 \mathrm{e}^{-\mathrm{j}\frac{2\pi}{J}2(i-1)} + (\bar{\boldsymbol{\alpha}}_2 + \bar{\boldsymbol{\alpha}}_3)\mathrm{e}^{-\mathrm{j}\frac{2\pi}{J}(i-1)} \in \mathbb{C}^{2(N+1)\times 2(N+1)}, \tag{7.9}$$

for $i = 1, \ldots, J$; cf. (6.24). This can be obtained by using a transformation matrix that is the Kronecker product of the J-dimensional Fourier matrix [199] and the $2(N+1)$-dimensional identity matrix. In order to assure the mean stability, the eigenvalues of matrices must lie within the unit circle in the complex plane. Notice that $\bar{\mathbf{A}}^{\mathrm{R}}$ is of dimension $2J(N+1)$, but $\bar{\mathbf{\Lambda}}_i$ is of dimension $2(N+1)$. Also, let us define

$$\theta = \mathrm{e}^{\mathrm{j}\frac{2\pi}{J}(i-1)}, \tag{7.10}$$

for $i = 1, \ldots, J$ to denote the J-th roots of unity. For $J \to \infty$, θ can take all the values on the unit circle in the complex plane. Thus, (7.9) yields the stability condition for the mean dynamics of the infinitely long ring with infinitely many vehicles is that all eigenvalues of matrix

$$\bar{\mathbf{\Lambda}}_\theta = \bar{\boldsymbol{\alpha}}_1 + \bar{\boldsymbol{\alpha}}_4 \mathrm{e}^{-2\mathrm{j}\theta} + (\bar{\boldsymbol{\alpha}}_2 + \bar{\boldsymbol{\alpha}}_3)\mathrm{e}^{-\mathrm{j}\theta} \in \mathbb{C}^{2(N+1)\times 2(N+1)}, \tag{7.11}$$

must lie within the unit circle in the complex plane for $0 \leq \theta \leq \pi$. Here, we utilized the fact that the eigenvalues of a real matrix appear as conjugate pairs. We emphasize that the limit $J \to \infty$ is taken such that h^* is kept constant.

Figure 7.3 shows the mean stability diagrams of the closed ring system in the $(K_{\mathrm{v}},K_{\mathrm{p}})$-plane for different values of packet delivery ratio p and numbers of vehicles J. The solid cyan curves correspond to mean stability boundaries for the closed ring of $J = 3, 9, 15, 21, 27$ vehicles such that the darker the color is, the larger J is. The regions enclosed by these curves are the mean stable regions. As the number of vehicles J increases, the mean stable regions converge to the corresponding mean stable regions of the closed ring system of infinitely many vehicles. The limit mean stable boundaries are represented

by the dashed cyan curves, and the corresponding mean stable regions are shown as light cyan shaded regions. We remark that as the number of vehicles in the closed ring increases, the mean stable regions shrink, but the mean stable conditions for a closed ring of J_1 cars is neither a necessary nor a sufficient condition for that of J_2 cars when $J_1 \leq J_2$.

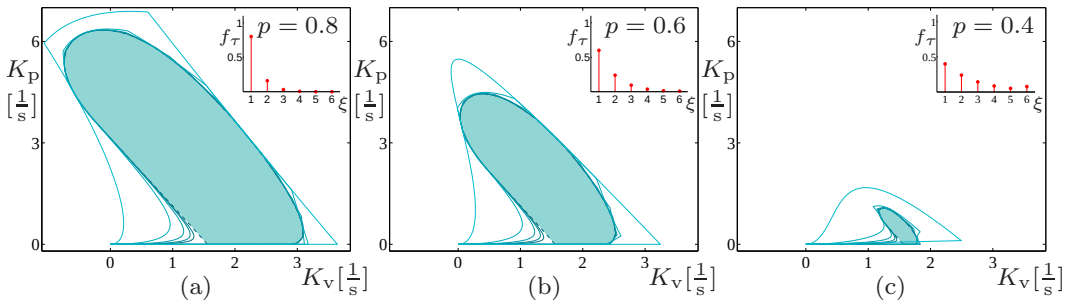

Figure 7.3: Mean stability diagrams for a closed ring of J vehicles in the $(K_{\mathrm{v}},K_{\mathrm{p}})$-plane for different values of packet delivery ratio p. The cyan curves represent stability boundaries. Each panel shows the boundaries corresponding to $J = 3, 9, 15, 21, 27$ from light cyan to dark cyan curves.

Similarly, to ensure stability of the second moment dynamics (7.7) for the closed ring, all eigenvalues of matrix $\bar{\bar{\mathbf{A}}}^{\mathrm{R}}$ must lie within the unit circle in the complex plane. Again we are faced with the same issues as in the case of the open chain, i.e., an enormous enumeration of high dimensional matrices $\mathbf{A}_{\boldsymbol{r}}^{\mathrm{R}} \otimes \mathbf{A}_{\boldsymbol{r}}^{\mathrm{R}}$ while constructing $\bar{\bar{\mathbf{A}}}^{\mathrm{R}}$, as well as frequent eigenvalue calculations for this high dimensional matrix while varying parameters. As laid out in Appendix G, by applying properties of Kronecker product and using perfect shuffles, the matrix $\bar{\bar{\mathbf{A}}}^{\mathrm{R}}$ can be transformed into a block circulant matrix $\hat{\bar{\mathbf{A}}}^{\mathrm{R}}$, and only weighted sums of N lower dimensional matrices are needed. This block circulant real matrix $\hat{\bar{\mathbf{A}}}^{\mathrm{R}}$ is unitarily similar to a block diagonal complex matrix with diagonal blocks

$$\bar{\bar{\mathbf{\Lambda}}}_i \in \mathbb{C}^{2^2 J(N+1)^2 \times 2^2 J(N+1)^2}\,, \tag{7.12}$$

for $j = 1\,, \ldots\,, J$, which are not shown here explicitly due to the complexity, but can be found in Appendix G. Thus, to assure the second moment stability of the closed ring, we need to make sure that all eigenvalues of matrices $\bar{\bar{\mathbf{\Lambda}}}_i$, lie within the unit circle in the complex plane. Here, we remark that $\bar{\bar{\mathbf{\Lambda}}}_i$ is a perturbed block penta-circulant matrix, but the perturbed block elements caused by vehicular connectivity prevent us from further simplifications. If one can succeed in reducing this eigenvalue problem of $\bar{\bar{\mathbf{\Lambda}}}_i$ to the eigenvalue problem of matrices of even lower dimension, possibly $2^2(N+1)^2$, then for the closed ring system of infinitely many vehicles, the stability condition for the second moment dynamics

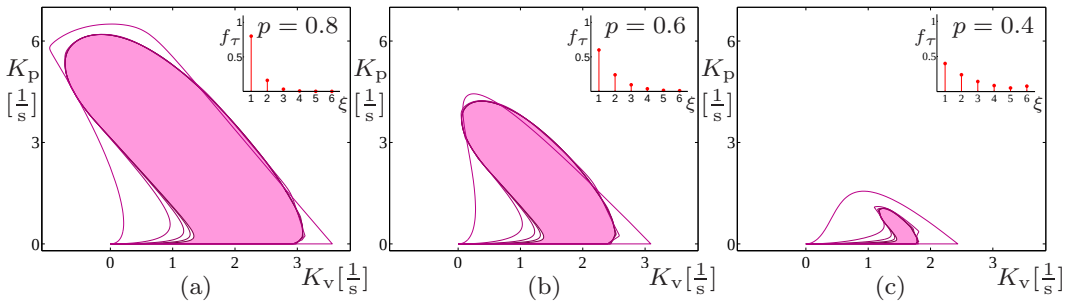

Figure 7.4: Second moment stability diagrams for a closed ring of J vehicles in the $(K_{\mathrm{v}},K_{\mathrm{p}})$-plane for different values of packet delivery ratio p. Each panel shows all the boundaries corresponding to $J = 3, 9, 15, 21, 27$ from light purple to dark purple curves.

can be obtained in the same way as that for the mean dynamics; cf. (7.11).

Figure 7.4 shows the stability diagrams of the second moment dynamics in the $(K_{\mathrm{v}},K_{\mathrm{p}})$-plane for different values of packet delivery ratio p and numbers of cars J. The purple curves correspond to the second moment stability boundaries for the closed ring of J =3, 9, 15, 21, 27 vehicles so that the darker the purple color is, the larger J is. Similar to the mean dynamics, as the number of vehicles J increases, the second moment stable region converges to a limit. However, this limit is hard to obtain due to the aforementioned perturbed terms in $\bar{\bar{\mathbf{\Lambda}}}_i$. Therefore, we use $J = 27$ to approximate this limit which is the largest number we can compute the second moment stable domain. The corresponding second moment stable regions are shaded with purple color in Figure 7.4. Again, as the number of vehicles increases, the second moment stable regions shrink in a similar way as the mean stable regions do.

To highlight the difference between mean stability and second moment stability, Figure 7.5 shows the stability diagrams in the $(K_{\mathrm{v}},K_{\mathrm{p}})$-plane for different values of packet delivery ratio p when $J = 27$. The same color scheme is used as those in Figures 7.3 and 7.4. The second moment stable regions are embedded in the corresponding mean stable regions as discussed before. As the packet delivery ratio p decreases, both the mean and second moment stable regions shrink. Figure 7.5 demonstrates that the mean stability can be used as a reasonable estimate for the second moment stability of the closed ring system when the packet delivery ratio p is sufficiently large.

7.3 Comparing Open Chain and Closed Ring Results

In this section, we compare the stability results of the open chain and closed ring (cf. Figure 1.1(a) and Figure 7.1) in the presence of stochastic delays, where all the vehicles

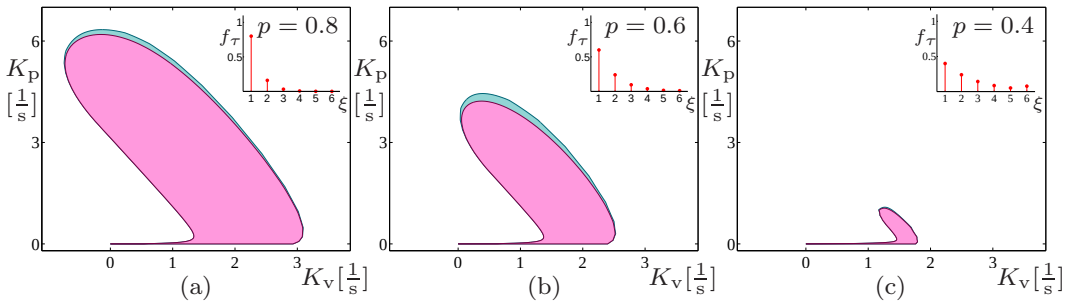

Figure 7.5: Mean and second moment stability diagrams for a closed ring of 27 vehicles in the $(K_\mathrm{v},K_\mathrm{p})$-plane for different values of packet delivery ratio p. Cyan and purple curves represent the boundaries for mean stability and second moment stability, respectively, while the cyan and purple shaded regions represent the mean stable regions and second moment stable regions, respectively.

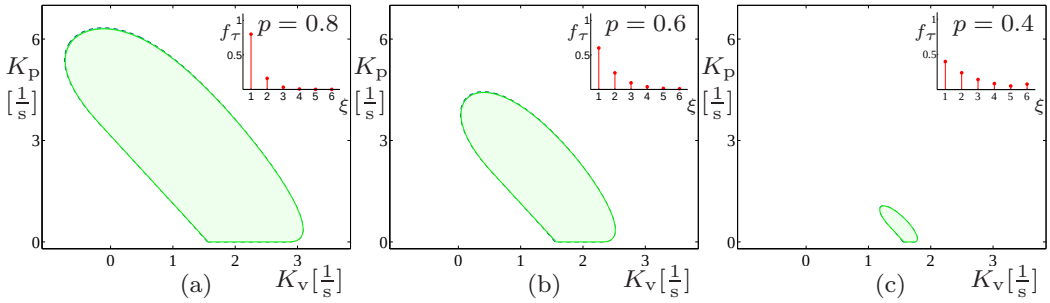

Figure 7.6: Comparison between the mean string stability of an open chain and the mean stability of a closed ring in the $(K_\mathrm{v},K_\mathrm{p})$-plane for different values of packet delivery ratio p. The solid green curves represent mean string stability boundaries for an open chain of $(3 + 1)$ vehicles, while the dashed cyan curves represent mean stability boundaries for a closed ring of infinitely many vehicles.

are described by the equations (6.1, 6.2).

Figure 7.6 shows the diagrams comparing the mean string stability for the open chain system of $(3 + 1)$ vehicles and the mean stability for the closed ring system of infinitely many vehicles in the $(K_\mathrm{v},K_\mathrm{p})$-plane for different values of packet delivery ratio p. The same color scheme is used as in Figures 6.4 and 7.3. We recall that the mean string stability for the open chain system has an extremely weak dependence on the number of vehicles in the system, so mean string stability for the open chain system of $(3 + 1)$ vehicles can be used as a good estimate for the open chain system of infinitely many vehicles. It can be seen that the mean string stability for the open chain and mean stability for the closed ring for the same parameters are practically indistinguishable. In other words, the mean string stability for the open chain system and mean stability for the closed ring system with the

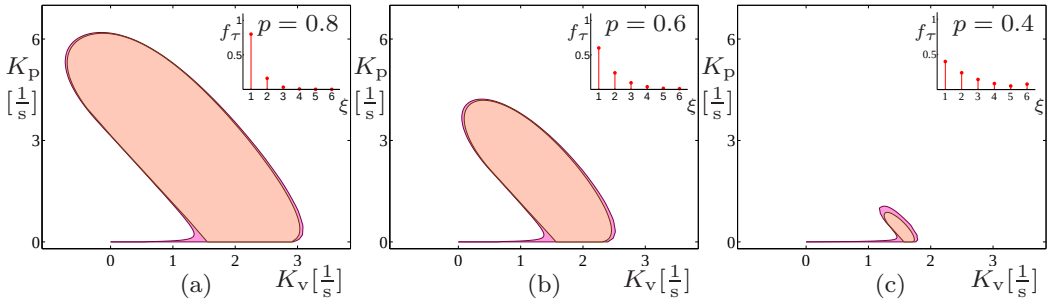

Figure 7.7: Comparison between the 1σ string stability of an open chain of (27+1) vehicles, and the second moment stability of a closed ring of 27 vehicles in the $(K_\mathrm{v},K_\mathrm{p})$-plane for different values of packet delivery ratio p. The solid orange curves and orange shaded regions correspond to the open chain, while the solid purple curves and purple shaded regions correspond to the closed ring.

same configuration converge to the same limit as the number of vehicles in the system goes to infinity.

Figure 7.7 compares the 1σ string stability for the open chain system of $(27 + 1)$ vehicles and the second moment stability for the closed ring system of 27 vehicles in the $(K_\mathrm{v},K_\mathrm{p})$-plane for different values of packet delivery ratio p. The same color scheme is used as in Figures 6.4 and 7.4. The difference between the domains in each panel is rather small except that the second moment stable regions for the closed ring system have extra "peninsulas" that indeed disappear as the number of vehicles J goes to infinity (similar to the mean stable regions). Therefore, the 1σ string stability for the open chain system and second moment stability for the closed ring system are essentially the same for large numbers of vehicles.

7.4 Summary

In this chapter, we analyzed the dynamics of large connected vehicle systems using closed ring configuration and compared it with the open chain configuration. We derived the mean, and second moment dynamics to characterize the dynamics in the vicinity of the uniform flow equilibrium. We used similar decomposition techniques as those in Chapter 6 that allowed us to significantly reduce the size of the eigenvalue problems when analyzing stability.

For the closed ring system, stability diagrams were drawn using the mean and the second moment dynamics. We illustrated that the stable regions shrink and converge to some limits as the number of vehicles increases. These limits can be obtained by analyzing the

case of infinitely many vehicles on the ring. Again we found that the mean stability is a good estimate for the second moment stability when the number of vehicles and packet delivery ratio are large enough. We also found that the mean string stable region of the open chain and mean stable region of the closed ring converge to the same limit as the number of vehicles goes to infinity. Similarly, the 1σ string stable region of the open chain and second moment stability of the closed ring converge to the same limit.

CHAPTER 8

Conclusions and Future Work

8.1 Conclusions

In this dissertation, we proposed a class of connected cruise controller that allowed connected automated vehicles to exploit information from multiple connected vehicles ahead using V2X communication, and investigated the system performance when these algorithms are implemented digitally on micro-controllers. We derived the stability conditions while taking into account the arising time-varying delays. The results showed that to ensure string stability, the information delays should not exceed a critical value.

In order to validate the proposed controllers experimentally, we built a scaled connected vehicle testbed consisting of a group of ground robots that can mimic the behaviors of real vehicles and provide us with insights about CCC design. With this testbed, V2X-based control showed advantages over sensor-based control in terms of signal quality. Moreover, the correspondence between the theoretical results and experimental outcomes demonstrated the validity of the proposed model-based design method. In the following multi-vehicle experiments, we found that the string stable/unstable properties of the two-car predecessor-follower pair were inherited by the cascaded predecessor-follower systems when all vehicles were set to be identical. We also demonstrated experimentally that string instability is related to the formation of traffic jams. We found that to attenuate the fluctuations, more than 50% of the vehicles ahead needs to be string stable in predecessor-follower systems (where each vehicle utilizes motion information of the vehicle immediately ahead). Whereas, if CAVs utilize motion information from multiple vehicles ahead, they may ensure head-to-tail string stability for much lower penetration levels. Finally, increasing the number of V2X signals can lead to more benefits in mitigating velocity fluctuations and maintaining robustness against the loss of certain communication links.

Then we shifted our focus to stochastic delay variations caused by packet drops in V2X communication. We used a Bernoulli process to describe the delay variations and

assumed that it was stationary. By incorporating the stochastic delay variations in the control loop, we first derived the stochastic dynamics for the two-car predecessor-follower pair and analyzed the effects of such delays on the system performance. To ensure almost sure stability of the equilibrium, we derived and analyzed the mean and the second moment dynamics of the linearized stochastic dynamics. Moreover, to characterize the stochastic disturbance attenuation, we derived the covariance dynamics and established the concept of $n\sigma$ string stability. Then, we extended our analytical method of stochastic disturbance attenuation to cascaded predecessor-follower systems. With a set of new decomposition techniques, stability conditions were generated to ensure smooth traffic flow based on the mean, second moment and covariance dynamics for large numbers of vehicles. The results showed that there is a correspondence between string stability of the large cascaded open chain system and stability of the large cascaded closed ring system in the stochastic sense.

8.2 Future Work

In the future, we may pursue multiple research directions based on the results obtained in this dissertation. First of all, we may consider higher fidelity vehicle models with more sophisticated controllers. Those models might include engine dynamics or lateral dynamics. This may allow us to design controllers that are optimized for fuel consumption or driver comfort, while remaining robust against parameter uncertainties, such as vehicle mass or road grade. When lateral dynamics are included, automatic lane changing might also be feasible for connected automated vehicles using V2X communication.

In the controller design for connected vehicle systems, we showed that CCC performance can be improved when more V2X signals are utilized. It may also be interesting to figure out how these signals may be used to achieve a certain level of performance while maintaining robustness against connectivity deficiencies. This depends on a systematic way of the connected cruise controller design, such that the maximum disturbance rejection ratio can be achieved for connected vehicle systems when human-driven vehicles are present.

In terms of stochastic delay variations caused by packet drops, only identical dynamics and identical CCC controllers were considered for cascaded predecessor-follower systems in this dissertation. A potential direction is to include heterogeneity due to non-identical dynamics or different controllers applied in cascaded systems or even in connected vehicle systems with more complex topologies. Also, including the engine dynamics in the stochastic model will make the method more practical and persuasive.

In this dissertation we derived the conditions for almost sure plant stability based on the

mean and covariance dynamics. Nonetheless, regarding string stability, we only proposed $n\sigma$ string stability to characterize disturbance attenuation, which cannot guarantee almost sure string stability. We may attempt other mathematical tools to create almost sure string stability.

Last but not least, we only used the stability diagrams to show the correspondence between the cascaded open chain system and closed ring system in the stochastic sense. A formal proof for such correspondence is still needed for these cascaded stochastic systems.

APPENDIX A

Control Loop Alignment

In this section, we explain communication-based control in detail and provide a way to ensure that the information delay is deterministic.

Let us consider the scenario where the controller of robot 1 uses the information of robot 0 obtained from wireless communication. Figure A.1 shows two different cases in control loop timing between robot 0 and 1. The horizontal axes are the timelines of different robots while the colored boxes represent different tasks/threads as explained in the legend at the top. One may notice that there might be several tasks/threads running at the same time, which is possible in multi-threading control systems.

As illustrated, to transceive data via wireless communication, a sequence of tasks should be performed on the transmitter, that is, sampling, processing (including converting from raw sensor data to physical data, filtering, estimation, etc.) and encoding according to the communication protocol before transmission. Upon the arrival of the transmitted data, the receiver decodes the data based on the protocol, and the information about the transmitter is updated and ready to be used in the receiver. This communication delay $\Delta_{\mathrm{c}}(k)$ varies among different periods, devices as well as data rates. We transceived approximately 7000 packets in an experiment and plot the resulting histogram of communication delay in Figure A.2(a), which is close to a gamma distribution indicated by the red curve.

Figure A.1(a) shows a scheme of three control cycles with period Δt (the same as wireless communication period) when the control loops of robot 0 and 1 are not aligned, i.e., there is an alignment error

$$\Delta_{\mathrm{A}}(k) = t(k^{(1)}) - t(k^{(0)})\,, \tag{A.1}$$

where $t(k^{(0)})$ and $t(k^{(1)})$ represent the closest two time instants correspond to $t(k)$ on robot 0 and 1, respectively. Note that this alignment error depends highly on the time difference when the controllers first start on different robots, but vaguely on different loops. Thus, we will not distinguish it among different loops, but consider Δ_{A} to be constant. However, the

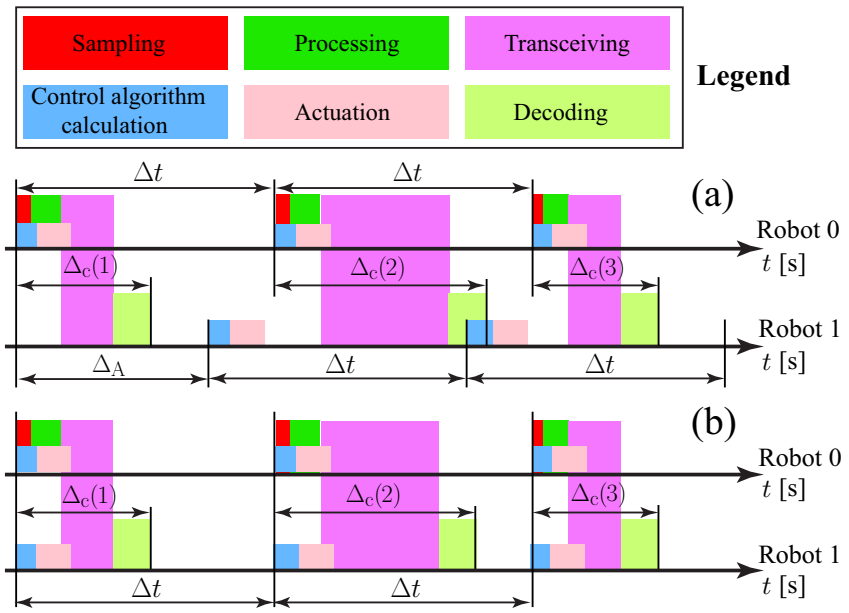

Figure A.1: (a) Control loop misaligned. (b) Control loop perfectly aligned.

communication delay $\Delta_{\mathrm{c}}(k)$ is changing stochastically at each step.

In the first control period in Figure A.1(a), the communication delay $\Delta_{\mathrm{c}}(1)$ is less than the alignment error Δ_{A}. Thus, this data is available before the first control loop starts on robot 1, that is

$$\Delta_{\mathrm{I}}(1) = \Delta_{\mathrm{A}}\,, \tag{A.2}$$

where $\Delta_{\mathrm{I}}(k)$ represents the information delay of robot 0 in the controller of robot 1 at k-th control loop. However, in the second control period, the communication delay $\Delta_{\mathrm{c}}(2)$ is greater than the alignment error Δ_{A}. Thus, this data is not available when the second control loop starts on robot 1. In this case, the robot 1 use the outdated information of robot 0 received previously, resulting in the information delay

$$\Delta_{\mathrm{I}}(2) = \Delta_{\mathrm{A}} + \Delta t\,. \tag{A.3}$$

Similarly, the information delay in the third control loop is

$$\Delta_{\mathrm{I}}(3) = \Delta_{\mathrm{A}}\,. \tag{A.4}$$

To sum up, we have

$$\Delta_{\mathrm{I}}(k) = \begin{cases} \Delta_{\mathrm{A}}, & \text{if } \Delta_{\mathrm{c}}(k) \leq \Delta_{\mathrm{A}}\,, \\ \Delta_{\mathrm{A}} + \Delta t, & \text{if } \Delta_{\mathrm{c}}(k) > \Delta_{\mathrm{A}}\,. \end{cases} \tag{A.5}$$

When no packet loss is considered, this information delay satisfies Bernoulli distribution with the PDF

$$f_{\Delta_{\mathrm{I}}(k)}(x) = p\,\delta(x - \Delta_{\mathrm{A}}) + (1-p)\,\delta\big(x - (\Delta_{\mathrm{A}} + \Delta t)\big)\,, \tag{A.6}$$

where $\delta(\cdot)$ is the Dirac delta function and

$$p = \mathbb{P}(\Delta_{\mathrm{c}}(k) \leq \Delta_{\mathrm{A}})\,. \tag{A.7}$$

Here, $\mathbb{P}$ is the probability measure.

Figure A.1(b) shows another scheme of three control cycles when the control loops of robot 0 and 1 are perfectly aligned, i.e., $\Delta_{\mathrm{A}} = 0$. From Figure A.2(a), we know that the current state of robot 0 is never available to robot 1 since

$$\mathbb{P}(\Delta_{\mathrm{c}}(k) \leq 0) \equiv 0\,, \tag{A.8}$$

but the previous state is always almost surely available since

$$\mathbb{P}(\Delta_{\mathrm{c}}(k) \leq \Delta t) = 1\,. \tag{A.9}$$

Thus, robot 1 is always almost surely using the information about robot 0 at the previous step, that is, the information delay is deterministic in every loop and equals the sampling time,

$$\Delta_{\mathrm{I}}(k) \equiv \Delta t\,. \tag{A.10}$$

In practice, the control loop alignment is not perfect as Figure A.1(b), but can be achieved to certain accuracy by shifting the next control loop based on the current loop alignment error. Figure A.2(b) plots the histogram of this alignment error after this control loop shifting algorithm is implemented. Notice that this alignment error reduces to the order of hundreds of microseconds. Indeed, the information delay Δ_{I} is also a constant in this case as explained below.

Figure A.2(a) also shows that the probability of that the communication delay over $\Delta_{\mathrm{c,max}} \approx 40$ milliseconds or below $\Delta_{\mathrm{c,min}} \approx 6$ milliseconds is rather small, due to the fact

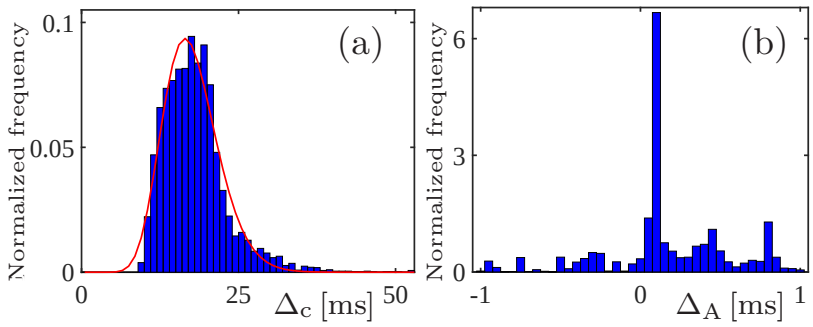

Figure A.2: (a) Histogram of communication delay. (b) Histogram of control loop alignment error.

that the minimum time $\Delta_{c,min}$ is required to go through the whole transceiving process, i.e.,

$$\mathbb{P}(\Delta_c(k) \leq \Delta_{c,min}) \approx 0\,, \qquad \mathbb{P}(\Delta_c(k) \leq \Delta_{c,max}) \approx 1\,. \tag{A.11}$$

Thus, when $\Delta_A \leq \Delta_{c,min}$, the current state of robot 0 is never available; while when $\Delta_A \geq -(\Delta t - \Delta_{c,max})$, the previous state is always almost surely available, i.e., the information delay

$$\Delta_I = \Delta t + \Delta_A\,, \quad -(\Delta t - \Delta_{c,max}) \leq \Delta_A \leq \Delta_{c,min}\,. \tag{A.12}$$

Moreover, Δ_A is very small in the experiment as shown in Figure A.2(b), so the control loops are viewed as perfectly aligned and (A.12) is approximated by (A.10) for the information delay.

APPENDIX B

Derivation of the Dynamic Model in Chapter 4

Equations (4.4, 4.5, 4.6) can be solved backward sequentially. Induction of (4.6) gives

$$\tilde{\varepsilon}_j(k+1) = \frac{\Delta t}{t_\mathrm{h}} \tilde{h}_j(k) - \Delta t\, \tilde{v}_j(k) + \tilde{\varepsilon}_j(k)\,, \tag{B.1}$$

while integration of (4.5) yields

$$\tilde{v}_j(t) = \mathrm{e}^{-c(t-t_k)} \left(\tilde{v}_j(k) - \frac{\tilde{a}_j^\mathrm{com}}{c} \right) + \frac{\tilde{a}_j^\mathrm{com}}{c}\,, \tag{B.2}$$

for $j = 1\,,\,\ldots\,,\,J$, where

$$\begin{aligned} \tilde{a}_j^\mathrm{com} = \sum_{i=0}^{j-1} \Big[\frac{\alpha_{j,\,i}}{t_\mathrm{h}} \cdot \frac{1}{j-i} \sum_{l=i+1}^{j} \tilde{h}_l(k-1) + \beta_{j,\,i} \tilde{v}_i(k-1) \\ - (\alpha_{j,\,i} + \beta_{j,\,i}) \tilde{v}_j(k-1) \Big] + \gamma_j\, \tilde{\varepsilon}_j(k)\,. \end{aligned} \tag{B.3}$$

Substituting (4.7, B.2) into (4.4) and then integrating both sides with initial condition, we obtain

$$\begin{aligned} \tilde{h}_1(t) = \tilde{h}_1(k) - \frac{v_0^\mathrm{amp}}{\omega} \big(\cos(\omega\, t) - \cos(\omega\, t_k) \big) \\ + \frac{\mathrm{e}^{-c(t-t_k)} - 1}{c} \left(\tilde{v}_1(k) - \frac{\tilde{u}_1}{c} \right) - \frac{\tilde{u}_1}{c} (t - t_k)\,, \end{aligned} \tag{B.4}$$

and

$$\begin{aligned} \tilde{h}_j(t) = \tilde{h}_j(t_k) + \frac{\tilde{a}_{j-1}^\mathrm{com} - \tilde{a}_j^\mathrm{com}}{c} (t - t_k) \\ - \frac{\mathrm{e}^{-c(t-t_k)} - 1}{c} \Big(\tilde{v}_{j-1}(k) - \tilde{v}_j(k) - \frac{\tilde{a}_{j-1}^\mathrm{com} - \tilde{a}_j^\mathrm{com}}{c} \Big)\,, \end{aligned} \tag{B.5}$$

for $j = 2\,,\,\ldots\,,\,J$.

Evaluating (B.4, B.5, B.2) at instant $t = t_{k+1}$ gives

$$\tilde{h}_1(k+1) = \tilde{h}_1(k) - \theta_1 \tilde{v}_1(k) + \theta_2 v_0^{\mathrm{amp}} \sin(k\,\omega\,\Delta t) + \theta_3 v_0^{\mathrm{amp}} \cos(k\omega\Delta t) - \theta_4 \tilde{u}_1\,, \quad \text{(B.6)}$$

$$\tilde{h}_j(k+1) = \tilde{h}_j(k) - \theta_1 \tilde{v}_j(k) + \theta_1 \tilde{v}_{j-1}(k) + \theta_4 \left(\tilde{a}_{j-1}^{\mathrm{com}} - \tilde{a}_j^{\mathrm{com}}\right)\,, \quad \text{(B.7)}$$

for $j = 2\,,\,\ldots\,,\,J$, and

$$\tilde{v}_j(k+1) = \mathrm{e}^{-c\Delta t} \tilde{v}_j(k) + \theta_1 \tilde{a}_j^{\mathrm{com}}\,, \quad \text{(B.8)}$$

for $j = 1\,,\,\ldots\,,\,J$, where θ_1, θ_2, θ_3 and θ_4 are the same as those defined in (2.13).

Through the use of (4.10, 4.11, B.3) and algebraic manipulations, we can simplify equations (B.6, B.7, B.8, B.1) and then combine them into the model (4.8) with

$$\boldsymbol{a}_{j,\,j} = \begin{bmatrix} 1 & -\theta_1 & -\gamma_j\theta_4 \\ 0 & \mathrm{e}^{-c\,\Delta t} & \gamma_j\theta_1 \\ \dfrac{\Delta t}{t_{\mathrm{h}}} & -\Delta t & 1 \end{bmatrix}\,, \qquad \boldsymbol{a}^{\tau}_{j,\,j} = \begin{bmatrix} -\dfrac{\overline{\alpha}_{j,\,j-1}\,\theta_4}{t_{\mathrm{h}}} & \overline{\kappa}^{\mathrm{s}}_j\theta_4 \\ \dfrac{\overline{\alpha}_{j,\,j-1}\,\theta_1}{t_{\mathrm{h}}} & -\overline{\kappa}^{\mathrm{s}}_j\theta_1 \\ 0 & 0 \end{bmatrix}\,, \quad \text{(B.9)}$$

for $j = 1\,,\,\ldots\,,\,J$,

$$\boldsymbol{a}_{j,\,j-1} = \begin{bmatrix} 0 & \theta_1 & \gamma_{j-1}\theta_4 \\ 0 & 0 & 0 \\ 0 & 0 & 0 \end{bmatrix}\,, \quad \boldsymbol{a}^{\tau}_{j,\,j-1} = \begin{bmatrix} \dfrac{\widehat{\alpha}_{j,\,j-2}\theta_4}{t_{\mathrm{h}}} & -\zeta_j\theta_4 \\ \dfrac{\overline{\alpha}_{j,\,j-2}\theta_1}{t_{\mathrm{h}}} & \beta_{j,\,j-1}\theta_1 \\ 0 & 0 \end{bmatrix}\,, \quad \boldsymbol{b}^{\tau}_j = \begin{bmatrix} \widehat{\beta}_{j,\,0}\theta_4 & 0 \\ \beta_{j,\,0}\theta_1 & 0 \\ 0 & 0 \end{bmatrix}\,, \quad \text{(B.10)}$$

for $j = 2\,,\,\ldots\,,\,J$,

$$\boldsymbol{a}^{\tau}_{j,\,l} = \begin{bmatrix} \dfrac{\widehat{\alpha}_{j,\,l-1}\theta_4}{t_{\mathrm{h}}} & \widehat{\beta}_{j,\,l}\theta_4 \\ \dfrac{\overline{\alpha}_{j,\,l-1}\theta_1}{t_{\mathrm{h}}} & \beta_{j,\,l}\theta_1 \\ 0 & 0 \end{bmatrix}\,, \quad \text{(B.11)}$$

for $j = 3\,,\,\ldots\,,\,J\,,\,l = 1\,,\ldots\,,\,j-2$, and

$$\boldsymbol{b}_0 = \begin{bmatrix} \theta_2 & \theta_3 \\ 0 & 0 \\ 0 & 0 \end{bmatrix}\,, \qquad \boldsymbol{b}_1^{\tau} = \begin{bmatrix} -\beta_{1,0}\theta_4 & 0 \\ \beta_{1,0}\theta_1 & 0 \\ 0 & 0 \end{bmatrix}\,, \tag{B.12}$$

where

$$\begin{aligned} &\overline{\alpha}_{r,l} = \sum_{i=0}^{l} \frac{\alpha_{r,i}}{r-i}\,, \qquad && \overline{\kappa}_r^{\mathrm{s}} = \sum_{i=0}^{r-1} (\alpha_{r,i} + \beta_{r,i})\,, \\ &\widehat{\alpha}_{r,l} = \overline{\alpha}_{r-1,l} - \overline{\alpha}_{r,l}\,, \qquad && \widehat{\beta}_{r,l} = \beta_{r-1,\,l} - \beta_{r,\,l}\,, \qquad && \zeta_r = \overline{\kappa}_{r-1}^{\mathrm{s}} + \beta_{r,r-1}\,. \end{aligned} \tag{B.13}$$

APPENDIX C

Open Chain vs. Closed Ring

In this part, we establish the relationships between two different cascaded systems – the open chain system and closed ring system. Both systems can be viewed as a concatenation of multiple identical subsystems, where the output of each subsystem is the input of its next subsystem. In the closed ring system, additionally, the output of the last subsystem is feed back as the input of the very first subsystem. Enlightened by the predecessor-follower system in the thesis, we made several assumptions on the properties that the subsystem should possess. To unveil the relationship between the two cascaded systems, we first assume that the subsystem can be written as a continuous-time linear time invariant (LTI) single-input-single-output (SISO) system without time delays. Along with the properties of the subsystem, it is shown that the head-to-tail string stability of the cascaded open chain system is equivalent to the string stability of a single subsystem; see Section 1.2 for definitions of head-to-tail string stability and string stability. Moreover, the string stability of a single subsystem is equivalent to the stability of the cascaded closed ring system consisting of infinitely many identical subsystems. Then we extend the results to continuous-time LTI systems with constant time delays, discrete-time LTI systems with or without constant time delays. We also show that the system with vector-valued dependent inputs (see (2.11, 4.9)) can be written as a SISO system with constant time delays.

C.1 Continuous-time LTI Systems without Delays

We first consider that a subsystem can be written as

$$\begin{aligned} \dot{x}_j &= \boldsymbol{a}\, x_j + \boldsymbol{b}\, u_j\,, \\ y_j &= \boldsymbol{c}\, x_j\,, \end{aligned} \tag{C.1}$$

where $x_j \in \mathbb{R}^n$, $u_j \in \mathbb{R}$ and $y_j \in \mathbb{R}$. The transfer function of (C.1) is

$$\gamma(s) \triangleq \frac{Y_j(s)}{U_j(s)} = \boldsymbol{c}(s\mathbf{I} - \boldsymbol{a})^{-1}\boldsymbol{b}\,. \tag{C.2}$$

Here we consider the scenario when the system possesses the following properties.

1. The subsystem (C.1) must be stable, i.e., all the eigenvalues of $\boldsymbol{a}$ must lie on the left hand side of the complex plane.

2. DC gain is 1 with zero phase lag, i.e.,

$$\gamma(0) = -\boldsymbol{c}\boldsymbol{a}^{-1}\boldsymbol{b} = 1\,. \tag{C.3}$$

   This is a common property when we discuss string stability for connected vehicle systems. As the predecessor's velocity is varying very slowly, the follower must be able to match its velocity with the predecessor's.

3. The system is "low pass", i.e.,

$$\lim_{\omega\to\infty} |\gamma(\mathrm{j}\omega)| = 0\,. \tag{C.4}$$

Base on the definitions of string stability in Section 1.2, one can obtain that the string stability condition of (C.1) is given by

$$\sup_{\omega>0} \left|\boldsymbol{c}(\mathrm{j}\omega\mathbf{I} - \boldsymbol{a})^{-1}\boldsymbol{b}\right| < 1\,. \tag{C.5}$$

Suppose there are J identical systems described by (C.1) satisfying the properties above, and they are cascaded in the way such that

$$u_j = y_{j-1}, \tag{C.6}$$

for $j = 2\,,\,\ldots\,,\,J$, then the cascaded open chain system becomes

$$\begin{aligned} \dot{x}_1 &= \boldsymbol{a}\,x_1 + \boldsymbol{b}\,u_1\,, \\ \dot{x}_j &= \boldsymbol{a}\,x_j + \boldsymbol{b}\,\boldsymbol{c}\,x_{j-1}\,, \qquad\qquad j = 2\,,\,\ldots\,,\,J\,, \\ y &= \boldsymbol{c}\,x_J\,. \end{aligned} \tag{C.7}$$

Moreover, if

$$u_1 = y_J \,, \tag{C.8}$$

we obtain a cascaded closed ring system, that is,

$$\begin{aligned} \dot{x}_1 &= \boldsymbol{a}\, x_1 + \boldsymbol{b}\, \boldsymbol{c}\, x_J \,, \\ \dot{x}_j &= \boldsymbol{a}\, x_j + \boldsymbol{b}\, \boldsymbol{c}\, x_{j-1} \,, \qquad\qquad j = 2 \,, \, \ldots \,, \, J \,. \end{aligned} \tag{C.9}$$

Our objective is to establish the relationship between string stability of the open chain system (C.7) and stability of the closed ring system (C.9).

Proposition C.1 *Head-to-tail string stability of the open chain system* (C.7) *is equivalent to string stability of the subsystem* (C.1).

Proposition C.2 *String stability of the subsystem* (C.1) *is equivalent to stability of the closed ring system* (C.9) *consisting of infinitely many identical subsystems.*

Proof: The subsystem (C.1) is being stable implies that all solutions to the characteristic equation

$$\det(\lambda\, \mathbf{I} - \boldsymbol{a}) = 0 \tag{C.10}$$

are located in the left half complex plane. That is, $\forall \lambda \in \{\lambda \in \mathbb{C} \,|\, \mathrm{Re}(\lambda) \geq 0\}$,

$$\det(\lambda \mathbf{I} - \boldsymbol{a}) \neq 0 \qquad \Longleftrightarrow \qquad (\lambda \mathbf{I} - \boldsymbol{a}) \text{ is invertible.} \tag{C.11}$$

To determine head-to-tail string stability of the open chain, the transfer function from u_1 to y has to be derived, that is,

$$\Gamma(s) = \frac{Y(s)}{U_1(s)} = \frac{Y(s)}{U_J(s)} \frac{Y_{J-1}(s)}{U_{J-1}(s)} \cdots \frac{Y_1(s)}{U_1(s)} = \left(\boldsymbol{c}(s\mathbf{I} - \boldsymbol{a})^{-1}\boldsymbol{b}\right)^J \,, \tag{C.12}$$

cf. (C.1, C.6), where $U_j(s)$ and $Y_j(s)$ are the Laplace transform of $u_j(t)$ and $y_j(t)$, respectively. In order to maintain head-to-tail string stability, the condition

$$\sup_{\omega > 0} |\Gamma(\mathrm{j}\, \omega)| < 1 \tag{C.13}$$

must hold. That is, the head-to-tail string stability boundary is

$$\sup_{\omega>0} \left| \left(\boldsymbol{c}(\mathrm{j}\omega\mathbf{I} - \boldsymbol{a})^{-1}\boldsymbol{b} \right)^{J} \right| = 1\,, \tag{C.14}$$

which can be rewritten as

$$\sup_{\omega>0} \left| \boldsymbol{c}(\mathrm{j}\omega\mathbf{I} - \boldsymbol{a})^{-1}\boldsymbol{b} \right|^{J} = 1 \qquad \Longleftrightarrow \qquad \sup_{\omega>0} \left| \boldsymbol{c}(\mathrm{j}\omega\mathbf{I} - \boldsymbol{a})^{-1}\boldsymbol{b} \right| = 1\,. \tag{C.15}$$

That is, head-to-tail string stability of (C.7) is equivalent to string stability of the subsystem (C.1).

Regarding the closed ring system (C.9), let us define the state

$$X = \begin{bmatrix} x_1 \\ \vdots \\ x_J \end{bmatrix}\,. \tag{C.16}$$

Thus, we obtain

$$\dot{X} = \mathbf{A}^{\mathrm{R}}\, X\,, \tag{C.17}$$

where

$$\mathbf{A}^{\mathrm{R}} = \begin{bmatrix} \boldsymbol{a} & 0 & \cdots & 0 & \boldsymbol{b}\,\boldsymbol{c} \\ \boldsymbol{b}\,\boldsymbol{c} & \boldsymbol{a} & 0 & \cdots & 0 \\ 0 & \boldsymbol{b}\,\boldsymbol{c} & \boldsymbol{a} & \ddots & \vdots \\ \vdots & \ddots & \ddots & \ddots & 0 \\ 0 & \cdots & 0 & \boldsymbol{b}\,\boldsymbol{c} & \boldsymbol{a} \end{bmatrix}\,, \tag{C.18}$$

yielding the characteristic equation

$$\det(\lambda\,\mathbf{I} - \mathbf{A}^{\mathrm{R}}) = \begin{bmatrix} \lambda\,\mathbf{I} - \boldsymbol{a} & 0 & \cdots & 0 & -\boldsymbol{b}\,\boldsymbol{c} \\ -\boldsymbol{b}\,\boldsymbol{c} & \lambda\,\mathbf{I} - \boldsymbol{a} & 0 & \ddots & 0 \\ 0 & -\boldsymbol{b}\,\boldsymbol{c} & \lambda\,\mathbf{I} - \boldsymbol{a} & \ddots & \vdots \\ \vdots & \ddots & \ddots & \ddots & 0 \\ 0 & \cdots & 0 & -\boldsymbol{b}\,\boldsymbol{c} & \lambda\,\mathbf{I} - \boldsymbol{a} \end{bmatrix} = 0\,. \tag{C.19}$$

Notice that the matrix is a banded block circulant matrix [203]. According to [199], a block circulant matrix is unitarily similar to a block diagonal matrix with diagonal blocks

$$(\lambda\,\mathbf{I} - \boldsymbol{a}) - \boldsymbol{b}\,\boldsymbol{c}\,\mathrm{e}^{-\mathrm{j}\frac{2\pi}{J}(l-1)}\,, \qquad l = 1\,,\,\ldots\,,\,J. \tag{C.20}$$

Thus, applying the generalized matrix determinant lemma in Corollary E.1 and the fact that similar matrices have the same determinant, we obtain

$$\begin{aligned}
\det(\lambda\,\mathbf{I} - \mathbf{A}^{\mathrm{R}}) &= \prod_{l=1}^{J} \det\left((\lambda\,\mathbf{I} - \boldsymbol{a}) - \boldsymbol{b}\,\boldsymbol{c}\,\mathrm{e}^{-\mathrm{j}\frac{2\pi}{J}(l-1)}\right) \\
&= \prod_{l=1}^{J} \left(\det(\lambda\,\mathbf{I} - \boldsymbol{a})\det(\mathrm{e}^{-\mathrm{j}\frac{2\pi}{J}(l-1)}\cdot 1)\det\left(\mathrm{e}^{\mathrm{j}\frac{2\pi}{J}(l-1)}\cdot 1 - \boldsymbol{c}(\lambda\,\mathbf{I} - \boldsymbol{a})^{-1}\boldsymbol{b}\right)\right) \\
&= \Big(\det(\lambda\,\mathbf{I} - \boldsymbol{a})\Big)^{J} \prod_{l=1}^{J} \left(\det\left(\mathrm{e}^{\mathrm{j}\frac{2\pi}{J}(l-1)} - \boldsymbol{c}(\lambda\,\mathbf{I} - \boldsymbol{a})^{-1}\boldsymbol{b}\right)\right) \\
&= \Big(\det(\lambda\,\mathbf{I} - \boldsymbol{a})\Big)^{J} \prod_{l=1}^{J} \left(\mathrm{e}^{\mathrm{j}\frac{2\pi}{J}(l-1)} - \boldsymbol{c}(\lambda\,\mathbf{I} - \boldsymbol{a})^{-1}\boldsymbol{b}\right) \\
&= \Big(\det(\lambda\,\mathbf{I} - \boldsymbol{a})\Big)^{J} \left(1 - \Big(\boldsymbol{c}(\lambda\,\mathbf{I} - \boldsymbol{a})^{-1}\boldsymbol{b}\Big)^{J}\right)\,.
\end{aligned} \tag{C.21}$$

In order to obtain the boundaries for the stability loss of the cascaded closed ring system, we consider the critical cases:

1. The rightmost eigenvalues cross the imaginary axis at $\lambda = \pm\mathrm{j}\omega_{\mathrm{cr}}$ for $\omega_{\mathrm{cr}} > 0$. Notice that (C.11) indicates that $\det(\mathrm{j}\omega_{\mathrm{cr}}\,\mathbf{I} - \boldsymbol{a}) \neq 0$. Thus, $\omega = \omega_{\mathrm{cr}}$ is a solution to the equation

$$\Big(\boldsymbol{c}(\mathrm{j}\omega\,\mathbf{I} - \boldsymbol{a})^{-1}\boldsymbol{b}\Big)^{J} = 1\,, \tag{C.22}$$

or equivalently,

$$\begin{aligned}
\Big|\boldsymbol{c}(\mathrm{j}\omega\,\mathbf{I} - \boldsymbol{a})^{-1}\boldsymbol{b}\Big| &= 1\,, \\
\angle\Big(\boldsymbol{c}(\mathrm{j}\omega\,\mathbf{I} - \boldsymbol{a})^{-1}\boldsymbol{b}\Big) &= \frac{2\,l\,\pi}{J}\,, \quad l = 1\,,\,\ldots\,,\,J\,.
\end{aligned} \tag{C.23}$$

When the closed ring is infinitely large, i.e., $J \to \infty$, the angle $\dfrac{2\,l\,\pi}{J}$ can take any value in the interval $[0\,,\,2\pi)$, i.e., the second condition in (C.23) can always be satisfied. But, in this case, $\lambda = \pm\mathrm{j}\omega_{\mathrm{cr}}$ being the rightmost solution yields the following

necessary condition that

$$\sup_{\omega>0} \left| \boldsymbol{c}(\mathrm{j}\omega\,\mathbf{I} - \boldsymbol{a})^{-1}\boldsymbol{b} \right| = 1\,, \tag{C.24}$$

and the supremum is achieved at $\omega = \omega_{\mathrm{cr}}$. Notice that this is the same as the string stability condition (C.15). We consider the following two cases to prove it by contradiction.

(a) If $\sup_{\omega>0} \left| \boldsymbol{c}(\mathrm{j}\omega\,\mathbf{I} - \boldsymbol{a})^{-1}\boldsymbol{b} \right| < 1$, then there is no solution to the equation (C.23). Thus, $\lambda = \pm\mathrm{j}\omega_{\mathrm{cr}}$ cannot be a solution.

(b) If $\sup_{\omega>0} \left| \boldsymbol{c}(\mathrm{j}\omega\,\mathbf{I} - \boldsymbol{a})^{-1}\boldsymbol{b} \right| > 1$, along with the low pass condition (C.4), one can show that there exists some other solution λ_1 on the right side of the complex plane satisfying the condition (C.23). This can be achieved by applying the intermediate value theorem and noticing that the function $f(s) = |\boldsymbol{c}(s\,\mathbf{I} - \boldsymbol{a})^{-1}\boldsymbol{b}|$ is continuous almost everywhere on the right side of the complex plane except at finite number of poles.

Thus, $\lambda = \pm\mathrm{j}\omega_{\mathrm{cr}}$ is not the rightmost solution.

2. The rightmost eigenvalue crosses the imaginary axis at $\lambda = 0$. This is a special case and we do not show the proof here.

We remark that it is only shown here that the subsystem is SISO system, but the results can also be extended to multiple-input-multiple-output (MIMO) systems. In the MIMO system, the definition of string stability will be different, but the proof techniques are similar.

C.2 Continuous-time LTI Systems with Constant Delays

The propositions C.1 and C.2 can be easily extended to linear systems with time delays. Let us consider the continuous-time systems with constant delays

$$\begin{aligned} \dot{x}_j &= \boldsymbol{a}\,x_j + \boldsymbol{a}_\tau\,x_j(t-\tau) + \boldsymbol{b}\,u_j + \boldsymbol{b}_\tau\,u_j(t-\tau)\,, \\ y_j &= \boldsymbol{c}\,x_j\,, \end{aligned} \tag{C.25}$$

possessing the same properties as those in Section C.1. Then the open chain of cascaded systems becomes

$$\begin{aligned}
\dot{x}_1 &= \boldsymbol{a}\, x_1 + \boldsymbol{a}_\tau\, x_1(t-\tau) + \boldsymbol{b}\, u_1 + \boldsymbol{b}_\tau\, u_1(t-\tau)\,, \\
\dot{x}_j &= \boldsymbol{a}\, x_j + \boldsymbol{a}_\tau\, x_j(t-\tau) + \boldsymbol{b}\,\boldsymbol{c}\, x_{j-1} + \boldsymbol{b}_\tau\,\boldsymbol{c}\, x_{j-1}(t-\tau)\,, \qquad j = 2\,,\,\ldots\,,\,J\,, \\
y &= \boldsymbol{c}\, x_J\,,
\end{aligned} \tag{C.26}$$

while the closed ring system becomes

$$\dot{X} = \mathbf{A}^{\mathrm{R}}\, X + \mathbf{A}^{\mathrm{R}}_\tau\, X(t-\tau)\,, \tag{C.27}$$

where

$$\mathbf{A}^{\mathrm{R}} = \begin{bmatrix} \boldsymbol{a} & 0 & \cdots & 0 & \boldsymbol{b}\,\boldsymbol{c} \\ \boldsymbol{b}\,\boldsymbol{c} & \boldsymbol{a} & 0 & \cdots & 0 \\ 0 & \boldsymbol{b}\,\boldsymbol{c} & \boldsymbol{a} & \ddots & \vdots \\ \vdots & \ddots & \ddots & \ddots & 0 \\ 0 & \cdots & 0 & \boldsymbol{b}\,\boldsymbol{c} & \boldsymbol{a} \end{bmatrix}, \quad \mathbf{A}^{\mathrm{R}}_\tau = \begin{bmatrix} \boldsymbol{a}_\tau & 0 & \cdots & 0 & \boldsymbol{b}_\tau\,\boldsymbol{c} \\ \boldsymbol{b}_\tau\,\boldsymbol{c} & \boldsymbol{a}_\tau & 0 & \cdots & 0 \\ 0 & \boldsymbol{b}_\tau\,\boldsymbol{c} & \boldsymbol{a}_\tau & \ddots & \vdots \\ \vdots & \ddots & \ddots & \ddots & 0 \\ 0 & \cdots & 0 & \boldsymbol{b}_\tau\,\boldsymbol{c} & \boldsymbol{a}_\tau \end{bmatrix}. \tag{C.28}$$

The characteristic equation for the subsystem (C.25) becomes

$$\det(\lambda\,\mathbf{I} - \boldsymbol{a} - \boldsymbol{a}_\tau\,\mathrm{e}^{-\lambda\tau}) = 0\,, \tag{C.29}$$

cf. (C.10). The transfer function of the open chain is

$$\Gamma(s) = \Big(\boldsymbol{c}(s\,\mathbf{I} - \boldsymbol{a} - \boldsymbol{a}_\tau \mathrm{e}^{-s\tau})^{-1}(\boldsymbol{b} + \boldsymbol{b}_\tau\,\mathrm{e}^{-s\tau})\Big)^J\,, \tag{C.30}$$

cf. (C.12), resulting in the corresponding changes in the string stability boundaries (C.14, C.15).

For the closed ring system, following the same method, we can derive the characteristic equation

$$\begin{aligned}
\det(\lambda\,\mathbf{I} - \mathbf{A}^{\mathrm{R}} - \mathbf{A}^{\mathrm{R}}_\tau \mathrm{e}^{-\lambda\tau}) = \big(\det(\lambda\,\mathbf{I} - \boldsymbol{a} - \boldsymbol{a}_\tau \mathrm{e}^{-\lambda\tau})\big)^J \\
\times \det\left(1 - \Big(\boldsymbol{c}(\lambda\,\mathbf{I} - \boldsymbol{a} - \boldsymbol{a}_\tau \mathrm{e}^{-\lambda\tau})^{-1}(\boldsymbol{b} + \boldsymbol{b}_\tau\,\mathrm{e}^{-\lambda\tau})\Big)^J\right).
\end{aligned} \tag{C.31}$$

The rest results change correspondingly while the proof techniques remain the same.

C.3 Discrete-time LTI Systems without Delays

In this section, we extend propositions C.1 and C.2 to discrete-time LTI systems without delays, by replacing the Laplace transform with Z transform. Again we only point out the changes.

Consider the subsystem is LTI system

$$\begin{aligned} x_j(k+1) &= \boldsymbol{a}\, x_j(k) + \boldsymbol{b}\, u_j(k)\,, \\ y_j(k) &= \boldsymbol{c}\, x_j(k)\,, \end{aligned} \tag{C.32}$$

where $x_j \in \mathbb{R}^n$, $u_j \in \mathbb{R}$ and $y_j \in \mathbb{R}$. The transfer function of (C.32) is

$$\gamma(z) \triangleq \frac{Y_j(z)}{U_j(z)} = \boldsymbol{c}(z\mathbf{I} - \boldsymbol{a})^{-1}\boldsymbol{b}\,, \tag{C.33}$$

and the frequency response at frequency ω is given by $\gamma(\mathrm{e}^{\mathrm{j}\omega\Delta t})$, where Δt is the update period of the system (C.32). We still assume that the subsystem (C.32) has the following properties.

1. The subsystem (C.32) is stable, i.e., all eigenvalues of $\boldsymbol{a}$ lie inside the unit circle in the complex plane.

2. DC gain is 1 with zero phase lag, i.e.,

$$\gamma(1) = \boldsymbol{c}(\mathbf{I} - \boldsymbol{a})^{-1}\boldsymbol{b} = 1\,. \tag{C.34}$$

3. The system is "low pass", i.e.,

$$|\gamma(\mathrm{e}^{\mathrm{j}\pi})| < |\gamma(1)| \qquad \Longleftrightarrow \qquad |\boldsymbol{c}(\mathbf{I} + \boldsymbol{a})^{-1}\boldsymbol{b}| < 1\,, \tag{C.35}$$

   cf. (C.4). The changes here result from the fact that the frequency response of a discrete-time system is periodic, and $\omega = \pi/\Delta t$ corresponds to Nyquist frequency.

The string stability condition of (C.32) is given by

$$\sup_{\omega>0} \left| \boldsymbol{c}(\mathrm{e}^{\mathrm{j}\omega\Delta t}\mathbf{I} - \boldsymbol{a})^{-1}\boldsymbol{b} \right| < 1\,. \tag{C.36}$$

The subsystem (C.32) is stable implies that all the solutions to the characteristic equa-

tion

$$\det(\lambda\,\mathbf{I} - \boldsymbol{a}) = 0 \tag{C.37}$$

are located inside the unit circle in the complex plane. That is, $\forall\lambda \in \{\lambda \in \mathbb{C}\,|\,|\lambda| \geq 1\}$,

$$\det(\lambda\mathbf{I} - \boldsymbol{a}) \neq 0 \qquad \Longleftrightarrow \qquad (\lambda\mathbf{I} - \boldsymbol{a}) \text{ is invertible.} \tag{C.38}$$

The cascaded open chain system becomes

$$\begin{aligned} x_1(k+1) &= \boldsymbol{a}\,x_1(k) + \boldsymbol{b}\,u_1(k)\,, \\ x_j(k) &= \boldsymbol{a}\,x_j(k) + \boldsymbol{b}\,\boldsymbol{c}\,x_{j-1}(k)\,, \qquad\qquad j = 2\,,\,\ldots\,,\,J\,, \\ y(k) &= \boldsymbol{c}\,x_J(k)\,. \end{aligned} \tag{C.39}$$

To determine head-to-tail string stability of the open chain (C.39), the transfer function from u_1 to y changes to

$$\Gamma(z) = \frac{Y(z)}{U_1(z)} = \frac{Y(z)}{U_J(z)}\frac{Y_{J-1}(z)}{U_{J-1}(z)}\cdots\frac{Y_1(z)}{U_1(z)} = \left(\boldsymbol{c}(z\mathbf{I} - \boldsymbol{a})^{-1}\boldsymbol{b}\right)^J\,, \tag{C.40}$$

where $U_j(z)$ and $Y_j(z)$ are the Z transform of $u_j(k)$ and $y_j(k)$, respectively. The condition to maintain head-to-tail string stability becomes

$$\sup_{\omega>0}|\Gamma(\mathrm{e}^{\mathrm{j}\,\omega\Delta t})| < 1\,, \tag{C.41}$$

which will result in the corresponding changes in (C.14, C.15), that is,

$$\sup_{\omega>0}\left|\boldsymbol{c}(\mathrm{e}^{\mathrm{j}\,\omega\Delta t}\mathbf{I} - \boldsymbol{a})^{-1}\boldsymbol{b}\right|^J = 1 \qquad \Longleftrightarrow \qquad \sup_{\omega>0}\left|\boldsymbol{c}(\mathrm{e}^{\mathrm{j}\,\omega\Delta t}\mathbf{I} - \boldsymbol{a})^{-1}\boldsymbol{b}\right| = 1\,. \tag{C.42}$$

Regarding the closed ring system, the equation C.17 changes to

$$X(k+1) = \mathbf{A}^{\mathrm{R}}\,X\,, \tag{C.43}$$

where the state remains the same as (C.16), while the system matrix is the same as given in (C.18), yielding the same characteristic equation as that in (C.19, C.21). However, the two critical cases for the stability losses changes as follows.

1. The eigenvalue with the largest magnitude crosses the unit circle at $\lambda = \mathrm{e}^{\pm\mathrm{j}\omega_{\mathrm{cr}}\Delta t}$ for $\omega_{\mathrm{cr}} \in (0\,,\,\pi)$. Similar to the analysis in the first case for continuous-time system,

$\omega = \omega_{\mathrm{cr}}$ is a solution to the equation

$$\Big(\boldsymbol{c}(\mathrm{e}^{\mathrm{j}\omega\Delta t}\,\mathbf{I} - \boldsymbol{a})^{-1}\boldsymbol{b}\Big)^{J} = 1\,, \tag{C.44}$$

or equivalently,

$$\Big|\boldsymbol{c}(\mathrm{e}^{\mathrm{j}\omega\Delta t}\,\mathbf{I} - \boldsymbol{a})^{-1}\boldsymbol{b}\Big| = 1\,, \tag{C.45}$$

$$\angle\Big(\boldsymbol{c}(\mathrm{e}^{\mathrm{j}\omega\Delta t}\,\mathbf{I} - \boldsymbol{a})^{-1}\boldsymbol{b}\Big) = \frac{2\,l\,\pi}{J}\,, \quad l = 1\,,\,\ldots\,,\,J\,. \tag{C.46}$$

cf. (C.22, C.23, C.23).

Thus, the stability boundary for the closed ring with infinitely many vehicles becomes

$$\sup_{\omega>0}\Big|\boldsymbol{c}(\mathrm{e}^{\mathrm{j}\omega\Delta t}\,\mathbf{I} - \boldsymbol{a})^{-1}\boldsymbol{b}\Big| = 1\,, \tag{C.47}$$

cf. (C.24).

2. The eigenvalue with the largest magnitude crosses the unit circle at $\lambda = 1$. This is also a special case, and we do not show the proof here.

3. The eigenvalue with the largest magnitude crosses the unit circle at $\lambda = -1$, , implying the boundary

$$\det(-\mathbf{I} - \mathbf{A}^{\mathrm{R}}) = 0 \qquad \Longleftrightarrow \qquad 1 - (-\boldsymbol{c}\,(\mathbf{I} + \boldsymbol{a})^{-1}\boldsymbol{b})^{J} = 0\,. \tag{C.48}$$

Note that this cannot be satisfied since the subsystem possesses the low pass property (C.35).

C.4 Discrete-time LTI Systems with Constant Delays

Similarly, propositions C.1 and C.2 can be extended to discrete-time LTI systems with constant delays, where the subsystem is described by

$$\begin{aligned} x_j(k+1) &= \boldsymbol{a}\,x_j(k) + \boldsymbol{a}_\tau\,x_j(k-\tau) + \boldsymbol{b}\,u_j(k) + \boldsymbol{b}_\tau\,u_j(k-\tau)\,, \\ y_j(k) &= \boldsymbol{c}\,x_j(k)\,. \end{aligned} \tag{C.49}$$

and possesses the same properties as those given in Section C.3. In this case, the open chain of cascaded systems changes to

$$\begin{aligned} x_1(k+1) &= \boldsymbol{a}\, x_1(k) + \boldsymbol{a}_\tau\, x_1(k-\tau) + \boldsymbol{b}\, u_1(k) + \boldsymbol{b}_\tau\, u_1(k-\tau)\,, \\ x_j(k+1) &= \boldsymbol{a}\, x_j(k) + \boldsymbol{a}_\tau\, x_j(k-\tau) + \boldsymbol{b}\,\boldsymbol{c}\, x_{j-1}(k) + \boldsymbol{b}_\tau\,\boldsymbol{c}\, x_{j-1}(k-\tau)\,, \quad j = 2\,,\,\ldots\,,\,J\,, \\ y(k) &= \boldsymbol{c}\, x_J(k)\,, \end{aligned} \tag{C.50}$$

while the closed ring system is

$$X(k+1) = \mathbf{A}^{\mathrm{R}}\, X(k) + \mathbf{A}^{\mathrm{R}}_\tau\, X(k-\tau)\,, \tag{C.51}$$

where the matrices are the same as (C.28).

The characteristic equation for the subsystem becomes

$$\det(\lambda\,\mathbf{I} - \boldsymbol{a} - \boldsymbol{a}_\tau\,\lambda^{-\tau}) = 0\,, \tag{C.52}$$

cf. (C.37). The transfer function of the open chain is

$$\Gamma(z) = \Big(\boldsymbol{c}(z\,\mathbf{I} - \boldsymbol{a} - \boldsymbol{a}_\tau z^{-\tau})^{-1}(\boldsymbol{b} + \boldsymbol{b}_\tau\, z^{-\tau})\Big)^J\,, \tag{C.53}$$

cf. (C.40), resulting in the corresponding changes in the string stability conditions in (C.42).

For the closed ring system, following the same method, we can derive the characteristic equation

$$\begin{aligned} \det(\lambda\,\mathbf{I} - \mathbf{A}^{\mathrm{R}} - A^{\mathrm{R}}_\tau\lambda^{-\tau}) = \big(\det(\lambda\,\mathbf{I} - \boldsymbol{a} - \boldsymbol{a}_\tau\lambda^{-\tau})\big)^J \\ \times \det\left(1 - \Big(\boldsymbol{c}(\lambda\,\mathbf{I} - \boldsymbol{a} - \boldsymbol{a}_\tau\lambda^{-\tau})^{-1}(\boldsymbol{b} + \boldsymbol{b}_\tau\,\lambda^{-\tau})\Big)^J\right)\,. \end{aligned} \tag{C.54}$$

The rest results change correspondingly while the proof techniques still remain the same as those for the discrete-time LTI systems without constant delays.

So far propositions C.1 and C.2 are shown to be valid for LTI SISO systems with or without time delays in the continuous-time or discrete-time domain. Here we show that the system used in the thesis can be converted to SISO systems. We take the input (2.11) for

(2.10) as an example. By using trigonometric identities, one can obtain that

$$\begin{aligned}
\tilde{v}_{j-1}^{\perp}(k) &= \tilde{v}_{j-1}^{\mathrm{amp}} \cos(k\omega\Delta t) \\
&= \tilde{v}_{j-1}^{\mathrm{amp}} \Big(\cos(\omega\Delta t) \cos\big((k-1)\omega\Delta t\big) - \sin(\omega\Delta t) \sin\big((k-1)\omega\Delta t\big) \Big) \\
&= \tilde{v}_{j-1}^{\mathrm{amp}} \frac{\cos(\omega\Delta t)}{\sin(\omega\Delta t)} \cos\big((k-1)\omega\Delta t\big) \sin(\omega\Delta t) - \tilde{v}_{j-1}^{\mathrm{amp}} \sin(\omega\Delta t) \sin\big((k-1)\omega\Delta t\big) \\
&= \tilde{v}_{j-1}^{\mathrm{amp}} \frac{\cos(\omega\Delta t)}{2\sin(\omega\Delta t)} \Big(\sin(k\omega\Delta t) - \sin\big((k-2)\omega\Delta t\big)) \Big) \\
&\quad - \tilde{v}_{j-1}^{\mathrm{amp}} \sin(\omega\Delta t) \sin\big((k-1)\omega\Delta t\big) \\
&= \frac{\cos(\omega\Delta t)}{2\sin(\omega\Delta t)} \tilde{v}_{j-1}(k) - \sin(\omega\Delta t) \tilde{v}_{j-1}(k-1) - \frac{\cos(\omega\Delta t)}{2\sin(\omega\Delta t)} \tilde{v}_{j-1}(k-2) \,.
\end{aligned} \tag{C.55}$$

Thus, the extra input $\tilde{v}_{j-1}^{\perp}(k)$ can be substituted with the linear combination of input of $\tilde{v}_{j-1}(k)$ and its delayed values. We remark that due to convenience, we use dependent multi-inputs for the analysis throughout this thesis.

APPENDIX D

Stochastic Stability

There are many types of stochastic stability defined in the literature, and their relationships and properties can be found in [162–166]. Here we are only interested in certain notions of stochastic stability and we will develop theorems using their corresponding definitions.

Definition D.1 *A random sequence* $\{X(k) \in \mathbb{R}^n\}_{k=0}^{+\infty}$ *converges to* X^* *almost surely if*

$$\mathbb{P}\big[\lim_{k\to\infty} X(k) = X^*\big] = 1\,. \tag{D.1}$$

If sequences generated by a stochastic dynamical system converge to X^* *almost surely, then the solution* $X(k) \equiv X^*$ *is almost surely asymptotically stable.*

Note that almost sure convergence is also called convergence with probability one.

Definition D.2 *A random sequence* $\{X(k) \in \mathbb{R}^n\}_{k=0}^{+\infty}$ *converges to* X^* *in the* p*-th moment if*

$$\lim_{k\to\infty} \mathbb{E}\big[\underbrace{\big(X(k) - X^*\big) \otimes \cdots \otimes \big(X(k) - X^*\big)}_{p \text{ times}}\big] = 0\,. \tag{D.2}$$

If sequences generated by a stochastic dynamical system converge to X^* *in the* p*-th moment, then the solution* $X(k) \equiv X^*$ *is asymptotically stable in the* p*-th moment.*

It can be shown that stability in the second moment implies stability in the first moment (often called mean stability). In general there is no relationship between almost sure stability and moment stability but based on [204] (Theorem 8 in Chapter 8) we can state the following theorem.

Theorem D.1 *For the discrete-time linear stochastic system* $X(k+1) = \mathbf{A}(k)X(k)$*, where* $\mathbf{A}(k)$ *are mutually independently identically distributed matrices, asymptotic stability in the second moment implies almost sure asymptotic stability.*

In Chapters 5-7 we investigated the covariance dynamics, so we state the following theorem.

Theorem D.2 *For a discrete-time stochastic system, the second moment* $\mathbb{E}[X(k)\otimes X(k)]$ *is asymptotically stable if and only if the first moment* $\mathbb{E}[X(k)]$ *and the covariance* $\mathbb{E}\big[\big(X(k)-\mathbb{E}[X(k)]\big)\otimes\big(X(k)-\mathbb{E}[X(k)]\big)\big]$ *are asymptotically stable.*

The proof can be constructed by exploiting the relationship between the mean, the second moment and the covariance; see Definition E.2. Also, using the definitions and theorems above we can state the following theorem.

Theorem D.3 *For the discrete-time linear stochastic system* $X(k+1)=\mathbf{A}(k)X(k)$*, where* $\mathbf{A}(k)$ *are mutually independently identically distributed matrices, if the system is stable in the first moment, then asymptotic stability in covariance implies asymptotic stability in the second moment and almost sure asymptotic stability.*

APPENDIX E

Matrix Fundamentals

E.1 Vectorization, Kronecker Product, and Perfect Shuffle

One can refer to [198–200] for more information on the fundamental properties of Kronecker product, vectorization operator and related transformations. Here we recall the following definitions and theorems, and list some properties used in this dissertation.

Definition E.1 *Let $h_i \in \mathbb{R}^n$ denote the i-th column of matrix $\mathbf{H} \in \mathbb{R}^{n\times m}$, i.e., $\mathbf{H} = [h_1 \quad h_2 \quad \dots \quad h_m]$. The vector operator defined by*

$$\overline{vec}(\mathbf{H}) = \begin{bmatrix} h_1^{\mathrm{T}} & h_2^{\mathrm{T}} & \dots & h_m^{\mathrm{T}} \end{bmatrix}^{\mathrm{T}} \in \mathbb{R}^{mn}\,, \tag{E.1}$$

inserts the columns of the matrix below each other.

Theorem E.1 *For matrices $\mathbf{A} \in \mathbb{R}^{m\times n}$, $\mathbf{B} \in \mathbb{R}^{n\times l}$, $\mathbf{C} \in \mathbb{R}^{p\times q}$, and $\mathbf{D} \in \mathbb{R}^{q\times r}$, we have*

$$(\mathbf{AB}) \otimes (\mathbf{CD}) = (\mathbf{A} \otimes \mathbf{C})(\mathbf{B} \otimes \mathbf{D})\,, \tag{E.2}$$

where $\otimes$ denotes Kronecker product.

Theorem E.2 *For any three matrices $\mathbf{A}$, $\mathbf{B}$ and $\mathbf{C}$ for which the matrix product $\mathbf{ABC}$ is defined, we can write*

$$\overline{vec}(\mathbf{ABC}) = (\mathbf{C}^{\mathrm{T}} \otimes \mathbf{A})\overline{vec}(\mathbf{B})\,. \tag{E.3}$$

Definition E.2 *For a random variable $X \in \mathbb{R}^n$, the mean and second moment are defined as $\mathbb{E}[X] \in \mathbb{R}^n$ and $\mathbb{E}[XX^{\mathrm{T}}] \in \mathbb{R}^{n\times n}$, where $\mathbb{E}$ denotes the expected value. Similarly, the*

second central moment or covariance matrix is defined as $\mathbb{E}\big[\big(X-\mathbb{E}[X]\big)\big(X-\mathbb{E}[X]\big)^{\mathrm{T}}\big] \in \mathbb{R}^{n\times n}$. *Using Definition E.1 and Theorem E.2, one may show that*

$$\begin{aligned}
&\overline{vec}\big(\mathbb{E}[XX^{\mathrm{T}}]\big) = \mathbb{E}[X\otimes X]\,, \\
&\overline{vec}\Big(\mathbb{E}\big[\big(X-\mathbb{E}[X]\big)\big(X-\mathbb{E}[X]\big)^{\mathrm{T}}\big]\Big) = \mathbb{E}\big[\big(X-\mathbb{E}[X]\big)\otimes\big(X-\mathbb{E}[X]\big)\big]\,.
\end{aligned} \tag{E.4}$$

Theorem E.3 *For any partitioned matrices*

$$\mathbf{A} = \begin{bmatrix} \mathbf{A}_{11} & \mathbf{A}_{12} \\ \mathbf{A}_{21} & \mathbf{A}_{22} \end{bmatrix} \in \mathbb{R}^{m_1\times n_1}\,, \tag{E.5}$$

and $\mathbf{B}\in\mathbb{R}^{m_2\times n_2}$,

$$\begin{bmatrix} \mathbf{A}_{11} & \mathbf{A}_{12} \\ \mathbf{A}_{21} & \mathbf{A}_{22} \end{bmatrix} \otimes \mathbf{B} = \begin{bmatrix} \mathbf{A}_{11}\otimes\mathbf{B} & \mathbf{A}_{12}\otimes\mathbf{B} \\ \mathbf{A}_{21}\otimes\mathbf{B} & \mathbf{A}_{22}\otimes\mathbf{B} \end{bmatrix}\,. \tag{E.6}$$

We also introduce a matrix transformation, called perfect shuffle [200, 201], to show the relation between the Kronecker product of two matrices and its commutative partner.

Definition E.3 *For any positive integers* m *and* n, *the* $(m,\,n)$ *perfect shuffle [200] is the permutation matrix*

$$\mathcal{S}_{m,\,n} = \begin{bmatrix} \mathbf{I}(1:n:r,:) \\ \mathbf{I}(2:n:r,:) \\ \vdots \\ \mathbf{I}(n:n:r,:) \end{bmatrix}\,, \tag{E.7}$$

where $r = mn$ *and* $\mathbf{I}\in\mathbb{R}^{r\times r}$ *is the identity matrix. Here the colon operator is used to denote arithmetic sequences, that is,* $k:n:r$ *represents an arithmetic sequence from* k *to* r *with common difference* n. *It can be shown that*

$$\mathcal{S}_{m,\,n} = \begin{bmatrix} \mathbf{I}(:,1:m:r) & \mathbf{I}(:,2:m:r) & \cdots & \mathbf{I}(:,m:m:r) \end{bmatrix}\,, \tag{E.8}$$

and

$$\mathcal{S}_{m,\,n} = \mathcal{S}_{n,\,m}^{\mathrm{T}}\,. \tag{E.9}$$

Theorem E.4 *For any matrices* $\mathbf{A}\in\mathbb{R}^{m_1\times n_1}$ *and* $\mathbf{B}\in\mathbb{R}^{m_2\times n_2}$,

$$\mathbf{B}\otimes\mathbf{A} = \mathcal{S}_{m_1,\,m_2}(\mathbf{A}\otimes\mathbf{B})\mathcal{S}_{n_1,\,n_2}^{\mathrm{T}}\,. \tag{E.10}$$

From [199, 203], we have the following definition for cyclic forward shift matrix.

Definition E.4 *The $N \times N$ cyclic forward shift matrix is given by*

$$\sigma_N = \begin{bmatrix} 0 & 1 & 0 & \dots & 0 \\ 0 & 0 & 1 & \ddots & \vdots \\ \vdots & \vdots & \ddots & \ddots & 0 \\ 0 & 0 & \dots & 0 & 1 \\ 1 & 0 & 0 & \dots & 0 \end{bmatrix}, \tag{E.11}$$

which is populated with ones along the superdiagonal and in the $(N, 1)$ position, and zeros otherwise. It satisfies

$$(\sigma_N)^N = \mathbf{I}. \tag{E.12}$$

E.2 Block Matrix Inversion

From [202], we rephrase the following theorem.

Theorem E.5 *For a partitioned square matrix*

$$\mathbf{\Phi} = \begin{bmatrix} \mathbf{A} & \mathbf{B} \\ \mathbf{C} & \mathbf{D} \end{bmatrix} \in \mathbb{R}^{m \times m}, \tag{E.13}$$

where $\mathbf{A} \in \mathbb{R}^{m_1 \times m_1}$, $\mathbf{B} \in \mathbb{R}^{m_1 \times m_2}$, $\mathbf{C} \in \mathbb{R}^{m_2 \times m_1}$, $\mathbf{D} \in \mathbb{R}^{m_2 \times m_2}$, and $m_1 + m_2 = m$. If $\mathbf{A}$ and $\mathbf{D}$ are invertible, then its inverse is given by

$$\mathbf{\Phi}^{-1} = \begin{bmatrix} \mathbf{S}_\mathbf{D}^{-1} & -\mathbf{A}^{-1}\mathbf{B}\mathbf{S}_\mathbf{A}^{-1} \\ -\mathbf{D}^{-1}\mathbf{C}\mathbf{S}_\mathbf{D}^{-1} & \mathbf{S}_\mathbf{A}^{-1} \end{bmatrix} \in \mathbb{R}^{m \times m}, \tag{E.14}$$

where

$$\begin{aligned} \mathbf{S}_\mathbf{A} &= \mathbf{D} - \mathbf{C}\mathbf{A}^{-1}\mathbf{B}\,, \\ \mathbf{S}_\mathbf{D} &= \mathbf{A} - \mathbf{B}\mathbf{D}^{-1}\mathbf{C}\,, \end{aligned} \tag{E.15}$$

are the Schur complement of $\mathbf{A}$ and $\mathbf{D}$ in $\mathbf{\Phi}$, respectively. Moreover,

$$\det(\mathbf{\Phi}) = \det(\mathbf{D}) \det(\mathbf{S}_\mathbf{D}) = \det(\mathbf{A}) \det(\mathbf{S}_\mathbf{A}). \tag{E.16}$$

Corollary E.1 *(Generalized Matrix Determinant Lemma) Given $\mathbf{A} \in \mathbb{R}^{m \times m}$, $\mathbf{U} \in \mathbb{R}^{m \times n}$,*

$\mathbf{V} \in \mathbb{R}^{n\times m}$, $\mathbf{W} \in \mathbb{R}^{n\times n}$, *where* $\mathbf{A}$ *and* $\mathbf{W}$ *are invertible, then*

$$\det(\mathbf{A}+\mathbf{UWV}) = \det(\mathbf{A})\det(\mathbf{W})\det(\mathbf{W}^{-1}+\mathbf{VA}^{-1}\mathbf{U})\,. \tag{E.17}$$

Theorem E.6 *For a block matrix* $\mathbf{A} \in \mathbb{R}^{nJ\times nJ}$,

$$\mathbf{A} = \begin{bmatrix} \boldsymbol{\alpha}_1 & & & & \\ \boldsymbol{\beta}_2 & \boldsymbol{\alpha}_2 & & & \\ \boldsymbol{\xi}_3 & \boldsymbol{\beta}_3 & \boldsymbol{\alpha}_3 & & \\ & \ddots & \ddots & \ddots & \\ & & \boldsymbol{\xi}_J & \boldsymbol{\beta}_J & \boldsymbol{\alpha}_J \end{bmatrix} \tag{E.18}$$

where $\boldsymbol{\alpha}_k, \boldsymbol{\beta}_k, \boldsymbol{\xi}_k \in \mathbb{R}^{n\times n}$ *and* $\boldsymbol{\alpha}_k^{-1}$ *exists. Its inverse is given by*

$$\mathbf{A}^{-1} = \begin{bmatrix} \boldsymbol{\theta}_{11} & & & & \\ \boldsymbol{\theta}_{21} & \boldsymbol{\theta}_{22} & & & \\ \boldsymbol{\theta}_{31} & \boldsymbol{\theta}_{32} & \boldsymbol{\theta}_{33} & & \\ \vdots & \ddots & \ddots & \ddots & \\ \boldsymbol{\theta}_{J1} & \dots & \boldsymbol{\theta}_{J(J-2)} & \boldsymbol{\theta}_{J(J-1)} & \boldsymbol{\theta}_{JJ} \end{bmatrix} \tag{E.19}$$

where

$$\begin{bmatrix} \boldsymbol{\theta}_{(k+1)j} \\ \boldsymbol{\theta}_{(k+2)j} \end{bmatrix} = \begin{bmatrix} \mathbf{0} & \mathbf{I} \\ -\boldsymbol{\alpha}_{k+2}^{-1}\boldsymbol{\xi}_{k+2} & -\boldsymbol{\alpha}_{k+2}^{-1}\boldsymbol{\beta}_{k+2} \end{bmatrix} \begin{bmatrix} \boldsymbol{\theta}_{kj} \\ \boldsymbol{\theta}_{(k+1)j} \end{bmatrix}, \tag{E.20}$$

for $k = 1, \dots, J-2$ *and* $1 \le j \le k$, *with*

$$\begin{bmatrix} \boldsymbol{\theta}_{jj} \\ \boldsymbol{\theta}_{(j+1)j} \end{bmatrix} = \begin{bmatrix} \boldsymbol{\alpha}_j^{-1} \\ -\boldsymbol{\alpha}_{j+1}^{-1}\boldsymbol{\beta}_{j+1}\boldsymbol{\alpha}_j^{-1} \end{bmatrix} = \begin{bmatrix} \mathbf{0} & \mathbf{I} \\ -\boldsymbol{\alpha}_{j+1}^{-1}\boldsymbol{\xi}_{j+1} & -\boldsymbol{\alpha}_{j+1}^{-1}\boldsymbol{\beta}_{j+1} \end{bmatrix} \begin{bmatrix} \mathbf{0} \\ \boldsymbol{\alpha}_j^{-1} \end{bmatrix}. \tag{E.21}$$

Proof: Assuming that $\mathbf{B} = \mathbf{A}^{-1}$ takes the form in (E.19) and by matching the entries on the left and right hand side of $\mathbf{BA} = \mathbf{I}$, we get

$$\begin{aligned} &\boldsymbol{\theta}_{jj}\boldsymbol{\alpha}_j = \mathbf{I}\,, \quad j = 1, \dots, J \\ &\boldsymbol{\theta}_{j(j-1)}\boldsymbol{\alpha}_{j-1} + \boldsymbol{\theta}_{jj}\boldsymbol{\beta}_j = \mathbf{0}\,, \quad j = 2, \dots, J \\ &\boldsymbol{\theta}_{j(k-2)}\boldsymbol{\alpha}_{k-2} + \boldsymbol{\theta}_{j(k-1)}\boldsymbol{\beta}_{k-1} + \boldsymbol{\theta}_{jk}\boldsymbol{\xi}_k = \mathbf{0}, \quad j = 3, \dots, J \text{ and } 1 \le k \le j\,, \end{aligned} \tag{E.22}$$

which yields

$$\begin{bmatrix} \boldsymbol{\theta}_{j(k-2)} & \boldsymbol{\theta}_{j(k-1)} \end{bmatrix} = \begin{bmatrix} \boldsymbol{\theta}_{j(k-1)} & \boldsymbol{\theta}_{jk} \end{bmatrix} \begin{bmatrix} -\boldsymbol{\beta}_{k-1}\boldsymbol{\alpha}_{k-2}^{-1} & \mathbf{I} \\ -\boldsymbol{\xi}_k\boldsymbol{\alpha}_{k-2}^{-1} & \mathbf{0} \end{bmatrix}, \tag{E.23}$$

for $k = 1, \ldots, J-2$ and $1 \le j \le k$, and

$$\begin{bmatrix} \boldsymbol{\theta}_{jj} \\ \boldsymbol{\theta}_{(j+1)j} \end{bmatrix} = \begin{bmatrix} \boldsymbol{\alpha}_j^{-1} \\ -\boldsymbol{\alpha}_{j+1}^{-1}\boldsymbol{\beta}_{j+1}\boldsymbol{\alpha}_j^{-1} \end{bmatrix} = \begin{bmatrix} \mathbf{0} & \mathbf{I} \\ -\boldsymbol{\alpha}_{j+1}^{-1}\boldsymbol{\xi}_{j+1} & -\boldsymbol{\alpha}_{j+1}^{-1}\boldsymbol{\beta}_{j+1} \end{bmatrix} \begin{bmatrix} \mathbf{0} \\ \boldsymbol{\alpha}_j^{-1} \end{bmatrix}.$$

One can also check if (E.23) are satisfied, $\mathbf{BA} = \mathbf{I}$. Thus $\mathbf{B} = \mathbf{A}^{-1}$.

Corollary E.2 *From Theorem E.6, we have*

$$\begin{bmatrix} \boldsymbol{\theta}_{(J-1)j} \\ \boldsymbol{\theta}_{Jj} \end{bmatrix} = \prod_{k=j+1}^{J} \begin{bmatrix} \mathbf{0} & \mathbf{I} \\ -\boldsymbol{\alpha}_k^{-1}\boldsymbol{\xi}_k & -\boldsymbol{\alpha}_k^{-1}\boldsymbol{\beta}_k \end{bmatrix} \begin{bmatrix} \mathbf{0} \\ \boldsymbol{\alpha}_j^{-1} \end{bmatrix}, \tag{E.24}$$

where the compact form of matrix product is the pre-multiplication. Especially for $j = 1$ we get

$$\begin{bmatrix} \boldsymbol{\theta}_{(J-1)1} \\ \boldsymbol{\theta}_{J1} \end{bmatrix} = \prod_{k=2}^{J} \begin{bmatrix} \mathbf{0} & \mathbf{I} \\ -\boldsymbol{\alpha}_k^{-1}\boldsymbol{\xi}_k & -\boldsymbol{\alpha}_k^{-1}\boldsymbol{\beta}_k \end{bmatrix} \begin{bmatrix} \mathbf{0} \\ \boldsymbol{\alpha}_1^{-1} \end{bmatrix}. \tag{E.25}$$

Corollary E.3 *From Theorem E.6, if*

$$\begin{aligned} &\boldsymbol{\alpha}_1 = \boldsymbol{\alpha}_2 = \cdots = \boldsymbol{\alpha}_J = \boldsymbol{\alpha}, \\ &\boldsymbol{\beta}_2 = \boldsymbol{\beta}_3 = \cdots = \boldsymbol{\beta}_J = \boldsymbol{\beta}, \\ &\boldsymbol{\xi}_3 = \boldsymbol{\xi}_4 = \cdots = \boldsymbol{\xi}_J = \boldsymbol{\xi}, \end{aligned} \tag{E.26}$$

then

$$\begin{bmatrix} \boldsymbol{\theta}_{J-1} \\ \boldsymbol{\theta}_J \end{bmatrix} = \begin{bmatrix} \mathbf{0} & \mathbf{I} \\ -\boldsymbol{\alpha}^{-1}\boldsymbol{\xi} & -\boldsymbol{\alpha}^{-1}\boldsymbol{\beta} \end{bmatrix}^{J-1} \begin{bmatrix} \mathbf{0} \\ \boldsymbol{\alpha}^{-1} \end{bmatrix}, \tag{E.27}$$

and

$$\begin{aligned}
\begin{bmatrix} \boldsymbol{\theta}_{J-1} & \boldsymbol{\theta}_{J-2} \\ \boldsymbol{\theta}_{J} & \boldsymbol{\theta}_{J-1} \end{bmatrix} &= \begin{bmatrix} \mathbf{0} & \mathbf{I} \\ -\boldsymbol{\alpha}^{-1}\boldsymbol{\xi} & -\boldsymbol{\alpha}^{-1}\boldsymbol{\beta} \end{bmatrix}^{J-2} \begin{bmatrix} \boldsymbol{\alpha}^{-1} & \mathbf{0} \\ -\boldsymbol{\alpha}^{-1}\boldsymbol{\beta}\boldsymbol{\alpha}^{-1} & \boldsymbol{\alpha}^{-1} \end{bmatrix} \\
&= \left(\begin{bmatrix} \boldsymbol{\alpha} & \mathbf{0} \\ \mathbf{0} & \boldsymbol{\alpha} \end{bmatrix}^{-1} \begin{bmatrix} \mathbf{0} & \mathbf{I} \\ -\boldsymbol{\xi}\boldsymbol{\alpha}^{-1} & -\boldsymbol{\beta}\boldsymbol{\alpha}^{-1} \end{bmatrix} \begin{bmatrix} \boldsymbol{\alpha} & \mathbf{0} \\ \mathbf{0} & \boldsymbol{\alpha} \end{bmatrix} \right)^{J-2} \\
&\quad \times \begin{bmatrix} \boldsymbol{\alpha} & \mathbf{0} \\ \mathbf{0} & \boldsymbol{\alpha} \end{bmatrix}^{-1} \begin{bmatrix} \mathbf{I} & \mathbf{0} \\ -\boldsymbol{\beta}\boldsymbol{\alpha}^{-1} & \mathbf{I} \end{bmatrix} \\
&= \begin{bmatrix} \boldsymbol{\alpha} & \mathbf{0} \\ \mathbf{0} & \boldsymbol{\alpha} \end{bmatrix}^{-1} \begin{bmatrix} \mathbf{0} & \mathbf{I} \\ -\boldsymbol{\xi}\boldsymbol{\alpha}^{-1} & -\boldsymbol{\beta}\boldsymbol{\alpha}^{-1} \end{bmatrix}^{J-2} \begin{bmatrix} \mathbf{I} & \mathbf{0} \\ -\boldsymbol{\beta}\boldsymbol{\alpha}^{-1} & \mathbf{I} \end{bmatrix}.
\end{aligned} \tag{E.28}$$

APPENDIX F

Derivations of Open chain

F.1 Simplification of the System Matrix

The matrix $\bar{\bar{\mathbf{A}}}$ for an open chain of J vehicles can be written as

$$\begin{aligned}\bar{\bar{\mathbf{A}}} &= \sum_{\boldsymbol{r}=1}^{N} w_{\boldsymbol{r}} \mathbf{A}_{\boldsymbol{r}} \otimes \mathbf{A}_{\boldsymbol{r}} \\ &= \sum_{\boldsymbol{r}=1}^{N} w_{\boldsymbol{r}} \begin{bmatrix} \boldsymbol{\alpha}_{1,r_1} & & & & & \\ \boldsymbol{\alpha}_{3,r_1}+\boldsymbol{\alpha}_{2,r_2} & \boldsymbol{\alpha}_{1,r_2} & & & & \\ \boldsymbol{\alpha}_{4,r_2} & \boldsymbol{\alpha}_{3,r_2}+\boldsymbol{\alpha}_{2,r_3} & \boldsymbol{\alpha}_{1,r_3} & & & \\ & \ddots & \ddots & \ddots & & \\ & & \boldsymbol{\alpha}_{4,r_{j-1}} & \boldsymbol{\alpha}_{3,r_{J-1}}+\boldsymbol{\alpha}_{2,r_J} & \boldsymbol{\alpha}_{1,r_J} \end{bmatrix} \otimes \mathbf{A}_{\boldsymbol{r}} \\ &= \begin{bmatrix} \hat{\mathbf{A}}_{1,1} & & & & & \\ \hat{\mathbf{A}}_{3,1}+\hat{\mathbf{A}}_{2,2} & \hat{\mathbf{A}}_{1,2} & & & & \\ \hat{\mathbf{A}}_{4,2} & \hat{\mathbf{A}}_{3,2}+\hat{\mathbf{A}}_{2,3} & \hat{\mathbf{A}}_{1,3} & & & \\ & \ddots & \ddots & \ddots & & \\ & & \hat{\mathbf{A}}_{4,J-1} & \hat{\mathbf{A}}_{3,J-1}+\hat{\mathbf{A}}_{2,J} & \hat{\mathbf{A}}_{1,J} \end{bmatrix}, \end{aligned} \tag{F.1}$$

where

$$\hat{\mathbf{A}}_{i,j} = \sum_{\boldsymbol{r}=1}^{N} w_{\boldsymbol{r}} \boldsymbol{\alpha}_{i,r_j} \otimes \mathbf{A}_{\boldsymbol{r}} = \sum_{\boldsymbol{r}=1}^{N} w_{\boldsymbol{r}} \hat{\mathbf{S}}_1 (\mathbf{A}_{\boldsymbol{r}} \otimes \boldsymbol{\alpha}_{i,r_j}) \hat{\mathbf{S}}_1^{\top} = \hat{\mathbf{S}}_1 \tilde{\mathbf{A}}_{i,j} \hat{\mathbf{S}}_1^{\top} . \tag{F.2}$$

Here,

$$\hat{\mathbf{S}}_1 = \mathcal{S}_{2J(N+1),2(N+1)} , \tag{F.3}$$

is the perfect shuffle and

$$\tilde{\mathbf{A}}_{i,j} = \sum_{\boldsymbol{r}=1}^{N} w_{\boldsymbol{r}} \mathbf{A}_{\boldsymbol{r}} \otimes \boldsymbol{\alpha}_{i,r_j} \,. \tag{F.4}$$

Therefore,

$$\bar{\bar{\mathbf{A}}} = \bar{\bar{\mathbf{S}}}_1 \tilde{\bar{\mathbf{A}}} \bar{\bar{\mathbf{S}}}_1^\top \,, \tag{F.5}$$

where

$$\bar{\bar{\mathbf{S}}}_1 = \mathbf{I}_J \otimes \hat{\mathbf{S}}_1 \,, \tag{F.6}$$

and

$$\tilde{\bar{\mathbf{A}}} = \begin{bmatrix} \tilde{\mathbf{A}}_{1,1} & & & & \\ \tilde{\mathbf{A}}_{3,1} + \tilde{\mathbf{A}}_{2,2} & \tilde{\mathbf{A}}_{1,2} & & & \\ \tilde{\mathbf{A}}_{4,2} & \tilde{\mathbf{A}}_{3,2} + \tilde{\mathbf{A}}_{2,3} & \tilde{\mathbf{A}}_{1,3} & & \\ & \ddots & \ddots & \ddots & \\ & & \tilde{\mathbf{A}}_{4,J-1} & \tilde{\mathbf{A}}_{3,J-1} + \tilde{\mathbf{A}}_{2,J} & \tilde{\mathbf{A}}_{1,J} \end{bmatrix} . \tag{F.7}$$

By defining

$$\begin{aligned} \bar{\hat{\boldsymbol{\alpha}}}_{i_1 i_2} &= \sum_{\substack{\boldsymbol{r}=1 \\ j_1 \neq j_2}}^{N} w_{\boldsymbol{r}} \boldsymbol{\alpha}_{i_1,r_{j_1}} \otimes \boldsymbol{\alpha}_{i_2,r_{j_2}} = \bar{\boldsymbol{\alpha}}_{i_1} \otimes \bar{\boldsymbol{\alpha}}_{i_2} \,, \\ \bar{\bar{\boldsymbol{\alpha}}}_{i_1 i_2} &= \sum_{\substack{\boldsymbol{r}=1 \\ j_1 = j_2}}^{N} w_{\boldsymbol{r}} \boldsymbol{\alpha}_{i_1,r_{j_1}} \otimes \boldsymbol{\alpha}_{i_2,r_{j_2}} = \sum_{l=1}^{N} w_l \boldsymbol{\alpha}_{i_1,l} \otimes \boldsymbol{\alpha}_{i_2,l} \,, \end{aligned} \tag{F.8}$$

we obtain that

$$\begin{aligned} \tilde{\mathbf{A}}_{i,1} &= \sum_{\boldsymbol{r}=1}^{N} w_{\boldsymbol{r}} \mathbf{A}_{\boldsymbol{r}} \otimes \boldsymbol{\alpha}_{i,r_1} \\ &= \begin{bmatrix} \bar{\bar{\boldsymbol{\alpha}}}_{1i} & & & & \\ \bar{\bar{\boldsymbol{\alpha}}}_{3i} + \bar{\hat{\boldsymbol{\alpha}}}_{2i} & \bar{\hat{\boldsymbol{\alpha}}}_{1i} & & & \\ \bar{\hat{\boldsymbol{\alpha}}}_{4i} & \bar{\hat{\boldsymbol{\alpha}}}_{3i} + \bar{\hat{\boldsymbol{\alpha}}}_{2i} & \bar{\hat{\boldsymbol{\alpha}}}_{1i} & & \\ & \ddots & \ddots & \ddots & \\ & & \bar{\hat{\boldsymbol{\alpha}}}_{4i} & \bar{\hat{\boldsymbol{\alpha}}}_{3i} + \bar{\hat{\boldsymbol{\alpha}}}_{2i} & \bar{\hat{\boldsymbol{\alpha}}}_{1i} \end{bmatrix} , \end{aligned}$$

$$\tilde{\mathbf{A}}_{i,2} = \sum_{\boldsymbol{r}=1}^{N} w_{\boldsymbol{r}} \mathbf{A}_{\boldsymbol{r}} \otimes \boldsymbol{\alpha}_{i,r_2}$$

$$= \begin{bmatrix} \bar{\bar{\boldsymbol{\alpha}}}_{1i} & & & & & \\ \bar{\bar{\boldsymbol{\alpha}}}_{3i} + \bar{\bar{\boldsymbol{\alpha}}}_{2i} & \bar{\bar{\boldsymbol{\alpha}}}_{1i} & & & & \\ \bar{\bar{\boldsymbol{\alpha}}}_{4i} & \bar{\bar{\boldsymbol{\alpha}}}_{3i} + \bar{\bar{\boldsymbol{\alpha}}}_{2i} & \bar{\bar{\boldsymbol{\alpha}}}_{1i} & & & \\ & \ddots & \ddots & \ddots & & \\ & & \bar{\bar{\boldsymbol{\alpha}}}_{4i} & \bar{\bar{\boldsymbol{\alpha}}}_{3i} + \bar{\bar{\boldsymbol{\alpha}}}_{2i} & \bar{\bar{\boldsymbol{\alpha}}}_{1i} \end{bmatrix},$$

$$\vdots \tag{F.9}$$

$$\tilde{\mathbf{A}}_{i,J-1} = \sum_{\boldsymbol{r}=1}^{N} w_{\boldsymbol{r}} \mathbf{A}_{\boldsymbol{r}} \otimes \boldsymbol{\alpha}_{i,r_J}$$

$$= \begin{bmatrix} \bar{\bar{\boldsymbol{\alpha}}}_{1i} & & & & & \\ \bar{\bar{\boldsymbol{\alpha}}}_{3i} + \bar{\bar{\boldsymbol{\alpha}}}_{2i} & \bar{\bar{\boldsymbol{\alpha}}}_{1i} & & & & \\ \bar{\bar{\boldsymbol{\alpha}}}_{4i} & \bar{\bar{\boldsymbol{\alpha}}}_{3i} + \bar{\bar{\boldsymbol{\alpha}}}_{2i} & \bar{\bar{\boldsymbol{\alpha}}}_{1i} & & & \\ & \ddots & \ddots & \ddots & & \\ & & \bar{\bar{\boldsymbol{\alpha}}}_{4i} & \bar{\bar{\boldsymbol{\alpha}}}_{3i} + \bar{\bar{\boldsymbol{\alpha}}}_{2i} & \bar{\bar{\boldsymbol{\alpha}}}_{1i} & \\ & & & \bar{\bar{\boldsymbol{\alpha}}}_{4i} & \bar{\bar{\boldsymbol{\alpha}}}_{3i} + \bar{\bar{\boldsymbol{\alpha}}}_{2i} & \bar{\bar{\boldsymbol{\alpha}}}_{1i} \end{bmatrix}, \tag{F.10}$$

$$\tilde{\mathbf{A}}_{i,J} = \sum_{\boldsymbol{r}=1}^{N} w_{\boldsymbol{r}} \mathbf{A}_{\boldsymbol{r}} \otimes \boldsymbol{\alpha}_{i,r_J}$$

$$= \begin{bmatrix} \bar{\bar{\boldsymbol{\alpha}}}_{1i} & & & & & \\ \bar{\bar{\boldsymbol{\alpha}}}_{3i} + \bar{\bar{\boldsymbol{\alpha}}}_{2i} & \bar{\bar{\boldsymbol{\alpha}}}_{1i} & & & & \\ \bar{\bar{\boldsymbol{\alpha}}}_{4i} & \bar{\bar{\boldsymbol{\alpha}}}_{3i} + \bar{\bar{\boldsymbol{\alpha}}}_{2i} & \bar{\bar{\boldsymbol{\alpha}}}_{1i} & & & \\ & \ddots & \ddots & \ddots & & \\ & & \bar{\bar{\boldsymbol{\alpha}}}_{4i} & \bar{\bar{\boldsymbol{\alpha}}}_{3i} + \bar{\bar{\boldsymbol{\alpha}}}_{2i} & \bar{\bar{\boldsymbol{\alpha}}}_{1i} & \\ & & & \bar{\bar{\boldsymbol{\alpha}}}_{4i} & \bar{\bar{\boldsymbol{\alpha}}}_{3i} + \bar{\bar{\boldsymbol{\alpha}}}_{2i} & \bar{\bar{\boldsymbol{\alpha}}}_{1i} \end{bmatrix}. \tag{F.11}$$

F.2 Simplification of Input Matrix

Notice that

$$\begin{aligned}
\bar{\bar{\mathbf{K}}}_1 &= \bar{\bar{\mathbf{A}}} - \bar{\mathbf{A}} \otimes \bar{\mathbf{A}} \\
&= \bar{\bar{\mathbf{A}}} - \begin{bmatrix} \bar{\boldsymbol{\alpha}}_1 & & & & \\ \bar{\boldsymbol{\alpha}}_3 + \bar{\boldsymbol{\alpha}}_2 & \bar{\boldsymbol{\alpha}}_1 & & & \\ \bar{\boldsymbol{\alpha}}_4 & \bar{\boldsymbol{\alpha}}_3 + \bar{\boldsymbol{\alpha}}_2 & \bar{\boldsymbol{\alpha}}_1 & & \\ & \ddots & \ddots & \ddots & \\ & & \bar{\boldsymbol{\alpha}}_4 & \bar{\boldsymbol{\alpha}}_3 + \bar{\boldsymbol{\alpha}}_2 & \bar{\boldsymbol{\alpha}}_1 \end{bmatrix} \otimes \bar{\mathbf{A}} \qquad \text{(F.12)} \\
&= \begin{bmatrix} \mathbf{F}_{1,1} & & & & \\ \mathbf{F}_{3,1} + \mathbf{F}_{2,2} & \mathbf{F}_{1,2} & & & \\ \mathbf{F}_{4,2} & \mathbf{F}_{3,2} + \mathbf{F}_{2,3} & \mathbf{F}_{1,3} & & \\ & \ddots & \ddots & \ddots & \\ & & \mathbf{F}_{4,J-1} & \mathbf{F}_{3,J-1} + \mathbf{F}_{2,J} & \mathbf{F}_{1,J} \end{bmatrix},
\end{aligned}$$

where

$$\begin{aligned}
\mathbf{F}_{i,1} &= \sum_{\boldsymbol{r}=1}^{N} w_{\boldsymbol{r}} \boldsymbol{\alpha}_{i,r_1} \otimes \mathbf{A}_{\boldsymbol{r}} - \bar{\boldsymbol{\alpha}}_i \otimes \bar{\mathbf{A}} \\
&= \hat{\mathbf{S}}_1 \left(\sum_{\boldsymbol{r}=1}^{N} w_{\boldsymbol{r}} \mathbf{A}_{\boldsymbol{r}} \otimes \boldsymbol{\alpha}_{i,r_1} - \bar{\mathbf{A}} \otimes \bar{\boldsymbol{\alpha}}_i \right) \hat{\mathbf{S}}_1^\top \\
&= \hat{\mathbf{S}}_1 \begin{bmatrix} \boldsymbol{f}_{1i} & & & & \\ \boldsymbol{f}_{3i} & \mathbf{0} & & & \\ \mathbf{0} & \mathbf{0} & \mathbf{0} & & \\ & \ddots & \ddots & \ddots & \\ & & \mathbf{0} & \mathbf{0} & \mathbf{0} \end{bmatrix} \hat{\mathbf{S}}_1^\top, \\
\mathbf{F}_{i,2} &= \sum_{\boldsymbol{r}=1}^{N} w_{\boldsymbol{r}} \boldsymbol{\alpha}_{i,r_2} \otimes \mathbf{A}_{\boldsymbol{r}} - \bar{\boldsymbol{\alpha}}_i \otimes \bar{\mathbf{A}} \\
&= \hat{\mathbf{S}}_1 \left(\sum_{\boldsymbol{r}=1}^{N} w_{\boldsymbol{r}} \mathbf{A}_{\boldsymbol{r}} \otimes \boldsymbol{\alpha}_{i,r_2} - \bar{\mathbf{A}} \otimes \bar{\boldsymbol{\alpha}}_i \right) \hat{\mathbf{S}}_1^\top
\end{aligned}$$

$$= \hat{\mathbf{S}}_1 \begin{bmatrix} \mathbf{0} & & & & \\ \boldsymbol{f}_{2i} & \boldsymbol{f}_{1i} & & & \\ \boldsymbol{f}_{4i} & \boldsymbol{f}_{3i} & \mathbf{0} & & \\ & \ddots & \ddots & \ddots & \\ & & \mathbf{0} & \mathbf{0} & \mathbf{0} \end{bmatrix} \hat{\mathbf{S}}_1^\top ,$$

$$\vdots$$

$$\begin{aligned} \mathbf{F}_{i,J-1} &= \sum_{\boldsymbol{r}=1}^{N} w_{\boldsymbol{r}} \boldsymbol{\alpha}_{i,r_{J-1}} \otimes \mathbf{A}_{\boldsymbol{r}} - \bar{\boldsymbol{\alpha}}_i \otimes \bar{\mathbf{A}} \\ &= \hat{\mathbf{S}}_1 \left(\sum_{\boldsymbol{r}=1}^{N} w_{\boldsymbol{r}} \mathbf{A}_{\boldsymbol{r}} \otimes \boldsymbol{\alpha}_{i,r_{J-1}} - \bar{\mathbf{A}} \otimes \bar{\boldsymbol{\alpha}}_i \right) \hat{\mathbf{S}}_1^\top \\ &= \hat{\mathbf{S}}_1 \begin{bmatrix} \mathbf{0} & & & & & \\ \mathbf{0} & \mathbf{0} & & & & \\ \mathbf{0} & \mathbf{0} & \mathbf{0} & & & \\ & \ddots & \ddots & \ddots & & \\ & & \mathbf{0} & \boldsymbol{f}_{2i} & \boldsymbol{f}_{1i} & \\ & & & \boldsymbol{f}_{4i} & \boldsymbol{f}_{3i} & \mathbf{0} \end{bmatrix} \hat{\mathbf{S}}_1^\top , \end{aligned} \tag{F.13}$$

$$\begin{aligned} \mathbf{F}_{i,J} &= \sum_{\boldsymbol{r}=1}^{N} w_{\boldsymbol{r}} \boldsymbol{\alpha}_{i,r_J} \otimes \mathbf{A}_{\boldsymbol{r}} - \bar{\boldsymbol{\alpha}}_i \otimes \bar{\mathbf{A}} \\ &= \hat{\mathbf{S}}_1 \left(\sum_{\boldsymbol{r}=1}^{N} w_{\boldsymbol{r}} \mathbf{A}_{\boldsymbol{r}} \otimes \boldsymbol{\alpha}_{i,r_J} - \bar{\mathbf{A}} \otimes \bar{\boldsymbol{\alpha}}_i \right) \hat{\mathbf{S}}_1^\top \\ &= \hat{\mathbf{S}}_1 \begin{bmatrix} \mathbf{0} & & & & & \\ \mathbf{0} & \mathbf{0} & & & & \\ \mathbf{0} & \mathbf{0} & \mathbf{0} & & & \\ & \ddots & \ddots & \ddots & & \\ & & \mathbf{0} & \mathbf{0} & \mathbf{0} & \\ & & & \mathbf{0} & \boldsymbol{f}_{2i} & \boldsymbol{f}_{1i} \end{bmatrix} \hat{\mathbf{S}}_1^\top , \end{aligned}$$

and

$$\boldsymbol{f}_{ij} = \bar{\bar{\boldsymbol{\alpha}}}_{ij} - \bar{\hat{\boldsymbol{\alpha}}}_{ij} . \tag{F.14}$$

Similarly,

$$
\begin{aligned}
\bar{\bar{\mathbf{K}}}_2 &= \sum_{\boldsymbol{r}=1}^{N} w_{\boldsymbol{r}} \mathbf{A}_{\boldsymbol{r}} \otimes \mathbf{B}_{r_1} - \bar{\mathbf{A}} \otimes \bar{\mathbf{B}} \\
&= \sum_{\boldsymbol{r}=1}^{N} w_{\boldsymbol{r}} \begin{bmatrix}
\boldsymbol{\alpha}_{1,r_1} & & & & & \\
\boldsymbol{\alpha}_{3,r_1} + \boldsymbol{\alpha}_{2,r_2} & \boldsymbol{\alpha}_{1,r_2} & & & & \\
\boldsymbol{\alpha}_{4,r_2} & \boldsymbol{\alpha}_{3,r_2} + \boldsymbol{\alpha}_{2,r_3} & \boldsymbol{\alpha}_{1,r_3} & & & \\
 & \ddots & \ddots & \ddots & & \\
 & & \boldsymbol{\alpha}_{4,r_{j-1}} & \boldsymbol{\alpha}_{3,r_{J-1}} + \boldsymbol{\alpha}_{2,r_J} & \boldsymbol{\alpha}_{1,r_J}
\end{bmatrix} \otimes \mathbf{B}_{r_1} \\
&\quad - \begin{bmatrix}
\bar{\boldsymbol{\alpha}}_1 & & & & \\
\bar{\boldsymbol{\alpha}}_3 + \bar{\boldsymbol{\alpha}}_2 & \bar{\boldsymbol{\alpha}}_1 & & & \\
\bar{\boldsymbol{\alpha}}_4 & \bar{\boldsymbol{\alpha}}_3 + \bar{\boldsymbol{\alpha}}_2 & \bar{\boldsymbol{\alpha}}_1 & & \\
 & \ddots & \ddots & \ddots & \\
 & & \bar{\boldsymbol{\alpha}}_4 & \bar{\boldsymbol{\alpha}}_3 + \bar{\boldsymbol{\alpha}}_2 & \bar{\boldsymbol{\alpha}}_1
\end{bmatrix} \otimes \bar{\mathbf{B}} \qquad \text{(F.15)} \\
&= \begin{bmatrix}
\mathbf{D}_1 & & & & \\
\mathbf{D}_3 & \mathbf{0} & & & \\
\mathbf{0} & \mathbf{0} & \mathbf{0} & & \\
 & \ddots & \ddots & \ddots & \\
 & & \mathbf{0} & \mathbf{0} & \mathbf{0}
\end{bmatrix},
\end{aligned}
$$

where

$$
\begin{aligned}
\mathbf{D}_i &= \sum_{\boldsymbol{r}=1}^{N} w_{\boldsymbol{r}} \boldsymbol{\alpha}_{i,r_1} \otimes \mathbf{B}_{r_1} - \bar{\boldsymbol{\alpha}}_i \otimes \bar{\mathbf{B}} = \hat{\mathbf{S}}_1 \Big(\sum_{r_1=1}^{N} w_{r_1} \mathbf{B}_{r_1} \otimes \boldsymbol{\alpha}_{i,r_1} - \bar{\mathbf{B}} \otimes \bar{\boldsymbol{\alpha}}_1 \Big) \hat{\mathbf{S}}_4^\top \\
&= \hat{\mathbf{S}}_1 \begin{bmatrix} \boldsymbol{d}_{i1} \\ \boldsymbol{d}_{i2} \\ \mathbf{0} \\ \vdots \\ \mathbf{0} \end{bmatrix} \hat{\mathbf{S}}_4^\top , \qquad \text{(F.16)}
\end{aligned}
$$

and

$$
\boldsymbol{d}_{ij} = \sum_{r_1=1}^{N} w_{r_1} \boldsymbol{\beta}_{j,r_1} \otimes \boldsymbol{\alpha}_{i,r_1} - \bar{\boldsymbol{\beta}}_j \otimes \bar{\boldsymbol{\alpha}}_i , \quad \hat{\mathbf{S}}_4 = \mathcal{S}_{2,2(N+1)} . \qquad \text{(F.17)}
$$

Also,

$$\bar{\bar{\mathbf{K}}}_3 = \sum_{\boldsymbol{r}=1}^{N} w_{\boldsymbol{r}} \mathbf{B}_{r_1} \otimes \mathbf{A}_{\boldsymbol{r}} - \bar{\mathbf{B}} \otimes \bar{\mathbf{A}} = \begin{bmatrix} \mathbf{G}_1 \\ \mathbf{G}_2 \\ \mathbf{0} \\ \vdots \\ \mathbf{0} \end{bmatrix}, \tag{F.18}$$

where

$$\begin{aligned}
\mathbf{G}_i &= \sum_{\boldsymbol{r}=1}^{N} \boldsymbol{\beta}_{i,r_1} \otimes \mathbf{A}_{\boldsymbol{r}} - \bar{\boldsymbol{\beta}}_i \otimes \bar{\mathbf{A}} = \hat{\mathbf{S}}_1 \Big(\sum_{\boldsymbol{r}=1}^{N} \mathbf{A}_{\boldsymbol{r}} \otimes \boldsymbol{\beta}_{i,r_1} - \bar{\mathbf{A}} \otimes \bar{\boldsymbol{\beta}}_i \Big) \hat{\mathbf{S}}_5^\top \\
&= \hat{\mathbf{S}}_1 \Big(\sum_{\boldsymbol{r}=1}^{N} w_{\boldsymbol{r}} \begin{bmatrix} \boldsymbol{\alpha}_{1,r_1} & & & & & \\ \boldsymbol{\alpha}_{3,r_1} + \boldsymbol{\alpha}_{2,r_2} & \boldsymbol{\alpha}_{1,r_2} & & & & \\ \boldsymbol{\alpha}_{4,r_2} & \boldsymbol{\alpha}_{3,r_2} + \boldsymbol{\alpha}_{2,r_3} & \boldsymbol{\alpha}_{1,r_3} & & & \\ & \ddots & \ddots & \ddots & & \\ & & \boldsymbol{\alpha}_{4,r_{j-1}} & \boldsymbol{\alpha}_{3,r_{J-1}} + \boldsymbol{\alpha}_{2,r_J} & \boldsymbol{\alpha}_{1,r_J} \end{bmatrix} \\
&\quad \otimes \boldsymbol{\beta}_{i,r_1} - \bar{\mathbf{A}} \otimes \bar{\boldsymbol{\beta}}_i \Big) \hat{\mathbf{S}}_5^\top \\
&= \hat{\mathbf{S}}_1 \begin{bmatrix} \boldsymbol{g}_{i1} & & & & \\ \boldsymbol{g}_{i3} & \mathbf{0} & & & \\ \mathbf{0} & \mathbf{0} & \mathbf{0} & & \\ & \ddots & \ddots & \ddots & \\ & & \mathbf{0} & \mathbf{0} & \mathbf{0} \end{bmatrix} \hat{\mathbf{S}}_5^\top,
\end{aligned} \tag{F.19}$$

and

$$\boldsymbol{g}_{ij} = \sum_{r_1=1}^{N} w_{r_1} \boldsymbol{\alpha}_{j,r_1} \otimes \boldsymbol{\beta}_{i,r_1} - \bar{\boldsymbol{\alpha}}_j \otimes \bar{\boldsymbol{\beta}}_i, \qquad \hat{\mathbf{S}}_5 = \mathcal{S}_{2J(N+1),2}. \tag{F.20}$$

Again,

$$\bar{\bar{\mathbf{K}}}_4 = \textstyle\sum_{\boldsymbol{r}=1}^{N} w_{\boldsymbol{r}} \mathbf{B}_{r_1} \otimes \mathbf{B}_{r_1} - \bar{\mathbf{B}} \otimes \bar{\mathbf{B}} = \begin{bmatrix} \mathbf{H}_1 \\ \mathbf{H}_2 \\ \mathbf{0} \\ \vdots \\ \mathbf{0} \end{bmatrix}, \tag{F.21}$$

where

$$\begin{aligned}\mathbf{H}_i &= \sum_{\boldsymbol{r}=1}^{N} \boldsymbol{\beta}_{i,r_1} \otimes \mathbf{B}_{r_1} - \bar{\boldsymbol{\beta}}_i \otimes \bar{\mathbf{B}} = \hat{\mathbf{S}}_1 \Big(\sum_{\boldsymbol{r}=1}^{N} \mathbf{B}_{r_1} \otimes \boldsymbol{\beta}_{i,r_1} - \bar{\mathbf{B}} \otimes \bar{\boldsymbol{\beta}}_i \Big) \hat{\mathbf{S}}_6^\top \\ &= \hat{\mathbf{S}}_1 \begin{bmatrix} \boldsymbol{h}_{i1} \\ \boldsymbol{h}_{i2} \\ \mathbf{0} \\ \vdots \\ \mathbf{0} \end{bmatrix} \hat{\mathbf{S}}_6^\top ,\end{aligned} \tag{F.22}$$

and

$$\boldsymbol{h}_{ij} = \sum_{r_1=1}^{N} w_{r_1} \boldsymbol{\beta}_{j,r_1} \otimes \boldsymbol{\beta}_{i,r_1} - \bar{\boldsymbol{\beta}}_j \otimes \bar{\boldsymbol{\beta}}_i \,, \qquad \hat{\mathbf{S}}_6 = \mathcal{S}_{2,2} \,. \tag{F.23}$$

Assuming that

$$\mathbf{Q} = \begin{bmatrix} \boldsymbol{q}_1 \\ \boldsymbol{q}_2 \\ \vdots \\ \boldsymbol{q}_J \end{bmatrix} , \tag{F.24}$$

then

$$\mathbf{Q} \otimes \mathbf{Q} = \begin{bmatrix} \boldsymbol{q}_1 \\ \boldsymbol{q}_2 \\ \vdots \\ \boldsymbol{q}_J \end{bmatrix} \otimes \mathbf{Q} = \begin{bmatrix} \boldsymbol{q}_1 \otimes \mathbf{Q} \\ \boldsymbol{q}_2 \otimes \mathbf{Q} \\ \vdots \\ \boldsymbol{q}_J \otimes \mathbf{Q} \end{bmatrix} , \tag{F.25}$$

Thus, we can calculate

$$\bar{\bar{\mathbf{K}}}_1(\mathbf{Q} \otimes \mathbf{Q}) = \begin{bmatrix} \mathbf{F}_{1,1}(\boldsymbol{q}_1 \otimes \mathbf{Q}) \\ (\mathbf{F}_{3,1} + \mathbf{F}_{2,2})(\boldsymbol{q}_1 \otimes \mathbf{Q}) + \mathbf{F}_{1,2}(\boldsymbol{q}_2 \otimes \mathbf{Q}) \\ \mathbf{F}_{4,2}(\boldsymbol{q}_1 \otimes \mathbf{Q}) + (\mathbf{F}_{3,2} + \mathbf{F}_{2,3})(\boldsymbol{q}_2 \otimes \mathbf{Q}) + \mathbf{F}_{1,3}(\boldsymbol{q}_3 \otimes \mathbf{Q}) \\ \vdots \\ \mathbf{F}_{4,J-1}(\boldsymbol{q}_{J-2} \otimes \mathbf{Q}) + (\mathbf{F}_{3,J-1} + \mathbf{F}_{2,J})(\boldsymbol{q}_{J-1} \otimes \mathbf{Q}) + \mathbf{F}_{1,J}(\boldsymbol{q}_J \otimes \mathbf{Q}) \end{bmatrix} , \tag{F.26}$$

where

$$\mathbf{F}_{i,1}(\boldsymbol{q}_j \otimes \mathbf{Q}) = \hat{\mathbf{S}}_1 \begin{bmatrix} \boldsymbol{f}_{1i} & & & & \\ \boldsymbol{f}_{3i} & \mathbf{0} & & & \\ \mathbf{0} & \mathbf{0} & \mathbf{0} & & \\ & \ddots & \ddots & \ddots & \\ & & \mathbf{0} & \mathbf{0} & \mathbf{0} \end{bmatrix} \begin{bmatrix} \boldsymbol{q}_1 \otimes \boldsymbol{q}_j \\ \boldsymbol{q}_2 \otimes \boldsymbol{q}_j \\ \vdots \\ \boldsymbol{q}_J \otimes \boldsymbol{q}_j \end{bmatrix} \hat{\mathbf{S}}_6^\top$$

$$= \hat{\mathbf{S}}_1 \begin{bmatrix} \boldsymbol{f}_{1i}(\boldsymbol{q}_1 \otimes \boldsymbol{q}_j) \\ \boldsymbol{f}_{3i}(\boldsymbol{q}_1 \otimes \boldsymbol{q}_j) \\ \mathbf{0} \\ \vdots \\ \mathbf{0} \end{bmatrix} \hat{\mathbf{S}}_6^\top,$$

$$\mathbf{F}_{i,2}(\boldsymbol{q}_j \otimes \mathbf{Q}) = \hat{\mathbf{S}}_1 \begin{bmatrix} \mathbf{0} & & & & \\ \boldsymbol{f}_{2i} & \boldsymbol{f}_{1i} & & & \\ \boldsymbol{f}_{4i} & \boldsymbol{f}_{3i} & \mathbf{0} & & \\ & \ddots & \ddots & \ddots & \\ & & \mathbf{0} & \mathbf{0} & \mathbf{0} \end{bmatrix} \begin{bmatrix} \boldsymbol{q}_1 \otimes \boldsymbol{q}_j \\ \boldsymbol{q}_2 \otimes \boldsymbol{q}_j \\ \vdots \\ \boldsymbol{q}_J \otimes \boldsymbol{q}_j \end{bmatrix} \hat{\mathbf{S}}_6^\top \tag{F.27}$$

$$= \hat{\mathbf{S}}_1 \begin{bmatrix} \mathbf{0} \\ \boldsymbol{f}_{2i}(\boldsymbol{q}_1 \otimes \boldsymbol{q}_j) + \boldsymbol{f}_{1i}(\boldsymbol{q}_2 \otimes \boldsymbol{q}_j) \\ \boldsymbol{f}_{4i}(\boldsymbol{q}_1 \otimes \boldsymbol{q}_j) + \boldsymbol{f}_{3i}(\boldsymbol{q}_2 \otimes \boldsymbol{q}_j) \\ \mathbf{0} \\ \vdots \\ \mathbf{0} \end{bmatrix} \hat{\mathbf{S}}_6^\top,$$

$$\vdots$$

$$\mathbf{F}_{i,J-1}(\boldsymbol{q}_j \otimes \mathbf{Q}) = \hat{\mathbf{S}}_1 \begin{bmatrix} \mathbf{0} & & & & & \\ \mathbf{0} & \mathbf{0} & & & & \\ \mathbf{0} & \mathbf{0} & \mathbf{0} & & & \\ & \ddots & \ddots & \ddots & & \\ & & \mathbf{0} & \boldsymbol{f}_{2i} & \boldsymbol{f}_{1i} & \\ & & & \boldsymbol{f}_{4i} & \boldsymbol{f}_{3i} & \mathbf{0} \end{bmatrix} \begin{bmatrix} \boldsymbol{q}_1 \otimes \boldsymbol{q}_j \\ \boldsymbol{q}_2 \otimes \boldsymbol{q}_j \\ \vdots \\ \boldsymbol{q}_J \otimes \boldsymbol{q}_j \end{bmatrix} \hat{\mathbf{S}}_6^\top$$

$$= \hat{\mathbf{S}}_1 \begin{bmatrix} & & \mathbf{0} & \\ & & \vdots & \\ & & \mathbf{0} & \\ \boldsymbol{f}_{2i}(\boldsymbol{q}_{J-2} \otimes \boldsymbol{q}_j) + \boldsymbol{f}_{1i}(\boldsymbol{q}_{J-1} \otimes \boldsymbol{q}_j) \\ \boldsymbol{f}_{4i}(\boldsymbol{q}_{J-2} \otimes \boldsymbol{q}_j) + \boldsymbol{f}_{3i}(\boldsymbol{q}_{J-1} \otimes \boldsymbol{q}_j) \end{bmatrix} \hat{\mathbf{S}}_6^\top ,$$

$$\mathbf{F}_{i,J}(\boldsymbol{q}_j \otimes \mathbf{Q}) = \hat{\mathbf{S}}_1 \begin{bmatrix} \mathbf{0} & & & & & \\ \mathbf{0} & \mathbf{0} & & & & \\ \mathbf{0} & \mathbf{0} & \mathbf{0} & & & \\ & \ddots & \ddots & \ddots & & \\ & & \mathbf{0} & \mathbf{0} & \mathbf{0} & \\ & & & \mathbf{0} & \boldsymbol{f}_{2i} & \boldsymbol{f}_{1i} \end{bmatrix} \begin{bmatrix} \boldsymbol{q}_1 \otimes \boldsymbol{q}_j \\ \boldsymbol{q}_2 \otimes \boldsymbol{q}_j \\ \vdots \\ \boldsymbol{q}_J \otimes \boldsymbol{q}_j \end{bmatrix} \hat{\mathbf{S}}_6^\top$$

$$= \hat{\mathbf{S}}_1 \begin{bmatrix} & & \mathbf{0} & \\ & & \vdots & \\ & & \mathbf{0} & \\ \boldsymbol{f}_{2i}(\boldsymbol{q}_{J-1} \otimes \boldsymbol{q}_j) + \boldsymbol{f}_{1i}(\boldsymbol{q}_J \otimes \boldsymbol{q}_j) \end{bmatrix} \hat{\mathbf{S}}_6^\top .$$

Moreover,

$$\mathbf{Q} \otimes \mathbf{I} = \begin{bmatrix} \boldsymbol{q}_1 \\ \boldsymbol{q}_2 \\ \vdots \\ \boldsymbol{q}_J \end{bmatrix} \otimes \mathbf{I} = \begin{bmatrix} \boldsymbol{q}_1 \otimes \mathbf{I} \\ \boldsymbol{q}_2 \otimes \mathbf{I} \\ \vdots \\ \boldsymbol{q}_J \otimes \mathbf{I} \end{bmatrix} , \tag{F.28}$$

so

$$\bar{\bar{\mathbf{K}}}_2(\mathbf{Q} \otimes \mathbf{I}) = \begin{bmatrix} \mathbf{D}_1(\boldsymbol{q}_1 \otimes \mathbf{I}) \\ \mathbf{D}_3(\boldsymbol{q}_1 \otimes \mathbf{I}) \\ \mathbf{0} \\ \vdots \\ \mathbf{0} \end{bmatrix} , \qquad \bar{\bar{\mathbf{K}}}_3(\mathbf{I} \otimes \mathbf{Q}) = \begin{bmatrix} \mathbf{G}_1(\mathbf{I} \otimes \mathbf{Q}) \\ \mathbf{G}_2(\mathbf{I} \otimes \mathbf{Q}) \\ \mathbf{0} \\ \vdots \\ \mathbf{0} \end{bmatrix} . \tag{F.29}$$

Therefore,

$$\bar{\bar{\mathbf{B}}} = \bar{\bar{\mathbf{K}}}_1(\mathbf{Q} \otimes \mathbf{Q}) + \bar{\bar{\mathbf{K}}}_2(\mathbf{Q} \otimes \mathbf{I}) + \bar{\bar{\mathbf{K}}}_3(\mathbf{I} \otimes \mathbf{Q}) + \bar{\bar{\mathbf{K}}}_4 := \begin{bmatrix} \bar{\bar{\mathbf{B}}}_1 \\ \bar{\bar{\mathbf{B}}}_2 \\ \vdots \\ \bar{\bar{\mathbf{B}}}_J \end{bmatrix} , \tag{F.30}$$

where

$$\bar{\bar{\mathbf{B}}}_j = \hat{\mathbf{S}}_1 \hat{\mathbf{B}}_j \hat{\mathbf{S}}_6^\top \,, \tag{F.31}$$

for $j = 1\,,\,\ldots\,,\,J$.

In particular,

$$\hat{\hat{\mathbf{B}}} = \begin{bmatrix} \hat{\mathbf{B}}_1 \\ \hat{\mathbf{B}}_2 \\ \vdots \\ \hat{\mathbf{B}}_J \end{bmatrix} \,, \tag{F.32}$$

and

$$\begin{aligned}
\hat{\mathbf{B}}_1 &= \hat{\mathbf{S}}_1^\top \bar{\bar{\mathbf{B}}}_1 \hat{\mathbf{S}}_6 = \hat{\mathbf{S}}_1^\top \big(\mathbf{F}_{1,1}(\boldsymbol{q}_1 \otimes \mathbf{Q}) + \mathbf{D}_1(\boldsymbol{q}_1 \otimes \mathbf{I}) + \mathbf{G}_1(\mathbf{I} \otimes \mathbf{Q}) + \mathbf{H}_1 \big) \hat{\mathbf{S}}_6 \\
&= \begin{bmatrix} \boldsymbol{f}_{11}(\boldsymbol{q}_1 \otimes \boldsymbol{q}_1) \\ \boldsymbol{f}_{31}(\boldsymbol{q}_1 \otimes \boldsymbol{q}_1) \\ \mathbf{0} \\ \vdots \\ \mathbf{0} \end{bmatrix} + \begin{bmatrix} \boldsymbol{d}_{11}(\mathbf{I} \otimes \boldsymbol{q}_1) \\ \boldsymbol{d}_{12}(\mathbf{I} \otimes \boldsymbol{q}_1) \\ \mathbf{0} \\ \vdots \\ \mathbf{0} \end{bmatrix} + \begin{bmatrix} \boldsymbol{g}_{11}(\boldsymbol{q}_1 \otimes \mathbf{I}) \\ \boldsymbol{g}_{13}(\boldsymbol{q}_1 \otimes \mathbf{I}) \\ \mathbf{0} \\ \vdots \\ \mathbf{0} \end{bmatrix} + \begin{bmatrix} \boldsymbol{h}_{11} \\ \boldsymbol{h}_{12} \\ \mathbf{0} \\ \vdots \\ \mathbf{0} \end{bmatrix} \\
&= \begin{bmatrix} \boldsymbol{f}_{11}(\boldsymbol{q}_1 \otimes \boldsymbol{q}_1) + \boldsymbol{d}_{11}(\mathbf{I} \otimes \boldsymbol{q}_1) + \boldsymbol{g}_{11}(\boldsymbol{q}_1 \otimes \mathbf{I}) + \boldsymbol{h}_{11} \\ \boldsymbol{f}_{31}(\boldsymbol{q}_1 \otimes \boldsymbol{q}_1) + \boldsymbol{d}_{12}(\mathbf{I} \otimes \boldsymbol{q}_1) + \boldsymbol{g}_{13}(\boldsymbol{q}_1 \otimes \mathbf{I}) + \boldsymbol{h}_{12} \\ \mathbf{0} \\ \vdots \\ \mathbf{0} \end{bmatrix} := \begin{bmatrix} \hat{\mathbf{B}}_{11} \\ \hat{\mathbf{B}}_{12} \\ \mathbf{0} \\ \vdots \\ \mathbf{0} \end{bmatrix} \,, \qquad \text{(F.33)} \\
\hat{\mathbf{B}}_2 &= \hat{\mathbf{S}}_1^\top \bar{\bar{\mathbf{B}}}_2 \hat{\mathbf{S}}_6 \\
&= \hat{\mathbf{S}}_1^\top \big((\mathbf{F}_{3,1} + \mathbf{F}_{2,2})(\boldsymbol{q}_1 \otimes \mathbf{Q}) + \mathbf{F}_{1,2}(\boldsymbol{q}_2 \otimes \mathbf{Q}) + \mathbf{D}_3(\boldsymbol{q}_1 \otimes \mathbf{I}) + \mathbf{G}_2(\mathbf{I} \otimes \mathbf{Q}) + \mathbf{H}_2 \big) \hat{\mathbf{S}}_6 \\
&= \begin{bmatrix} \boldsymbol{f}_{13}(\boldsymbol{q}_1 \otimes \boldsymbol{q}_3) \\ \boldsymbol{f}_{33}(\boldsymbol{q}_1 \otimes \boldsymbol{q}_3) + \boldsymbol{f}_{22}(\boldsymbol{q}_1 \otimes \boldsymbol{q}_1) + \boldsymbol{f}_{12}(\boldsymbol{q}_2 \otimes \boldsymbol{q}_1) \\ \boldsymbol{f}_{42}(\boldsymbol{q}_1 \otimes \boldsymbol{q}_1) + \boldsymbol{f}_{32}(\boldsymbol{q}_2 \otimes \boldsymbol{q}_1) \\ \mathbf{0} \\ \vdots \\ \mathbf{0} \end{bmatrix} + \begin{bmatrix} \mathbf{0} \\ \boldsymbol{f}_{21}(\boldsymbol{q}_1 \otimes \boldsymbol{q}_2) + \boldsymbol{f}_{11}(\boldsymbol{q}_2 \otimes \boldsymbol{q}_2) \\ \boldsymbol{f}_{41}(\boldsymbol{q}_1 \otimes \boldsymbol{q}_2) + \boldsymbol{f}_{31}(\boldsymbol{q}_2 \otimes \boldsymbol{q}_2) \\ \mathbf{0} \\ \vdots \\ \mathbf{0} \end{bmatrix}
\end{aligned}$$

$$+\begin{bmatrix}\boldsymbol{d}_{31}(\mathbf{I}\otimes\boldsymbol{q}_1)\\ \boldsymbol{d}_{32}(\mathbf{I}\otimes\boldsymbol{q}_1)\\ \mathbf{0}\\ \vdots\\ \mathbf{0}\end{bmatrix}+\begin{bmatrix}\boldsymbol{g}_{21}(\boldsymbol{q}_1\otimes\mathbf{I})\\ \boldsymbol{g}_{23}(\boldsymbol{q}_1\otimes\mathbf{I})\\ \mathbf{0}\\ \vdots\\ \mathbf{0}\end{bmatrix}+\begin{bmatrix}\boldsymbol{h}_{21}\\ \boldsymbol{h}_{22}\\ \mathbf{0}\\ \vdots\\ \mathbf{0}\end{bmatrix}:=\begin{bmatrix}\hat{\mathbf{B}}_{21}\\ \hat{\mathbf{B}}_{22}\\ \hat{\mathbf{B}}_{23}\\ \mathbf{0}\\ \vdots\\ \mathbf{0}\end{bmatrix},$$

$$\vdots$$

$$\begin{aligned}\hat{\mathbf{B}}_J &= \hat{\mathbf{S}}_1^\top\bar{\bar{\mathbf{B}}}_J\hat{\mathbf{S}}_6\\ &= \hat{\mathbf{S}}_1^\top\Big(\mathbf{F}_{4,J-1}(\boldsymbol{q}_{J-2}\otimes\mathbf{Q})+(\mathbf{F}_{3,J-1}+\mathbf{F}_{2,J})(\boldsymbol{q}_{J-1}\otimes\mathbf{Q})+\mathbf{F}_{1,J}(\boldsymbol{q}_J\otimes\mathbf{Q})\Big)\hat{\mathbf{S}}_6\\ &= \begin{bmatrix}\mathbf{0}\\ \vdots\\ \mathbf{0}\\ \boldsymbol{f}_{24}(\boldsymbol{q}_{J-2}\otimes\boldsymbol{q}_{J-2})+\boldsymbol{f}_{14}(\boldsymbol{q}_{J-1}\otimes\boldsymbol{q}_{J-2})\\ \boldsymbol{f}_{44}(\boldsymbol{q}_{J-2}\otimes\boldsymbol{q}_{J-2})+\boldsymbol{f}_{34}(\boldsymbol{q}_{J-1}\otimes\boldsymbol{q}_{J-2})\end{bmatrix}\\ &+\begin{bmatrix}\mathbf{0}\\ \vdots\\ \mathbf{0}\\ \boldsymbol{f}_{23}(\boldsymbol{q}_{J-2}\otimes\boldsymbol{q}_{J-1})+\boldsymbol{f}_{13}(\boldsymbol{q}_{J-1}\otimes\boldsymbol{q}_{J-1})\\ \boldsymbol{f}_{43}(\boldsymbol{q}_{J-2}\otimes\boldsymbol{q}_{J-1})+\boldsymbol{f}_{33}(\boldsymbol{q}_{J-1}\otimes\boldsymbol{q}_{J-1})+\boldsymbol{f}_{22}(\boldsymbol{q}_{J-1}\otimes\boldsymbol{q}_J)+\boldsymbol{f}_{12}(\boldsymbol{q}_J\otimes\boldsymbol{q}_J)\end{bmatrix}\\ &+\begin{bmatrix}\mathbf{0}\\ \vdots\\ \mathbf{0}\\ \boldsymbol{f}_{2J}(\boldsymbol{q}_{J-1}\otimes\boldsymbol{q}_J)+\boldsymbol{f}_{1J}(\boldsymbol{q}_J\otimes\boldsymbol{q}_J)\end{bmatrix}:=\begin{bmatrix}0\\ \vdots\\ 0\\ \hat{\mathbf{B}}_{J,J-1}\\ \hat{\mathbf{B}}_{J,J}\end{bmatrix},\end{aligned}$$

Thus,

$$\bar{\bar{\mathbf{B}}}=\begin{bmatrix}\bar{\bar{\mathbf{B}}}_1\\ \bar{\bar{\mathbf{B}}}_2\\ \vdots\\ \bar{\bar{\mathbf{B}}}_J\end{bmatrix}=\begin{bmatrix}\hat{\mathbf{S}}_1\hat{\mathbf{B}}_1\hat{\mathbf{S}}_6^\top\\ \hat{\mathbf{S}}_1\hat{\mathbf{B}}_2\hat{\mathbf{S}}_6^\top\\ \vdots\\ \hat{\mathbf{S}}_1\hat{\mathbf{B}}_J\hat{\mathbf{S}}_6^\top\end{bmatrix}=\bar{\bar{\mathbf{S}}}_1\begin{bmatrix}\hat{\mathbf{B}}_1\\ \hat{\mathbf{B}}_2\\ \vdots\\ \hat{\mathbf{B}}_J\end{bmatrix}\bar{\bar{\mathbf{S}}}_6^\top:=\bar{\bar{\mathbf{S}}}_1\hat{\bar{\mathbf{B}}}\bar{\bar{\mathbf{S}}}_6^\top. \tag{F.34}$$

F.3 Transfer Function for the Mean Dynamics

Assuming that

$$(z\bar{\mathbf{I}} - \bar{\mathbf{A}})^{-1} = \begin{bmatrix} \boldsymbol{\theta}_1 & & & & \\ \boldsymbol{\theta}_2 & \boldsymbol{\theta}_1 & & & \\ \boldsymbol{\theta}_3 & \boldsymbol{\theta}_2 & \boldsymbol{\theta}_1 & & \\ \vdots & \ddots & \ddots & \ddots & \\ \boldsymbol{\theta}_J & \dots & \boldsymbol{\theta}_3 & \boldsymbol{\theta}_2 & \boldsymbol{\theta}_1 \end{bmatrix}, \tag{F.35}$$

and by applying Theorem E.6, one can get

$$\begin{bmatrix} \boldsymbol{\theta}_J & \boldsymbol{\theta}_{J-1} \end{bmatrix} = \begin{bmatrix} \mathbf{0} & \tilde{\boldsymbol{\alpha}}_1^{-1} \end{bmatrix} \begin{bmatrix} \mathbf{0} & \mathbf{I} \\ \bar{\boldsymbol{\alpha}}_4 \tilde{\boldsymbol{\alpha}}_1^{-1} & \bar{\boldsymbol{\alpha}}_{23} \tilde{\boldsymbol{\alpha}}_1^{-1} \end{bmatrix}^{J-2} \begin{bmatrix} \mathbf{I} & \mathbf{0} \\ \bar{\boldsymbol{\alpha}}_{23} \tilde{\boldsymbol{\alpha}}_1^{-1} & \mathbf{I} \end{bmatrix}, \tag{F.36}$$

where

$$\tilde{\boldsymbol{\alpha}}_1 = z\mathbf{I} - \bar{\boldsymbol{\alpha}}_1 = \left[\begin{array}{c|cccc} z\mathbf{I} - \boldsymbol{a}_1 & -w_1\boldsymbol{a}_3 & -w_2\boldsymbol{a}_3 & \dots & -w_N\boldsymbol{a}_3 \\ \hline -\mathbf{I} & z\mathbf{I} & & & \\ & -\mathbf{I} & z\mathbf{I} & & \\ & & \ddots & \ddots & \\ & & & -\mathbf{I} & z\mathbf{I} \end{array}\right], \tag{F.37}$$

$$\bar{\boldsymbol{\alpha}}_{23} = \bar{\boldsymbol{\alpha}}_2 + \bar{\boldsymbol{\alpha}}_3 = \left[\begin{array}{c|ccc} \boldsymbol{a}_2 & w_1(\boldsymbol{a}_4 + \boldsymbol{a}_5) & \dots & w_N(\boldsymbol{a}_4 + \boldsymbol{a}_5) \\ \hline \mathbf{0} & \mathbf{0} & \dots & \mathbf{0} \end{array}\right].$$

Assuming

$$\tilde{\boldsymbol{\alpha}}_1^{-1} = \begin{bmatrix} \boldsymbol{\kappa}_1 & \boldsymbol{\kappa}_2 \\ \boldsymbol{\kappa}_3 & \boldsymbol{\kappa}_4 \end{bmatrix}, \tag{F.38}$$

and applying block matrix inverse [202], we get

$$
\begin{aligned}
\boldsymbol{\kappa}_1 &= \left(z\mathbf{I} - \boldsymbol{a}_1 - \begin{bmatrix} -w_1\boldsymbol{a}_3 & -w_2\boldsymbol{a}_3 & \dots & -w_N\boldsymbol{a}_3 \end{bmatrix} \begin{bmatrix} z\mathbf{I} & & & \\ -\mathbf{I} & z\mathbf{I} & & \\ & \ddots & \ddots & \\ & & -\mathbf{I} & z\mathbf{I} \end{bmatrix}^{-1} \begin{bmatrix} -\mathbf{I} \\ \mathbf{0} \\ \vdots \\ \mathbf{0} \end{bmatrix} \right)^{-1} \\
&= \left(z\mathbf{I} - \boldsymbol{a}_1 - \begin{bmatrix} w_1\boldsymbol{a}_3 & w_2\boldsymbol{a}_3 & \dots & w_N\boldsymbol{a}_3 \end{bmatrix} \begin{bmatrix} \frac{1}{z}\mathbf{I} & \mathbf{0} & \cdots & \mathbf{0} \\ \frac{1}{z^2}\mathbf{I} & \frac{1}{z}\mathbf{I} & \cdots & \mathbf{0} \\ \vdots & \vdots & \ddots & \vdots \\ \frac{1}{z^N}\mathbf{I} & \frac{1}{z^{N-1}}\mathbf{I} & \cdots & \frac{1}{z}\mathbf{I} \end{bmatrix} \begin{bmatrix} \mathbf{I} \\ \mathbf{0} \\ \vdots \\ \mathbf{0} \end{bmatrix} \right)^{-1} \\
&= \left(z\mathbf{I} - \boldsymbol{a}_1 - \sum_{i=1}^{N} \frac{w_i}{z^i}\boldsymbol{a}_3 \right)^{-1} , \qquad \text{(F.39)} \\
\boldsymbol{\kappa}_3 &= -\begin{bmatrix} z\mathbf{I} & & & \\ -\mathbf{I} & z\mathbf{I} & & \\ & \ddots & \ddots & \\ & & -\mathbf{I} & z\mathbf{I} \end{bmatrix}^{-1} \begin{bmatrix} -\mathbf{I} \\ \mathbf{0} \\ \vdots \\ \mathbf{0} \end{bmatrix} \boldsymbol{\kappa}_1 = \begin{bmatrix} \frac{1}{z}\boldsymbol{\kappa}_1 \\ \frac{1}{z^2}\boldsymbol{\kappa}_1 \\ \vdots \\ \frac{1}{z^N}\boldsymbol{\kappa}_1 \end{bmatrix} .
\end{aligned}
$$

Therefore,

$$
\begin{aligned}
\boldsymbol{c}\tilde{\boldsymbol{\alpha}}_1^{-1} &= \begin{bmatrix} c_1 & 0' & \dots & 0' \end{bmatrix} \begin{bmatrix} \boldsymbol{\kappa}_1 & \boldsymbol{\kappa}_2 \\ \boldsymbol{\kappa}_3 & \boldsymbol{\kappa}_4 \end{bmatrix} = \begin{bmatrix} c_1\boldsymbol{\kappa}_1 & c_1\boldsymbol{\kappa}_2 \end{bmatrix} , \\
\bar{\boldsymbol{\alpha}}_4\tilde{\boldsymbol{\alpha}}_1^{-1} &= \begin{bmatrix} \boldsymbol{\kappa}_5 & * \\ \mathbf{0} & \mathbf{0} \end{bmatrix} , \qquad \bar{\boldsymbol{\alpha}}_{23}\tilde{\boldsymbol{\alpha}}_1^{-1} = \begin{bmatrix} \boldsymbol{\kappa}_7 & * \\ \mathbf{0} & \mathbf{0} \end{bmatrix} ,
\end{aligned} \qquad \text{(F.40)}
$$

where $*$ are block matrices we do not need later, and

$$
\begin{aligned}
\boldsymbol{\kappa}_5 &= \begin{bmatrix} w_1\boldsymbol{a}_6 & w_2\boldsymbol{a}_6 & \dots & w_N\boldsymbol{a}_6 \end{bmatrix} \boldsymbol{\kappa}_3 = \sum_{i=1}^{N} \frac{w_i}{z^i}\boldsymbol{a}_6\boldsymbol{\kappa}_1 , \\
\boldsymbol{\kappa}_7 &= \boldsymbol{a}_2\boldsymbol{\kappa}_1 + \begin{bmatrix} w_1(\boldsymbol{a}_4+\boldsymbol{a}_5) & w_2(\boldsymbol{a}_4+\boldsymbol{a}_5) & \dots & w_N(\boldsymbol{a}_4+\boldsymbol{a}_5) \end{bmatrix} \boldsymbol{\kappa}_3 \qquad \text{(F.41)} \\
&= \boldsymbol{a}_2\boldsymbol{\kappa}_1 + \sum_{i=1}^{N} \frac{w_i}{z^i}(\boldsymbol{a}_4+\boldsymbol{a}_5)\boldsymbol{\kappa}_1 .
\end{aligned}
$$

Thus, the transfer function of the mean dynamics becomes

$$
\begin{aligned}
\Gamma(z) &= \bar{\mathbf{C}}(z\bar{\mathbf{I}} - \bar{\mathbf{A}})^{-1}\bar{\mathbf{B}} \\
&= \begin{bmatrix} \mathbf{0} & \dots & \mathbf{0} & \boldsymbol{c} \end{bmatrix}
\begin{bmatrix}
\boldsymbol{\theta}_1 & & & & \\
\boldsymbol{\theta}_2 & \boldsymbol{\theta}_1 & & & \\
\boldsymbol{\theta}_3 & \boldsymbol{\theta}_2 & \boldsymbol{\theta}_1 & & \\
\vdots & \ddots & \ddots & \ddots & \\
\boldsymbol{\theta}_J & \dots & \boldsymbol{\theta}_3 & \boldsymbol{\theta}_2 & \boldsymbol{\theta}_1
\end{bmatrix}
\begin{bmatrix} \bar{\boldsymbol{\beta}}_1 \\ \bar{\boldsymbol{\beta}}_2 \\ \mathbf{0} \\ \vdots \\ \mathbf{0} \end{bmatrix} \\
&= \boldsymbol{c} \begin{bmatrix} \boldsymbol{\theta}_J & \boldsymbol{\theta}_{J-1} \end{bmatrix}
\begin{bmatrix} \bar{\boldsymbol{\beta}}_1 \\ \bar{\boldsymbol{\beta}}_2 \end{bmatrix} \\
&= \boldsymbol{c} \begin{bmatrix} \mathbf{0} & \tilde{\boldsymbol{\alpha}}_1^{-1} \end{bmatrix}
\begin{bmatrix} \mathbf{0} & \mathbf{I} \\ \bar{\boldsymbol{\alpha}}_4\tilde{\boldsymbol{\alpha}}_1^{-1} & \bar{\boldsymbol{\alpha}}_{23}\tilde{\boldsymbol{\alpha}}_1^{-1} \end{bmatrix}^{J-2}
\begin{bmatrix} \mathbf{I} & \mathbf{0} \\ \bar{\boldsymbol{\alpha}}_{23}\tilde{\boldsymbol{\alpha}}_1^{-1} & \mathbf{I} \end{bmatrix}
\begin{bmatrix} \bar{\boldsymbol{\beta}}_1 \\ \bar{\boldsymbol{\beta}}_2 \end{bmatrix} \\
&= \begin{bmatrix} 0' & 0' & c_1\boldsymbol{\kappa}_1 & c_1\boldsymbol{\kappa}_2 \end{bmatrix}
\begin{bmatrix} \mathbf{0} & \mathbf{0} & \mathbf{I} & \mathbf{0} \\ \mathbf{0} & \mathbf{0} & \mathbf{0} & \mathbf{I} \\ \boldsymbol{\kappa}_5 & * & \boldsymbol{\kappa}_7 & * \\ \mathbf{0} & \mathbf{0} & \mathbf{0} & \mathbf{0} \end{bmatrix}^{J-2}
\begin{bmatrix} \mathbf{I} & \mathbf{0} & \mathbf{0} & \mathbf{0} \\ \mathbf{0} & \mathbf{I} & \mathbf{0} & \mathbf{0} \\ \boldsymbol{\kappa}_7 & * & \mathbf{I} & \mathbf{0} \\ \mathbf{0} & \mathbf{0} & \mathbf{0} & \mathbf{I} \end{bmatrix}
\begin{bmatrix} \boldsymbol{b}_1 + \boldsymbol{b}_2\bar{\mathbf{R}} \\ \mathbf{0} \\ \boldsymbol{b}_3\bar{\mathbf{R}} \\ \mathbf{0} \end{bmatrix} \\
&= c_1 \begin{bmatrix} \mathbf{0} & \mathbf{0} & \boldsymbol{\kappa}_1 & \boldsymbol{\kappa}_2 \end{bmatrix}
\begin{bmatrix} \mathbf{0} & \mathbf{0} & \mathbf{I} & \mathbf{0} \\ \mathbf{0} & \mathbf{0} & \mathbf{0} & \mathbf{I} \\ \boldsymbol{\kappa}_5 & * & \boldsymbol{\kappa}_7 & * \\ \mathbf{0} & \mathbf{0} & \mathbf{0} & \mathbf{0} \end{bmatrix}^{J-2}
\begin{bmatrix} \mathbf{I} & \mathbf{0} \\ \mathbf{0} & \mathbf{0} \\ \boldsymbol{\kappa}_7 & \mathbf{I} \\ \mathbf{0} & \mathbf{0} \end{bmatrix}
\begin{bmatrix} \boldsymbol{b}_1 + \boldsymbol{b}_2\bar{\mathbf{R}} \\ \boldsymbol{b}_3\bar{\mathbf{R}} \end{bmatrix} \qquad \text{(F.42)} \\
&= c_1 \begin{bmatrix} \mathbf{0} & \mathbf{0} & \boldsymbol{\kappa}_1 & \boldsymbol{\kappa}_2 \end{bmatrix}
\begin{bmatrix} \mathbf{0} & \mathbf{0} & \mathbf{I} & \mathbf{0} \\ \mathbf{0} & \mathbf{0} & \mathbf{0} & \mathbf{I} \\ \boldsymbol{\kappa}_5 & * & \boldsymbol{\kappa}_7 & * \\ \mathbf{0} & \mathbf{0} & \mathbf{0} & \mathbf{0} \end{bmatrix}^{J-3}
\begin{bmatrix} \mathbf{0} & \mathbf{I} \\ \mathbf{0} & \mathbf{0} \\ \boldsymbol{\kappa}_5 & \boldsymbol{\kappa}_7 \\ \mathbf{0} & \mathbf{0} \end{bmatrix}
\begin{bmatrix} \mathbf{I} & \mathbf{0} \\ \boldsymbol{\kappa}_7 & \mathbf{I} \end{bmatrix}
\begin{bmatrix} \boldsymbol{b}_1 + \boldsymbol{b}_2\bar{\mathbf{R}} \\ \boldsymbol{b}_3\bar{\mathbf{R}} \end{bmatrix} \\
&= c_1 \begin{bmatrix} \mathbf{0} & \mathbf{0} & \boldsymbol{\kappa}_1 & \boldsymbol{\kappa}_2 \end{bmatrix}
\begin{bmatrix} \mathbf{0} & \mathbf{0} & \mathbf{I} & \mathbf{0} \\ \mathbf{0} & \mathbf{0} & \mathbf{0} & \mathbf{I} \\ \boldsymbol{\kappa}_5 & * & \boldsymbol{\kappa}_7 & * \\ \mathbf{0} & \mathbf{0} & \mathbf{0} & \mathbf{0} \end{bmatrix}^{J-4}
\begin{bmatrix} \mathbf{0} & \mathbf{I} \\ \mathbf{0} & \mathbf{0} \\ \boldsymbol{\kappa}_5 & \boldsymbol{\kappa}_7 \\ \mathbf{0} & \mathbf{0} \end{bmatrix} \\
&\quad \times \begin{bmatrix} \mathbf{0} & \mathbf{I} \\ \boldsymbol{\kappa}_5 & \boldsymbol{\kappa}_7 \end{bmatrix}
\begin{bmatrix} \mathbf{I} & \mathbf{0} \\ \boldsymbol{\kappa}_7 & \mathbf{I} \end{bmatrix}
\begin{bmatrix} \boldsymbol{b}_1 + \boldsymbol{b}_2\bar{\mathbf{R}} \\ \boldsymbol{b}_3\bar{\mathbf{R}} \end{bmatrix}
\end{aligned}
$$

$$
\begin{aligned}
&= \cdots \\
&= c_1 \begin{bmatrix} \mathbf{0} & \mathbf{0} & \boldsymbol{\kappa}_1 & \boldsymbol{\kappa}_2 \end{bmatrix} \begin{bmatrix} \mathbf{0} & \mathbf{I} \\ \mathbf{0} & \mathbf{0} \\ \boldsymbol{\kappa}_5 & \boldsymbol{\kappa}_7 \\ \mathbf{0} & \mathbf{0} \end{bmatrix} \begin{bmatrix} \mathbf{0} & \mathbf{I} \\ \boldsymbol{\kappa}_5 & \boldsymbol{\kappa}_7 \end{bmatrix}^{J-3} \begin{bmatrix} \mathbf{I} & \mathbf{0} \\ \boldsymbol{\kappa}_7 & \mathbf{I} \end{bmatrix} \begin{bmatrix} \boldsymbol{b}_1 + \boldsymbol{b}_2 \bar{\mathbf{R}} \\ \boldsymbol{b}_3 \bar{\mathbf{R}} \end{bmatrix} \\
&= c_1 \begin{bmatrix} \mathbf{0} & \boldsymbol{\kappa}_1 \end{bmatrix} \begin{bmatrix} \mathbf{0} & \mathbf{I} \\ \boldsymbol{\kappa}_5 & \boldsymbol{\kappa}_7 \end{bmatrix}^{J-2} \begin{bmatrix} \mathbf{I} & \mathbf{0} \\ \boldsymbol{\kappa}_7 & \mathbf{I} \end{bmatrix} \begin{bmatrix} \boldsymbol{b}_1 + \boldsymbol{b}_2 \bar{\mathbf{R}} \\ \boldsymbol{b}_3 \bar{\mathbf{R}} \end{bmatrix}.
\end{aligned}
$$

F.4 Transfer Function for the Covariance Dynamics

Assuming that

$$
(z\bar{\bar{\mathbf{I}}} - \tilde{\bar{\mathbf{A}}})^{-1} = \begin{bmatrix} \bar{\bar{\boldsymbol{\theta}}}_{11} & & & & \\ \bar{\bar{\boldsymbol{\theta}}}_{21} & \bar{\bar{\boldsymbol{\theta}}}_{22} & & & \\ \bar{\bar{\boldsymbol{\theta}}}_{31} & \bar{\bar{\boldsymbol{\theta}}}_{32} & \bar{\bar{\boldsymbol{\theta}}}_{33} & & \\ \vdots & \ddots & \ddots & \ddots & \\ \bar{\bar{\boldsymbol{\theta}}}_{J1} & \dots & \bar{\bar{\boldsymbol{\theta}}}_{J(J-2)} & \bar{\bar{\boldsymbol{\theta}}}_{J(J-1)} & \bar{\bar{\boldsymbol{\theta}}}_{JJ} \end{bmatrix}, \tag{F.43}
$$

and by applying Theorem E.6, one can get The transfer function is given by

$$
\begin{aligned}
\Gamma(z) &= \bar{\bar{\mathbf{C}}}(z\bar{\bar{\mathbf{I}}} - \bar{\bar{\mathbf{A}}})^{-1}\bar{\bar{\mathbf{B}}} = \begin{bmatrix} \mathbf{0} & \dots & \mathbf{0} & \boldsymbol{c} \otimes \bar{\mathbf{C}} \end{bmatrix} \bar{\bar{\mathbf{S}}}_1 (z\bar{\bar{\mathbf{I}}} - \tilde{\bar{\mathbf{A}}})^{-1} \bar{\bar{\mathbf{S}}}_1^\top \bar{\bar{\mathbf{S}}}_1 \hat{\bar{\mathbf{B}}} \hat{\mathbf{S}}_6^\top \\
&= \begin{bmatrix} \mathbf{0} & \dots & \mathbf{0} & (\bar{\mathbf{C}} \otimes \boldsymbol{c}) \hat{\mathbf{S}}_1^\top \end{bmatrix} \bar{\bar{\mathbf{S}}}_1 (z\bar{\bar{\mathbf{I}}} - \tilde{\bar{\mathbf{A}}})^{-1} \hat{\bar{\mathbf{B}}} \hat{\mathbf{S}}_6^\top \\
&= \begin{bmatrix} \mathbf{0} & \dots & \mathbf{0} & (\bar{\mathbf{C}} \otimes \boldsymbol{c}) \end{bmatrix} (z\bar{\bar{\mathbf{I}}} - \tilde{\bar{\mathbf{A}}})^{-1} \hat{\bar{\mathbf{B}}} \bar{\bar{\mathbf{S}}}_6^\top \\
&= \begin{bmatrix} \mathbf{0} & \dots & \mathbf{0} & \bar{\mathbf{C}} \otimes \boldsymbol{c} \end{bmatrix} \begin{bmatrix} \bar{\bar{\boldsymbol{\theta}}}_{11} & & & & \\ \bar{\bar{\boldsymbol{\theta}}}_{21} & \bar{\bar{\boldsymbol{\theta}}}_{22} & & & \\ \bar{\bar{\boldsymbol{\theta}}}_{31} & \bar{\bar{\boldsymbol{\theta}}}_{32} & \bar{\bar{\boldsymbol{\theta}}}_{33} & & \\ \vdots & \ddots & \ddots & \ddots & \\ \bar{\bar{\boldsymbol{\theta}}}_{J1} & \dots & \bar{\bar{\boldsymbol{\theta}}}_{J(J-2)} & \bar{\bar{\boldsymbol{\theta}}}_{J(J-1)} & \bar{\bar{\boldsymbol{\theta}}}_{JJ} \end{bmatrix} \begin{bmatrix} \hat{\mathbf{B}}_1 \\ \hat{\mathbf{B}}_2 \\ \vdots \\ \hat{\mathbf{B}}_J \end{bmatrix} \bar{\bar{\mathbf{S}}}_6^\top \\
&= \sum_{j=1}^{J} (\bar{\mathbf{C}} \otimes \boldsymbol{c}) \bar{\bar{\boldsymbol{\theta}}}_{Jj} \hat{\mathbf{B}}_j \hat{\mathbf{S}}_6^\top := \sum_{j=1}^{J} \Gamma_j .
\end{aligned} \tag{F.44}
$$

Notice that Γ_j can be further simplified, but we stop here due to the computational feasibility.

APPENDIX G

Derivations of Closed Ring

The system matrix $\bar{\bar{\mathbf{A}}}^{\mathrm{R}}$ for a closed ring of J vehicles can be written as

$$\begin{aligned}
\bar{\bar{\mathbf{A}}}^{\mathrm{R}} &= \sum_{\boldsymbol{r}=1}^{N} w_{\boldsymbol{r}} \mathbf{A}_{\boldsymbol{r}}^{\mathrm{R}} \otimes \mathbf{A}_{\boldsymbol{r}}^{\mathrm{R}} \\
&= \sum_{\boldsymbol{r}=1}^{N} w_{\boldsymbol{r}} \begin{bmatrix}
\boldsymbol{\alpha}_{1,r_1} & & & & \boldsymbol{\alpha}_{4,r_J} & \boldsymbol{\alpha}_{3,r_J}+\boldsymbol{\alpha}_{2,r_1} \\
\boldsymbol{\alpha}_{3,r_1}+\boldsymbol{\alpha}_{2,r_2} & \boldsymbol{\alpha}_{1,r_2} & & & & \boldsymbol{\alpha}_{4,r_1} \\
\boldsymbol{\alpha}_{4,r_2} & \boldsymbol{\alpha}_{3,r_2}+\boldsymbol{\alpha}_{2,r_3} & \boldsymbol{\alpha}_{1,r_3} & & & \\
& \ddots & \ddots & \ddots & & \\
& & \boldsymbol{\alpha}_{4,r_{j-1}} & \boldsymbol{\alpha}_{3,r_{J-1}}+\boldsymbol{\alpha}_{2,r_J} & & \boldsymbol{\alpha}_{1,r_J}
\end{bmatrix} \\
&\quad \otimes \mathbf{A}_{\boldsymbol{r}}^{\mathrm{R}} \qquad \text{(G.1)} \\
&= \begin{bmatrix}
\hat{\mathbf{A}}_{1,1}^{\mathrm{R}} & & & & \hat{\mathbf{A}}_{4,J}^{\mathrm{R}} & \hat{\mathbf{A}}_{3,J}^{\mathrm{R}}+\hat{\mathbf{A}}_{2,1}^{\mathrm{R}} \\
\hat{\mathbf{A}}_{3,1}^{\mathrm{R}}+\hat{\mathbf{A}}_{2,2}^{\mathrm{R}} & \hat{\mathbf{A}}_{1,2}^{\mathrm{R}} & & & & \hat{\mathbf{A}}_{4,1}^{\mathrm{R}} \\
\hat{\mathbf{A}}_{4,2}^{\mathrm{R}} & \hat{\mathbf{A}}_{3,2}^{\mathrm{R}}+\hat{\mathbf{A}}_{2,3}^{\mathrm{R}} & \hat{\mathbf{A}}_{1,3}^{\mathrm{R}} & & & \\
& \ddots & \ddots & \ddots & & \\
& & \hat{\mathbf{A}}_{4,J-1}^{\mathrm{R}} & \hat{\mathbf{A}}_{3,J-1}^{\mathrm{R}}+\hat{\mathbf{A}}_{2,J}^{\mathrm{R}} & & \hat{\mathbf{A}}_{1,J}^{\mathrm{R}}
\end{bmatrix},
\end{aligned}$$

where

$$\hat{\mathbf{A}}_{i,j}^{\mathrm{R}} = \sum_{\boldsymbol{r}=1}^{N} w_{\boldsymbol{r}} \boldsymbol{\alpha}_{i,r_j} \otimes \mathbf{A}_{\boldsymbol{r}}^{\mathrm{R}} = \sum_{\boldsymbol{r}=1}^{N} w_{\boldsymbol{r}} \hat{\mathbf{S}}_1 (\mathbf{A}_{\boldsymbol{r}}^{\mathrm{R}} \otimes \boldsymbol{\alpha}_{i,r_j}) \hat{\mathbf{S}}_1^{\top} = \hat{\mathbf{S}}_1 \tilde{\mathbf{A}}_{i,j}^{\mathrm{R}} \hat{\mathbf{S}}_1^{\top} . \qquad \text{(G.2)}$$

Here,

$$\hat{\mathbf{S}}_1 = \mathcal{S}_{2J(N+1),2(N+1)} \qquad \text{(G.3)}$$

is a perfect shuffle and

$$\tilde{\mathbf{A}}^{\mathrm{R}}_{i,j} = \sum_{\boldsymbol{r}=1}^{N} w_{\boldsymbol{r}} \mathbf{A}^{\mathrm{R}}_{\boldsymbol{r}} \otimes \boldsymbol{\alpha}_{i,r_j} \,. \tag{G.4}$$

Therefore,

$$\bar{\bar{\mathbf{A}}}^{\mathrm{R}} = \bar{\bar{\mathbf{S}}}_1 \tilde{\bar{\mathbf{A}}}^{\mathrm{R}} \bar{\bar{\mathbf{S}}}_1^{\top} \,, \tag{G.5}$$

where

$$\bar{\bar{\mathbf{S}}}_1 = \mathbf{I}_J \otimes \hat{\mathbf{S}}_1 \,, \tag{G.6}$$

and

$$\tilde{\bar{\mathbf{A}}}^{\mathrm{R}} = \begin{bmatrix} \tilde{\mathbf{A}}^{\mathrm{R}}_{1,1} & & & & \tilde{\mathbf{A}}^{\mathrm{R}}_{4,J} & \tilde{\mathbf{A}}^{\mathrm{R}}_{3,J} + \tilde{\mathbf{A}}^{\mathrm{R}}_{2,1} \\ \tilde{\mathbf{A}}^{\mathrm{R}}_{3,1} + \tilde{\mathbf{A}}^{\mathrm{R}}_{2,2} & \tilde{\mathbf{A}}^{\mathrm{R}}_{1,2} & & & & \tilde{\mathbf{A}}^{\mathrm{R}}_{4,1} \\ \tilde{\mathbf{A}}^{\mathrm{R}}_{4,2} & \tilde{\mathbf{A}}^{\mathrm{R}}_{3,2} + \tilde{\mathbf{A}}^{\mathrm{R}}_{2,3} & \tilde{\mathbf{A}}^{\mathrm{R}}_{1,3} & & & \\ & \ddots & \ddots & \ddots & & \\ & & \tilde{\mathbf{A}}^{\mathrm{R}}_{4,J-1} & \tilde{\mathbf{A}}^{\mathrm{R}}_{3,J-1} + \tilde{\mathbf{A}}^{\mathrm{R}}_{2,J} & \tilde{\mathbf{A}}^{\mathrm{R}}_{1,J} & \end{bmatrix} . \tag{G.7}$$

By defining

$$\begin{aligned} \bar{\hat{\boldsymbol{\alpha}}}_{i_1 i_2} &= \sum_{\substack{\boldsymbol{r}=1 \\ j_1 \neq j_2}}^{N} w_{\boldsymbol{r}} \boldsymbol{\alpha}_{i_1,r_{j_1}} \otimes \boldsymbol{\alpha}_{i_2,r_{j_2}} = \bar{\boldsymbol{\alpha}}_{i_1} \otimes \bar{\boldsymbol{\alpha}}_{i_2} \,, \\ \bar{\bar{\boldsymbol{\alpha}}}_{i_1 i_2} &= \sum_{\substack{\boldsymbol{r}=1 \\ j_1 = j_2}}^{N} w_{\boldsymbol{r}} \boldsymbol{\alpha}_{i_1,r_{j_1}} \otimes \boldsymbol{\alpha}_{i_2,r_{j_2}} = \sum_{l=1}^{N} w_l \boldsymbol{\alpha}_{i_1,l} \otimes \boldsymbol{\alpha}_{i_2,l} \,, \end{aligned} \tag{G.8}$$

we obtain that

$$\begin{aligned} \tilde{\mathbf{A}}^{\mathrm{R}}_{i,1} &= \sum_{\boldsymbol{r}=1}^{N} w_{\boldsymbol{r}} \mathbf{A}^{\mathrm{R}}_{\boldsymbol{r}} \otimes \boldsymbol{\alpha}_{i,r_1} \\ &= \begin{bmatrix} \bar{\boldsymbol{\alpha}}_{1i} & & & \bar{\hat{\boldsymbol{\alpha}}}_{4i} & \bar{\hat{\boldsymbol{\alpha}}}_{3i} + \bar{\boldsymbol{\alpha}}_{2i} \\ \bar{\boldsymbol{\alpha}}_{3i} + \bar{\hat{\boldsymbol{\alpha}}}_{2i} & \bar{\hat{\boldsymbol{\alpha}}}_{1i} & & & \bar{\boldsymbol{\alpha}}_{4i} \\ \bar{\hat{\boldsymbol{\alpha}}}_{4i} & \bar{\hat{\boldsymbol{\alpha}}}_{3i} + \bar{\hat{\boldsymbol{\alpha}}}_{2i} & \bar{\hat{\boldsymbol{\alpha}}}_{1i} & & \\ & \ddots & \ddots & \ddots & \\ & & \bar{\hat{\boldsymbol{\alpha}}}_{4i} & \bar{\hat{\boldsymbol{\alpha}}}_{3i} + \bar{\hat{\boldsymbol{\alpha}}}_{2i} & \bar{\hat{\boldsymbol{\alpha}}}_{1i} \end{bmatrix} , \end{aligned}$$

$$
\begin{aligned}
\tilde{\mathbf{A}}^{\mathrm{R}}_{i,2} &= \sum_{\boldsymbol{r}=1}^{N} w_{\boldsymbol{r}} \mathbf{A}^{\mathrm{R}}_{\boldsymbol{r}} \otimes \boldsymbol{\alpha}_{i,r_2} \\
&= \begin{bmatrix}
\bar{\hat{\boldsymbol{\alpha}}}_{1i} & & & & \bar{\hat{\boldsymbol{\alpha}}}_{4i} & \bar{\hat{\boldsymbol{\alpha}}}_{3i} + \bar{\hat{\boldsymbol{\alpha}}}_{2i} \\
\bar{\hat{\boldsymbol{\alpha}}}_{3i} + \bar{\bar{\boldsymbol{\alpha}}}_{2i} & \bar{\bar{\boldsymbol{\alpha}}}_{1i} & & & & \bar{\hat{\boldsymbol{\alpha}}}_{4i} \\
\bar{\bar{\boldsymbol{\alpha}}}_{4i} & \bar{\bar{\boldsymbol{\alpha}}}_{3i} + \bar{\hat{\boldsymbol{\alpha}}}_{2i} & \bar{\hat{\boldsymbol{\alpha}}}_{1i} & & & \\
& \ddots & \ddots & \ddots & & \\
& & \bar{\hat{\boldsymbol{\alpha}}}_{4i} & \bar{\hat{\boldsymbol{\alpha}}}_{3i} + \bar{\hat{\boldsymbol{\alpha}}}_{2i} & \bar{\hat{\boldsymbol{\alpha}}}_{1i}
\end{bmatrix}, \qquad \text{(G.9)} \\
\tilde{\mathbf{A}}^{\mathrm{R}}_{i,3} &= \sum_{\boldsymbol{r}=1}^{N} w_{\boldsymbol{r}} \mathbf{A}^{\mathrm{R}}_{\boldsymbol{r}} \otimes \boldsymbol{\alpha}_{i,r_3} \\
&= \begin{bmatrix}
\bar{\hat{\boldsymbol{\alpha}}}_{1i} & & & & & \bar{\hat{\boldsymbol{\alpha}}}_{4i} & \bar{\hat{\boldsymbol{\alpha}}}_{3i} + \bar{\hat{\boldsymbol{\alpha}}}_{2i} \\
\bar{\hat{\boldsymbol{\alpha}}}_{3i} + \bar{\hat{\boldsymbol{\alpha}}}_{2i} & \bar{\hat{\boldsymbol{\alpha}}}_{1i} & & & & & \bar{\hat{\boldsymbol{\alpha}}}_{4i} \\
\bar{\hat{\boldsymbol{\alpha}}}_{4i} & \bar{\hat{\boldsymbol{\alpha}}}_{3i} + \bar{\bar{\boldsymbol{\alpha}}}_{2i} & \bar{\bar{\boldsymbol{\alpha}}}_{1i} & & & & \\
& \bar{\bar{\boldsymbol{\alpha}}}_{4i} & \bar{\bar{\boldsymbol{\alpha}}}_{3i} + \bar{\hat{\boldsymbol{\alpha}}}_{2i} & \bar{\hat{\boldsymbol{\alpha}}}_{1i} & & & \\
& & \ddots & \ddots & \ddots & & \\
& & & \bar{\hat{\boldsymbol{\alpha}}}_{4i} & \bar{\hat{\boldsymbol{\alpha}}}_{3i} + \bar{\hat{\boldsymbol{\alpha}}}_{2i} & \bar{\hat{\boldsymbol{\alpha}}}_{1i}
\end{bmatrix}, \\
&\vdots \\
\tilde{\mathbf{A}}^{\mathrm{R}}_{i,J} &= \sum_{\boldsymbol{r}=1}^{N} w_{\boldsymbol{r}} \mathbf{A}^{\mathrm{R}}_{\boldsymbol{r}} \otimes \boldsymbol{\alpha}_{i,r_J} \\
&= \begin{bmatrix}
\bar{\hat{\boldsymbol{\alpha}}}_{1i} & & & & \bar{\bar{\boldsymbol{\alpha}}}_{4i} & \bar{\bar{\boldsymbol{\alpha}}}_{3i} + \bar{\hat{\boldsymbol{\alpha}}}_{2i} \\
\bar{\hat{\boldsymbol{\alpha}}}_{3i} + \bar{\hat{\boldsymbol{\alpha}}}_{2i} & \bar{\hat{\boldsymbol{\alpha}}}_{1i} & & & & \bar{\hat{\boldsymbol{\alpha}}}_{4i} \\
\bar{\hat{\boldsymbol{\alpha}}}_{4i} & \bar{\hat{\boldsymbol{\alpha}}}_{3i} + \bar{\hat{\boldsymbol{\alpha}}}_{2i} & \bar{\hat{\boldsymbol{\alpha}}}_{1i} & & & \\
& \ddots & \ddots & \ddots & & \\
& & \bar{\hat{\boldsymbol{\alpha}}}_{4i} & \bar{\hat{\boldsymbol{\alpha}}}_{3i} + \bar{\bar{\boldsymbol{\alpha}}}_{2i} & \bar{\bar{\boldsymbol{\alpha}}}_{1i}
\end{bmatrix},
\end{aligned}
$$

where

$$
\bar{\hat{\boldsymbol{\alpha}}}_{1i} = \bar{\boldsymbol{\alpha}}_1 \otimes \bar{\boldsymbol{\alpha}}_i = \begin{bmatrix}
\boldsymbol{a}_1 \otimes \bar{\boldsymbol{\alpha}}_i & w_1 \boldsymbol{a}_3 \otimes \bar{\boldsymbol{\alpha}}_i & w_2 \boldsymbol{a}_3 \otimes \bar{\boldsymbol{\alpha}}_i & \dots & w_N \boldsymbol{a}_3 \otimes \bar{\boldsymbol{\alpha}}_i \\
\mathbf{I} \otimes \bar{\boldsymbol{\alpha}}_i & & & & \\
& \mathbf{I} \otimes \bar{\boldsymbol{\alpha}}_i & & & \\
& & \ddots & & \\
& & & \mathbf{I} \otimes \bar{\boldsymbol{\alpha}}_i &
\end{bmatrix},
$$

$$\bar{\bar{\boldsymbol{\alpha}}}_{2i} = \bar{\boldsymbol{\alpha}}_2 \otimes \bar{\boldsymbol{\alpha}}_i = \begin{bmatrix} \boldsymbol{a}_2 \otimes \bar{\boldsymbol{\alpha}}_i & w_1 \boldsymbol{a}_4 \otimes \bar{\boldsymbol{\alpha}}_i & w_2 \boldsymbol{a}_4 \otimes \bar{\boldsymbol{\alpha}}_i & \dots & w_N \boldsymbol{a}_4 \otimes \bar{\boldsymbol{\alpha}}_i \\ \mathbf{0} & \mathbf{0} & \mathbf{0} & \dots & \mathbf{0} \end{bmatrix}, \tag{G.10}$$

$$\bar{\bar{\boldsymbol{\alpha}}}_{3i} = \bar{\boldsymbol{\alpha}}_3 \otimes \bar{\boldsymbol{\alpha}}_i = \begin{bmatrix} \mathbf{0} & w_1 \boldsymbol{a}_5 \otimes \bar{\boldsymbol{\alpha}}_i & w_2 \boldsymbol{a}_5 \otimes \bar{\boldsymbol{\alpha}}_i & \dots & w_N \boldsymbol{a}_5 \otimes \bar{\boldsymbol{\alpha}}_i \\ \mathbf{0} & \mathbf{0} & \mathbf{0} & \dots & \mathbf{0} \end{bmatrix},$$

$$\bar{\bar{\boldsymbol{\alpha}}}_{4i} = \bar{\boldsymbol{\alpha}}_4 \otimes \bar{\boldsymbol{\alpha}}_i = \begin{bmatrix} \mathbf{0} & w_1 \boldsymbol{a}_6 \otimes \bar{\boldsymbol{\alpha}}_i & w_2 \boldsymbol{a}_6 \otimes \bar{\boldsymbol{\alpha}}_i & \dots & w_N \boldsymbol{a}_6 \otimes \bar{\boldsymbol{\alpha}}_i \\ \mathbf{0} & \mathbf{0} & \mathbf{0} & \dots & \mathbf{0} \end{bmatrix},$$

and

$$\begin{aligned}
\bar{\bar{\boldsymbol{\alpha}}}_{1i} &= \sum_{\boldsymbol{r}=1}^{N} w_{\boldsymbol{r}} \begin{bmatrix} \boldsymbol{a}_1 & \delta_{1r_j} \boldsymbol{a}_3 & \delta_{2r_j} \boldsymbol{a}_3 & \dots & \delta_{Nr_j} \boldsymbol{a}_3 \\ \mathbf{I} & & & & \\ & \mathbf{I} & & & \\ & & \ddots & & \\ & & & \mathbf{I} & \end{bmatrix} \otimes \boldsymbol{\alpha}_{i,r_j} \\
&= \begin{bmatrix} \boldsymbol{a}_1 \otimes \bar{\boldsymbol{\alpha}}_i & w_1 \boldsymbol{a}_3 \otimes \boldsymbol{\alpha}_{i,1} & w_2 \boldsymbol{a}_3 \otimes \boldsymbol{\alpha}_{i,2} & \dots & w_N \boldsymbol{a}_3 \otimes \boldsymbol{\alpha}_{i,N} \\ \mathbf{I} \otimes \bar{\boldsymbol{\alpha}}_i & & & & \\ & \mathbf{I} \otimes \bar{\boldsymbol{\alpha}}_i & & & \\ & & \ddots & & \\ & & & \mathbf{I} \otimes \bar{\boldsymbol{\alpha}}_i & \end{bmatrix}, \\
\bar{\bar{\boldsymbol{\alpha}}}_{2i} &= \sum_{\boldsymbol{r}=1}^{N} w_{\boldsymbol{r}} \begin{bmatrix} \boldsymbol{a}_2 & \delta_{1r_j} \boldsymbol{a}_4 & \delta_{2r_j} \boldsymbol{a}_4 & \dots & \delta_{Nr_j} \boldsymbol{a}_4 \\ \mathbf{0} & \mathbf{0} & \mathbf{0} & \dots & \mathbf{0} \end{bmatrix} \otimes \boldsymbol{\alpha}_{i,r_j} \\
&= \begin{bmatrix} \boldsymbol{a}_2 \otimes \bar{\boldsymbol{\alpha}}_i & w_1 \boldsymbol{a}_4 \otimes \boldsymbol{\alpha}_{i,1} & w_2 \boldsymbol{a}_4 \otimes \boldsymbol{\alpha}_{i,2} & \dots & w_N \boldsymbol{a}_4 \otimes \boldsymbol{\alpha}_{i,N} \\ \mathbf{0} & \mathbf{0} & \mathbf{0} & \dots & \mathbf{0} \end{bmatrix}, \\
\bar{\bar{\boldsymbol{\alpha}}}_{3i} &= \sum_{\boldsymbol{r}=1}^{N} w_{\boldsymbol{r}} \begin{bmatrix} \mathbf{0} & \delta_{1r_j} \boldsymbol{a}_5 & \delta_{2r_j} \boldsymbol{a}_5 & \dots & \delta_{Nr_j} \boldsymbol{a}_5 \\ \mathbf{0} & \mathbf{0} & \mathbf{0} & \dots & \mathbf{0} \end{bmatrix} \otimes \boldsymbol{\alpha}_{i,r_j} \\
&= \begin{bmatrix} \mathbf{0} & w_1 \boldsymbol{a}_5 \otimes \boldsymbol{\alpha}_{i,1} & w_2 \boldsymbol{a}_5 \otimes \boldsymbol{\alpha}_{i,2} & \dots & w_N \boldsymbol{a}_5 \otimes \boldsymbol{\alpha}_{i,N} \\ \mathbf{0} & \mathbf{0} & \mathbf{0} & \dots & \mathbf{0} \end{bmatrix}, \\
\bar{\bar{\boldsymbol{\alpha}}}_{4i} &= \sum_{\boldsymbol{r}=1}^{N} w_{\boldsymbol{r}} \begin{bmatrix} \mathbf{0} & \delta_{1r_j} \boldsymbol{a}_6 & \delta_{2r_j} \boldsymbol{a}_6 & \dots & \delta_{Nr_j} \boldsymbol{a}_6 \\ \mathbf{0} & \mathbf{0} & \mathbf{0} & \dots & \mathbf{0} \end{bmatrix} \otimes \boldsymbol{\alpha}_{i,r_j} \\
&= \begin{bmatrix} \mathbf{0} & w_1 \boldsymbol{a}_6 \otimes \boldsymbol{\alpha}_{i,1} & w_2 \boldsymbol{a}_6 \otimes \boldsymbol{\alpha}_{i,2} & \dots & w_N \boldsymbol{a}_6 \otimes \boldsymbol{\alpha}_{i,N} \\ \mathbf{0} & \mathbf{0} & \mathbf{0} & \dots & \mathbf{0} \end{bmatrix}.
\end{aligned} \tag{G.11}$$

Define $J \times J$ block cyclic forward shift matrix

$$\mathbf{S}_2 = \sigma_J \otimes \mathbf{I}_{2^2(N+1)^2}, \tag{G.12}$$

where σ_J is a $J \times J$ cyclic forward shift matrix. Therefore,

$$\mathbf{S}_2^n = \sigma_J^n \otimes \mathbf{I}_{2^2(N+1)^2}\,, \qquad \mathbf{S}_2^J = \mathbf{I}_J \otimes \mathbf{I}_{2^2(N+1)^2} = \mathbf{I}_{2^2J(N+1)^2}\,. \tag{G.13}$$

Then by defining the permutation matrix

$$\boldsymbol{\Sigma}_2 = \begin{bmatrix} \sigma_J^{-1} & & & \\ & \sigma_J^0 & & \\ & & \sigma_J^1 & \\ & & & \sigma_J^{J-2} \end{bmatrix} \otimes \mathbf{I}_{2^2(N+1)^2} = \begin{bmatrix} \mathbf{S}_2^{-1} & & & \\ & \mathbf{S}_2^0 & & \\ & & \mathbf{S}_2^1 & \\ & & & \mathbf{S}_2^{J-2} \end{bmatrix}, \tag{G.14}$$

where Theorem E.3 is used, we can obtain that

$$\begin{aligned} \hat{\tilde{\mathbf{A}}}^{\mathrm{R}} &= \boldsymbol{\Sigma}_2 \tilde{\tilde{\mathbf{A}}}^{\mathrm{R}} \boldsymbol{\Sigma}_2^\top \\ &= \begin{bmatrix} \tilde{\mathbf{A}}_{1,2}^{\mathrm{R}} & & & & \mathbf{S}_2^2\tilde{\mathbf{A}}_{4,3}^{\mathrm{R}} & \mathbf{S}_2(\tilde{\mathbf{A}}_{3,2}^{\mathrm{R}} + \tilde{\mathbf{A}}_{2,3}^{\mathrm{R}}) \\ \mathbf{S}_2(\tilde{\mathbf{A}}_{3,2}^{\mathrm{R}} + \tilde{\mathbf{A}}_{2,3}^{\mathrm{R}}) & \tilde{\mathbf{A}}_{1,2}^{\mathrm{R}} & & & & \mathbf{S}_2^2\tilde{\mathbf{A}}_{4,3}^{\mathrm{R}} \\ \mathbf{S}_2^2\tilde{\mathbf{A}}_{4,3}^{\mathrm{R}} & \mathbf{S}_2(\tilde{\mathbf{A}}_{3,2}^{\mathrm{R}} + \tilde{\mathbf{A}}_{2,3}^{\mathrm{R}}) & \tilde{\mathbf{A}}_{1,2}^{\mathrm{R}} & & & \\ & \ddots & \ddots & \ddots & & \\ & & \mathbf{S}_2^2\tilde{\mathbf{A}}_{4,3}^{\mathrm{R}} & \mathbf{S}_2(\tilde{\mathbf{A}}_{3,2}^{\mathrm{R}} + \tilde{\mathbf{A}}_{2,3}^{\mathrm{R}}) & & \tilde{\mathbf{A}}_{1,2}^{\mathrm{R}} \end{bmatrix}, \end{aligned} \tag{G.15}$$

by noticing that

$$\begin{aligned} \mathbf{S}_2^{j-2}\tilde{\mathbf{A}}_{1,j}^{\mathrm{R}}(\mathbf{S}_2^{j-2})^\top &= \tilde{\mathbf{A}}_{1,2}^{\mathrm{R}}\,, & \mathbf{S}_2^{j-2}\tilde{\mathbf{A}}_{2,j}^{\mathrm{R}}(\mathbf{S}_2^{j-3})^\top &= \mathbf{S}_2\tilde{\mathbf{A}}_{2,3}^{\mathrm{R}}\,, \\ \mathbf{S}_2^{j-1}\tilde{\mathbf{A}}_{3,j}^{\mathrm{R}}(\mathbf{S}_2^{j-2})^\top &= \mathbf{S}_2\tilde{\mathbf{A}}_{3,2}^{\mathrm{R}}\,, & \mathbf{S}_2^{j-1}\tilde{\mathbf{A}}_{4,j}^{\mathrm{R}}(\mathbf{S}_2^{j-3})^\top &= \mathbf{S}_2^2\tilde{\mathbf{A}}_{4,3}^{\mathrm{R}}\,, \end{aligned} \tag{G.16}$$

for $1 \leq j \leq J$. Thus, $\bar{\bar{\mathbf{A}}}^{\mathrm{R}}$ is similar to the block circulant matrix $\hat{\bar{\mathbf{A}}}^{\mathrm{R}}$ where the blocks are

$$\tilde{\mathbf{A}}^{\mathrm{R}}_{1,2} = \begin{bmatrix} \bar{\bar{\boldsymbol{\alpha}}}_{11} & & & & \bar{\bar{\boldsymbol{\alpha}}}_{41} & \bar{\bar{\boldsymbol{\alpha}}}_{31} + \bar{\bar{\boldsymbol{\alpha}}}_{21} \\ \bar{\bar{\boldsymbol{\alpha}}}_{31} + \bar{\bar{\boldsymbol{\alpha}}}_{21} & \bar{\bar{\boldsymbol{\alpha}}}_{11} & & & & \bar{\bar{\boldsymbol{\alpha}}}_{41} \\ \bar{\bar{\boldsymbol{\alpha}}}_{41} & \bar{\bar{\boldsymbol{\alpha}}}_{31} + \bar{\bar{\boldsymbol{\alpha}}}_{21} & \bar{\bar{\boldsymbol{\alpha}}}_{11} & & & \\ & \ddots & \ddots & \ddots & & \\ & & \bar{\bar{\boldsymbol{\alpha}}}_{41} & \bar{\bar{\boldsymbol{\alpha}}}_{31} + \bar{\bar{\boldsymbol{\alpha}}}_{21} & \bar{\bar{\boldsymbol{\alpha}}}_{11} & \end{bmatrix},$$

$$\mathbf{S}_2\tilde{\mathbf{A}}^{\mathrm{R}}_{2,3} = \begin{bmatrix} \bar{\bar{\boldsymbol{\alpha}}}_{32} + \bar{\bar{\boldsymbol{\alpha}}}_{22} & \bar{\bar{\boldsymbol{\alpha}}}_{12} & & & & \bar{\bar{\boldsymbol{\alpha}}}_{42} \\ \bar{\bar{\boldsymbol{\alpha}}}_{42} & \bar{\bar{\boldsymbol{\alpha}}}_{32} + \bar{\bar{\boldsymbol{\alpha}}}_{22} & \bar{\bar{\boldsymbol{\alpha}}}_{12} & & & \\ & \bar{\bar{\boldsymbol{\alpha}}}_{42} & \bar{\bar{\boldsymbol{\alpha}}}_{32} + \bar{\bar{\boldsymbol{\alpha}}}_{22} & \bar{\bar{\boldsymbol{\alpha}}}_{12} & & \\ & & \ddots & \ddots & \ddots & \\ \bar{\bar{\boldsymbol{\alpha}}}_{12} & & & \bar{\bar{\boldsymbol{\alpha}}}_{42} & \bar{\bar{\boldsymbol{\alpha}}}_{32} + \bar{\bar{\boldsymbol{\alpha}}}_{22} & \end{bmatrix},$$

$$\mathbf{S}_2\tilde{\mathbf{A}}^{\mathrm{R}}_{3,2} = \begin{bmatrix} \bar{\bar{\boldsymbol{\alpha}}}_{33} + \bar{\bar{\boldsymbol{\alpha}}}_{23} & \bar{\bar{\boldsymbol{\alpha}}}_{13} & & & \bar{\bar{\boldsymbol{\alpha}}}_{43} \\ \bar{\bar{\boldsymbol{\alpha}}}_{43} & \bar{\bar{\boldsymbol{\alpha}}}_{33} + \bar{\bar{\boldsymbol{\alpha}}}_{23} & \bar{\bar{\boldsymbol{\alpha}}}_{13} & & \\ & \bar{\bar{\boldsymbol{\alpha}}}_{43} & \bar{\bar{\boldsymbol{\alpha}}}_{33} + \bar{\bar{\boldsymbol{\alpha}}}_{23} & \bar{\bar{\boldsymbol{\alpha}}}_{13} & \\ & & \ddots & \ddots & \ddots \\ \bar{\bar{\boldsymbol{\alpha}}}_{13} & & & \bar{\bar{\boldsymbol{\alpha}}}_{43} & \bar{\bar{\boldsymbol{\alpha}}}_{33} + \bar{\bar{\boldsymbol{\alpha}}}_{23} \end{bmatrix}, \tag{G.17}$$

$$\mathbf{S}_2^2\tilde{\mathbf{A}}^{\mathrm{R}}_{4,3} = \begin{bmatrix} \bar{\bar{\boldsymbol{\alpha}}}_{44} & \bar{\bar{\boldsymbol{\alpha}}}_{34} + \bar{\bar{\boldsymbol{\alpha}}}_{24} & \bar{\bar{\boldsymbol{\alpha}}}_{14} & & & \\ & \bar{\bar{\boldsymbol{\alpha}}}_{44} & \bar{\bar{\boldsymbol{\alpha}}}_{34} + \bar{\bar{\boldsymbol{\alpha}}}_{24} & \bar{\bar{\boldsymbol{\alpha}}}_{14} & & \\ & & \ddots & \ddots & \ddots & \\ \bar{\bar{\boldsymbol{\alpha}}}_{14} & & & \bar{\bar{\boldsymbol{\alpha}}}_{44} & \bar{\bar{\boldsymbol{\alpha}}}_{34} + \bar{\bar{\boldsymbol{\alpha}}}_{24} & \\ \bar{\bar{\boldsymbol{\alpha}}}_{34} + \bar{\bar{\boldsymbol{\alpha}}}_{24} & \bar{\bar{\boldsymbol{\alpha}}}_{14} & & & & \bar{\bar{\boldsymbol{\alpha}}}_{44} \end{bmatrix}.$$

Based on the results in [199], the eigenvalues of $\bar{\bar{\mathbf{A}}}^{\mathrm{R}}$ (or $\hat{\bar{\mathbf{A}}}^{\mathrm{R}}$) are given by the eigenvalues of matrices

$$\begin{aligned} \bar{\bar{\mathbf{\Lambda}}}_i &= \tilde{\mathbf{A}}^{\mathrm{R}}_{1,2} + \mathbf{S}_2^2\tilde{\mathbf{A}}^{\mathrm{R}}_{4,3}\mathrm{e}^{-\mathrm{j}\frac{2\pi}{J}2(i-1)} + \mathbf{S}_2(\tilde{\mathbf{A}}^{\mathrm{R}}_{3,2} + \tilde{\mathbf{A}}^{\mathrm{R}}_{2,3})\mathrm{e}^{-\mathrm{j}\frac{2\pi}{J}(i-1)} \\ &= \tilde{\mathbf{A}}^{\mathrm{R}}_{1,2} + \mathbf{S}_2^2\tilde{\mathbf{A}}^{\mathrm{R}}_{4,3}\theta^{-2} + \mathbf{S}_2(\tilde{\mathbf{A}}^{\mathrm{R}}_{3,2} + \tilde{\mathbf{A}}^{\mathrm{R}}_{2,3})\theta^{-1}, \end{aligned} \tag{G.18}$$

for $1 \leq i \leq J$, where

$$\theta = \mathrm{e}^{\mathrm{j}\frac{2\pi}{J}(i-1)}. \tag{G.19}$$

One can calculate that

$$\bar{\bar{\Lambda}}_i = \left[\begin{array}{ccc|ccc} \bar{\bar{\chi}}_1 & \bar{\bar{\eta}}_1 & \bar{\bar{\phi}}_1 & & \bar{\bar{\xi}}_0 & \bar{\bar{\zeta}}_0 \\ \bar{\bar{\zeta}}_1 & \bar{\bar{\chi}}_2 & \bar{\bar{\eta}}_2 & \bar{\bar{\phi}}_0 & & \bar{\bar{\xi}}_0 \\ \bar{\bar{\xi}}_1 & \bar{\bar{\zeta}}_2 & \bar{\bar{\chi}}_3 & \bar{\bar{\eta}}_0 & \ddots & \\ \hline & \bar{\bar{\xi}}_0 & \bar{\bar{\zeta}}_0 & \bar{\bar{\chi}}_0 & \ddots & \bar{\bar{\phi}}_0 \\ \bar{\bar{\phi}}_0 & & \ddots & \ddots & \ddots & \bar{\bar{\eta}}_0 \\ \bar{\bar{\eta}}_0 & \bar{\bar{\phi}}_0 & & \bar{\bar{\xi}}_0 & \bar{\bar{\zeta}}_0 & \bar{\bar{\chi}}_0 \end{array}\right], \tag{G.20}$$

is a perturbed block penta-circulant matrix where

$$\begin{aligned}
\bar{\bar{\chi}}_0 &= \bar{\hat{\alpha}}_{11} + \bar{\hat{\alpha}}_{44}\theta^{-2} + (\bar{\hat{\alpha}}_{32} + \bar{\hat{\alpha}}_{22} + \bar{\hat{\alpha}}_{33} + \bar{\hat{\alpha}}_{23})\theta^{-1}\,, \\
\bar{\bar{\chi}}_1 &= \bar{\hat{\alpha}}_{11} + \bar{\hat{\alpha}}_{44}\theta^{-2} + (\bar{\hat{\alpha}}_{32} + \bar{\hat{\alpha}}_{22} + \bar{\hat{\alpha}}_{33} + \bar{\bar{\alpha}}_{23})\theta^{-1}\,, \\
\bar{\bar{\chi}}_2 &= \bar{\bar{\alpha}}_{11} + \bar{\bar{\alpha}}_{44}\theta^{-2} + (\bar{\hat{\alpha}}_{32} + \bar{\bar{\alpha}}_{22} + \bar{\bar{\alpha}}_{33} + \bar{\hat{\alpha}}_{23})\theta^{-1}\,, \\
\bar{\bar{\chi}}_3 &= \bar{\hat{\alpha}}_{11} + \bar{\hat{\alpha}}_{44}\theta^{-2} + (\bar{\bar{\alpha}}_{32} + \bar{\hat{\alpha}}_{22} + \bar{\hat{\alpha}}_{33} + \bar{\hat{\alpha}}_{23})\theta^{-1}\,, \\
\bar{\bar{\eta}}_0 &= (\bar{\hat{\alpha}}_{34} + \bar{\hat{\alpha}}_{24})\theta^{-2} + (\bar{\hat{\alpha}}_{12} + \bar{\hat{\alpha}}_{13})\theta^{-1}\,, \\
\bar{\bar{\eta}}_1 &= (\bar{\hat{\alpha}}_{34} + \bar{\bar{\alpha}}_{24})\theta^{-2} + (\bar{\hat{\alpha}}_{12} + \bar{\bar{\alpha}}_{13})\theta^{-1}\,, \\
\bar{\bar{\eta}}_2 &= (\bar{\bar{\alpha}}_{34} + \bar{\hat{\alpha}}_{24})\theta^{-2} + (\bar{\bar{\alpha}}_{12} + \bar{\hat{\alpha}}_{13})\theta^{-1}\,, \\
\bar{\bar{\zeta}}_0 &= (\bar{\hat{\alpha}}_{31} + \bar{\hat{\alpha}}_{21}) + (\bar{\hat{\alpha}}_{42} + \bar{\hat{\alpha}}_{43})\theta^{-1}\,, \\
\bar{\bar{\zeta}}_1 &= (\bar{\hat{\alpha}}_{31} + \bar{\bar{\alpha}}_{21}) + (\bar{\hat{\alpha}}_{42} + \bar{\bar{\alpha}}_{43})\theta^{-1}\,, \\
\bar{\bar{\zeta}}_2 &= (\bar{\bar{\alpha}}_{31} + \bar{\hat{\alpha}}_{21}) + (\bar{\bar{\alpha}}_{42} + \bar{\hat{\alpha}}_{43})\theta^{-1}\,, \\
\bar{\bar{\xi}}_0 &= \bar{\hat{\alpha}}_{41}\,, \\
\bar{\bar{\xi}}_1 &= \bar{\bar{\alpha}}_{41}\,, \\
\bar{\bar{\phi}}_0 &= \bar{\hat{\alpha}}_{14}\theta^{-1}\,, \\
\bar{\bar{\phi}}_1 &= \bar{\bar{\alpha}}_{14}\theta^{-1}\,.
\end{aligned} \tag{G.21}$$

BIBLIOGRAPHY

[1] D. Schrank, B. Eisele, T. Lomax, and J. Bak, "2015 urban mobility scorecard," Texas A&M Transportation Institute, Tech. Rep., 2015.

[2] MnDOT, "2016 congestion report: Metropolitan freeway system," Minnesota Department of Transportation, Tech. Rep., 2016.

[3] R. Millar, "The 2017 corridor capacity report: The 16th edition of the annual congestion report," Washington State Department of Transportation, Tech. Rep., 2017.

[4] G. Cookson, "INRIX global traffic scorecard," INRIX Research, Tech. Rep., 2018.

[5] C. McKnight, H. Levinson, K. Ozbay, C. Kamga, and R. Paaswell, "Impact of traffic congestion on bus travel time in northern New Jersey," *Transportation Research Record: Journal of the Transportation Research Board*, vol. 1884, pp. 27–35, 2004.

[6] Y. Xiao, N. Coulombel, and A. de Palma, "The valuation of travel time reliability: Does congestion matter?" *Transportation Research Part B: Methodological*, vol. 97, pp. 113–141, 2017.

[7] USDOT, "2016 fatal motor vehicle crashes: Overview," National Highway Traffic Safety Administration, Tech. Rep., 2017.

[8] M. Treiber, A. Kesting, and C. Thiemann, "How much does traffic congestion increase fuel consumption and emissions? Applying a fuel consumption model to the NGSIM trajectory data," in *87th Annual Meeting of the Transportation Research Board*, 2008.

[9] I. D. Greenwood, R. C. Dunn, and R. R. Raine, "Estimating the effects of traffic congestion on fuel consumption and vehicle emissions based on acceleration noise," *Journal of Transportation Engineering*, vol. 133, no. 2, pp. 96–104, 2007.

[10] M. Errampalli, V. Senathipathi, and D. Thamban, "Effect of congestion on fuel cost and travel time cost on multi-lane highways in India," *International Journal for Traffic & Transport Engineering*, vol. 5, no. 4, pp. 458–472, 2015.

[11] G. T. Taoka, "Brake reaction times of unalerted drivers," *ITE journal*, vol. 59, pp. 19–21, 1989.

[12] H. Summala, "Brake reaction times and driver behavior analysis," *Transportation Human Factors*, vol. 2, no. 3, pp. 217–226, 2000.

[13] Y. D. Wong and P. K. Goh, "Perception-braking response time of unalerted drivers at signalized intersections," *ITE Journal*, vol. 71, pp. 73–76, 2001.

[14] J. R. Setti, H. Rakha, and I. El-Shawarby, "Analysis of brake perception-reaction times on high-speed signalized intersection approaches," *2006 IEEE Intelligent Transportation Systems Conference*, pp. 689–694, 2006.

[15] G. Orosz, R. E. Wilson, R. Szalai, and G. Stépán, "Exciting traffic jams: Nonlinear phenomena behind traffic jam formation on highways," *Physical Review E*, vol. 80, p. 046205, 2009.

[16] G. Orosz, R. E. Wilson, and G. Stépán, "Traffic jams: dynamics and control," *Philosophical Transactions of the Royal Society A*, vol. 368, no. 1928, pp. 4455–4479, 2010.

[17] J3016, "Taxonomy and definitions for terms related to driving automation systems for on-road motor vehicles," SAE International, SAE Standard, 2016.

[18] G. Araniti, C. Campolo, M. Condoluci, A. Iera, and A. Molinaro, "LTE for vehicular networking: a survey," *IEEE Communications Magazine*, vol. 51, no. 5, pp. 148–157, 2013.

[19] J. J. Blum, A. Eskandarian, and L. J. Hoffman, "Challenges of intervehicle ad hoc networks," *IEEE Transactions on Intelligent Transportation Systems*, vol. 5, no. 4, pp. 347–351, 2004.

[20] E. C. Eze, S. Zhang, and E. Liu, "Vehicular ad hoc networks (VANETs): Current state, challenges, potentials and way forward," in *20th International Conference on Automation and Computing*, 2014, pp. 176–181.

[21] F. Dressler, H. Hartenstein, O. Altintas, and O. K. Tonguz, "Inter-vehicle communication: Quo vadis," *IEEE Communications Magazine*, vol. 52, no. 6, pp. 170–177, 2014.

[22] A. Festag, "Standards for vehicular communication – from IEEE 802.11p to 5G," *Elektrotechnik & Informationstechnik*, vol. 132, no. 7, pp. 409–416, 2015.

[23] 5G Americas, "V2X cellular solutions," Tech. Rep., 2016.

[24] H. Ahmed, S. Pierre, and A. Quintero, "A flexible testbed architecture for VANET," *Vehicular Communications*, vol. 9, pp. 115–126, 2017.

[25] 5GAA, "An assessment of LTE-V2X (PC5) and 802.11p direct communications technologies for improved road safety in the EU," Tech. Rep., 2017.

[26] M. Charitos and G. Kalivas, "MIMO HetNet IEEE 802.11p - LTE deployment in a vehicular urban environment," *Vehicular Communications*, vol. 9, pp. 222–232, 2017.

[27] S. Boussoufa-Lahlah, F. Semchedine, and L. Bouallouche-Medjkoune, "Geographic routing protocols for vehicular ad hoc networks (VANETs): A survey," *Vehicular Communications*, vol. 11, pp. 20–31, 2018.

[28] M. Muhammad and G. A. Safdar, "Survey on existing authentication issues for cellular-assisted V2X communication," *Vehicular Communications*, vol. 12, pp. 50–65, 2018.

[29] R. Molina-Masegosa and J. Gozalvez, "LTE-V for sidelink 5G V2X vehicular communications: A new 5G technology for short-range vehicle-to-everything communications," *IEEE Vehicular Technology Magazine*, vol. 12, no. 4, pp. 30–39, 2017.

[30] S. Chen, J. Hu, Y. Shi, Y. Peng, J. Fang, R. Zhao, and L. Zhao, "Vehicle-to-everything (v2x) services supported by LTE-based systems and 5G," *IEEE Communications Standards Magazine*, vol. 1, no. 2, pp. 70–76, 2017.

[31] A. Papathanassiou and A. Khoryaev, "Cellular V2X as the essential enabler of superior global connected transportation services," *IEEE 5G Tech Focus*, vol. 1, no. 2, 2017.

[32] GSMA, "Cellular vehicle-to-everything (C-V2X) – enabling intelligent transport," Brochure, 2018.

[33] IEEE Std 1609.3-2010 (Revision of IEEE Std 1609.3-2007), "IEEE standard for wireless access in vehicular environments (WAVE) - networking services," IEEE Vehicular Technology Society, IEEE Standard, 2010.

[34] B. Williams, *Intelligent Transport Systems Standards*. Artech House Publishers, 2008.

[35] A. Festag, "Cooperative intelligent transport systems standards in europe," *IEEE Communications Magazine*, vol. 52, no. 12, pp. 166–172, 2014.

[36] M.1453-2, "Intelligent transport systems - dedicated short range communications at 5.8 GHz," International Telecommunication Union, ITU-R Standard, 2005.

[37] ISO 15628, "Intelligent transport systems – dedicated short range communication (DSRC) – DSRC application layer," International Organization for Standardization, ISO standard, 2013.

[38] J. B. Kenney, "Dedicated short-range communications (DSRC) standards in the United States," *Proceedings of the IEEE*, vol. 99, no. 7, pp. 1162–1182, 2011.

[39] J2735, "Dedicated short range communications (DSRC) message set dictionary," SAE International, SAE Standard, 2016.

[40] TS 102 792, "Intelligent transport systems (ITS); mitigation techniques to avoid interference between european CEN dedicated short range communication (CEN DSRC) equipment and intelligent transport systems (ITS) operating in the 5 GHz frequency range," European Telecommunications Standards Institute, ETSI Standard, 2015.

[41] TS 102 723-1, "Intelligent transport systems (ITS); OSI cross-layer topics; part 1: Architecture and addressing schemes," European Telecommunications Standards Institute, ETSI Standard, 2012.

[42] EN 12253, "Road transport and traffic telematics – dedicated short range communication (DSRC) – physical layer using microwave at 5.8 GHz," European Committee for Standardization, EN Standard, 2004.

[43] EN 12795, "Road transport and traffic telematics – dedicated short range communication (DSRC) – DSRC data link layer: medium access and logical link control," European Committee for Standardization, EN Standard, 2003.

[44] EN 12834, "Road transport and traffic telematics – dedicated short range communication (DSRC) – DSRC application layer," European Committee for Standardization, EN Standard, 2003.

[45] EN 13372, "Road transport and traffic telematics (RTTT) – dedicated short-range communication – profiles for RTTT applications," European Committee for Standardization, EN Standard, 2004.

[46] STD-T75, "DSRC application sub-layer," Association of Radio Industries and Businesses (ARIB), ARIB standard, 2001.

[47] STD-T88, "Dedicated short-range communication system," Association of Radio Industries and Businesses (ARIB), ARIB standard, 2004.

[48] STD-T110, "Dedicated short-range communication (DSRC) basic application interface," Association of Radio Industries and Businesses (ARIB), ARIB standard, 2012.

[49] GB/T 31024.1-2014, "Cooperative intelligent transport systems – dedicated short range communications – part 1: General technical requirements," Standardization Administration of China (SAC), China National Standard, 2015.

[50] GB/T 31024.2-2014, "Cooperatiion of roadside to vehicle – dedicated short range communications – part 2: Specification of medium access control layer and physical layer," Standardization Administration of China (SAC), China National Standard, 2015.

[51] S. E. Li, Y. Zheng, K. Li, and J. Wang, "An overview of vehicular platoon control under the four-component framework," in *2015 IEEE Intelligent Vehicles Symposium (IV)*, 2015, pp. 286–291.

[52] W. S. Levine and M. Athans, "On the optimal error regulation of a string of moving vehicles," *IEEE Transactions on Automatic Control*, vol. 11, no. 3, pp. 355–361, 1966.

[53] J. G. Bender and R. E. Fenton, "A study of automatic car following," *IEEE Transactions on Vehicular Technology*, vol. 18, no. 3, pp. 134–140, 1969.

[54] D. E. Whitney and M. Tomizuka, "Normal and emergency control of a string of vehicles by fixed reference sampled-data control," *IEEE Transactions on Vehicular Technology*, vol. 21, no. 4, pp. 128–138, 1972.

[55] W. Garrard and A. Kornhauser, "Design of optimal feedback systems for longitudinal control of automated transit vehicles," *Transportation Research*, vol. 7, no. 2, pp. 125–144, 1973.

[56] K. Chu, "Decentralized control of high-speed vehicular strings," *Transportation Science*, vol. 8, no. 4, pp. 361–384, 1974.

[57] R. J. Caudill and W. L. Garrard, "Vehicle-follower, longitudinal control for automated transit vehicles," *IFAC Proceedings Volumes*, vol. 9, no. 4, pp. 195–209, 1976.

[58] H. Y. Chiu, G. B. Stupp, Jr., and S. J. Brown, Jr., "Vehicle-follower control with variable-gains for short headway automated guideway transit systems," *Journal of Dynamic Systems, Measurement, and Control*, vol. 99, no. 3, pp. 183–189, 1977.

[59] S. E. Shladover, "Longitudinal control of automated guideway transit vehicles within platoons," *Journal of Dynamic Systems, Measurement and Control*, vol. 100, no. 4, pp. 302–310, 1978.

[60] S. J. Sklar, J. P. Bevans, , and G. Stein, ""Safe-approach" vehicle-follower control," *IEEE Transactions on Vehicular Technology*, vol. VT-28, no. 1, pp. 56–62, 1979.

[61] D. E. Olson and W. L. Garrard, "Model-follower longitudinal control for automated guideway transit vehicles," *IEEE Transactions on Vehicular Technology*, vol. 28, no. 1, pp. 36–45, 1979.

[62] A. S. Hauksdottir and R. E. Fenton, "On the design of a vehicle longitudinal controller," *IEEE Transactions on Vehicular Technology*, vol. 34, no. 4, pp. 182–187, 1985.

[63] S. E. Shladover, "Longitudinal control of automotive vehicles in close-formation platoons," *Journal of Dynamic Systems, Measurement, and Control*, vol. 113, no. 2, pp. 231–241, 1991.

[64] S. Sheikholeslam and C. A. Desoer, "Control of interconnected nonlinear dynamical systems: The platoon problem," *IEEE Transactions on Automatic Control*, vol. 37, no. 6, pp. 806–810, 1992.

[65] ——, "Longitudinal control of a platoon of vehicles with no communication of lead vehicle information: a system level study," *IEEE Transactions on Vehicular Technology*, vol. 42, no. 4, pp. 546–554, 1993.

[66] P. A. Ioannou and C. C. Chien, "Autonomous intelligent cruise control," *IEEE Transactions on Vehicular Technology*, vol. 42, no. 4, pp. 657–672, 1993.

[67] L. Nilsson, "Safety effects of adaptive cruise controls in critical traffic situations," in *Proceedings of the Second World Congress on Intelligent Transport Systems*, Yokohama, Japan, 1995, pp. 1254–1259.

[68] R. D. Ervin, A. Nagarajan, and E. Argalas, "Adaptive cruise control: An industry outlook on product features and marketing," University of Michigan Transportation Research Institute, Tech. Rep., 1997, UMTRI-97-38.

[69] Y. Zhang, B. Kosmatopoulos, P. A. Ioannou, and C. C. Chien, "Autonomous intelligent cruise control using front and back information for tight vehicle following maneuvers," *IEEE Transactions on Vehicular Technology*, vol. 48, no. 1, pp. 319–328, 1999.

[70] C.-Y. Liang and H. Peng, "Optimal adaptive cruise control with guaranteed string stability," *Vehicle System Dynamics*, vol. 32, no. 4-5, pp. 313–330, 1999.

[71] R. Rajamani and C. Zhu, "Semi-autonomous adaptive cruise control systems," *IEEE Transactions on Vehicular Technology*, vol. 51, no. 5, pp. 1186–1192, 2002.

[72] G. Marsden, M. McDonald, and M. Brackstone, "Towards an understanding of adaptive cruise control," *Transportation Research Part C: Emerging Technologies*, vol. 9, no. 1, pp. 33 – 51, 2001.

[73] J. VanderWerf, S. E. Shladover, M. A. Miller, and N. Kourjanskaia, "Effects of adaptive cruise control systems on highway traffic flow capacity," *Transportation Research Record: Journal of the Transportation Research Board*, vol. 1800, no. 1, pp. 78–84, 2002.

[74] J. Zhang and P. Ioannou, "Integrated roadway/adaptive cruise control system: Safety, performance, environmental and near term deployment considerations," University of California, Berkeley, California PATH Research Report, 2004, UCB-ITS-PRR-2004-32.

[75] L. C. Davis, "Effect of adaptive cruise control systems on mixed traffic flow near an on-ramp," *Physica A: Statistical Mechanics and its Applications*, vol. 379, no. 1, pp. 274–290, 2007.

[76] A. Kesting, M. Treiber, and D. Helbing, "Enhanced intelligent driver model to access the impact of driving strategies on traffic capacity," *Philosophical Transactions of the Royal Society A: Mathematical, Physical and Engineering Sciences*, vol. 368, no. 1928, pp. 4585–4605, 2010.

[77] J. C. F. de Winter, R. Happee, M. H. Martens, and N. A. Stanton, "Effects of adaptive cruise control and highly automated driving on workload and situation awareness: A review of the empirical evidence," *Transportation Research Part F: Traffic Psychology and Behaviour*, vol. 27, pp. 196–217, 2014.

[78] Y. Li, Z. Li, H. Wang, W. Wang, and L. Xing, "Evaluating the safety impact of adaptive cruise control in traffic oscillations on freeways," *Accident Analysis & Prevention*, vol. 104, pp. 137–145, 2017.

[79] D. de Bruin, J. Kroon, R. van Klaveren, and M. Nelisse, "Design and test of a cooperative adaptive cruise control system," in *Proceedings of IEEE Intelligent Vehicles Symposium*, 2004, pp. 392–396.

[80] G. J. L. Naus, R. P. A. Vugts, J. Ploeg, M. R. J. G. van de Molengraft, and M. Steinbuch, "String-stable CACC design and experimental validation: A frequency-domain approach," *IEEE Transactions on Vehiclular Technology*, vol. 59, no. 9, pp. 429–436, 2010.

[81] M. Şentürk, I. M. C. Uygan, and L. Güvenç, "Mixed cooperative adaptive cruise control for light commercial vehicles," in *2010 IEEE International Conference on Systems, Man and Cybernetics*, 2010, pp. 1506–1511.

[82] C. Desjardins and B. Chaib-draa, "Cooperative adaptive cruise control: a reinforcement learning approach," *IEEE Transactions on Intelligent Transportation Systems*, vol. 12, no. 4, pp. 1248–1260, 2011.

[83] K. Lidström, K. Sjöberg, U. Holmberg, J. Andersson, F. Bergh, M. Bjäde, and S. Mak, "A modular CACC system integration and design," *IEEE Transactions on Intelligent Transportation System*, vol. 13, no. 3, pp. 1050–1061, 2012.

[84] S. Oncu, J. Ploeg, N. van de Wouw, and H. Nijmeijer, "Cooperative adaptive cruise control: Network-aware analysis of string stability," *IEEE Transactions on Intelligent Transportation Systems*, vol. 15, no. 4, pp. 1527–1537, 2014.

[85] J. Ploeg, "Analysis and design of controllers for cooperative and automated driving," Ph.D. dissertation, TNO, 2014.

[86] V. Milanes, S. Shladover, J. Spring, C. Nowakowski, H. Kawazoe, and M. Nakamura, "Cooperative adaptive cruise control in real traffic situations," *IEEE Transactions on Intelligent Transportation Systems*, vol. 15, no. 1, pp. 296–305, 2014.

[87] S. E. Shladover, C. Nowakowski, X.-Y. Lu, and R. Ferlis, "Cooperative adaptive cruise control definitions and operating concepts," *Transportation Research Record: Journal of the Transportation Research Board*, vol. 2489, pp. 145–152, 2015.

[88] J. Ploeg, E. Semsar-Kazerooni, G. Lijster, N. van de Wouw, and H. Nijmeijer, "Graceful degradation of cooperative adaptive cruise control," *IEEE Transactions on Intelligent Transportation Systems*, vol. 16, no. 1, pp. 488–497, 2015.

[89] M. Amoozadeh, H. Deng, C.-N. Chuah, H. M. Zhang, and D. Ghosal, "Platoon management with cooperative adaptive cruise control enabled by VANET," *Vehicular Communications*, vol. 2, no. 2, pp. 110 – 123, 2015.

[90] K. C. Dey, L. Yan, X. Wang, Y. Wang, H. Shen, M. Chowdhury, L. Yu, C. Qiu, and V. Soundararaj, "A review of communication, driver characteristics, and controls aspects of cooperative adaptive cruise control (CACC)," *IEEE Transactions on Intelligent Transportation Systems*, vol. 17, no. 2, pp. 491–509, 2016.

[91] B. van Arem, C. J. G. van Driel, and R. Visser, "The impact of cooperative adaptive cruise control on traffic-flow characteristics," *IEEE Transactions on Intelligent Transportation Systems*, vol. 7, no. 4, pp. 429–436, 2006.

[92] V. Milanés, J. Alonso, L. Bouraoui, and J. Ploeg, "Cooperative maneuvering in close environments among cybercars and dual-mode cars," *IEEE Transactions on Intelligent Transportation Systems*, vol. 12, no. 1, pp. 15–24, 2011.

[93] USDOT, "Cooperative adaptive cruise control: Human factors analysis," Federal Highway Administration, Tech. Rep., 2013.

[94] J. Ploeg, N. van de Wouw, and H. Nijmeijer, "$\mathcal{L}_p$ string stability of cascaded systems: Application to vehicle platooning," *IEEE Transactions on Control Systems Technology*, vol. 22, no. 2, pp. 786–793, 2014.

[95] M. di Bernardo, A. Salvi, and S. Santini, "Distributed consensus strategy for platooning of vehicles in the presence of time varying heterogeneous communication delays," *IEEE Transactions on Intelligent Transportation Systems*, vol. 16, no. 1, pp. 102–112, 2015.

[96] A. Askari, D. A. Farias, A. A. Kurzhanskiy, and P. Varaiya, "Effect of adaptive and cooperative adaptive cruise control on throughput of signalized arterials," *CoRR*, vol. abs/1703.01657, 2017.

[97] S. E. Shladover, C. A. Desoer, J. K. Hedrick, M. Tomizuka, J. Walrand, W. B. Zhang, D. H. McMahon, H. Peng, S. Sheikholeslam, and N. McKeown, "Automated vehicle control developments in the PATH program," *IEEE Transactions on Vehicular Technology*, vol. 40, no. 1, pp. 114–130, 1991.

[98] R. Rajamani and S. E. Shladover, "An experimental comparative study of autonomous and cooperative vehicle-follower control systems," *Transportation Research Part C: Emerging Technologies*, vol. 9, no. 1, pp. 15–31, 2001.

[99] C. Nowakowski, S. E. Shladover, and D. Cody, "Cooperative adaptive cruise control: testing drivers' choices of following distances," University of California, Berkeley, California PATH Research Report, 2010.

[100] C. Nowakowski, S. E. Shladover, X.-Y. Lu, D. Thompson, and A. Kailas, "Cooperative adaptive cruise control (CACC) for truck platooning: Operational concept

alternatives," University of California, Berkeley, California PATH Research Report, 2015.

[101] E. Chan, P. Gilhead, P. Jelínek, P. Krejčí, and T. Robin, "Cooperative control of SARTRE automated platoon vehicles," in *19th ITS World Congress*. Vienna, Austria: ITS, 2012.

[102] E. Chan, *SARTRE automated platooning vehicles*. Wiley-Blackwell, 2016, ch. 10, pp. 137–150.

[103] J. Ploeg, S. Shladover, H. Nijmeier, and N. Van de Wouw, "Introduction to the special issue on the 2011 Grand Cooperative Driving Challenge," *IEEE Transactions on Intelligent Transportation Systems*, vol. 13, no. 3, pp. 989–993, 2012.

[104] A. Geiger, M. Lauer, F. Moosmann, B. Ranft, H. Rapp, C. Stiller, and J. Ziegler, "Team AnnieWAY's entry to the 2011 Grand Cooperative Driving Challenge," *IEEE Transactions on Intelligent Transportation Systems*, vol. 13, no. 3, pp. 1008–1017, 2012.

[105] L. Guvenc, I. M. C. Uygan, K. Kahraman, R. Karaahmetoglu, I. Altay, M. Senturk, M. T. Emirler, A. E. H. Karci, B. A. Guvenc, E. Altug, M. C. Turan, O. S. Tas, E. Bozkurt, U. Ozguner, K. Redmill, A. Kurt, and B. Efendioglu, "Cooperative adaptive cruise control implementation of team Mekar at the Grand Cooperative Driving Challenge," *IEEE Transactions on Intelligent Transportation Systems*, vol. 13, no. 3, pp. 1062–1074, 2012.

[106] J. Mårtensson, A. Alam, S. Behere, M. A. A. Khan, J. Kjellberg, K. Y. Liang, H. Pettersson, and D. Sundman, "The development of a cooperative heavy-duty vehicle for the GCDC 2011: Team Scoop," *IEEE Transactions on Intelligent Transportation Systems*, vol. 13, no. 3, pp. 1033–1049, 2012.

[107] C. Englund, L. Chen, J. Ploeg, E. Semsar-Kazerooni, A. Voronov, H. H. Bengtsson, and J. Didoff, "The Grand Cooperative Driving Challenge 2016: boosting the introduction of cooperative automated vehicles," *IEEE Wireless Communications*, vol. 23, no. 4, pp. 146–152, 2016.

[108] M. Aramrattana, J. Detournay, C. Englund, V. Frimodig, O. U. Jansson, T. Larsson, W. Mostowski, V. D. Rodrłguez, T. Rosenstatter, and G. Shahanoor, "Team Halmstad approach to cooperative driving in the Grand Cooperative Driving Challenge 2016," *IEEE Transactions on Intelligent Transportation Systems*, vol. 19, no. 4, pp. 1248–1261, 2018.

[109] A. Alam, B. Besselink, V. Turri, J. Martensson, and K. H. Johansson, "Heavy-duty vehicle platooning for sustainable freight transportation: A cooperative method to enhance safety and efficiency," *IEEE Control Systems*, vol. 35, no. 6, pp. 34–56, 2015.

[110] J. Larson, K. Y. Liang, and K. H. Johansson, "A distributed framework for coordinated heavy-duty vehicle platooning," *IEEE Transactions on Intelligent Transportation Systems*, vol. 16, no. 1, pp. 419–429, 2015.

[111] K.-Y. Liang, "Fuel-effcient heavy-duty vehicle platoon formation," PhD thesis, KTH Royal Institute of Technology, Stockholm, Sweden, 2016.

[112] V. Turri, B. Besselink, and K. H. Johansson, "Cooperative look-ahead control for fuel-efficient and safe heavy-duty vehicle platooning," *IEEE Transactions on Control Systems Technology*, vol. 25, no. 1, pp. 12–28, 2017.

[113] X.-Y. Lu and S. Shladover, "Integrated ACC and CACC development for heavy-duty truck partial automation," in *Proceeding of American Control Conference*, 2017, pp. 4938–4945.

[114] N. J. Goodall, B. B. Park, and B. L. Smith, "Microscopic estimation of arterial vehicle positions in a low-penetration-rate connected vehicle environment," *Journal of Transportation Engineering*, vol. 140, no. 10, p. 04014047, 2014.

[115] J. Argote-Cabañero, E. Christofa, and A. Skabardonis, "Connected vehicle penetration rate for estimation of arterial measures of effectiveness," *Transportation Research Part C: Emerging Technologies*, vol. 60, pp. 298–312, 2015.

[116] A. I. Delis, I. K. Nikolos, and M. Papageorgiou, "Simulation of the penetration rate effects of ACC and CACC on macroscopic traffic dynamics," in *2016 IEEE 19th International Conference on Intelligent Transportation Systems (ITSC)*, 2016, pp. 336–341.

[117] A. Validi, T. Ludwig, and C. Olaverri-Monreal, "Analyzing the effects of V2V and ADAS-ACC penetration rates on the level of road safety in intersections: Evaluating simulation platforms SUMO and scene suite," in *2017 IEEE International Conference on Vehicular Electronics and Safety (ICVES)*, 2017, pp. 38–43.

[118] J. I. Ge and G. Orosz, "Dynamics of connected vehicle systems with delayed acceleration feedback," *Transportation Research Part C: Emerging Technologies*, vol. 46, pp. 46–64, 2014.

[119] G. Orosz, "Connected cruise control: modeling, delay effects, and nonlinear behavior," *Vehicle System Dynamics*, vol. 54, no. 8, pp. 1147–1176, 2016.

[120] G. Orosz, J. I. Ge, C. R. He, S. S. Avedisov, W. B. Qin, and L. Zhang, "Seeing beyond the line of sight – controlling connected automated vehicles," *ASME Mechanical Engineering Magazine*, vol. 139, no. 12, pp. S8–S12, 2017.

[121] L. Zhang and G. Orosz, "Motif-based design for connected vehicle systems in presence of heterogeneous connectivity structures and time delays," *IEEE Transactions on Intelligent Transportation Systems*, vol. 17, no. 6, pp. 1638–1651, 2016.

[122] S. Yu and Z. Shi, "Dynamics of connected cruise control systems considering velocity changes with memory feedback," *Measurement*, vol. 64, pp. 34–48, 2015.

[123] S. S. Avedisov and G. Orosz, "Nonlinear network modes in cyclic systems with applications to connected vehicles," *Journal of Nonlinear Science*, vol. 25, no. 4, pp. 1015–1049, 2015.

[124] L. Zhang and G. Orosz, "Consensus and disturbance attenuation in multi-agent chains with nonlinear control and time delays," *International Journal of Robust and Nonlinear Control*, vol. 27, no. 5, pp. 781–803, 2017.

[125] J. I. Ge and G. Orosz, "Optimal control of connected vehicle systems with communication delay and driver reaction time," *IEEE Transactions on Intelligent Transportation Systems*, vol. 18, no. 8, pp. 2056–2070, 2017.

[126] C. R. He, W. B. Qin, N. Ozay, and G. Orosz, "Optimal gear shift schedule design for automated vehicles: Hybrid system based analytical approach," *IEEE Transactions on Control Systems Technology*, vol. PP, no. 99, pp. 1–13, 2018.

[127] T. G. Molnár, W. B. Qin, T. Insperger, and G. Orosz, "Application of predictor feedback to compensate time delays in connected cruise control," *IEEE Transactions on Intelligent Transportation Systems*, vol. 19, no. 2, pp. 545–559, 2018.

[128] J. I. Ge, G. Orosz, D. Hajdu, T. Insperger, and J. Moehlis, *To Delay or not to delay - stability of connected cruise control*. Springer, 2017, vol. 7, ch. 18, pp. 263–282.

[129] M. Huang, W. Gao, and Z.-P. Jiang, "Connected cruise control for a platoon of human-operated and autonomous vehicles using adaptive dynamic programming," in *36th Chinese Control Conference (CCC)*, 2017, pp. 9478–9483.

[130] ——, "Connected cruise control with delayed feedback and disturbance: An adaptive dynamic programming approach," *International Journal of Adaptive Control and Signal Processing*, pp. 1–15, 2017.

[131] A. A. Peters, "Stability and string stability analysis of formation control architectures for platooning," PhD thesis, National University of Ireland Maynooth, 2015.

[132] Y. Zheng, S. E. Li, K. Li, and L. Y. Wang, "Stability margin improvement of vehicular platoon considering undirected topology and asymmetric control," *IEEE Transactions on Control Systems Technology*, vol. 24, no. 4, pp. 1253–1265, 2016.

[133] L. Peppard, "String stability of relative-motion PID vehicle control systems," *IEEE Transactions on Automatic Control*, vol. 19, no. 5, pp. 579–581, 1974.

[134] D. Swaroop and J. K. Hedrick, "String stability of interconnected systems," *IEEE Transactions on Automatic Control*, vol. 41, no. 3, pp. 349–357, 1996.

[135] J. Eyre, D. Yanakiev, and I. Kanellakopoulos, "A simplified framework for string stability analysis of automated vehicles," *Vehicle System Dynamics*, vol. 30, no. 5, pp. 375–405, 1998.

[136] P. Cook, "Conditions for string stability," *Systems & Control Letters*, vol. 54, no. 10, pp. 991–998, 2005.

[137] L. Xiao and F. Gao, "Practical string stability of platoon of adaptive cruise control vehicles," *IEEE Transactions on Intelligent Transportation Systems*, vol. 12, no. 4, pp. 1184–1194, 2011.

[138] B. Besselink and K. H. Johansson, "String stability and a delay-based spacing policy for vehicle platoons subject to disturbances," *IEEE Transactions on Automatic Control*, vol. 62, no. 9, pp. 4376–4391, 2017.

[139] S. Stüdli, M. M. Seron, and R. H. Middleton, "Network systems and string stability," *CoRR*, vol. abs/1702.05826, 2017.

[140] I. Lestas and G. Vinnicombe, "Scalability in heterogeneous vehicle platoons," in *2007 American Control Conference*, 2007, pp. 4678–4683.

[141] L. Xiao, F. Gao, and J. Wang, "On scalability of platoon of automated vehicles for leader-predecessor information framework," in *2009 IEEE Intelligent Vehicles Symposium*, 2009, pp. 1103–1108.

[142] Y. Zheng, S. E. Li, J. Wang, D. Cao, and K. Li, "Stability and scalability of homogeneous vehicular platoon: Study on the influence of information flow topologies," *IEEE Transactions on Intelligent Transportation Systems*, vol. 17, no. 1, pp. 14–26, 2016.

[143] A. Askari, D. A. Farias, A. A. Kurzhanskiy, and P. Varaiya, "Measuring impact of adaptive and cooperative adaptive cruise control on throughput of signalized intersections," *CoRR*, vol. abs/1611.08973, 2016.

[144] A. Talebpour and H. S. Mahmassani, "Influence of connected and autonomous vehicles on traffic flow stability and throughput," *Transportation Research Part C: Emerging Technologies*, vol. 71, pp. 143–163, 2016.

[145] J. Lioris, R. Pedarsani, F. Y. Tascikaraoglu, and P. Varaiya, "Platoons of connected vehicles can double throughput in urban roads," *Transportation Research Part C: Emerging Technologies*, vol. 77, pp. 292–305, 2017.

[146] D. Yanakiev and I. Kanellakopoulos, "Nonlinear spacing policies for automated heavy-duty vehicles," *IEEE Transactions on Vehicular Technology*, vol. 47, no. 4, pp. 1365–1377, 1998.

[147] K. Santhanakrishnan and R. Rajamani, "On spacing policies for highway vehicle automation," *IEEE Transactions on Intelligent Transportation Systems*, vol. 4, no. 4, pp. 198–204, 2003.

[148] S. Tak, S. Park, and H. Yeo, "Comparison of various spacing policies for longitudinal control of automated vehicles," *Transportation Research Record: Journal of the Transportation Research Board*, vol. 2561, pp. 34–44, 2016.

[149] M. Wang, W. Daamen, S. P. Hoogendoorn, and B. van Arem, "Rolling horizon control framework for driver assistance systems. Part I: Mathematical formulation and non-cooperative systems," *Transportation Research Part C: Emerging Technologies*, vol. 40, pp. 271–289, 2014.

[150] S. Lee, B. G. Heydecker, J. Kim, and S. Park, "Stability analysis on a dynamical model of route choice in a connected vehicle environment," *Transportation Research Part C: Emerging Technologies*, 2017, available online.

[151] P. K. Khosla, "Effect of sampling rates on the performance of model-based control schemes," in *Dynamics of Controlled Mechanical Systems*, 1987, pp. 271–284.

[152] H. Hirata, "Sample rate effects on disturbance rejection for digital control systems," PhD thesis, Stanford University, Stanford, CA, 1989.

[153] G. Stépán, "Vibrations of machines subjected to digital force control," *International Journal of Solids and Structures*, vol. 38, no. 10, pp. 2149–2159, 2001.

[154] T. Insperger and G. Stépán, *Semi-Discretization for Time-Delay Systems: Stability and Engineering Applications*, ser. Applied Mathematical Sciences. Springer, 2011, vol. 178.

[155] S. Yi, P. W. Nelson, and A. G. Ulsoy, *Time-delay systems: Analysis and control using the Lambert W function*. World Scientific Publishing Co., 2010.

[156] T. Insperger and G. Stépán, *Semi-Discretization for Time-Delay Systems: Stability and Engineering Applications*. Springer, 2011.

[157] G. Stépán, *Retarded dynamical systems: stability and characteristic functions*. Longman Scienfific & Technical, 1989.

[158] K. Gu, V. L. Kharitonov, and J. Chen, *Stability of Time-Delay Systems*. Springer Science & Business Media, 2003.

[159] C. L. Phillips and H. T. Nagle, *Digital Control System Analysis and Design*, 3rd ed. Prentice-Hall, 1995.

[160] G. F. Franklin, M. L. Workman, and D. Powell, *Digital Control of Dynamic Systems*, 3rd ed., 1997.

[161] D. Caveney, "Cooperative vehicular safety applications," *IEEE Control Systems Magazine*, vol. 30, no. 4, pp. 38–53, 2010.

[162] A. F. Karr, *Probability*. Springer, 1993.

[163] K. J. Åström, *Introduction to Stochastic Control Theory*. Academic Press, Inc., 1970.

[164] Statlect, "Sequences of random variables and their convergence," http://www.statlect.com/seqrnd1.htm, accessed: 2015-01-19.

[165] R. Khasminskii, *Stochastic Stability of Differential Equations*, 2nd ed. Springer, 2012.

[166] L. Shaikhet, *Lyapunov Functionals and Stability of Stochastic Functional Differential Equations*. Springer, 2013.

[167] R. Krtolica, U. Ozguner, H. Chan, H. Goktas, J. Winkelman, and M. Liubakka, "Stability of linear feedback systems with random communication delays," in *Proceedings of the American Control Conference*, 1991, pp. 2648–2653.

[168] M. M. Gomez, G. Orosz, and R. M. Murray, "Stability of discrete-time systems with stochastically delayed feedback," in *European Control Conference*, 2013, pp. 2609–2614.

[169] O. Costa and M. Fragoso, "Stability results for discrete-time linear systems with markovian jumping parameters," *Journal of Mathematical Analysis and Applications*, vol. 179, no. 1, pp. 154–178, 1993.

[170] E. I. Verriest and W. Michiels, "Stability analysis of systems with stochastically varying delays," *Systems & Control Letters*, vol. 58, pp. 783–791, 2009.

[171] W. B. Qin and G. Orosz, "Digital effects and delays in connected vehicles: Linear stability and simulations," in *Proceedings of the ASME Dynamical Systems and Control Conference*, no. DSCC2013-3830. ASME, 2013, p. V002T30A001.

[172] ——, "Experimental validation on connected vehicles subject to digital effects and delays," *IEEE Transactions on Control Systems Technology*, 2018, under review.

[173] D. Smely, S. Rührup, R. K. Schmidt, J. Kenney, and K. Sjöberg, *Decentralized Congestion Control Techniques for VANETs*. Springer International Publishing, 2015, ch. 6, pp. 165–191.

[174] C. B. Math, H. Li, S. H. de Groot, and I. G. Niemegeers, "V2X application-reliability analysis of data-rate and message-rate congestion control algorithms," *IEEE Communications Letters*, vol. 21, no. 6, pp. 1285–1288, 2017.

[175] H.-J. G "The effect of decentralized congestion control on collective perception in dense traffic scenarios," *Computer Communications*, vol. 122, pp. 76–83, 2018.

[176] IEEE Std 1588-2008 (Revision of IEEE Std 1588-2002), "IEEE standard for a precision clock synchronization protocol for networked measurement and control systems," IEEE Instrumentation and Measurement Society, IEEE Standard, 2008.

[177] D. Mills, "Simple network time protocol (SNTP) version 4 for IPv4, IPv6 and OSI," *Network Working Group*, 2006.

[178] M. Ussoli and G. Prytz, "SNTP time synchronization accuracy measurements," in *2013 IEEE 18th Conference on Emerging Technologies Factory Automation (ETFA)*, 2013, pp. 1–4.

[179] S. Gao, A. Lim, and D. Bevly, "An empirical study of DSRC V2V performance in truck platooning scenarios," *Digital Communications and Networks*, vol. 2, no. 4, pp. 233 – 244, 2016.

[180] K. B. Howell, *Principles of Fourier Analysis*. Chapman & Hall/CRC, 2001.

[181] D. Bachrathy and G. Stépán, "Bisection method in higher dimensions and the efficiency number," *Periodica Polytechnica*, vol. 56, no. 2, pp. 81–86, 2012.

[182] H. Winner, *Adaptive Cruise Control*. Springer London, 2012, ch. 24, pp. 613–656.

[183] W. B. Qin and G. Orosz, "Experimental validation on connected cruise control with flexible connectivity topologies," *IEEE/ASME Transactions on Mechatronics*, 2018, under review.

[184] W. B. Qin, M. M. Gomez, and G. Orosz, "Stability analysis of connected cruise control with stochastic delays," in *Proceedings of the American Control Conference*, 2014, pp. 4624–4629.

[185] M. M. Gomez, W. B. Qin, G. Orosz, and R. M. Murray, "Exact stability analysis of discrete-time linear systems with stochastic delays," in *Proceedings of the American Control Conference*, 2014, pp. 5534–5539.

[186] W. B. Qin, M. M. Gomez, and G. Orosz, "Moment-based plant and string stability analysis of connected cruise control with stochastic delays," in *Proceedings of the American Control Conference*, 2015, pp. 2747–2752.

[187] ——, "Stability and frequency response under stochastic communication delays with applications to connected cruise control design," *IEEE transaction on Intelligent Transportation Systems*, vol. 18, no. 2, pp. 388–403, 2017.

[188] V. Gupta, A. F. Dana, J. P. Hespanha, R. M. Murray, and B. Hassibi, "Data transmission over networks for estimation and control," *IEEE Transactions on Automatic Control*, vol. 54, no. 8, pp. 1807–1819, 2009.

[189] F. Bai and H. Krishnan, "Reliability analysis of DSRC wireless communication for vehicle safety applications," in *Proceedings of the IEEE Intelligent Transportation Systems Conference*. IEEE, 2006.

[190] I. Kolmanovsky and T. Makenberg, "Stochastic stability of a class of nonlinear systems with randomly varying time-delay," in *Proceedings of the American Control Conference*, 2000, pp. 4304–4308.

[191] P. Park, "A delay-dependent stability criterion for systems with uncertain time-invariant delays," *IEEE Transactions on Automatic Control*, vol. 44, no. 4, pp. 876–877, 1999.

[192] H. Gao and T. Chen, "New results on stability of discrete-time systems with time-varying state delay," *IEEE Transactions on Automatic Control*, vol. 52, no. 2, pp. 328–334, 2007.

[193] D. Yue, Y. Zhang, E. Tian, and C. Peng, "Delay-distribution-dependent exponential stability criteria for discrete-time recurrent neural networks with stochastic delay," *IEEE Transactions on Neural Networks*, vol. 19, no. 7, pp. 1299–1306, 2008.

[194] C. Kuehn, *Moment Closure – A Brief Review*. Cham: Springer International Publishing, 2016, pp. 253–271.

[195] W. Feller, *An Introduction to Probability Theory and Its Applications*. John Wiley & Sons, Inc., 1950, vol. 1.

[196] W. B. Qin and G. Orosz, "Scalable stability analysis on large connected vehicle systems subject to stochastic communication delays," *Transportation Research Part C: Emerging Technolgies*, vol. 83, pp. 39–60, 2017.

[197] L. N. Trefethen and D. Bau, III, *Numerical Linear Algebra*. SIAM, 1997.

[198] A. Laub, *Matrix Analysis for Scientists and Engineers*. The Society for Industrial and Applied Mathematics, 2005.

[199] B. J. Olson, S. W. Shaw, C. Shi, C. Pierre, and R. G. Parker, "Circulant matrices and their application to vibration analysis," *Appl. Mech. Rev*, vol. 66, no. 4, 2014.

[200] C. F. Loan, "The ubiquitous Kronecker product," *Journal of Computational and Applied Mathematics*, vol. 123, no. 1-2, pp. 85–100, 2000.

[201] M. Davio, "Kronecker products and shuffle algebra," *IEEE Transactions on Computers*, vol. C-30, no. 2, pp. 116–125, 1981.

[202] H. V. Henderson and S. R. Searle, "On deriving the inverse of a sum of matrices," *SIAM Review*, vol. 23, no. 1, pp. 53–60, 1981.

[203] P. J. Davis, *Circulant Matrices*. John Wiley & Sons, Inc., 1979.

[204] H. Kushner, *Introduction to Stochastic Control*. Holt, Rinehart and Winston, Inc., 1971.